

A COMPARISON OF STAR FORMATION WITHIN
THE GALACTIC CENTRE AND GALACTIC DISC

Ashley Thomas Barnes

A thesis submitted in partial fulfilment of the requirements of
Liverpool John Moores University
for the degree of
Doctor of Philosophy.
May 8, 2018

For my parents and grandparents.

Abstract

Stars are of fundamental importance to the entire field of astronomy. The conversion of elements and the distribution of energy throughout the lifetime of stars drives the evolution of the Universe. Despite this, we do not have a unified understanding of the formation process for all stars. This thesis attempts to move forward this understanding, by focussing on the question: *How do the initial conditions of star-forming regions vary across environments, and do these influence the process of star formation?*

To investigate the initial conditions of star formation, regions on the verge of forming stars have to be first identified and analysed. These regions have to be untouched by the disruptive effects of stellar feedback, such that the natal conditions of the gas – e.g. kinematics and chemistry – are not destroyed. Quiescent regions that are expected to form low-mass stars have been well studied over the past few decades, and the general process of low-mass star formation is well understood. Only relatively recently, however, has a group of objects being identified as being potential hosts of these initial stages of high-mass star formation: Infrared Dark Clouds (IRDCs). The study of these objects is difficult, due to both their rarity and complexity. An end-to-end understanding of high-mass star formation is, therefore, much less developed compared to their lower mass counterparts.

This thesis presents the study of a sample of IRDCs within the Disc and Centre of the Milky Way; two *very* different environments. Several key aspects of the star formation process within IRDCs from these environments are investigated.

Firstly, a chemical signpost – the deuterium fraction of N_2H^+ – is used to identify the regions of dense and cold gas on the verge of forming high-mass stars within a quiescent Disc IRDC, which can be used to study the initial conditions for star formation. Omitting potential beam dilution effects, chemical modelling suggests that the cloud

could have reached a global chemical equilibrium, and, if so, would also be dynamically old (survived for several free-fall times). This timescale, with estimates of the embedded stellar mass, is used to determine star formation rates and efficiencies.

Secondly, the kinematic structures within two apparently similar Disc IRDCs are identified using dense gas tracers – C^{18}O and N_2H^+ . The properties of these structures appear to be very similar, hinting at a similar formation scenario for both clouds, or, potentially, that these may be inherent to the larger Disc IRDC population. The dynamics of these filaments also show that they may be merging, which would suggest a compressive mode of turbulence driving. These structures are then linked to the larger kinematic structures – identified using a lower density tracing molecule, ^{13}CO – and found to show good coherence with the brightest, most extended structures. These are then placed in the context of the previously identified Galactic scale structures, and in doing so show that IRDCs could be the densest parts of much larger arm or inter-arm filamentary structures.

Thirdly, the level of star formation within the Galactic Centre is investigated on both global (~ 100 pc) and local (~ 1 pc) scales. On a global scale, the star formation rate has been determined from all the available observational star formation diagnostics – i.e. direct counting of young stellar objects and integrated light measurements – and found to be in agreement with previous studies; i.e. around one-to-two orders of magnitude lower than predicted by the star formation models. On individual cloud scales, the star formation efficiency per free-fall time is in better agreement with the model predictions. However, uncertainties on the properties of these regions, such as the mode of turbulence driving, limit the further verification or falsification of the star formation theories.

Lastly, the investigation of the local scale star formation within the Galactic Centre highlighted a particular part of the parameter space as the most promising to further test the star formation theories. In light of this, high-spatial resolution ALMA observations have been taken of two Galactic Centre clouds within this regime. Early results show that they have a complex structure, similar to that seen within Disc IRDCs, containing both filamentary and core-like features. Investigation of the brightest, most compact

core region shows that it contains a very rich chemistry, and, of particular interest, is the rigorous detection of the pre-biotic molecule formamide (NH_2CHO).

When placing the results of this thesis in the bigger context of star formation theory, they appear to show interesting implications for the initially posed question – what is the influence of environment on the process of star formation? It is found here that despite the very different cloud scale properties of these regions, the star formation efficiency per free-fall time is surprisingly similar. To investigate this, the properties of the individual sites of high-mass star formation, the high-mass star-forming cores, are compared. Interestingly, despite the different environmental conditions, several key properties of the cores, such as their size and mass distribution, are also found to be very similar.

The similarity of high-mass core properties and star formation rate per free fall time implies that once a region has produced high-mass cores, the evolution of these cores towards star formation must be similar. The difference in the global/environmental properties of the gas must then be setting the total star formation rate within these regions, by limiting the number of cores that can form. In particular, the mode of turbulence driving may play a major role in governing the fraction of gas that can be converted into stars per free-fall time within these two environments.

Publications

Within this thesis, the work within Chapters 2, 3 and 4 has been presented in the following jointly authored publications:

- 1 *Widespread deuteration across the IRDC G035.39-00.33*
Barnes A. T., Kong S., Tan J. C., Henshaw J. D., Caselli P., Jimnez-Serra I., Fontani F., 2016, MNRAS, 458, 1990
- 2 *Similar complex kinematics within two massive, filamentary infrared dark clouds*
Barnes A. T., Henshaw J. D., Caselli P., Jimnez-Serra I., Tan J. C., Fontani F., Pon A., and Ragan S., 2018, MNRAS, 475, 5268
- 3 *Star formation rates and efficiencies in the Galactic Centre*
Barnes A. T., Longmore S. N., Battersby C., Bally J., Kruijssen J. M. D., Henshaw J. D., Walker D. L., 2017, MNRAS, 469, 2263

Whilst writing this thesis, A. T. Barnes has also contributed to following publications:

- 4 *H₂O Southern Galactic Plane Survey (HOPS): Paper III - properties of dense molecular gas across the inner MilkyWay*
Longmore, S. N., Walsh, A. J., Purcell, C. R., Burke, D. J., Henshaw, J., Walker, D., Urquhart, J., **Barnes A. T.**, et al., 2017, MNRAS, 470, 1462L
- 5 *¹⁵N fractionation in infrared-dark cloud cores*
Zeng, S., Jimnez-Serra, I., Cosentino, G., Viti, S., **Barnes A. T.**, Henshaw, J. D., Caselli, P., Fontani, F., Hily-Blant, P., 2017, A&A, 603A, 22Z

- 6 *Unveiling the early-stage anatomy of a protocluster hub with ALMA*
Henshaw, J. D., Jimnez-Serra, I., Longmore, S. N., Caselli, P., Pineda, J. E.,
Avison, A., **Barnes A. T.**, Tan, J. C., Fontani, F., 2017, MNRAS, 464L, 31H
- 7 *Investigating the structure and fragmentation of a highly filamentary IRDC*
Henshaw, J. D., Caselli, P., Fontani, F., Jimnez-Serra, I., Tan, J. C., Longmore,
S. N., Pineda, J. E., Parker, R. J., **Barnes A. T.**, 2016, MNRAS, 463, 146H
- 8 *Molecular gas kinematics within the central 250 pc of the Milky Way*
Henshaw, J. D., Longmore, S. N., Kruijssen, J. M. D., Davies, B., Bally, J.,
Barnes A. T., et al., 2016, MNRAS, 457, 2675H

And the following conference proceedings:

- 9 *Star formation rates on global and cloud scales within the Galactic Centre*
Barnes A. T., Longmore, S. N., Battersby, C., Bally, J., Kruijssen, J. M. D.,
2017, IAUS, 322, 147B
- 10 *^{15}N fractionation in infrared-dark clouds*
Zeng, S., Jimnez-Serra, I., Cosentino, G., Viti, S., **Barnes A. T.**, Henshaw, J. D.,
Caselli, P., Fontani, F., Hily-Blant, P., 2017, A&A, 360
- 11 *Using young massive star clusters to understand star formation and feedback in
high-redshift-like environments*
Longmore, S., **Barnes A. T.**, Battersby, C., Bally, J., Kruijssen, J. M. Diederik,
Dale, J., Henshaw, J., Walker, D., Rathborne, J., Testi, L., Ott, J., Ginsburg, A.,
2014, EAS, 75, 43L

Contents

Contents	iv
List of Tables	ix
List of Figures	xi
1 Introduction	1
1.1 Molecular clouds	1
1.1.1 Observables within molecular clouds	2
1.1.2 Structure	10
1.1.3 Formation mechanism	11
1.2 Star formation	14
1.2.1 Star formation timescales	17
1.2.2 Density probability distribution function	19
1.2.3 Core and stellar initial mass function (CMF/IMF)	20
1.2.4 Low-mass star formation	22
1.2.5 High-mass star formation	24
1.3 High-mass star-forming regions	26
1.3.1 Chemistry	27

1.3.2	Kinematics	30
1.4	Star formation in different environments	31
1.4.1	Environmentally independent relations	31
1.4.2	Environmentally dependent models	33
1.4.3	An extreme environment to test star formation	37
1.5	Observational techniques	40
1.5.1	Receivers	40
1.5.2	Types of telescope	43
2	Widespread deuteration across the IRDC G035.39-00.33	51
2.1	Preface	51
2.2	Introduction	51
2.2.1	IRDC G035.39-00.33	52
2.3	Observations	53
2.4	Results	55
2.5	Analysis	59
2.5.1	Column density	59
2.5.2	Deuterium fraction	59
2.6	Discussion	60
2.6.1	Comparison to other star-forming regions	60
2.6.2	Comparison to the physical properties of the cloud	62
2.6.3	Comparison with chemical models	63
2.6.4	Caveats of the Kong et al. (2015) chemical model	69

2.7	Summary	70
3	Similar complex kinematics within two massive, filamentary infrared dark clouds	72
3.1	Preface	72
3.2	Introduction	72
3.2.1	IRDC G034.43+00.24	73
3.2.2	Observational tools required to investigate the kinematic structure	75
3.3	Observations	77
3.4	Results	79
3.4.1	Moment analysis	79
3.4.2	Channel map analysis	81
3.5	Analysis	83
3.5.1	Spectral line fitting and velocity coherent features	83
3.5.2	Velocity gradients	90
3.5.3	Comparing the N_2H^+ (1 – 0) and C^{18}O (1 – 0) centroid velocities	91
3.5.4	Velocity dispersions	94
3.6	CO depletion	96
3.7	Discussion	97
3.7.1	The kinematic structure of Cloud F	98
3.7.2	Cloud F in the context of other star-forming regions	102
3.7.3	Connection between IRDC and GMC scales for Cloud F	111

3.8	Conclusions	118
4	Star formation rates and efficiencies in the Galactic Centre	120
4.1	Preface	120
4.2	Introduction	120
4.3	Bolometric luminosity maps of the Galactic Centre	124
4.4	Global (~ 100 pc) scale star formation	131
4.4.1	Determining the global star formation rate	131
4.4.2	Comparison to star formation rates within the literature	132
4.4.3	Comparison to star formation rates predicted from theoretical models	136
4.4.4	Implications for the global star formation rate	138
4.5	Local (~ 1 pc) scale star formation	139
4.5.1	Determining the gas and embedded stellar masses from infrared observations	139
4.5.2	Determining the embedded stellar masses from additional observations	141
4.5.3	Uncertainties	143
4.5.4	Deriving the star formation efficiency and star formation rates	151
4.5.5	Deriving the star formation efficiency per free-fall time assuming a model of tidally triggered star formation	153
4.5.6	Comparison to theoretical models	155
4.6	Discussion and conclusions	162
5	Investigating the Galactic Centre clouds with ALMA	170

5.1	Preface	170
5.2	Introduction	170
5.3	Observations	171
5.3.1	ALMA interferometric observations	171
5.3.2	Combination of the ALMA and single dish continuum observations	177
5.3.3	ALMA line observations	178
5.4	Results	181
5.4.1	Preliminary results: moment maps analysis	181
5.4.2	Preliminary results: examination of the cores	191
5.5	Summary	198
6	Conclusions	201
6.1	Summary	201
6.2	Future work	208
6.2.1	Primary objective	208
6.2.2	Secondary objective	213
A	ALMA observations	216
	Bibliography	230

List of Tables

1.1	Table of the critical densities and star formation efficiency per free-fall time for the different environmentally dependant models for star formation.	36
1.2	Table of angular resolutions attainable with infrared, radio and optical single dish telescopes.	43
2.1	Parameters of G035.39-00.33 IRAM-30m observations.	53
2.2	Table of results from the Kong et al. (2015) chemical model.	66
3.1	Physical properties of IRDC G034.43+00.24 and G035.39-00.33.	75
3.2	Parameters of G034.43+00.24 IRAM-30m observations	78
3.3	Parameters of G034.43+00.24 N_2H^+ (1 – 0) and C^{18}O (1 – 0) velocity components.	87
3.4	Parameters of G034.43+00.24 ^{13}CO (1 – 0) velocity components.	114
4.1	Summary of Galactic centre survey data	126
4.2	Luminosities towards several Galactic Centre sources.	129
4.3	Summary of various star formation rate conversion factors.	133
4.4	Summary of star formation rate measurements within the literature.	137
4.5	Properties of the Galactic Centre sources.	152

4.6	Properties of the Galactic Centre sources with star formation assumptions.	156
4.7	Summary of parameters used for Figures 4.7, 4.8 and 4.9.	166
5.1	Information of ALMA Galactic Centre observations.	173
5.2	Parameters of ALMA observations	173
5.3	Table molecular transitions identified from ALMA observations. . . .	182
5.4	Continued from Table 5.3.	183
5.5	Continued from Table 5.3.	184
5.6	Continued from Table 5.3.	185
5.7	Continued from Table 5.3.	186
5.8	Continued from Table 5.3.	187
5.9	Properties of the Galactic Centre cores.	191
6.1	Physical properties of IRDCs.	209
A.1	Table of unidentified lines from ALMA Galactic Centre observations.	216

List of Figures

1.1	An example of a Bok Globule and a Filament.	3
1.2	Kennicutt-Schmidt relation plot originally produced by Bigiel et al. (2008) , taken here from Kennicutt & Evans (2012)	15
1.3	Extinction probability distribution function of Lupus V and Lupus I, taken from Kainulainen et al. (2009)	19
1.4	Examples of several initial mass functional forms, taken from Offner et al. (2014)	20
1.5	The column density threshold relation from Lada et al. (2012)	33
1.6	Predicted density probability distribution functions from Krumholz & McKee (2005)	38
1.7	The Galactic Centre observed with <i>Spitzer</i> and <i>Herschel</i>	39
1.8	Example of the down-converting of emission by a heterodyne receiver.	41
1.9	Schematic of a single-dish telescope and an interferometer.	46
2.1	Mass surface density map of G035.39-00.33 (Kainulainen & Tan, 2013).	54
2.2	Average N_2D^+ ($2 - 1$) across G035.39-00.33.	56
2.3	Individual spectra of N_2D^+ ($2 - 1$) across G035.39-00.33.	57
2.4	Integrated intensity maps of N_2D^+ ($2 - 1$) and N_2H^+ ($1 - 0$) across G035.39-00.33.	58

2.5	Deuterium fraction map of G035.39-00.33.	60
2.6	Column densities of N_2H^+ and N_2D^+ across G035.39-00.33, compared to other low- and high-mass star-forming regions.	61
2.7	Column densities of N_2H^+ and N_2D^+ , mass surface density and CO depletion across G035.39-00.33.	64
2.8	Time evolution of OPR^{H_2} and $D_{frac}^{N_2H^+}$ from Kong et al. (2015) chemical models.	67
2.9	Time to reach the observed $D_{frac}^{N_2H^+}$ from Kong et al. (2015) chemical models.	68
3.1	Mass surface density map of G035.39-00.33 (Kainulainen & Tan, 2013).	74
3.2	Average N_2H^+ (1 – 0) and $C^{18}O$ (1 – 0) across G034.43+00.24.	78
3.3	Moment maps of N_2H^+ (1 – 0) and $C^{18}O$ (1 – 0) across G034.43+00.24.	80
3.4	Channel maps of N_2H^+ (1 – 0) and $C^{18}O$ (1 – 0) across G034.43+00.24.	82
3.5	Individual spectra of N_2H^+ (1 – 0) across G034.43+00.24.	84
3.6	Individual spectra of $C^{18}O$ (1 – 0) across G034.43+00.24.	85
3.7	Position-position-velocity diagrams of N_2H^+ (1 – 0) and $C^{18}O$ (1 – 0) across G034.43+00.24.	86
3.8	Maps of $V_{LSR}(N_2H^+ - C^{18}O)$ across G034.43+00.24 and G035.39-00.33.	92
3.9	Histograms of $V_{LSR}(N_2H^+ - C^{18}O)$ across G034.43+00.24 and G035.39-00.33.	92
3.10	Histograms of velocity dispersions across G034.43+00.24 and G035.39-00.33.	95
3.11	Average spectrum of the N_2H^+ (1 – 0) and $C^{18}O$ (1 – 0) across G035.39-00.33.	103

3.12	Individual spectra of N_2H^+ (1 – 0) and C^{18}O (1 – 0) across G035.39-00.33.	104
3.13	Position-position-velocity diagrams of N_2H^+ (1 – 0) and C^{18}O (1 – 0) across G035.39-00.33.	105
3.14	Individual spectra of ^{13}CO (1 – 0) across G034.43+00.24.	113
3.15	Position-position-velocity diagrams of ^{13}CO (1 – 0) across G034.43+00.24.	116
4.1	Average spectral energy distribution within Galactic Centre.	124
4.2	Maps of 24 μm , 70 μm , warm and cool luminosities.	125
4.3	Warm and cool luminosities as a function of galactic longitude.	129
4.4	Three colour map of the Galactic Centre.	142
4.5	Radius against mass for Galactic Centre sources.	144
4.6	Luminosity against mass for clusters.	149
4.7	Star formation efficiency per free-fall time as a function of Mach number, virial parameter and magnetic field strength, calculated with the original fiducial values and a turbulence driving parameter, $b = 0.33$	161
4.8	Star formation efficiency per free-fall time as a function of Mach number, virial parameter and magnetic field strength, calculated with the fiducial values from Federrath & Klessen (2012) and a turbulence driving parameter, $b = 0.33$	163
4.9	Star formation efficiency per free-fall time as a function of Mach number, virial parameter and magnetic field strength, calculated with the fiducial values from Federrath & Klessen (2012) and a turbulence driving parameter, $b = 0.22$	164

4.10	Star formation efficiency per free-fall time as a function of function of turbulence driving parameter.	165
5.1	BOLOCAM observations across the Galactic Centre (Ginsburg et al., 2013), showing coverage of ALMA observations.	171
5.2	Continuum observations of Cloud D.	179
5.3	Continuum observations of Cloud E/F.	180
5.4	Moment maps of HCN $v=0(3-2)$ and $\text{HCO}^+(3-2)$ towards Cloud D.	188
5.5	Moment maps of HCN $v=0(3-2)$ and $\text{HCO}^+(3-2)$ towards Cloud E/F.	189
5.6	Moment maps of c-HCCCH $v=0(7(0,7)-6(1,6))$ towards Clouds D and E/F.	190
5.7	Continuum observations of both clouds, plotted on same intensity and spatial scale.	193
5.8	Cloud E/F core 1 spectra.	194
5.9	Cloud E/F core 1 spectra.	195
5.10	Cloud E/F core 2 spectra.	196
5.11	Cloud E/F core 2 spectra.	197
5.12	Moment maps and spectra of NH_2CHO towards the Cloud E/F core 1 region.	199
5.13	Moment maps and spectra of HCN $v=0(3-2)$ and $\text{HCO}^+(3-2)$ in Cloud E/F core 1 region.	200
6.1	Mass-radius plot for Galactic Centre and Disc cores and clouds	206
6.2	Mass surface density maps of the IRDC sample.	212

6.3	A preliminary 5 GHz VLA continuum image.	215
A.1	Moment maps of lines detected in Cloud D.	217
A.2	Moment maps of lines detected in Cloud D.	218
A.3	Moment maps of lines detected in Cloud E/F.	219
A.4	Moment maps of lines detected in Cloud E/F.	220
A.5	Moment maps of lines detected in Cloud E/F.	221
A.6	Moment maps of lines detected in Cloud E/F.	222
A.7	Moment maps of lines detected in Cloud E/F.	223
A.8	Moment maps of lines detected in Cloud E/F.	224
A.9	Moment maps of lines detected in Cloud E/F.	225
A.10	Moment maps of lines detected in Cloud E/F.	226
A.11	Moment maps of lines detected in Cloud E/F.	227
A.12	Moment maps of lines detected in Cloud E/F.	228
A.13	Moment maps of lines detected in Cloud E/F.	229

Chapter 1

Introduction

The lifecycle of stars is one of the fundamental drivers in the development of the current day universe. In particular, high-mass stars ($> 8 M_{\odot}$) are thought to play a dominant role in this evolution, due to the large amounts of energy, momentum and enriched material which they disperse throughout their lifetimes. The initial conditions of the gas which forms both high- and low-mass stars effectively govern their stellar lifecycles, hence it is crucial to have a complete understanding of the star formation process if we are to understand its broad influence on the Universe.

This thesis investigates how star formation varies across the range of environments present within the Milky Way. To do so, the chemical, kinematic and star forming properties on various scales are studied within two *very* different environments: i) the “mundane” environment of the Galactic Disc and ii) the “extreme” environment present within the Galactic Centre. In this section, the relevant background required for the thesis is presented.

1.1 Molecular clouds

The interstellar medium (ISM) can be split into its constituent phases of gas (e.g. [Field, Goldsmith & Habing, 1969](#); [McKee & Ostriker, 1977](#); [Ikeuchi, Habe & Tanaka, 1984](#)).

The process of star formation, however, is exclusively observed within only the densest ($n_{\text{H}_2} \sim 10^{2-5} \text{ cm}^{-3}$), coldest ($T \sim 10 - 30 \text{ K}$) of these: the molecular phase (Stahler & Palla, 2005). The molecular phase of the ISM typically resides within so-called molecular “clouds”; referred to this way due to their resemblance to clouds seen on Earth. Indeed, in the photographic plates from the initial survey of these objects by Barnard (1919), an example of which is shown in the left panel of Figure 1.1, several highly extinct cloud-like structures can be seen against the background emission from the Milky Way. Accurate distance measurements to molecular clouds have allowed us to determine their physical properties, and we now know their mass and size distributions range by orders of magnitude. For example, Bok Globules are the approximately sub-parsec scale, one-to-ten Solar mass objects (Bok & Reilly, 1947; Launhardt et al., 2010; see right panel of Figure 1.1), whilst giant molecular clouds can span hundreds of parsecs and contain millions of Solar masses of gas (GMCs; e.g. Roman-Duval et al., 2010; Ragan et al., 2014; Hernandez & Tan, 2015). As the formation processes, evolutionary stages and properties of these clouds are intrinsically linked to the stars which they can produce, this section gives an overview of our current understanding of molecular clouds, beginning with how their properties are determined from astronomical observations.

1.1.1 Observables within molecular clouds

1.1.1.1 Molecules

Molecular clouds are primarily composed of molecular hydrogen (H_2 ; ~ 70 per cent of the mass) and inert atomic helium (~ 28 per cent of the mass; Allen, 1973). Neither of these, however, emit strongly at the temperatures found within molecular clouds ($T \sim 10 - 30 \text{ K}$). The remaining mass of molecular clouds is within so-called metals (~ 2 per cent), the majority of which is in the form of interstellar dust (see section 1.1.1.2 for an introduction), but also included is, for example, water (H_2O), carbon monoxide (CO), molecular nitrogen (N_2), hydrogen peroxide (OH). Again, however, not all of these molecules can emit strongly within molecular clouds. Those which

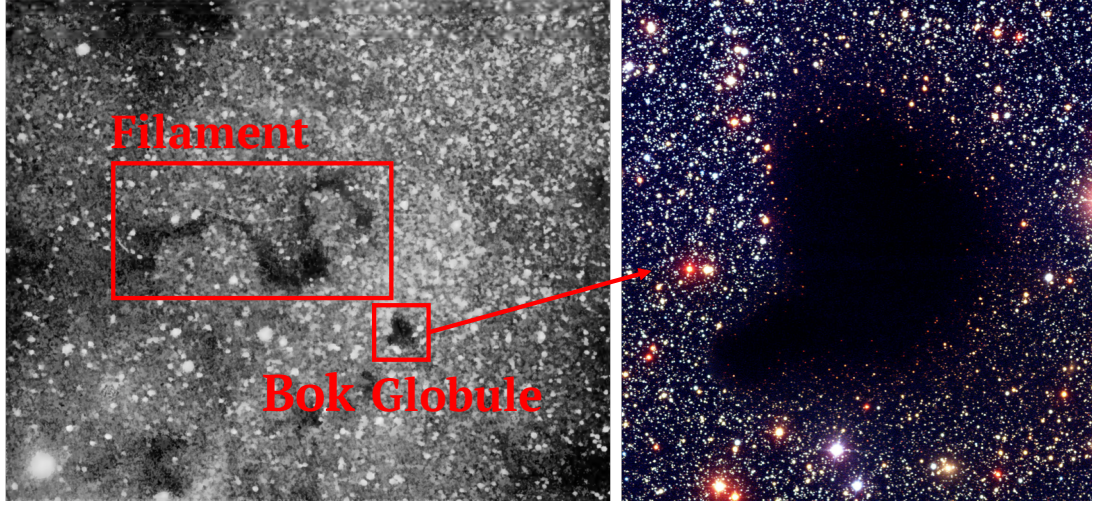


Figure 1.1: [left panel] Photographic plate taken from [Barnard \(1919\)](#) towards the region north of Theta Ophiuchi, which shows extended extinction features against the background stellar population of the Milky Way. Highlighted are regions classified as a “Bok Globule” ([Barnard 68](#); [Bok & Reilly, 1947](#)) and a “Filament” ([Schneider & Elmegreen, 1979](#)). [right panel] The region identified as highly obscured region Barnard 68, taken in the optical using the FOcal Reducer and low dispersion Spectrograph on the Very Large Telescope (credit ESO).

have a permanent dipole moment are typically the easiest to observe, due to the low excitation energies required for molecular rotational transitions. In the simplest case, the pure rotational energy levels of a diatomic molecule are described by a single quantum number, J , and its moment of inertia, $I = mr_e^2$, where m is the molecular reduced mass¹ and r_e is the equilibrium nuclear separation. Transitions between energy levels are limited by the selection rule $\Delta J = \pm 1$, hence the difference in energy, ΔE_{rot} , between levels J and $J - 1$ can be described by,

$$\Delta E_{\text{rot}} = h\nu = 2BJ = \frac{h^2 J}{4\pi^2 m r_e^2}, \quad J = 1, 2, 3 \dots \quad (1.1)$$

where ν is the frequency of the photon produced by the transition, $B = \hbar^2/2I$ is the rotational constant, \hbar is the reduced Planck constant, and h is the Planck constant. Observationally, CO is a particularly useful molecule as its rotational transitions have rest frequencies (or wavelengths, λ) in the sub-millimetre to millimetre range where the atmospheric transmission is high and therefore can be easily observed by ground-

¹The reduced mass for a two component system is given as $m = (m_a m_b)/(m_a + m_b)$, where m_a and m_b are the masses of the constituent molecules.

based telescopes; not the case with, for example, the transitions of H₂O.

As the current understanding of molecular clouds, and their properties, comes from their emission (or absorption), the next few paragraphs give a brief overview of radiative transfer theory, and presented in Section 1.5 is an overview of how the current generation telescopes are used to detect this emission/absorption.

The observed emission, or intensity, I_ν , of a source at a given frequency ν , can be simply described as the sum of the background and cloud's emission, minus the emission lost due to absorption by the cloud. These two can be encapsulated in the following loss, $dI_{\nu-}$, and gains terms, $dI_{\nu+}$, defined for an emitting slab of thickness, ds ,

$$\frac{dI_\nu}{ds} = \frac{dI_{\nu-}}{ds} + \frac{dI_{\nu+}}{ds} = -\kappa_\nu I_\nu + \varepsilon_\nu, \quad (1.2)$$

where κ_ν is the linear absorption coefficient, and ε_ν emissivity. The optical depth, τ_ν , can be described as $d\tau_\nu = -\kappa_\nu ds$, such that

$$\frac{dI_\nu}{d\tau_\nu} + I_\nu = \frac{\varepsilon_\nu}{\kappa_\nu}. \quad (1.3)$$

If a region is in local thermal dynamic equilibrium, when the emission and absorption are equal, then Kirchhoff's law states that,

$$\frac{\varepsilon_\nu}{\kappa_\nu} = B_\nu(T). \quad (1.4)$$

Here the Planck function is given in terms of frequency, $B_\nu(T)$, as,

$$B_\nu(T) = \frac{2h\nu^3}{c^2} \frac{1}{\exp(h\nu/k_B T) - 1}, \quad (1.5)$$

where c is the speed of light, k_B is Boltzmann's constant, and T is the temperature. With equations 1.4 and 1.5, the integral of equation 1.3 becomes the equation of radiative transfer,

$$I_\nu = I_0 \exp(-\tau_\nu) + B_\nu(T)[1 - \exp(-\tau_\nu)], \quad (1.6)$$

where I_0 is the background intensity. In radio astronomy, it is useful to use the concept

of a “brightness temperature”, T_b , which is defined as the temperature of a blackbody which would give the observed intensity, I_ν , within the observed frequency range. At radio wavelengths $h\nu/k_B T \ll 1$, and so $\exp(h\nu/k_B T) \approx h\nu/k_B T$, hence the Planck function simplifies to the Rayleigh-Jeans law,

$$B_\nu(T) \approx \frac{2\nu^2}{c^2} k_B T. \quad (1.7)$$

The equation of radiative transfer (equation 1.6) can, therefore, be written as the so-called “detection equation”,

$$T_b = T_{\text{bg}} \exp(-\tau_\nu) + T[1 - \exp(-\tau_\nu)]. \quad (1.8)$$

For the sake of simplicity, assuming that $T_{\text{bg}} = 0$, then there are two limiting cases for this equation. In the optically thin case, where $\tau_\nu \ll 1$, then $T_b = \tau_\nu T$, whereas in the optically thick case where $\tau_\nu \gg 1$, then $T_b = T$.

The observed emission in the optically thin regime is simply a sum of the emission of each emitting molecule along the line of sight (i.e. within the telescope beam). Therefore, the total energy isotropically emitted per cubic metre per second from a transition from energy level j to i is given as $h\nu_{ji} n_j A_{ji}$, where the n_j is the number density for level j (cm^{-3}), and A_{ji} is Einstein coefficient for the rate of spontaneous emission of a photon (s^{-1}). A difficulty arises here, however, in the calculation of the number density,

$$n_j = n_i \frac{g_j}{g_i} \exp(-h\nu_{ji}/k_B T), \quad (1.9)$$

where g_j and g_i are the statistical weights of levels j (upper) and i (lower), respectively. As, ideally, within molecular clouds the excitation/de-excitation occurs by collisions with other molecules, and hence the temperature, T , can be described by the kinetic temperature, T_{kin} (i.e. the thermalised case, where equation 1.9 directly applies). However, it is possible that other mechanisms may be controlling the level populations, and in this case T is described by a generic “excitation temperature”, T_{ex} (e.g. where $T_{\text{ex}} < T_{\text{bg}}$, where an additional term in equation 1.9 is required).² The transition be-

²This regime is present when $n_{\text{H}_2} < n_{\text{crit}}$ (see equation 1.10).

tween these two regimes occurs when the collisional (de-excitation) rate is equal to the rate of spontaneous emission of a photon (de-excitation rate). This happens at a critical density, n_{crit} ,

$$n_{\text{crit}} = \frac{A_{ji}}{\langle \sigma_{\text{cross}} v_{\text{therm}} \rangle}, \quad (1.10)$$

where σ_{cross} is the collisional cross section of a molecule and v_{therm} is the thermal velocity of the gas.³ The CO molecule has $\sigma_{\text{cross}} \sim 10^{-15} \text{ cm}^2$, $A_{ji} \sim 10^{-9} \text{ s}^{-1}$, and $v_{\text{therm}} \sim 10^5 \text{ cm s}^{-1}$, which gives $n_{\text{crit}}(\text{CO}) \sim 10^3 \text{ cm}^{-3}$.

Alternatively, [Evans \(1999\)](#) introduced the notion of a more observationally motivated “effective” critical density, defined when the integrated intensity from a transition equals 1 K km s^{-1} . This was produced for reference to sub-thermally excited emission, detected towards regions with densities below the observed line’s critical density. Expanding upon this, recently [Shirley \(2015\)](#) used radiative transfer modelling to determine this effective critical density for several commonly observed molecular transitions (e.g. NH_3 , HCN , HCO^+). These authors found that the critical densities of these lines can be up to one to two orders of magnitude higher than the effective critical density. The effective critical density for CO was not calculated by either of these works, nevertheless, as typical densities within molecular clouds are $> 10^3 \text{ cm}^{-3}$, CO is typically assumed to be a good tracer of the bulk molecular gas.

Accurate measurements of the density distribution within molecular clouds are difficult to obtain, as only the projected structure can be observed. The volume density integrated along the line-of-sight is called the column density, N_{tot} , which, in the optically thin regime ($\tau_\nu < 1$), can be determined as (derived from equation 1.8, without the Rayleigh Jeans law),

$$N_{\text{tot}} = \frac{8\pi W}{\lambda^3 A_{ji}} \frac{g_i}{g_j} \frac{1}{J_\nu(T_{\text{ex}}) - J_\nu(T_{\text{bg}})} \frac{1}{1 - \exp(-h\nu/k_B T_{\text{ex}})} \frac{Q_{\text{rot}}}{g_i \exp(-E_i/k_B T_{\text{ex}})}, \quad (1.11)$$

where W is the integrated intensity of the line, A_{ji} is the Einstein coefficient for a transition from energy level j to i , λ is the wavelength of photon emitted from the

³Where $v_{\text{therm}} \approx (3k_B T/m_H)^{1/2}$, where T is the cloud temperature ($\sim 30 \text{ K}$), m_H is the mass of hydrogen and k_B is the Boltzmann constant.

transition (see equation 1.1), $J_\nu(T_{\text{ex}})$ and $J_\nu(T_{\text{bg}})$ are the equivalent Rayleigh-Jeans excitation temperature T_{ex} , and background temperature T_{bg} , E_i is the energy of the lower energy level. In the regime where only rotational transitions are possible, the number of degenerate states is given as $g_J = 2J + 1$, hence the allowed rotational energies are,

$$E_J = J(J + 1)hB, \quad (1.12)$$

where the symbols are identical to equation 1.1, and the partition function, Q_{rot} is given as,

$$Q_{\text{rot}} = \sum_{J=0}^{\infty} g_J \exp(-E_J/k_B T_{\text{ex}}) = \sum_{J=0}^{\infty} (2J + 1) \exp(-E_J/k_B T_{\text{ex}}). \quad (1.13)$$

The dimensionless molecular abundances of molecules, which can be determined by dividing their column densities to that expected from molecular hydrogen (see Section 1.1.1.2), are used for comparison to chemical models (e.g. Kong et al., 2015). Frerking, Langer & Wilson (1982) determine the abundance of CO to be 8.5×10^{-5} within the Solar neighbourhood. This, however, is seen to vary across different environments within the Galaxy. For example, using the abundance gradients in the Galactic Disc from Wilson & Matteucci (1992) and the abundance of CO from Frerking, Langer & Wilson (1982), Fontani et al. (2006) find that the abundance of CO can be given as $X^{\text{ref}}(\text{CO}) = 9.5 \times 10^{-5} \exp(1.105 - 0.13 d_{\text{GC}})$, where d_{GC} is the Galactocentric distance.

Following the discussion so far presented here, it would appear that CO is an ideal tracer of bulk gas properties. Indeed, it is common to directly convert the intensity of CO into a molecular hydrogen mass, i.e. total molecular gas mass, using the so-called ‘‘X-factor’’ (Bolatto, Wolfire & Leroy, 2013). Discussed below are several problems of using CO emission as a tracer of all the molecular gas.

Firstly, recent simulations by Duarte-Cabral & Dobbs (2016), have shown that molecular hydrogen can exist at densities within the sub-thermally excited regime of CO; in ‘‘CO-dark’’ gas. This CO-dark gas is typically extended across large spatial scales

($\sim 10 - 100$ pc), where the density is lower than the CO critical density ($\sim 10^3$ cm $^{-3}$). The amount of dark molecular gas is inherently hard to measure. Nevertheless, several studies have suggested that it could be responsible for 20 – 70 per cent of a given cloud’s mass (Langer et al., 2014; Tang et al., 2016), and potentially equal to the mass of the Milky Way inferred from CO (Grenier, Casandjian & Terrier, 2005).

Secondly, towards regions of high column density, molecular line emission can become optically thick ($\tau_\nu > 1$; i.e. when an emitted photon cannot leave the medium without being re-absorbed). Emission is weakened within these regions, which, if not accounted for, can cause measurements of the column density and abundance to be significantly underestimated. Higher J -transition observations, which have higher critical densities, can be used to mitigate this effect. Alternatively, isotopologues can be used (for CO, e.g. ^{13}CO and C^{18}O), as these are typically less abundant and, therefore, their emission lines also have lower optical depths.

Thirdly, towards the very densest and coldest regions within molecular clouds CO can “freeze-out” (or deplete) onto dust-grain surfaces, and therefore cannot emit (Caselli et al., 1999). However, unlike CO, nitrogen-bearing species do not freeze out, and, in particular, NH_3 , HCN and N_2H^+ , appear to actually preferentially trace dense and cold gas. This is due to the fact that CO, largely frozen out, is unable to effectively destroy their molecular ion precursors (Caselli et al., 2002a), and that nitrogen chemistry takes longer to evolve, so large fractions of the volatile nitrogen can still be in the gas phase within dense, cold regions (Flower, Pineau Des Forêts & Walmsley, 2006). CO depletion, therefore, can boost the formation of nitrogen-bearing species within molecular clouds. Along with these, to date,⁴ around 200 molecules have been observed across the ISM, many of which are also useful probes of molecular cloud properties (Section 1.3.1 for further discussion on deuterated molecular species).

⁴As of January 2018 (<https://www.astro.uni-koeln.de/cdms/molecules>).

1.1.1.2 Dust

An additional crucial component of the ISM is dust, despite only constituting around a percent of the total mass. Within molecular clouds, the dust grains are thought to have a core, formed of silicates and carbon, surrounded by a mantle of ices and molecules depleted from the gas (e.g. CO), and have continuous power-law size distribution from ~ 0.001 to $1.0 \mu\text{m}$ (Mathis, Rumpl & Nordsieck, 1977; Draine & Lee, 1984).⁵ The grains are responsible for extinction at comparable wavelengths to their sizes, hence in the optical to near-infrared regimes (as shown in Figure 1.1). At mid-infrared to millimetre wavelengths, on the other hand, the dust grains can be seen in emission. These processes can both be described by the equation of radiative transfer, shown in equation 1.6. This represents the sum of: i) the incident intensity attenuated by the total optical depth, $I_0 \exp(-\tau_\nu)$, ii) plus the source emission attenuated by the optical depth, $B_\nu [1 - \exp(-\tau_\nu)]$.

At optical to near-infrared wavelengths, for typical molecular cloud column densities, the dust obscures the background emission. As the optical depth at these wavelengths is very high ($\tau_\nu > 1$), hence the background term tends to zero, leaving $I_\nu \rightarrow 0$. Furthermore, at these wavelengths, $h\nu \gg k_B T$, therefore the cloud's own black-body emission is negligible. The now typically adopted conversion from extinction to column density of molecular hydrogen is given as (Bohlin, Savage & Drake, 1978; Fitzpatrick, 1999)

$$N(\text{H}_2)/A_v = 9.4 \times 10^{20} \text{ cm}^{-2} \text{ mag}^{-1}, \quad (1.14)$$

where A_v is the extinction seen at $\sim 5510 \text{ \AA}$.

At longer wavelengths ($> 100 \mu\text{m}$), for typical molecular cloud column densities, the optical depth is typically low ($\tau_\nu < 1$), and equation 1.6 can be simplified using a Taylor expansion to $I_\nu = I_0 + \tau_\nu B_\nu$. Strong background emission sources which are

⁵The power-law distribution from Mathis, Rumpl & Nordsieck (1977) takes the form, $\frac{dn}{da} \propto na^{-3.5}$, where n is the dust-grain number density and a is the dust grain radius. This distribution, therefore, gives that the majority of the total dust grain mass is within large dust grains and the majority of the total area is within small grains. Several more recent works have extended the distribution to smaller ($< 10^3$ Carbon atoms) Polycyclic aromatic hydrocarbons (PAHs) to account for the significant extinction seen at UV wavelengths (Weingartner & Draine, 2001; Draine, 2009).

both extended and unassociated with the molecular cloud of interest are typically not observed at these longer wavelengths, and therefore $I_\nu = \tau_\nu B_\nu$. The optical depth can be expressed as $\tau_\nu = \Sigma \kappa_\nu$, where Σ (g cm^{-2}) is the mass surface density and κ_ν ($\text{g}^{-1} \text{cm}^2$) is the linear absorption coefficient (Ossenkopf & Henning, 1994). At mid-to-far infrared wavelength the dust opacity can be approximated as $\kappa_\nu = \kappa_0 (\nu/\nu_0)^\beta$, where $\nu_0 = 505 \text{ GHz}$, $\kappa_0 = 4.0 \text{ cm}^2 \text{ g}^{-1}$ and $\beta = 1.75$ (Battersby et al., 2011). With this approximation, measurements of the dust emission at these wavelengths can be used to determine both the dust temperature and mass surface density (or column density) of the cloud. It is, therefore, possible to get the important physical parameters of molecular clouds from both dust extinction and continuum measurements.

1.1.2 Structure

Observations of molecular clouds show that they have complex hierarchical structure (e.g. Blitz & Stark, 1986). Despite their self-similar nature, Williams, Blitz & McKee (2000) developed a now widely used, yet still controversial, nomenclature of three distinct structure groups: “clouds”, “clumps” and “cores”. The clouds represent the largest scale ($\sim 1 - 100 \text{ pc}$), most massive ($\sim 10^{2-6} M_\odot$), and least dense ($\sim 10^{1-3} \text{ cm}^{-3}$) structures in the hierarchy. Recent evidence suggests that the largest clouds could span a significant length of the Milky Way’s spiral arms (Ragan et al., 2014; Zucker, Battersby & Goodman, 2015, 2017). Within clouds are then clumps, which are typically referred to having scales of $\sim 0.1 - 1 \text{ pc}$, masses of $\sim 10^{1-2} M_\odot$, and densities $\sim 10^{3-4} \text{ cm}^{-3}$. These are the intermediate structures which are expected to form bound stellar clusters (see Section 1.2). The individual sites of the star, and binary-star, formation are described as “cores”, which have sizes $\sim 0.01 - 0.1 \text{ pc}$, masses $\sim 10^{0.1-1} M_\odot$, and, importantly for star formation, the highest densities of $\sim 10^{4-6} \text{ cm}^{-3}$ and lowest temperatures $T \sim 5 - 15 \text{ K}$ (e.g. Polychroni et al., 2013).

This relatively simple classification does, however, have several issues. Firstly, it is very difficult to conclusively determine if a core will result in the formation of an individual star. Indeed, several protostellar cores, identified in single-dish observations,

have been shown to fragment when using interferometric observations (e.g. [Pineda et al., 2011b, 2015](#)). This can be a particular issue for the most massive cores, as these are typically seen at larger distances (see Section 1.2.5), and hence the spatial resolution achievable with current generation telescopes can be limited (c.f. [Henshaw et al., 2014, 2017](#)).

Secondly, cloud structures do not appear simple and circular, but rather complex and filamentary (see review by [André, 2017](#)). For example, highlighted in Figure 1.1 is a cloud which was classified as being filamentary in the first dedicated study of these structures ([Schneider & Elmegreen, 1979](#)). More recently, the interest in filaments has significantly increased with the advent of high-resolution, space-based mid-to-far-infrared telescopes (e.g. *Herschel*; [Pilbratt et al., 2010](#)). As surveys such as the *Herschel* infrared Galactic Plane Survey (Hi-GAL; [Molinari et al., 2010](#)) and the *Herschel* Gould Belt Survey ([André et al., 2010](#)) have revealed the ubiquity of filaments within star-forming regions across the Milky Way ([André et al., 2010](#); [Meñshchikov et al., 2010](#); [Arzoumanian, 2011](#)). In addition, the majority of star formation appears to reside within filamentary structures ([Könyves et al., 2015](#); [Marsh et al., 2016](#)), which suggests that they may play a role in the mass accretion process (e.g. [Peretto et al., 2013](#); [Hacar et al., 2017](#); [Motte, Bontemps & Louvet, 2017](#)).

1.1.3 Formation mechanism

The different formation mechanisms of molecular clouds, and the short or long lifetimes which they infer, are still a subject of much ongoing debate. In general, these formation mechanisms can be split into two broad categories. The “bottom-up” scenario, where clouds are produced by the agglomeration of less massive clouds, and the “top-down” scenario, where clouds form from the large-scale flows and/or instabilities present across the Galaxy.

In the bottom-up scenario, molecular clouds are produced by the agglomeration of independent atomic hydrogen clouds through the process of inelastic cloud-cloud collisions. This process is thought to be most prominent within the spiral arms of the

Milky Way, where the large-scale gravitational potential allows clouds to gather to high number densities, which can then collapse through their own self-gravity (Casoli & Combes, 1982; Kwan & Valdes, 1987). The continuous cloud-cloud collision process provides an efficient mechanism for replenishing the turbulence within the growing cloud, and hence producing the near virial state observed in the majority of molecular clouds (Tasker & Tan, 2009). Recent estimates of the timescales involved in this formation mechanism are, however, very large. McKee & Ostriker (2007), for example, estimate that even in the ideal case, that a cloud of $10^6 M_{\odot}$ produced from $10^4 M_{\odot}$ clouds via this process would have a formation timescale of ~ 40 Myrs; longer than the time taken for stellar feedback to completely disrupt the cloud ($\sim 20 - 30$ Myr; Krumholz, Matzner & McKee, 2006).

In light of the bottom-up scenario's shortfalls (Blitz & Shu, 1980), a top-down scenario for cloud formation was introduced (e.g. Elmegreen, 1979). This top-down scenario can be split into two further sub-scenarios of how the gas is concentrated from the large scales, either by converging flows or Galactic instabilities. In the former, large-scale, low-density atomic hydrogen flows collide and condense to form dense molecular clouds at the collision interface (Vázquez-Semadeni et al., 2007). Several dynamic processes within the Galaxy have been proposed to drive these supersonic flows, such as expanding H II regions, supernova remnants and spiral density waves (Hartmann, Ballesteros-Paredes & Bergin, 2001; Heitsch et al., 2008). Gómez & Vázquez-Semadeni (2014) show that this scenario can produce filamentary structures similar to those seen in observations, and suggest that this mechanism may be responsible for their formation.

In the top-down formation scenario caused by Galactic instabilities, two processes could trigger the collapse of clouds. These are typically referred to as the Parker instability (Parker, 1966) and Jeans instability (Jeans, 1902; Toomre, 1964). The Parker instability occurs when the magnetic field, which, when in equilibrium is parallel the Galactic plane, is distorted out of the plane. This causes ions to fall along the field lines, back into the plane where the gravitational potential is lowest. The now lighter region containing this bent magnetic field feels a buoyancy out of the plane, which then

further pushes the field out of the plane, causing the instability to grow. This process, in theory, would be most favourable within the spiral arms of the Galaxy, where the density difference in-and-out of the Galactic plane is highest (Mouschovias, Shu & Woodward, 1974). However, simulations have shown that this is a self-limiting process, and cannot form structures similar to the largest observed molecular clouds (e.g. Kim, Ostriker & Stone, 2002).

In the Jeans instability scenario, self-gravity can lead to a runaway gravitational collapse in the absence of external mechanisms. A limiting factor within the Disc of the Galaxy is, however, shear, which can be described via the Toomre Q parameter (Toomre, 1964),

$$Q = \frac{\kappa c_s}{\pi G \Sigma_{\text{gal}}}. \quad (1.15)$$

Here κ is the epicyclic frequency, c_s is the mean sound speed of the gas, G is the gravitational constant, Σ_{gal} is the mean gas surface density. This equation represents the balance of rotational support and gravitational collapse, in the approximation of an infinitely flat, unmagnetised disc, where gravitational collapsing regions can form if Q is sufficiently low. Several numerical simulations of systems with a finite disc height, magnetic fields, and stellar feedback show that gravitationally bound clouds can form when $Q < 1.5$ (e.g. Kim, Ostriker & Stone, 2003). To get the most realistic picture of star formation, however, the spiral arm structure of the Galaxy has to be taken into account, as this has a strong influence on the gas dynamics. When doing so, Shetty & Ostriker (2006) find gas condensations with masses up to $\sim 10^7 M_\odot$, hence the upper end of the observed molecular cloud mass spectrum.

In reality, the cloud formation process is not the product of any one formation mechanism, but rather a combination of those described above. As Krumholz, Matzner & McKee (2006) suggest, it is likely that the top-down scenario is primarily responsible for largest structures ($\sim 10^{5-7} M_\odot$), whereas the bottom-up scenario is responsible for clouds on smaller scales ($\sim 10^{1-4} M_\odot$).

Here, several fundamental aspects of molecular clouds have been discussed, which are placed in the context of star formation in the following section.

1.2 Star formation

As discussed in the previous section, molecular clouds come in a variety of forms, which can harbour a complex structure and can be formed by several mechanisms. Nevertheless, in the most simplistic sense, the process of forming a star is the same throughout; occurring when gravity dominates the dynamics and collapse can occur. When this happens the cloud can collapse over a free-fall time,

$$t_{\text{ff}} = \left(\frac{\pi^2 R_c^3}{8GM_c} \right)^{1/2} = \left(\frac{3\pi}{32G\rho_c} \right)^{1/2}, \quad (1.16)$$

where R_c is the radius of cloud, M_c is the total mass of the cloud, G is gravitational constant and ρ_c is the average cloud density. Taking a typical molecular cloud number density of 10^3 cm^{-3} , i.e. close to the critical density of CO (see Section 1.1.1.1), gives a free-fall time of $\sim 1 \text{ Myr}$. If the total molecular gas mass within the Milky Way ($\sim 5 \times 10^8 M_\odot$; e.g. Roman-Duval et al., 2016) was collapsing to form stars over this timescale, we would observe a star formation rate higher than $100 M_\odot \text{ yr}^{-1}$. This, however, is not the case; the observed star formation rate is around two orders of magnitude lower ($\sim 1 M_\odot \text{ yr}^{-1}$; Murray & Rahman, 2010; Lee, Murray & Rahman, 2012). The fraction of the total cloud mass, M_{gas} , which is converted into stellar mass, $M_{*,\text{tot}}$, referred to as the star formation efficiency,

$$\epsilon \equiv \frac{M_{*,\text{tot}}}{M_{\text{gas}} + M_{*,\text{tot}}}, \quad (1.17)$$

must, therefore, be very low; around a few per cent (e.g. Myers et al., 1986). The inefficiency of star formation is not limited to our own Milky Way, but also extends to galaxies which harbour similar environments (e.g. Leroy et al., 2017). Shown in Figure 1.2 is the so-called “Kennicutt-Schmidt relation”, which is the relation between the star formation rate surface density and the total (atomic and molecular) gas surface density (Schmidt, 1959; Kennicutt, 1998b). The diagonal lines shown on the plot are values of constant ϵ . This plot, originally produced by Bigiel et al. (2008), has been split into three gas mass surface density regimes, represented by the vertical dashed

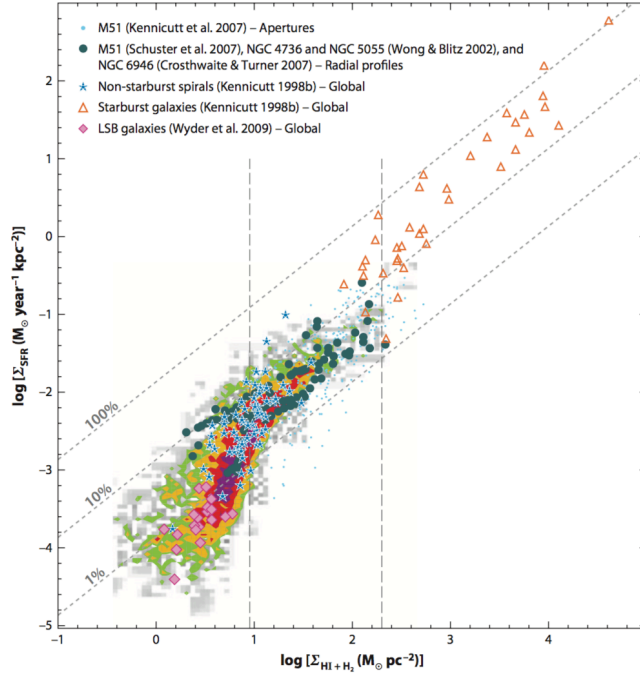


Figure 1.2: A plot originally produced by [Bigiel et al. \(2008\)](#), taken here from [Kennicutt & Evans \(2012\)](#), showing the star formation rate surface densities against the total (atomic and molecular) gas surface densities for various sets of measurements (see [Bigiel et al., 2008](#) and references therein). The three dotted grey diagonal lines extending from lower left to upper right reflect a constant global star-formation efficiency, $\epsilon = [1, 10, 100]$ per cent (see equation 1.17). The vertical dashed lines separate the low, moderate and high gas mass surface density regimes.

lines. In the lower two density regimes, which includes galaxies similar to our own, the ϵ stays within a few per cent. Only at the highest gas mass surface density regime, observed within extreme starburst galaxies, does ϵ appear to significantly increase. To account for the inefficiency of star formation, several mechanisms have been proposed which inhibit the gravitational collapse of molecular clouds.

The virial parameter, α_{vir} , is the most simplistic and typically used quantity to describe the stability of a cloud. In the ideal case of a spherical cloud of uniform density supported by only kinetic energy (i.e. no magnetic fields), the virial parameter can take the form ([Jeans, 1902](#)),

$$\alpha_{\text{vir}} = \frac{5\sigma_{\nu}^2 R_c}{GM_c}, \quad (1.18)$$

where σ_{ν} is the line-of-sight velocity dispersion, and the other parameters are equivalent to those in equation 1.16. When $\alpha_{\text{vir}} < 2$ the cloud is sub-virial and should

collapse, whereas if $\alpha_{\text{vir}} > 2$ the cloud is super-virial and should expand. The cloud can then only be stable when $\alpha_{\text{vir}} = 2$. The majority of clouds are observed to be in this stable state, both within the Milky Way (e.g. [Heyer et al., 2009](#)) and other Galaxies (e.g. [Leroy et al., 2016](#)).

The correlations between the masses, sizes and velocity dispersions – the three parameters in the virial equation – of star-forming regions are well known, and referred to as the “Larson relations” ([Larson, 1981](#)),⁶

$$\sigma_\nu(\text{kms}^{-1}) = 1.43 R_c(\text{pc})^{0.38}, \quad (1.19)$$

$$\sigma_\nu(\text{kms}^{-1}) = 0.42 M_c(M_\odot)^{0.20} \quad (1.20)$$

hence,

$$\langle n_{\text{H}_2} \rangle (\text{cm}^{-3}) = 1600 R_c(\text{pc})^{-1.10}, \quad (1.21)$$

where n_{H_2} is number density of molecular hydrogen within the cloud. The interpretation of these relations is that the motion of the gas within clouds, as measured from the velocity dispersion of molecular line emission, are dominated by random turbulence. The turbulence is composed of a hierarchy of different size isotropic “eddies”, through which the turbulent energy cascades from the largest scale (input from an e.g. large-scale colliding flow) down to the scale where the energy can be effectively dissipated by the cloud ([Kolmogorov, 1941](#)). Indeed, within most molecular clouds the non-thermal, turbulent, component of the velocity dispersion is larger than the thermal velocity dispersion, or the sound speed of the gas,

$$c_s = \sqrt{\frac{k_B T}{\mu m_{\text{H}}}}, \quad (1.22)$$

where μ_{H_2} is the mean molecular weight of the gas ($\mu_{\text{H}_2} = 2.33$ a.m.u). The Larson relations have been further investigated by many studies across a range of environments, both within our own Galaxy and within other galaxies ([Solomon et al., 1987](#); [Bolatto et al., 2008](#); [Shetty et al., 2012](#); [Kauffmann et al., 2016](#)). Despite some variation of the

⁶Shown here in terms of the cloud radius for comparison to equation 1.18.

power-law index, a consequence of these relations is that the vast majority of molecular clouds are close to virial equilibrium.

1.2.1 Star formation timescales

Several theories have been proposed to account for the inefficiency of star formation within molecular clouds, which are based on the complex interplay of turbulence (with the addition of magnetic fields) and gravity (see review [Ballesteros-Paredes et al., 2007](#)). These can be split into two regimes, governed by the molecular cloud lifetimes that they infer: i.e. long (supported) or short (transient) lived.

1.2.1.1 Star formation within supported molecular clouds

In the classical star formation scenario, support against gravitational collapse is provided by thermal gas pressure and magnetic fields ([Shu, Adams & Lizano, 1987](#)). Magnetic fields can provide support within molecular clouds, by inhibiting the flow of ions perpendicular to the magnetic field lines ([Mouschovias & Spitzer, 1976](#)). Collapse can still proceed, however, as neutrals can still drift across the field lines, albeit with drag caused by the ions, via the process of ambipolar diffusion ([Mestel & Spitzer, 1956](#)). The timescale over which it would take the magnetic field to return to its original configuration, after being distorted by the collapse of the cloud, is referred to as the ambipolar diffusion timescale, t_{AD} , which can be defined as,

$$t_{\text{AD}} = \frac{4\pi n_i n_n m_n L^2 \langle \sigma v_{\text{drift}} \rangle}{B^2} \approx 10 (n_{\text{H}_2}/10^4 \text{cm}^{-3})^{-1.42} \text{Myr} \quad (1.23)$$

where n_i and n_n are the number densities of the ions and neutrals, respectively, m_n is the neutral molecular mass, L is the diameter of the cloud, $\langle \sigma v_{\text{drift}} \rangle$ is the momentum transfer rate coefficient for ion-neutral scattering, and B is the magnetic field strength. An approximation for how the ambipolar diffusion timescale depends on the hydrogen number density can be determined by following the assumptions from [Draine \(2011\)](#), which is also shown above. Assuming a typical average cloud density, this timescale

is much longer than the free-fall time of the gas (e.g. for $n_{\text{H}_2} = 10^4 \text{ cm}^{-3}$, $t_{\text{AD}} \sim 10 \text{ Myr}$, and $t_{\text{ff}} \sim 0.3 \text{ Myr}$), hence the scenario of magnetic field support posits a slow mode of star formation (Mac Low & Klessen, 2004). A recent addition to this theory is super-sonic turbulence, which allows star formation to progress on shorter timescales (e.g. Heitsch et al., 2004). To account for the decay of turbulence within these regions, constant turbulence driving is required (e.g. Mac Low et al., 1998; Mac Low, 1999), via, for example, outflows from the newly formed stars (e.g. Carroll et al., 2009) or the gravitational collapse and accretion of material onto the cloud (Vázquez-Semadeni, Cantó & Lizano, 1998; Vázquez-Semadeni et al., 2010).

In this general picture, molecular clouds are long-lived, or dynamically old ($> t_{\text{ff}}$), structures, which are close to a global virial equilibrium (see equation 1.18). Star formation can still proceed on the small scales, within compact sub-virial parts of the cloud. However, as this accounts for only a small fraction of the total cloud's mass, this process is inefficient.

1.2.1.2 Star formation within transient molecular clouds

An alternative, more recently proposed scenario is that molecular clouds are transient structures, which produce stars and disperse over a short timescale (Ballesteros-Paredes, Hartmann & Vázquez-Semadeni, 1999). Such clouds could be, for example, produced by the top-down colliding flow scenario of molecular clouds formation, as discussed within Section 1.1.3 (also see Vázquez-Semadeni et al., 2007). In this scenario, the dense molecular gas is formed on a very short timescale ($\sim 1 \text{ Myr}$; Hartmann, Ballesteros-Paredes & Bergin, 2001), which could then quickly collapse and form stars. The feedback from these newly formed stars then quickly causes the dispersal of the host cloud, halting further star formation. This would then naturally explain the small age spread observed within recently formed clusters, such as within Taurus ($\sim \text{few Myr}$; Palla & Stahler, 2000). Moreover, this scenario does not require a mechanism for the constant driving of turbulence for support.

In this general picture, molecular clouds are short-lived, or dynamically young ($\sim t_{\text{ff}}$),

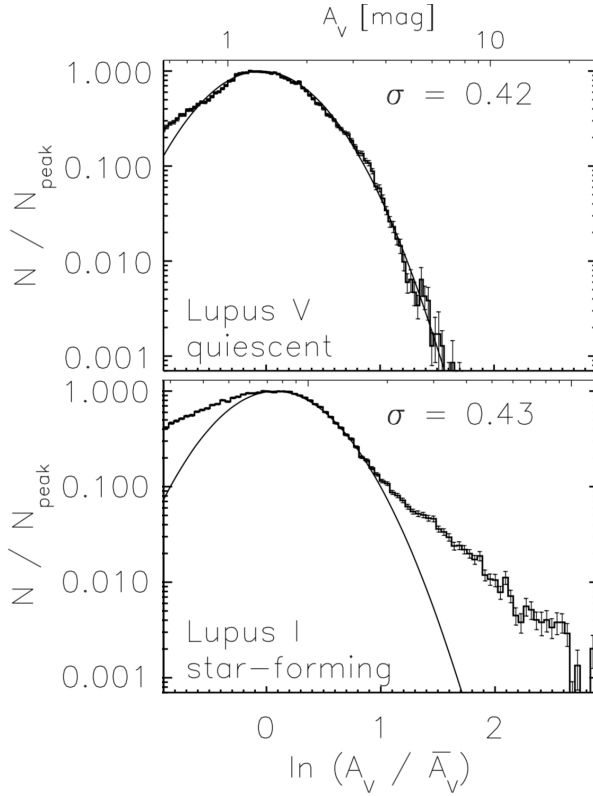


Figure 1.3: A plot taken from [Kainulainen et al. \(2009\)](#), showing the extinction (i.e. column density; see equation 1.14) probability distribution function for [upper panel] Lupus V, quiescent source, and [lower panel] Lupus I, an actively star-forming source. Note that both sources show a log-normal distribution at low values of extinction, however, only the star-forming source has a power-law component at high extinction values.

structures, which quickly produce stars. However, as these stars are formed, they begin to release a large amount of energy and momentum, which causes the dispersal of the host cloud. This transient nature of the clouds allows for an overall low star formation efficiency.

1.2.2 Density probability distribution function

A natural outcome of hierarchical turbulence within virialised molecular clouds is the formation of a log-normal density distribution (ρ -PDF; [Vazquez-Semadeni, 1994](#)). When turbulence is dominant, any given independent parcel of gas within the cloud experiences random turbulent shocks, which cause cumulative density enhancements. In the central limit theorem, these independent compressions cause the density probability distribution function to have a log-normal profile (e.g. [Ostriker, Stone & Gammie, 2001](#)). Observationally, using stellar extinction measurements towards IC 5146 (also see [Lada et al., 1994](#)), [Padoan, Jones & Nordlund \(1997\)](#) were the first to identify this log-normal density distribution. Such distributions are now thought to be common

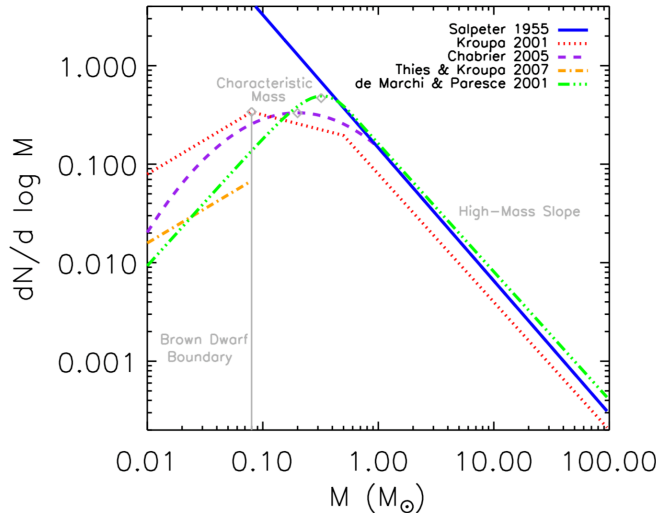


Figure 1.4: A plot originally produced by [Offner et al. \(2014\)](#), showing the different forms of the stellar initial mass function. Apart from the [Salpeter \(1955\)](#) slope, the profiles have been normalised such that the integrated mass is unity.

within quiescent molecular clouds ([Padoan et al., 2014](#)), an example of which is shown in [Figure 1.3](#) ([Kainulainen et al., 2009](#)).

As molecular clouds become sub-virial, and gravity dominates over the turbulent motions, their probability distribution functions show an additional power-law component at the higher densities (referred to as a “power-law tail”). The material within the power-law tail is found towards the dense core regions, which are gravitationally collapsing (e.g [Nordlund & Padoan, 1999](#)). As clouds evolve, these existing cores can grow and increase in density. Additionally, lower density material can become unstable, and begin to collapse into cores. Over time, this causes the cloud’s log-normal distributions to diverge to a power-law at increasingly lower densities, and the power-law exponent to decrease (see discussion in [Padoan et al., 2014](#)). Shown in [Figure 1.3](#) is the extinction probability distribution function for the star-forming source Lupus I, which contains both log-normal and power-law components ([Kainulainen et al., 2009](#)).

1.2.3 Core and stellar initial mass function (CMF/IMF)

It is currently unclear how, and if, there is any link between the density probability distribution function of molecular clouds and the mass distribution function of their resultant young stellar populations (or IMF; see [Offner et al., 2014](#)). It could be intriguing, nonetheless, that despite the many functional forms of the IMF, the most commonly used of which are presented in [Figure 1.2.3](#) (see [Offner et al., 2014](#)), all show a broadly

similar distribution that is qualitatively comparable to the log-normal ρ -PDF from star forming regions. Several authors have proposed that there is a link between the stellar IMF and the mass distribution of gravitationally bound cores within star forming regions, in a so-called “core mass function” (CMF; e.g. [Alves, Lombardi & Lada, 2007](#); [Kainulainen & Tan, 2013](#); [Könyves et al., 2015](#)). This link was originally proposed by [Alves, Lombardi & Lada \(2007\)](#), as an explanation for the similar shape of the mass distribution of the dense core population within the Pipe nebula, identified using near-infrared extinction maps, and an IMF. These authors suggested that a $\epsilon \sim 30$ per cent could explain the systematic offset of the CMF distribution towards higher masses. However, it must be noted any links between the gas mass distribution (either through the ρ -PDF or CMF) and the stellar mass function is still highly debated (e.g. [Goodwin et al., 2008](#)), and many caveats have to be considered when doing so (e.g. the stellar binary fraction).

Despite the open question on the formation of the IMF, the form of the IFM has been well studied for several decades, and, in general, it is found to be “universal”, showing little variation as a function of both environment and cosmic time (see [Bastian, Covey & Meyer, 2010](#)). A typically used approximation is to describe the IMF as a composite of power-laws, which take the form,

$$dN/d\log(m) \propto m^{-\Gamma}, \quad (1.24)$$

where m is the mass of a star, N is the number of stars within a logarithmic mass bin $\log m + d\log(m)$. Over a non-logarithmic mass range this can be expressed as,

$$dN/dm \propto m^{-\alpha}, \quad \alpha = \Gamma + 1, \quad (1.25)$$

where α and Γ are the slopes of the mass function. For example, the IMF proposed by

Kroupa (2001) takes the form,

$$\begin{aligned}\alpha &= 0.3, & 0.01 < m(M_{\odot}) < 0.08, \\ \alpha &= 1.3, & 0.08 < m(M_{\odot}) < 0.5, \\ \alpha &= 2.3, & m > 0.5(M_{\odot}).\end{aligned}\tag{1.26}$$

It worth noting, however, that some variation in the IMF has been suggested for extreme environments. For example, Bartko et al. (2010) found the nuclear star cluster, located around a parsec from Sgr A*, may have a top-heavy IMF. On the other hand, Conroy & van Dokkum (2012) and Cappellari et al. (2012) have found indirect evidence for bottom-heavy IMFs in early-type galaxies.

1.2.4 Low-mass star formation

Within any given stellar population, the IMF predicts that stars with a mass of around $\sim 0.3M_{\odot}$ are significantly more common than those with higher masses (e.g. $> 8 M_{\odot}$). Therefore, a large number of stars (i.e. a larger cluster size) is required before you statistically expect to find a high mass star (i.e. only one $8 M_{\odot}$ star for every $10^3 M_{\odot}$ cluster). The cluster mass function posits a similar relation to the stellar IMF, whereby lower mass clusters are significantly more common than their higher mass counterparts (Bahcall & Cen, 1993). With these two relations it is possible to propose that there is then an overabundance of star-forming regions that will go on to produce low mass clusters, which will contain only lower mass stars (hence be referred to as low-mass star-forming regions). There is, therefore, more of these low-mass star-forming regions closer to the Sun, as larger distances (i.e. volumes) are required to statistically include a higher mass cluster forming region that will have a higher chance of forming a high mass star. Due to their proximity, these regions can be studied in much greater detail than high-mass star forming regions. As a result, the general end-to-end process of low-mass star formation is thought to be well understood (see Shu, Adams & Lizano, 1987), although several key details are still debated (André et al., 2014).

The process of low-mass star formation begins with so-called “starless” cores, which are compact, gravitational bound regions (i.e. $\alpha_{\text{vir}} < 1$; see equation 1.18), without any sign of an embedded stellar object. These starless cores then have the correct initial conditions to form a star, and can be described as “prestellar”. During the initial collapse of a prestellar core, the dust opacity is optically thin at infrared wavelengths (i.e. at the peak of the spectral energy distribution), hence any energy produced by the collapse can be quickly radiated away and the core can remain in a near-isothermal state. As the collapse proceeds, both the density and the optical depth gradually increase. When the core reaches a density of around $\sim 10^{-13} \text{ g cm}^{-3}$ (number density of $n_{\text{H}_2} \sim 10^{11} \text{ cm}^{-3}$), the dust becomes optically thick and the energy produced by the collapse can no longer be efficiently radiated away. This trapped energy causes the temperature to rise, creating support against collapse, thus forming a so-called “hydrostatic” core (Larson, 1967). The identification of a hydrostatic core is difficult as they have very short lifetimes and a rigorous investigation is required to rule out the presence of any embedded low-luminosity stellar object (e.g. Schnee et al., 2012). As such, few potential hydrostatic cores have so far been identified (Enoch et al., 2010; Pineda et al., 2011a; Pezzuto et al., 2012).

As the hydrostatic core accretes material from the natal cloud, its temperature increases. This continues up to around $\sim 2000 \text{ K}$, when molecular hydrogen can be dissociated. At which point, the energy required to maintain the support of the core is taken up by the production of atomic hydrogen, and the gas pressure is no longer sufficient to inhibit collapse. This leads to the second phase of (near) isothermal collapse, which continues until i) all molecular hydrogen is disassociated to atomic hydrogen, and then ii) all the atomic hydrogen and helium is then ionised. At this point, a “protostellar” object is formed.

The protostellar object can continue to grow through the accretion of material from the natal cloud. The conservation of angular momentum from the large ($\sim 0.1 \text{ pc}$) initial prestellar scale down to the protostellar scale ($\sim 100\text{s AU}$), causes a rotating accretion disc to form around the compact protostellar object. The coupling between the angular momentum and magnetic fields within the disc is thought to be responsible for the

ubiquitously observed outflows and jets seen from protostellar objects (see [Li et al., 2014](#); [Bally, 2016](#)).

1.2.5 High-mass star formation

High-mass stars can be distinguished from their lower mass counterparts by their unique evolutionary stages and the strong influence they have on their host environment. A boundary is typically placed at $\sim 8 M_{\odot}$, as stars above this mass are sufficiently massive enough to: i) emit a significant amount of ultraviolet radiation in their early evolutionary stages to form H II regions, and ii) retain enough mass to be the progenitors of Type II supernovae in their late evolutionary stages. Both of these are efficient mechanisms of injecting energy into the ISM. A further motivation for this separation in mass stems from the timescales involved in their formation. The Kelvin-Helmholtz timescale is defined as,

$$t_{\text{KH}} = \frac{1}{2} \frac{E_{\text{G}}}{L_*} = \frac{1}{2} \frac{GM_*^2}{R_* L_*}, \quad (1.27)$$

where $E_{\text{G}} = GM_*^2/R_*$ is the gravitational potential of the star, and M_* , R_* and L_* are the stellar mass, radius and luminosity, respectively. This is the timescale over which the energy produced by the gravitational collapse of the object can be radiated away by its luminosity. The Kelvin-Helmholtz timescale, expressed as $t_{\text{KH}} \propto M_*^{-1}$ when assuming $L_* \propto M_*^3$, can be compared to the free-fall time (i.e. $t_{\text{ff}} \propto M_*^{-0.5}$; see equation 1.16). In the low-mass regime, $t_{\text{KH}} > t_{\text{ff}}$, and hence the early evolutionary stages mentioned in the previous section can occur, and the star reaches the main sequence after it has finished accreting material. In the high-mass regime, however, $t_{\text{KH}} < t_{\text{ff}}$. High-mass stars, therefore, reach the main sequence whilst heavily embedded in the natal cloud and still accreting material.

The IMF has a negative slope above $\sim 1 M_{\odot}$ (see figure 1.2.3), indicating that high-mass stars are rare. Therefore, statistically, stars with masses $> 8 M_{\odot}$, and the formations sites of these stars, are found at greater distances than lower mass stars ($< 1 M_{\odot}$). Indeed, only a handful of high-mass star-forming regions are thought to reside within

close proximity to the Sun (i.e. Orion at < 500 pc; [Matthews et al., 2010](#); [Plambeck et al., 2013](#)). Therefore, the observations necessary to understand the star formation process within these regions, at the same level of detail as for low-mass regions, are difficult to obtain (see Section 1.5).

Despite the limitations in observing high-mass star-forming regions, over the past two decades several theories have been proposed to describe how enough mass is concentrated in such a small volume to form a high-mass star. These are typically grouped into two families of models, “core accretion” ([McKee & Tan, 2002, 2003](#)) and “competitive accretion” ([Bonnell et al., 1997](#)), which are discussed in detail below (also see [Tan et al., 2014](#)).

The core accretion model is, in essence, a scaled up version of the formation mechanism for low-mass stars, where star formation can occur within a gravitationally bound “high-mass starless core”. Within these cores, non-thermal supersonic velocity dispersions are observed to overwhelmingly dominate the thermal velocity dispersion ([Myers & Fuller, 1992](#); [Caselli & Myers, 1995](#)). In the “turbulent core” model, [McKee & Tan \(2002, 2003\)](#) proposed that non-thermal, supersonic turbulence could provide enough support against the gravitational collapse (see equation 1.18). A problem with this, however, is that turbulence within such high-mass cores should produce substructure, which could cause fragmentation and the production of a population of low-mass stars, rather than a single high-mass star ([Dobbs, Bonnell & Clark, 2005](#)). [Tan et al. \(2013\)](#) suggest, however, that support against such fragmentation could be provided by strong magnetic fields ($\sim 0.1 - 1$ mG). There is currently a lot of debate if any high-mass starless cores, which definitively do not fragment on smaller scales, have been detected ([Tan et al., 2013](#); [Cyganowski et al., 2014](#); [Kong et al., 2016](#)).

The competitive accretion model was produced as an explanation for why high-mass stars are primarily found within clusters (e.g. [Lada & Lada, 2003](#)). In this model, the initial cloud/clump is highly fragmented, which allows many low-mass cores to form. These cores initially form with masses similar to the thermal Jeans mass (see equation 1.18 for when $\alpha = 2$ and $\sigma_v = c_s$), and are spatially distributed according to the global density profile. Those within the centre have higher mass accretion

rates throughout their lifetimes, compared to those further from the centre, due to the continued funnelling of gas down the global gravitational potential (Bonnell et al., 2001). Beneficial outcomes of this scenario are the general shape of the IMF, as many low-mass stars have to be produced for a single high-mass star (Bonnell et al., 1997), and the mass segregation seen within both young and old stellar clusters (Bonnell & Davies, 1998; Fregeau et al., 2002). Note, however, that simulations by Clark, Bonnell & Klessen (2008) show that the competitive accretion scenario can cause some IMF variation depending on the initial conditions of the system (e.g. on mass of the turnover), which is not in agreement with the observed near universal IMF properties (Bastian, Covey & Meyer, 2010).

Krumholz, McKee & Klein (2005) have, however, pointed out that the competitive accretion scenario would require a strongly gravitationally bound cloud, which is generally not observed (e.g. Tasker & Tan, 2009). Moreover, some evidence of isolated star formation has been observed (Bressert et al., 2012), along with the aforementioned high-mass starless core candidates (Tan et al., 2013; Cyganowski et al., 2014; Kong et al., 2016).

These two competing scenarios for high-mass star formation both appear to have their pros and cons. This is not too surprising given that the observations of high-mass star-forming regions required to test these theories are still limited. The advent of high-sensitivity, high-spatial and spectral resolution observations have only recently allowed examination of the physical properties, such as the dynamics and chemistry, within the initial stages of high-mass star formation, which will be discussed in the following section.

1.3 High-mass star-forming regions

To gain an end-to-end understanding of the high-mass star formation process, one needs to study the initial conditions under which they form, before protostellar feedback removes information (e.g. kinematic and chemical) of the environment in which

their earliest evolutionary stages occur. Therefore, observations of quiescent star-forming regions have to be made in order to study the initial conditions of high-mass star, and stellar cluster, formation. This necessitates the identification of molecular clouds with sufficient mass and density to form high-mass stars, which currently exhibit a low star formation activity.

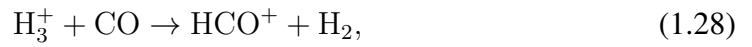
Infrared dark clouds (IRDCs) are a group of molecular clouds that were first identified in the mid-nineties as promising astro-laboratories in which to study the initial conditions of high-mass star formation (Carey et al., 1998). These were initially identified with the Infrared Space Observatory (*ISO*; 15 μm ; Perault et al., 1996) and the Mid-course Space Experiment (*MSX*; 7 to 25 μm ; Egan et al., 1998) as regions of strong mid-infrared extinction against the background Galactic emission. Subsequent studies of large IRDC samples, using a range of wavelengths, have highlighted a handful of clouds which appear to be particularly good candidates to host the formation sites of high-mass stars (Simon et al., 2006a,b; Rathborne, Jackson & Simon, 2006; Peretto & Fuller, 2009; Butler & Tan, 2009, 2012; Kainulainen & Tan, 2013). These are typically the densest clouds ($n_{\text{H}_2} \sim 10^{3-5} \text{cm}^{-3}$; e.g. Peretto et al., 2010; Hernandez et al., 2011; Butler & Tan, 2012), as high-densities have been suggested as a fundamental requirement for the formation of high-mass stars (Krumholz & McKee, 2008; Kauffmann & Pillai, 2010). In the following sections, the chemical and kinematic properties of these regions are discussed.

1.3.1 Chemistry

The use of emission from molecules other than CO to investigate the dense gas properties was discussed in Section 1.1.1.1. In particular, nitrogen-bearing species were highlighted as useful in cold and dense environments, where CO is depleted on the dust grains, due to their enhanced abundances. In IRDCs, where the average density is typically around an order of magnitude higher than estimated for lower mass star-forming regions, the enhanced abundance of these species can be extended beyond the core regions (Miettinen, 2014). N_2H^+ , for example, typically traces only the dens-

est cores in low mass star-forming regions (e.g. Caselli et al., 2002a; André et al., 2007; Friesen et al., 2010), however, this is found to be widespread across IRDCs (e.g Tackenberg et al., 2014; Henshaw et al., 2013).

In addition to the nitrogen-bearing species, the abundances of deuterated molecules can become enhanced within cold and dense environments. As the following reaction occurs at a significantly lower rate in regions with significantly depleted CO (Dalgarno & Lepp, 1984),

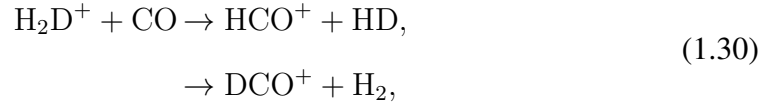


hence the abundances of H_3^+ is increased. The enhancement of H_3^+ boosts the production of H_2D^+ , via the following exothermic proton-deuteron exchange reaction (Paganì, Salez & Wannier, 1992; Walmsley, Flower & Pineau des Forêts, 2004):



where $\Delta E = 232$ K, hence this reaction proceeds from left to right at temperatures found within molecular clouds to further increasing the $\text{H}_2\text{D}^+/\text{H}_3^+$ ratio (~ 30 K; e.g. Millar, Bennett & Herbst, 1989). It should be noted, however, that an additional factor in this reaction is the spin isomer states of the H_2 and D_2 molecules, that is the ortho-hydrogen (parallel spin isomer) and parahydrogen (antiparallel spin isomer) states. At high temperatures collisions between molecules are frequent and the statistical ratio these spin states can be achieved (3:1), however, within molecular clouds that have a very low temperatures (< 20 K), much lower values of the ortho-to-para ratio are expected, due to the complex competition interchange between the two states via gas and drain surface interactions (see Dalgarno, Black & Weisheit, 1973; Flower, 2003). It is assumed that for the reaction shown in equation 1.29 the hydrogen in the para-state, however, when orthohydrogen is the reaction partner with H_2D^+ , the backward reaction is exothermic if H_2D^+ is in the ortho-state (e.g. Sipilä, Caselli & Harju, 2013). Therefore, the reaction shown in equation 1.29 above can only efficiently proceed from left to right for the low values of the ortho-to-para ratio, as observed within molecular clouds ($\sim 0.1 - 0.01$; Crabtree et al., 2011; Xu et al., 2016a). Within regions of high

CO depletion, an excess of H_2D^+ can build up, as the following destructive reaction also proceeds at a lower rate,



causing its relative abundance ratio with respect to H_3^+ to increase to orders of magnitude higher than the interstellar $[\text{D}]/[\text{H}]$ ratio ($\sim 1.5 \times 10^{-5}$; e.g. [Oliveira et al., 2003](#); [Linsky et al., 2006](#)). Once these deuterated isotopologues have formed, they can easily cede a deuteron to other neutral species and enhance their abundances. For example, the reactions of H_2D^+ with N_2 can produce N_2D^+ , and thereby significantly increase its abundance ratio with respect to N_2H^+ : $\text{D}_{\text{frac}}^{\text{N}_2\text{H}^+}$ (this notation is taken from [Kong et al., 2015](#), where the non-deuterated counterpart is shown in superscript).

[Fontani et al. \(2006\)](#) found $\text{D}_{\text{frac}} \sim 0.015$ toward the high-mass protostellar object IRAS 05345+3157, and [Miettinen, Hennemann & Linz \(2011\)](#) found $\text{D}_{\text{frac}} \sim 0.002 - 0.028$ toward several high-mass clumps within IRDCs. [Fontani et al. \(2011\)](#) found $\text{D}_{\text{frac}} \sim 0.2$ towards several potential high-mass starless cores embedded in quiescent IRDCs, comparable to the values seen in low-mass cores ($\sim 0.1 - 0.7$; e.g. [Crapsi et al., 2004](#); [Belloche et al., 2006](#); [Friesen et al., 2010](#); [Friesen, Kirk & Shirley, 2013](#); [Crapsi et al., 2005](#); [Pagani et al., 2009](#); [Bourke et al., 2012](#)).

Silicon-bearing molecules (e.g. SiO) are important probes of energetic processes in molecular clouds. These typically trace particularly energetic regions, as they are generated by the sputtering of dust grains within shocked regions ([Flower et al., 1996](#)). This, therefore, is useful in pinpointing embedded protostellar sources, due to the strong shocks produced by jets and outflows (see review by [Bally, 2016](#)). In addition, recently, narrow line-width SiO emission from several IRDCs has been attributed to the shocked material caused by colliding or merging clouds, and hence an indicator of the cloud formation history (e.g. via colliding flows; [Jiménez-Serra et al., 2010](#); [Cosentino et al., 2018](#)).

1.3.2 Kinematics

Extinction (or continuum) observations of star-forming regions allow us to investigate many physical properties. These, however, become limited in the analysis of physical structures, as they can only probe the cloud as projected in two-dimensions. Molecular line observations, on the other hand, also have the frequency (or velocity) dimension, hence can be used to determine the relative motions of the gas along the line-of-sight by considering the Doppler shift of the line;

$$V = \frac{\Delta\nu}{\nu_{\text{rest}}}c, \quad (1.31)$$

where $\Delta\nu$ is the observed offset from the line rest frequency, ν_{rest} , c is the speed of light, and V_{LSR} is the velocity of the material. Therefore, molecular line maps can show the phase-space (i.e. position-position-velocity) representation of a region’s true three-dimensional structure. Determination of the kinematic structures within molecular clouds is important in assessing the role of the physical structure in the star formation process. Studies of the kinematic structure of molecular clouds are discussed below.

Observations of low-mass star-forming regions have shown that even those with relatively simple extinction morphologies, can contain a complex network of velocity components (e.g. [Hacar et al., 2013, 2016c](#); [Hacar, Tafalla & Alves, 2017](#)). These velocity components are thought to play an important role in the process of mass concentration (e.g. [Hacar et al., 2016b](#)). [Tafalla & Hacar \(2015\)](#) proposed a “fray and fragment” scenario, whereby clouds initially fray to form subsonic filaments, or so-called “fibres” ([Hacar et al., 2013](#)), which then can accumulate mass to become gravitationally unstable and fragment into chains of closely-spaced cores.

The velocity structure observed within high-mass star-forming regions is typically more complex than their lower mass counterparts, with multiple velocity components observed for the majority of line-of-sights across IRDCs (e.g. [Henshaw et al., 2013](#)). Reliably disentangling these regions is, therefore, more difficult (e.g. [Jiménez-Serra et al., 2010, 2014](#); [Devine et al., 2011](#); [Henshaw et al., 2013, 2014](#); [Pon et al., 2016b](#)).

Nevertheless, the identified coherent filamentary structures observed within high-mass star-forming regions appear to have scaled-up properties compared to low mass filaments; typically having larger masses, lengths and (supersonic) velocity dispersions (e.g. [Henshaw et al., 2013, 2014](#)). [Hacar et al. \(2016a\)](#) suggest that these larger velocity dispersions could be an effect of artificially broadening caused by the relative velocities between unresolved fibres. A theory supported by the recent identification of a complex network of fibre-like structures within the Orion A “Integral Filament” ([Hacar et al., 2018](#); also see [Kainulainen et al., 2017](#)). Nevertheless, the importance of such small-scale structures in forming high-mass (and also low mass) stars is still debated. An example alternative scenario is that global collapse of clouds occurs along larger scale filaments, which concentrate mass within a “hub”-structure where high-mass stars can form ([Peretto et al., 2013](#); [Williams et al., 2018](#)). An investigation of the role of these structures in IRDCs is presented in Chapter 4.

1.4 Star formation in different environments

To develop a full picture of the star formation process, one needs to understand how this varies as a function of both *time* – as has been discussed – and *environment*. Several star formation models have had varying degrees of success in linking the observed physical properties of star-forming regions to the observed star-formation rate – i.e. how the gas is converted to stars. These can be grouped into two main categories: the “environmentally independent” relations (e.g. [Lada, Lombardi & Alves, 2010](#); [Lada et al., 2012](#)) and the “environmentally dependent” models (e.g. [Krumholz & McKee, 2005](#); [Padoan & Nordlund, 2011](#); [Hennebelle & Chabrier, 2011](#)), which are discussed in this section.

1.4.1 Environmentally independent relations

The star-formation rate relations referred to as “environmentally independent”, are those which do not require measurements of the environmental properties of a star-

forming system in order to predict its star formation rate. Rather, these are based on the assumption that any given parcel of gas will be converted to stars at a fixed rate, and through a single mechanism, and therefore only require information regarding the amount of star-forming material within a system. The most widely known of these is the ‘‘column density’’ threshold relation (Lada, Lombardi & Alves, 2010; Lada et al., 2012). Lada, Lombardi & Alves (2010) found that, for local clouds, a correlation exists between the gas mass at high extinctions ($A_K > 0.8$ mag; identified as being ‘‘dense’’) and the number of embedded YSOs identified in the infrared. These authors estimate that this gas has a hydrogen column density of the order $6.7 \times 10^{21} \text{ cm}^{-2}$ (or $\sim 10^4 \text{ cm}^{-3}$; assuming no line of sight contamination, and a typical spherical core of radius ~ 0.1 pc). They measure the star formation rates of clouds from the number of embedded YSOs (N_{YSO}), assuming an initial mass function median mass ($M_{\text{IMF}} \sim 0.5 M_{\odot}$), and a median age spread of the clouds ($t_{\text{age}} \sim 2$ Myr), such that

$$\text{SFR}(M_{\odot} \text{ yr}^{-1}) = \frac{N_{\text{YSO}} M_{\text{IMF}}(M_{\odot})}{t_{\text{age}}(\text{yr})}. \quad (1.32)$$

Lada, Lombardi & Alves (2010) show that the amount of dense gas and the level of star formation are correlated. The measured depletion time of the dense gas is 20 Myr, which implies,

$$\text{SFR}(M_{\odot} \text{ yr}^{-1}) = \begin{cases} 0 & \text{if } N(\text{H}_2) < 6.7 \times 10^{21} \text{ cm}^{-2}, \\ 4.6 \times 10^{-8} M_{\text{gas}}(M_{\odot}) & \text{if } N(\text{H}_2) \geq 6.7 \times 10^{21} \text{ cm}^{-2}. \end{cases} \quad (1.33)$$

This relation was further expanded to incorporate extragalactic sources (Lada et al., 2012), increasing application of this relation to sources which range around eight orders of magnitude in (dense gas) mass range. Shown in Figure 1.5 is the star formation rate as a function of dense gas mass for the sources used by Lada et al. (2012), over-plotted with the relation from equation 1.33. Krumholz & McKee (2008) have determined an alternative threshold for the formation of high-mass stars of $N(\text{H}_2) \geq 6 \times 10^{23} \text{ cm}^{-2}$ (or $\geq 1 \text{ g cm}^{-2}$); two orders of magnitude higher than the Lada, Lombardi & Alves (2010) and Lada et al. (2012) relation.

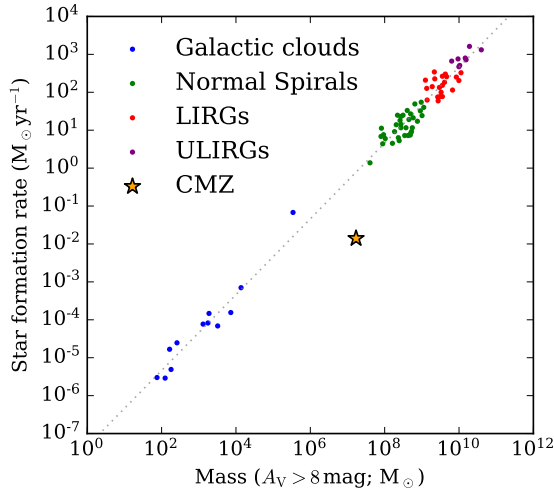


Figure 1.5: A plot originally produced by Lada et al. (2012), showing the star formation rate as a function of gas mass at high extinctions, determined above a visual extinction of $A_V \sim 8$ mag. The data points shown are from local Galactic clouds ([blue]; Lada, Lombardi & Alves, 2010), normal spiral galaxies [green], luminous infrared galaxies (LIRG; [red]) and ultra luminous infrared galaxies (ULIRG; purple; Gao & Solomon, 2004; Lada et al., 2012). Also shown here, not in the original, is the central 200 pc of the Milky Way (CMZ; Longmore et al., 2013a). The dash diagonal line represents the scaling relation shown in equation 1.33 (Lada et al., 2012).

1.4.2 Environmentally dependent models

The environmentally dependent (or “volumetric”) models are based on the assumption that the gas in star-forming regions follows a log-normal density distribution (see Section 1.2.2), which can be described by four dimensionless physical properties: the turbulent Mach number, the type of turbulence, the virial parameter, and the magnetic field strength (see review by Padoan et al., 2014). The lognormal distribution is expressed as,

$$p(s) = \frac{1}{(2\pi\sigma_s^2)^{1/2}} \exp\left[-\frac{(s-s_0)^2}{2\sigma_s^2}\right], \quad (1.34)$$

for the logarithmic normalised density,

$$s = \ln(x) = \ln(\rho/\tilde{\rho}), \quad (1.35)$$

where $s_0 = -\sigma_s^2/2$. The standard deviation of the log-normal function is given as,

$$\sigma_s^2 = \ln\left(1 + b^2 \mathcal{M}^2 \frac{\beta}{\beta + 1}\right), \quad (1.36)$$

where \mathcal{M} is the three-dimensional turbulent sonic Mach number,⁷ and β is used to quantify the strength of the magnetic field ($\beta = 2\mathcal{M}_A^2/\mathcal{M}^2$; where \mathcal{M}_A is the Alfvénic

⁷The three-dimensional Mach number, denoted by \mathcal{M} , is used throughout this work.

Mach number). As $\mathcal{M}_A = \sigma_v/v_A$ and $\mathcal{M} = \sigma_v/c_s$, where σ_v is the observed sonic velocity dispersion, c_s is the sound velocity of the gas, and v_A is the Alfvén velocity, strong magnetic fields are represented by low values of β , and a hydrodynamical (rather than magnetohydrodynamic) expression of equation 1.36 can be obtained by setting $\beta \rightarrow \infty$. The parameter, b , in equation 1.36 is referred to as the turbulence driving parameter and used to distinguish between solenoidal (divergence-free, $b \sim 0.33$) and compressive (curl-free, $b \sim 1$) driven turbulence (Federrath, Klessen & Schmidt, 2008). The turbulence driving parameter is inherently difficult to determine (see Federrath et al., 2016 for method), and only a few estimates have been made for star forming regions within the Galactic Disc ($b \approx 0.5$; Federrath et al., 2016; Orkisz et al., 2017), and more extreme environments, ($b = 0.22 \pm 0.12$; Federrath et al., 2016).

These models use the dimensionless star formation efficiency per free-fall time, ϵ_{ff} , to describe the level of star formation within a region. This can be expressed as the integral of the probability distribution function above the critical overdensity of collapse, $s_{\text{crit}} = \ln(x_{\text{crit}}) = \ln(\rho_{\text{crit}}/\tilde{\rho})$, where ρ_{crit} is the density when gravitational collapse begins to dominate. This integral is given as,

$$\epsilon_{\text{ff}} = \frac{\epsilon_{\text{core}}}{\phi_t} \int_{s_{\text{crit}}}^{\infty} \frac{t_{\text{ff}}(\tilde{\rho})}{t_{\text{ff}}(\rho)} \frac{\rho}{\tilde{\rho}} p(s) ds = \frac{\epsilon_{\text{core}}}{\phi_t} \int_{x_{\text{crit}}}^{\infty} \frac{t_{\text{ff}}(\tilde{\rho})}{t_{\text{ff}}(\rho)} p(x) dx, \quad (1.37)$$

where ϵ_{core} is the fraction of core mass which forms the protostar, and ϕ_t is the gas replenishment factor, such that $\phi_t t_{\text{ff}}$ is the replenishment time (Krumholz & McKee, 2005).

There are two possible physical interpretations of this integral, which differ in the treatment of the density dependence of the free-fall time ($t_{\text{ff}}(\tilde{\rho})/t_{\text{ff}}(\rho)$). Assuming a constant free-fall time based on the mean properties of the cloud, simplifies the integral, and gives a “single-free-fall” solution where all the gas collapses over the same timescale ($t_{\text{ff}}(\tilde{\rho})/t_{\text{ff}}(\rho) = \text{constant}$). On the other hand, assuming that the free-fall time varies as a function of density, as suggested initially by Hennebelle & Chabrier (2011), requires the integral to be solved over the log-normal probability distribution. In this “multi-free-fall” time solution, smaller, denser structures can decouple from

their lower density environment, and collapse on shorter timescales than the global free-fall time ($t_{\text{ff}}(\rho > \tilde{\rho}) < t_{\text{ff}}(\tilde{\rho})$). This may be more representative of the hierarchical structure observed in star-forming regions. Shown in Table 1.1 are the single-free-fall and multi-free-fall solutions of the analytic models from [Krumholz & McKee \(2005, KM05\)](#), [Padoan & Nordlund \(2011, PN11\)](#), and [Hennebelle & Chabrier \(2013, HC13\)](#).

As a visualisation of how the predicted probability density function, critical density and star formation efficiency per free-fall time can vary, shown in Figure 1.6 is the simplest model, the single-free-fall [KM05](#), determined for various values of the Mach number, virial parameter, magnetic field parameter and the turbulence driving parameter. The default values used to create these distributions are:

$$\mathcal{M} = 5 \rightarrow \text{moderately super-sonic,}$$

$$\alpha_{\text{vir}} = 1 \rightarrow \text{virialised,}$$

$$\beta = 0.5 \rightarrow \text{moderately magnetised,}$$

$$b = 0.4 \rightarrow \text{an equal mix of compressive and solenoidal turbulence driving,}$$

which are shown in the central column. The left and right columns then show the density distributions when varying one of these parameters to an extreme low or high value. Shown on each panel is a vertical dashed line which represents the critical density, and a shaded region below the curve, which represents the star formation efficiency per free-fall time (i.e. integral of the density probability distribution function above the critical density). Several interesting physical interpretations can be drawn here: i) increasing \mathcal{M} increases both the standard deviation of the distribution and critical density, which results in a high ϵ_{ff} at low \mathcal{M} (when the turbulent support against gravity is low), low ϵ_{ff} at moderate values of \mathcal{M} , and again high ϵ_{ff} at high \mathcal{M} (when the turbulence can force collapse within shocked regions); ii) making the gas more stable against gravity, or increasing α_{vir} , increases the critical density and thereby decreases the ϵ_{ff} ; iii) increasing the magnetic field strength, or *decreasing* β , has a similar effect to mach number (see i); iv) increasing b from solenoidal to compressive turbulence driving increases the standard deviation of the distribution, allowing for higher

Table 1.1: Table originally produced by Federrath & Klessen (2012), taken from Padoan et al. (2014), showing the forms of six analytical models for star formation. In columns are the references of the analytical models, the free-fall time factor, the critical density for collapse (x_{crit}), and the star formation efficiency per free-fall time (ϵ_{ff}). Note that the KM05 and KM05 multi-ff deviations using the three-dimensional Mach number are presented (see Federrath & Klessen, 2012). The function $f(\beta)$, entering the critical density in the PN11 and multi-ff PN11 models is given as $f(\beta) = (1 + 0.925\beta^{-3/2})^{2/3} / (1 + \beta^{-1})^2$. The added turbulent contribution $\tilde{\rho}_{\text{crit,turb}}$ in the critical density of the HC13 model is given as $\tilde{\rho}_{\text{crit,turb}} = (\pi^2/15) y_{\text{cut}}^{-1} \alpha_{\text{vir}}$ (Hennebelle & Chabrier, 2011).

Analytic model	Free-fall time factor	Critical density $x_{\text{crit}} = \exp(s_{\text{crit}}) = \rho_{\text{crit}} / \tilde{\rho}$	Star formation efficiency per free-fall time ϵ_{ff}
KM05	1	$(\pi^2/5) \phi_x^2 \alpha_{\text{vir}} \mathcal{M}^2 (1 + \beta^{-1})^{-1}$	$\epsilon_{\text{core}} / (2\phi_t) \{1 + \text{erf}[(\sigma_s^2 - 2s_{\text{crit}}) / (8\sigma_s^2)^{1/2}]\}$
PN11	$t_{\text{ff}}(\rho_0) / t_{\text{ff}}(\rho_{\text{crit}})$	$(0.067) \theta^{-2} \alpha_{\text{vir}} \mathcal{M}^2 f(\beta)$	$\epsilon_{\text{core}} / (2\phi_t) \{1 + \text{erf}[(\sigma_s^2 - 2s_{\text{crit}}) / (8\sigma_s^2)^{1/2}]\} \exp[(1/2)s_{\text{crit}}]$
HC13	$t_{\text{ff}}(\rho_0) / t_{\text{ff}}(\rho)$	$(\pi^2/5) y_{\text{cut}}^{-2} \alpha_{\text{vir}} \mathcal{M}^{-2} (1 + \beta^{-1})^{-1} + \tilde{\rho}_{\text{crit,turb}}$	$\epsilon_{\text{core}} / (2\phi_t) \{1 + \text{erf}[(\sigma_s^2 - 2s_{\text{crit}}) / (2\sigma_s^2)^{1/2}]\} \exp[(3/8)\sigma_s^2]$
KM05 multi-ff	$t_{\text{ff}}(\rho_0) / t_{\text{ff}}(\rho)$	$(\pi^2/5) \phi_x^2 \alpha_{\text{vir}} \mathcal{M}^2 (1 + \beta^{-1})^{-1}$	$\epsilon_{\text{core}} / (2\phi_t) \{1 + \text{erf}[(\sigma_s^2 - 2s_{\text{crit}}) / (2\sigma_s^2)^{1/2}]\} \exp[(3/8)\sigma_s^2]$
PN11 multi-ff	$t_{\text{ff}}(\rho_0) / t_{\text{ff}}(\rho)$	$(0.067) \theta^{-2} \alpha_{\text{vir}} \mathcal{M}^2 f(\beta)$	$\epsilon_{\text{core}} / (2\phi_t) \{1 + \text{erf}[(\sigma_s^2 - 2s_{\text{crit}}) / (2\sigma_s^2)^{1/2}]\} \exp[(3/8)\sigma_s^2]$
HC13 multi-ff	$t_{\text{ff}}(\rho_0) / t_{\text{ff}}(\rho)$	$(\pi^2/5) y_{\text{cut}}^{-2} \alpha_{\text{vir}} \mathcal{M}^{-2} (1 + \beta^{-1})^{-1}$	$\epsilon_{\text{core}} / (2\phi_t) \{1 + \text{erf}[(\sigma_s^2 - 2s_{\text{crit}}) / (2\sigma_s^2)^{1/2}]\} \exp[(3/8)\sigma_s^2]$

ϵ_{ff} , due to the significantly higher efficiency of concentrating material through compressive (curl-free) turbulence compared to solenoidal (divergence-free) turbulence. Further interpretation of how each model varies as a function of the individual physical parameters is given in Chapter 4.

1.4.3 An extreme environment to test star formation

The environmentally independent and dependent models for star formation have been rigorously tested for star-forming regions within the local environment, for which they all provide similarly accurate predictions of the star formation rate (and efficiency; see Federrath & Klessen, 2012). Therefore, testing the predictive power of these models within an extreme environment is required. Such environments exist within starburst galaxies, and high redshift galaxies at the epoch of peak star formation density at $z \sim 1 - 3$ (Swinbank et al., 2011). Lada et al. (2012) have attempted such a study in their determination of an environmentally independent star formation model (see Figure 1.5). However, the resolution required to accurately probe the star formation rate within these regions is not attainable with current generation telescopes, and will not be within the foreseeable future.

The inner few hundred parsecs of the Milky Way, known as the “Central Molecular Zone” (CMZ), harbours an extreme environment, with factors of a few to several orders of magnitude larger: average density, temperature, pressure, velocity dispersion, interstellar radiation field and cosmic ray ionisation rate. Fortunately, the CMZ resides at a fraction of the distance to extragalactic sources (8.34 ± 0.16 kpc; Reid et al., 2014), allowing for the high spatial resolution observations, required to test the star formation theories (Kruijssen & Longmore, 2013).

It has been previously noted that despite harbouring this vast reservoir of dense gas, the CMZ appears to be underproducing stars with respect to nearby star-forming regions in the Galactic disc (e.g. Guesten & Downes, 1983; Caswell et al., 1983; Taylor, Morris & Schulman, 1993). Indeed, Figure 1.5 shows how the CMZ appears to be around two orders of magnitude below the environmentally invariant model of star formation of

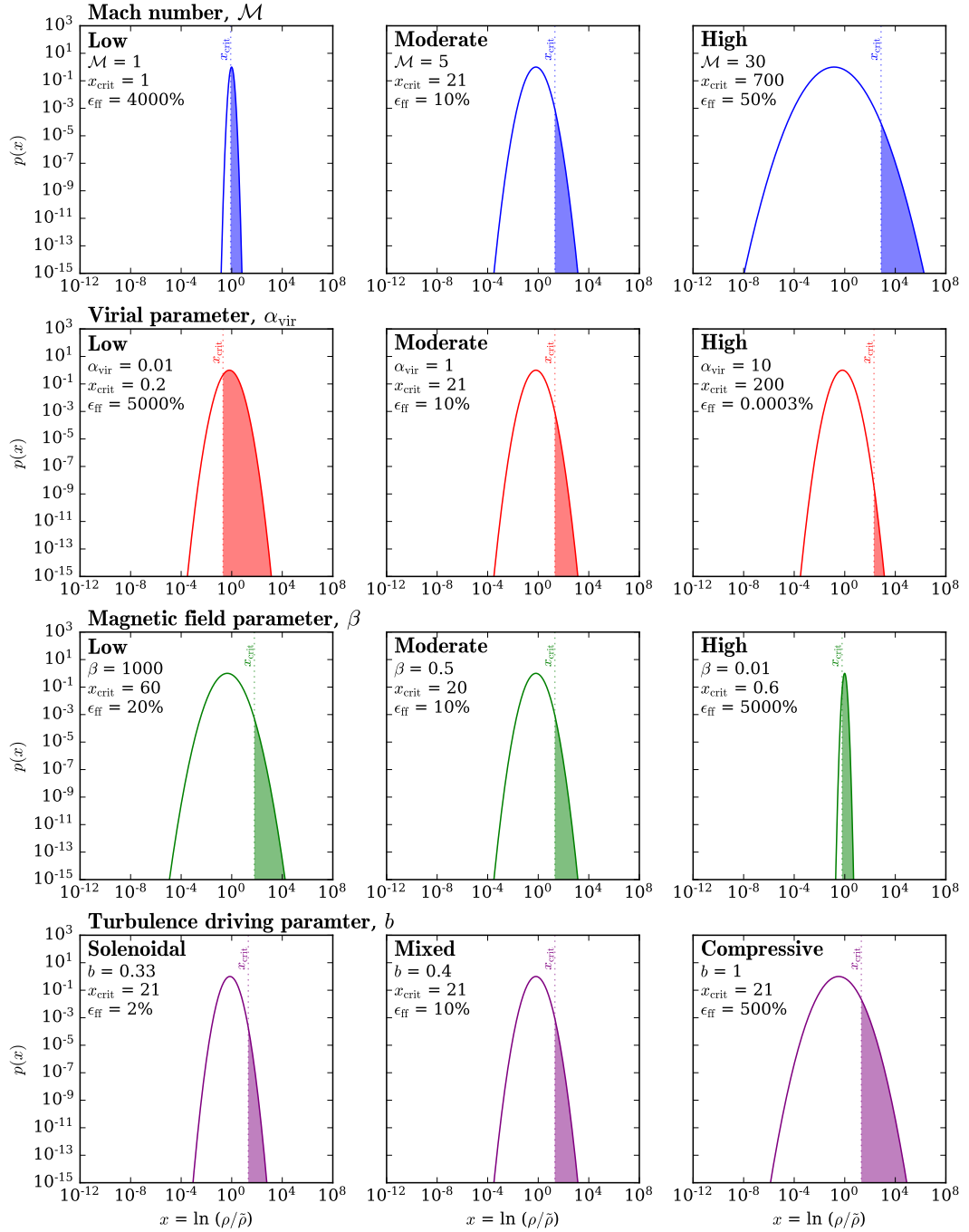


Figure 1.6: The predicted density probability distribution function from the [KM05](#) model, for a range of physical parameters. The default values for each plot are $\mathcal{M} = 5$, $\alpha_{\text{vir}} = 1$, $\beta = 0.5$, and $b = 0.4$, which are individually varied to extremes in the left and right columns. The value of the property being varied, the critical density, and star formation efficiency per free-fall time are given in the upper left of each panel. The vertical dotted line represents the value of the critical density, and the shaded region represents the integral of the density probability distribution function above the critical density (i.e. the star formation efficiency per free-fall time). Fiducial values used to create this plot are those adopted by the original work: $\epsilon_{\text{core}} = 1$, $\phi_t = 1.19$ and $\phi_x = 1.12$ (see Chapter 4 for more discussion of the fiducial values).

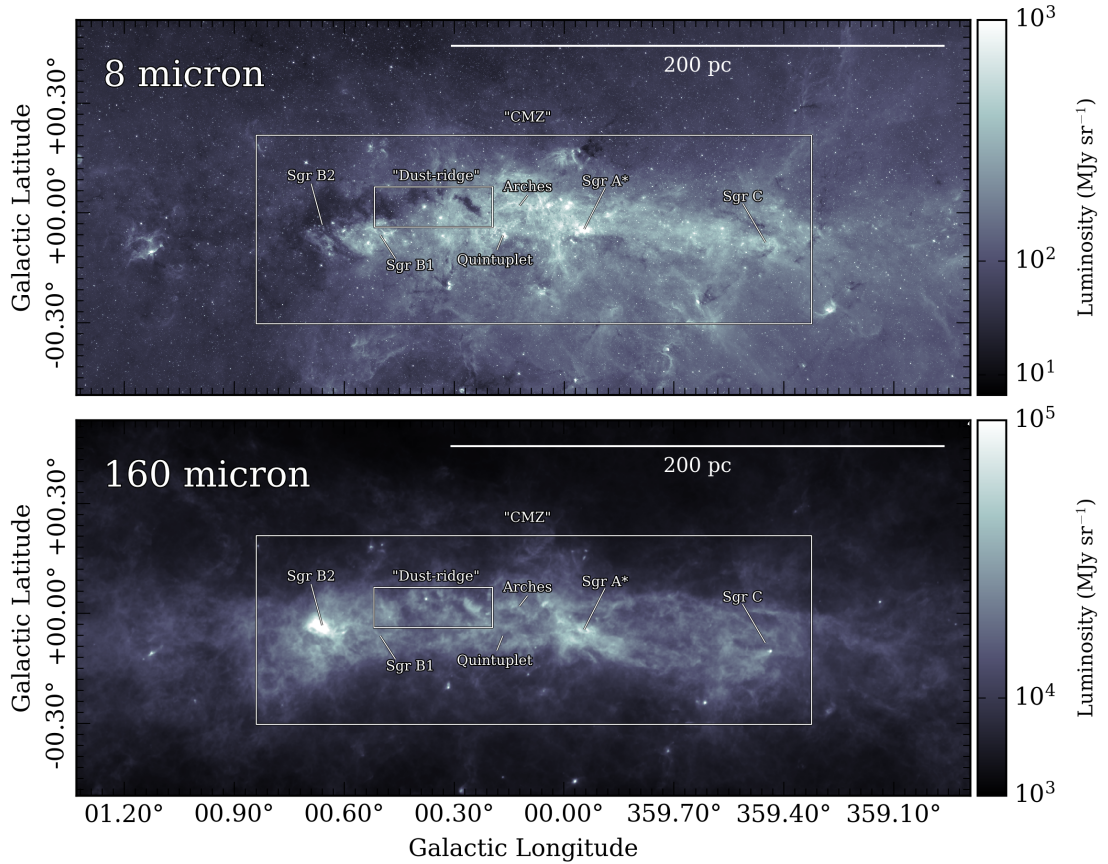


Figure 1.7: The Galactic Centre observed at wavelengths of [upper panel] $8\ \mu\text{m}$ from *Spitzer* (GLIMPSE; Churchwell et al., 2009) and [lower panel] $160\ \mu\text{m}$ from *Herschel* (Hi-GAL survey; Molinari et al., 2010). Labeled are the sources of interest throughout this region. Shown in the upper right is a scale-bar representing a projected length of $\sim 200\ \text{pc}$ at a distance of $\sim 8.3\ \text{kpc}$ (Reid et al., 2014).

Lada, Lombardi & Alves (2010), when taking the dense gas mass and star formation rate determined by Longmore et al. (2013a).

Figure 1.7 shows how the Galactic Centre is seen within the near- and far-infrared, taken with *Spitzer* and *Herschel* (Churchwell et al., 2009; Molinari et al., 2010). The large overlaid rectangle on each plot is the approximate area defined as the CMZ for the purposes of this thesis ($\sim 200\ \text{pc}$ in width). Also labeled are prominent sources within this region, such the quiescent regions within the “dust-ridge”, star-forming sources (e.g. Sgr B2), H II complexes (e.g. Sgr B1), young high-mass clusters (e.g. Arches and Quintuplet), and the supermassive black hole at the centre of the Milky Way (Sgr A*). The CMZ region contains a lot of complex sources, which are known to influence

the process, and impede the measurements of star formation. Further discussion of testing both the environmentally dependent and independent models for star formation within this extreme, complex region is presented in Chapter 4.

1.5 Observational techniques

In the previous sections, it has been highlighted that the properties of young star-forming regions are best probed using mid- to far-infrared ($\lambda \sim 3.6 \mu\text{m} - 500 \mu\text{m}$) and radio ($\lambda \sim 500 \mu\text{m} - 1 \text{m}$) wavelengths. As this thesis is primarily observationally based, this section presents a brief summary of the tools required to observe the emission across these wavelength regimes from star-forming regions.

1.5.1 Receivers

Given that humans cannot directly see infrared and radio wavelengths, astronomy within these regimes has only recently been possible with the advent of electronic receivers. On current generation infrared and radio telescopes, two types of receivers are commonly used: “bolometers” and “heterodyne” receivers.

1.5.1.1 Bolometer receivers

Bolometer receivers work by directly converting the incoming radiation to an electronic response signal. In the most basic terms, these work as incoming photons heat a thermally conductive material within the receiver, thereby increasing its electronic resistance. This is detected as an increase in voltage of an applied current across the material. This measurable signal is then directly proportional to the intensity of the incoming radiation.

Bolometers are useful, as they can achieve a flat spectral response over a very wide-bandwidth, which, when they are also cryogenically cooled to very low temperatures ($< 2 \text{K}$), can provide very high broad-band sensitivities. As the blackbody spectral

energy distribution at a typical cloud temperature peaks within this regime ($\lambda_{\text{peak}} = b/T$, where b is Wien's displacement constant; e.g. $\lambda_{\text{peak}}(10 \text{ K}) \sim 300 \mu\text{m}$), these are useful in continuum measurements of molecular clouds. Molecular line observations are difficult with bolometers due to their typically low spectral resolution, nevertheless, it is possible to do pseudo-spectroscopy with bolometers that are fitted with filters.

This thesis makes use of the bolometers on the Caltech Submillimeter Observatory (BOLOCAM), *Spitzer* (Infrared Array Camera, IRAC, and Multiband Imaging Photometer for *Spitzer*, MIPS) and *Herschel* (the Photoconductor Array Camera and Spectrometer, PACS, and Spectral and Photometric Imaging Receiver, SPIRE).

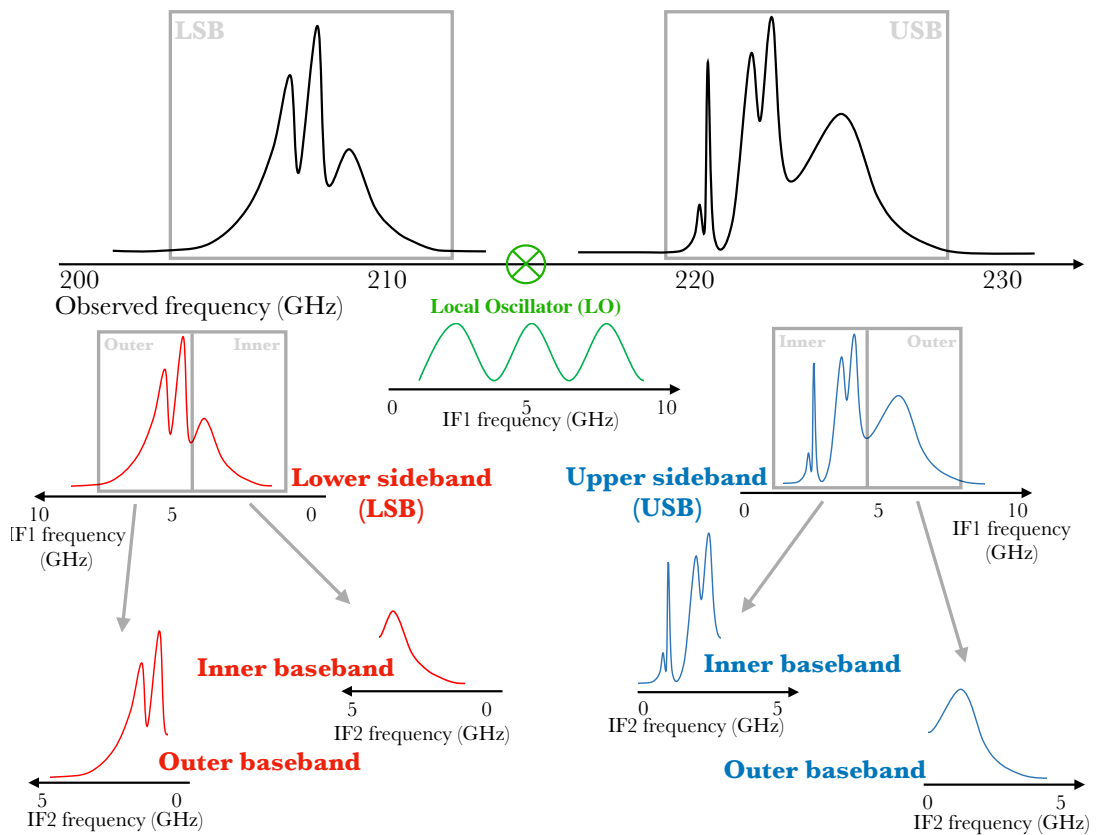


Figure 1.8: A graphical representation of how a heterodyne receiver splits and down-converts observed emission. This example shows a cartoon spectrum between 200 – 230 GHz, which has been centred on the frequency of the local oscillator (LO). The sinusoidal profile driven by the LO is shown in green, and covers the IF of 0 – 8 GHz. The result of mixing the observed emission from the upper and lower sidebands with the LO signal is shown in red and blue [left and right, respectively]. The sidebands are then shown to be split further into inner and outer basebands, which span a second IF of 0 – 8 GHz. This example can be directly related to the Band 6 receivers on ALMA, and the PolyFix receivers on the NOEMA interferometer.

1.5.1.2 Heterodyne receivers

Heterodyne receivers are more complex than bolometers, as they can preserve both the intensity and phase of the detected emission. These are described as heterodyne, as the detected signal is down-converted to a lower frequency, or “intermediate frequency” (IF). This works as the detected signal is mixed with the lower frequency sinusoidal signal, driven by a “local oscillator” (LO), to produce beat frequency signals. This mixing produces several modulation products, the first order of which are referred to as the upper and lower sidebands (USB and LSB, respectively), which are centred at a given offset from the LO and have a set bandwidth (both governed by the type of receiver). The treatment of these sidebands during IF processing can then vary depending on the available hardware and scientific objectives. For example, to ease computing loads, the IF bands can then be further split into basebands, which typically consist of inner (closer to LO frequency) and outer (further from LO frequency) components. Further splitting can be produced if the separate (linear or circular) polarisation products are required (e.g. for magnetic field measurements), or if higher spectral resolution, smaller bandwidth windows are needed (e.g. for spectral lines). An example of this procedure can be seen in Figure 1.8, which can be directly related to the heterodyne receivers on ALMA and NOEMA.

The versatility of heterodyne receivers makes them ideal for both broad-band, low spectral resolution continuum observations and narrow-band, high spectral resolution molecular line observations. Their ability to retain the phase of the detected emission makes them a particularly crucial component for interferometric observations, which will be discussed below. Observations which were taken with telescopes using heterodyne receivers used within this thesis are with the IRAM-30m (EMIR, ABCD) and ALMA (Band 6).

Table 1.2: A table of the resolutions attainable with several current generation infrared and radio telescopes, and an example optical telescope for comparison. Shown in the columns is the telescope name, the wavelength regime probed by the telescope, the approximate dish diameter, a typical wavelength used for observation with the telescope, and the angular resolution calculated from the shown dish diameter and wavelength.

Telescope	Wavelength regime	Dish diameter	Wavelength	Resolution
<i>Hubble</i>	optical	~ 2 m	500 nm	0.05''
<i>Spitzer</i>	mid-infrared	~ 1 m	5 μm	2''
<i>Herschel</i>	far-infrared	~ 3 m	200 μm	15''
IRAM-30m	millimetre radio	~ 30 m	3 mm	20''
GBT	centimetre radio	~ 100 m	15 mm	30''
FAST	centimetre radio	~ 500 m	21 cm	80''

1.5.2 Types of telescope

1.5.2.1 Single dish telescopes

Telescopes that have a single continuous collecting area (i.e. a single mirror or single dish) are generically referred to here as “single dish telescopes”. These can use both of the aforementioned receiver types, and can range in size from several metres to several hundred metres, depending on their application. For example, as the atmosphere is opaque at infrared wavelengths, infrared telescopes typically have to be space-based and are therefore limited in their size to around a metre (e.g. *Spitzer* and *Herschel*). This is, however, not an issue for longer wavelengths (> 1 mm), where the atmosphere is more transparent, hence telescopes can be ground-based, at either high-altitude (for sub-millimetre-to-millimetre) or sea-level (for millimetre-meter), and, therefore, significantly larger in size. The relation between the size of the telescope, or the dish diameter D , and the achievable angular resolution, θ , is given as $\theta \approx \lambda/D$. Shown in Table 1.2 are the angular resolutions attainable by several current generation telescopes. The current limit in angular resolution of infrared and millimetre radio single dish telescopes is the order a few arcsec to tens of arcsec (where $1'' = 1000$ au at 1 kpc). However, to achieve a comparable resolution to optical telescopes, an order of magnitude increase in the dish size would be required. A simple schematic diagram of a single dish telescope is shown in Figure 1.9.

The aim of astronomical observations is to obtain the physical parameters of the emitting regions, such as those described in the previous sections (e.g. temperatures, densities, column densities). To derive these quantities from the detected data, firstly the properties of the receiving system have to be accurately known. In other words, the data have to be calibrated to remove sources of uncertainty, which can arise from variations within the system electronics and the atmosphere. Particular care has to be taken during the calibration of ground based observations due to the significant variation of the atmosphere as a function of time; over timescales of minutes to hours, compared to the system electronics that are typically stable for several hours. Moreover, as the atmosphere becomes increasingly more unstable at higher frequencies, hence any variations have to be accounted for increasingly more often; e.g. for the sub-millimetre observations the timescale for significant variation is of the order minutes, whereas for centimetre observations this timescale is closer to an hour. The observational and reduction procedures used to mitigate the effects of atmospheric and electronic noise, and, therefore, generate images from single telescopes, are described below.

In the case of millimetre and sub-millimetre heterodyne systems, the following procedure is required. Firstly, the measured voltage from the receiver has to be calibrated, such that it can be converted to a physical brightness temperature (see equation 1.8; or flux density in the case of continuum observations, see equation 1.6). There are two procedures to calibrate the voltage signal, but these use broadly the same principle. The first is the “chopper wheel” method, which, for example, is implemented on the IRAM-30m. This method requires both a cold source (e.g. liquid nitrogen cooled source, or empty part of the sky) and a hot source (e.g. room temperature source) to be placed in front of the detector. Measurement of these known temperature sources allow terms such as the system noise temperature, ambient temperature (temperature of the atmosphere) and sky opacity to be determined (Penzias & Burrus, 1973). The second, slightly different method of solving for the noise temperature involves the switching of diodes, rather than using hot and cold loads (O’Neil, 2002). This method is implemented on, for example, the GBT. In the case of a bolometer, rather than using the chopper wheel or diode system, a source with known flux density is observed to cali-

brate the system temperature. For each of these methods, a pointing correction is then conducted by scanning over an unresolved source of known position and correcting for any offsets. The focus can then be corrected for by varying the distance of the secondary mirror from the primary, whilst observing a known source, and determining the distance that provides the minimum PSF response (i.e. smallest measured size of the point source). The source and an “off” position containing no emission can then be observed for several hours before the above procedure has to be repeated.⁸ In the “position switching” calibration method, the off position refers to a part of sky containing no emission, which is subtracted from the source to remove atmospheric variations. As position switching typically requires re-pointing the telescope,⁹ it is not feasible to switch between the on-source and blank-sky observations at a rapid rate. Therefore, the time stability of the telescope and atmosphere have to be taken into account when determining the time between on-off position observations (i.e. such that both can be observed at a rate higher than the atmospheric variation). The off position should be reasonably close to the source, and, if also possible, at the same elevation, such that the atmospheric conditions are similar to those of the primary observation. In the “frequency switching” calibration method, the off position refers to a part of the bandwidth which contains no emission. This is obtained by changing the central frequency of the observations, whilst keeping the same telescope pointing. This method is more time-efficient as it does not require movement of the telescope. However, for this, the stability of the system as a function of frequency has to be taken into account, whereby the noise (e.g. combined system response and atmosphere) in both the primary and frequency switched observation must be virtually identical. Later corrections, for example, converting between the antenna and main beam brightness temperature using the beam and forward efficiencies can be applied during data reduction.

⁸An off position may not be needed if a baseline can be fitted to the spectral regions of an observation which are known to contain no signal from the object of interest. This baseline is then treated as the off-source observation, and subtracted from the source emission.

⁹Not the case for the “wobbler switching” method, where the secondary mirror is adjusted slightly such that the focus is on an off position.

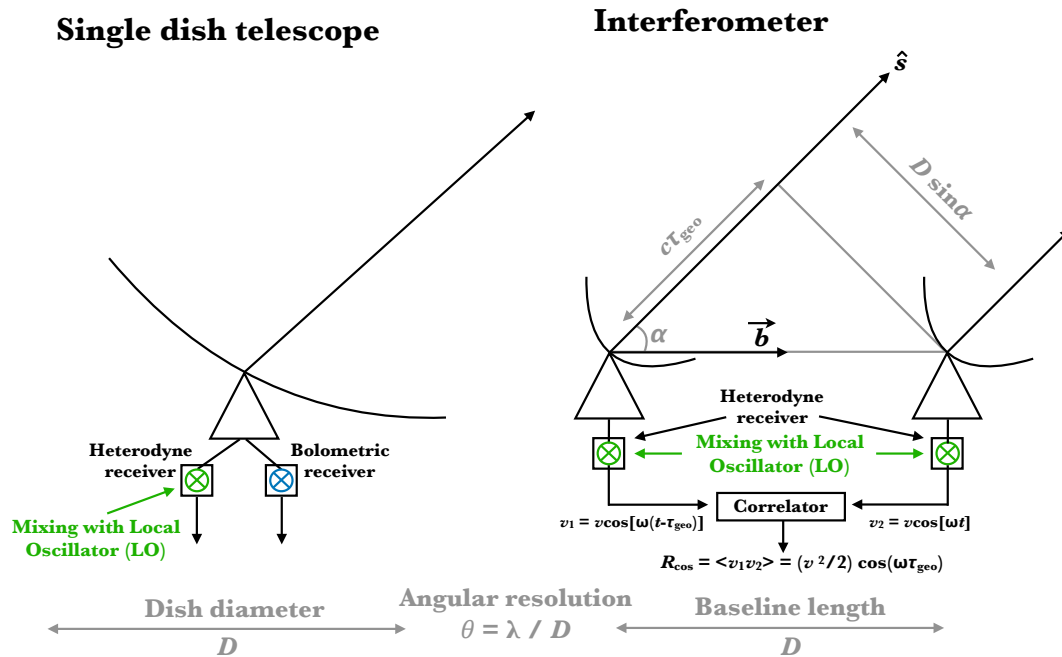


Figure 1.9: A schematic diagram of a single dish telescope [left] and an interferometer [right]. Shown for the single dish telescope is the incoming radiation shown as an arrow, the dish, and the available receiver types. Shown for the interferometer is the incoming planar radiation shown as arrows (at an angle between the baseline vector and source vector, $\alpha = \vec{b} \cdot \hat{s}$), the dishes, the receivers and the correlator. Demonstrated here is the most simple case of the sinusoidal wavefront varying with time, t , with a phase of ω and a detected voltage amplitude of v ; i.e. $\cos(\omega t)$. This is received at different times by the two dishes, given the geometric delay defined by the separation of the two dishes (τ_{geo}). The response of the signals of the two dishes after being correlated (product and average) is also shown as $R = (v^2/2) \cos(\omega\tau_{\text{geo}})$. The strongest response signal is detected when $\omega\tau_{\text{geo}}$ is a multiple of π and weakest when $\omega\tau_{\text{geo}}$ is a multiple of $\pi/2$. The single dish diameter and baseline of the interferometer are highlighted below the schematics, which are both used to determine the angular resolution.

1.5.2.2 Interferometers

To overcome the limited angular resolution of single-dish observations, arrays of single-dish telescopes, called interferometers, are used. Interferometers can produce a much higher angular resolution image, as the process of aperture synthesis allows the maximum separation between elements in the interferometer, rather than individual dish size, to govern the achievable angular resolution.

The projected separation between any two dishes, as seen from the source, is referred to as a “baseline”. The most simplistic case of a single baseline, or two element interferometer, is shown in Figure 1.9. In this example, the simplest incoming planar

wavefront from a point source is chosen; a sinusoid varying with time, t , with a phase of ω and a detected voltage amplitude of v ; i.e. $\cos(\omega t)$. This wavefront is received and converted to a voltage signal at different times by the two dishes, governed by their separation (i.e. a geometric delay; τ_{geo}). The key differentiating step from single-dish telescopes is that now the signals from the two dishes is correlated (product and average) to produce a response,

$$R_{\text{cos}} = (v^2/2) \cos(\omega\tau_{\text{geo}}). \quad (1.38)$$

The strongest response signal is detected when $\omega\tau_{\text{geo}}$ is a multiple of π and weakest when $\omega\tau_{\text{geo}}$ is a multiple of $\pi/2$. This response then varies sinusoidally with the change of source direction in the interferometer frame, to produce a fringe pattern with a phase,

$$\phi = \omega\tau_{\text{geo}} = \frac{\omega}{c} D \cos\alpha, \quad (1.39)$$

where c is the speed of light, D is the baseline length and α is the angle to the source (see figure 1.9), and

$$\frac{d\phi}{d\alpha} = \frac{\omega}{c} D \sin\alpha = \frac{2\pi D}{\lambda} \sin\alpha, \quad (1.40)$$

where wavelength of the emission is given as $\omega = 2\pi c/\lambda$. Therefore, the fringe phase is an exquisitely sensitive measure of point source position if the projected baseline is many wavelengths long. To improve the point-source response, more baselines are required; an interferometer with N dishes can contain $N(N-1)/2$ baselines. The synthesised beam (the point-source response obtained by averaging the outputs of all baselines) rapidly approaches a Gaussian as N increases (i.e. as individual baseline fringe patterns are convolved).

Outlined here is the most simplistic case, and for sources with an extended brightness distribution, $I_\nu(\hat{s})$, the responses from both the cosine, R_{cos} , and sine, R_{sin} correlations are required. The cosine response integrated over the solid angle, $d\Omega$, of a source brightness distribution can be given as,

$$R_{\text{cos}} = \int I_\nu(\hat{s}) \cos(\omega\tau_{\text{geo}}) d\Omega. \quad (1.41)$$

When combining the cosines and sines responses, it is convenient to write them as complex exponential. This is referred to as a complex visibility, V_ν , and given as,

$$V_\nu = R_{\text{cos}} - i R_{\text{sin}} = \int I_\nu(\hat{s}) \exp(-i \omega \tau_{\text{geo}}) d\Omega. \quad (1.42)$$

The geometric delay is the product source vector and baseline vector, $\tau_{\text{geo}} = (\vec{b} \cdot \hat{s})/c$, where c is the speed of light. Therefore, in more physically useful units, equation 1.42 can be given as,

$$V_\nu = \int I_\nu(\hat{s}) \exp\left(\frac{-i 2\pi (\vec{b} \cdot \hat{s})}{\lambda}\right) d\Omega. \quad (1.43)$$

To return to the brightness distribution of the source, the inverse Fourier transform of the visibilities have to be taken.

In practice, several steps have to be taken to calibrate the telescope, before the raw observations can be used to produce science ready images. Similarly to single-dish observations, this calibration procedure is required to set the absolute flux-scale of the observations, and to compensate for the sources of error in the observations. Interferometers, however, require special attention to be paid towards the phase of the observations, which can have large variations as a function of time due to the atmosphere. Without accurately accounting for the phase, the correlated signal between any two baselines would be incoherent, and a source image would not be producible. As previously mentioned in the discussion of single dish reduction techniques, the atmosphere becomes increasingly unstable at higher frequencies, and therefore needs to be calibrated out more regularly. Moreover, interferometers with large baselines, also require increased attention to the atmospheric variations, due to the increased likelihood of a change in atmospheric conditions between the more distant dishes in the array. The steps to calibrate out the uncertainties caused by the atmosphere and the electronics (e.g bandpass) are briefly discussed below:

- i) (Phase calibration) Variations in the phase between dishes can be created by changes in atmospheric conditions. This has to be accounted for by intermittently observing a point source near the science target and measuring its phase

change as a function of time. As the point source should have a constant phase (and amplitude), a model for each visibility can be produced. This can be extrapolated to the total observational period, and used to solve for phase variations in the science target observations. The cycle time for observing the phase calibrator and source(s) should decrease with increasing frequency, as the atmosphere is less stable. For example, the suggested cycle lengths for Ku (12–18 GHz) and Q (40–50 GHz) Band observations in the most compact configuration of the Very Large Array (VLA) are 20 minutes and 6 minutes, respectively. Moreover, the cycle time also decreases for increasing baselines. For example, the suggested cycle lengths for Ku band observations in the most compact (maximum baseline of ~ 1 km) and extended (maximum baseline of ~ 35 km) configurations of the VLA are 20 minutes and 5 minutes, respectively.

- ii) (Bandpass calibration) Changes in the receiver's response can cause a slow time variation in the bandpass (amplitude or phase as a function of frequency). Again, this can be corrected for by observing a bright point source, creating a model, and solving for both phase and amplitude variations. The ideal source required for this calibration is a bright, flat, featureless spectrum source, which will allow the change in system response to be measured as a function of frequency. Accurate bandpass calibration is crucial in the detection of spectral features, especially those which are weak and broad. Inaccurate bandpass calibration can also limit the dynamic range of continuum observations.
- iii) (Flux calibration) As the amplitude of visibilities does not have an absolute flux scale, a reference source with known flux has to be observed to convert them into physical units (e.g. Jansky). This should be a well-studied source, which does not significantly vary over time, and if the source is resolved, or has spectral lines, it must be very well modelled (e.g. for the case of a Solar System object, such as Titan or Neptune, which can be both resolved and contain molecular line emission).
- iv) (Imaging) With all the corrections applied, the visibilities can be inverse Fourier transformed into the image plane. However, as the Fourier plane is typically only

finitely sampled by the observations, traditional linear deconvolution methods cannot be used to recover the source brightness distribution, and complex non-linear deconvolution algorithms are required to interpolate and extrapolate to the visibility function. The most widely used of these is the “clean” algorithm, which was first implemented by Högbom (1974). The initial derivation of this algorithm makes several simple assumptions of the emission (e.g. it is composed of point sources), and works by iteratively finding the peak value in the observed emission (residual map) and subtracting a small gain of a point source convolved with the point spread function (dirty beam), until a threshold is reached. In doing so, a point source distribution representative of the emission is produced (model image), which is convolved with the point spread function to create the final image. More recent iterations of the algorithm have made several notable improvements, such as better solving for extended sources (important for studies of molecular clouds). More advanced techniques such as self-calibration, which is the iterative process of repeating steps ii) and iii) using the source itself, are also possible to potentially improve the resultant image quality.

Unlike single-dish observations which recover all size scales down to the angular resolution, due to the limited Fourier plane coverage, images produced with interferometers will only be able to recover a limited range of spatial scales. The largest recoverable spatial scale (i.e. the primary beam) of the observations is set by the smallest baseline, which is limited by the closest dishes can be placed without causing shadowing effects. This can be somewhat mitigated by limiting the size of the dishes such that the smallest baseline can be decreased, such as the 7 m dishes with ALMA (full array contains 12 m dishes). However, to completely remove this effect, comparable frequency observations have to be taken a single dish telescope, and combined during or after imaging (e.g. via feathering).

Chapter 2

Widespread deuteration across the IRDC G035.39-00.33

2.1 Preface

This chapter presents work which has been published by [Barnes et al. \(2016\)](#). The observations for this work were originally proposed by P. Caselli, which were then taken and reduced by I. Jiménez-Serra. The data analysis and interpretation were conducted by A. T. Barnes. The chemical modelling results presented in this work were provided by S. Kong ([Kong et al., 2015](#)). The initial draft of the publication was written by A. T. Barnes, who then incorporated comments from co-authors and an anonymous referee in the final draft.

2.2 Introduction

The deuterium fraction is a good tracer of the cold and dense gas within star-forming regions. The deuterium fraction of N_2H^+ is a particularly sensitive tracer, compared to other N-bearing species, of the physical properties and chemistry found within quiescent regions on the verge of forming stars ([Fontani et al., 2015](#)). Given this, in regions

where the physical and chemical properties can be accurately constrained, modelling of the observed deuteration of N_2H^+ can be used to infer molecular cloud lifetimes (Kong et al., 2015). This, therefore, is a powerful diagnostic in differentiating between the “slow” and “fast” modes of star formation, as discussed in Section 1.2.1.

In light of this, this chapter presents an analysis of the deuterium fraction across the high-mass star-forming region, G035.39-00.33, with the aim of pinpointing the regions on the verge of massive star formation. As this is a particularly well studied molecular cloud, and hence its physical and chemical properties are relatively well understood, chemically modelling is used to infer a lifetime of the cloud, which is placed into the context of star formation within supported and transient molecular cloud theories (see Section 1.2.1).

2.2.1 IRDC G035.39-00.33

The IRDC G035.39-00.33 is a relatively close-by (2.9 ± 0.5 kpc; Simon et al., 2006b),¹ massive ($17,000 \pm 5000 M_\odot$; Kainulainen & Tan, 2013) and highly filamentary cloud (Butler & Tan, 2009, 2012), which currently shows minimal signs of ongoing star formation (Chambers et al., 2009; Carey et al., 2009; Nguyen Luong et al., 2011). This IRDC, therefore, is an ideal candidate in which to study the initial stages of massive star formation (see section 3.2.1 for further discussion on the selection process of G035.39-00.33; Simon et al., 2006a,b; Rathborne, Jackson & Simon, 2006; Butler & Tan, 2009).

In recent years, G035.39-00.33 has been the subject of an in-depth analysis, which has found: large-scale shocks (Jiménez-Serra et al., 2010), that the cloud is in a near virial state (Hernandez et al., 2012), a high level of fragmentation (Henshaw et al., 2016a, 2017), a complex kinematic structure (Henshaw et al., 2013; Jiménez-Serra et al., 2014; Henshaw et al., 2014), low gas and dust temperatures (Sokolov et al., 2017), and widespread CO depletion (Hernandez et al., 2011). The latter two of these

¹Following Hernandez et al. (2011) we adopt the kinematic distances of Simon et al. (2006b), who assumed the Clemens (1985) rotation curve. This leads to a distance of 2.9 kpc for G035.39-00.33. The uncertainties in this distance are likely to be of order 0.5 kpc, which could result, for example, from line-of-sight noncircular motions of $\sim 8 \text{ km s}^{-1}$.

Table 2.1: Observational parameters.

Observational parameter	N ₂ D ⁺ (2 – 1)	N ₂ H ⁺ (1 – 0)	C ¹⁸ O (1 – 0)
Frequency, ν (MHz)	154217.18 ^a	93176.7637 ^b	109782.1780 ^c
HPBW, θ (") ^d	16	26	23
Velocity Resolution, Δv (km s ⁻¹)	3.04×10^{-1}	6.28×10^{-2}	5.33×10^{-2}
Observation date	09-10/08/2009	19/02/2009	13/08/2008
Receiver and backend	EMIR/VESPA	ABCD/VESPA	ABCD/VESPA
Beam Efficiency	0.66	0.74	0.73
Forward Efficiency	0.93	0.95	0.97
rms level, σ_{rms} (K)	0.04	0.13	0.10

a: Shown is the frequency of main hyperfine component of N₂D⁺ (J, F₁, F = 2,3,4 → 1,2,3), from [Dore et al. \(2004\)](#).

b: Shown is the frequency of main hyperfine component. The isolated component N₂H⁺ (J, F₁, F = 1,0,1 → 0,1,2) has a frequency of 93176.2522 MHz ([Pagani, Daniel & Dubernet, 2009](#)).

c: [Cazzoli, Puzzarini & Lapinov \(2003\)](#)

d: Calculated as $\theta_{\text{HPBW}} = 1.16 \lambda / D$, where λ and D are the wavelength and telescope diameter, respectively (see <http://www.iram.es/IRAMES/mainWiki/Iram30mEfficiencias>).

studies highlight this cloud as the ideal candidate in which to use the deuterium fraction as a tracer of quiescent gas that will soon form stars.

The mass surface density map of G035.39-00.33 derived from combined near- and mid-infrared extinction is presented in [Figure 2.1](#). Several sources of interest within and around the cloud have been labelled. For brevity, we henceforth refer to G035.39-00.33 as “Cloud H”, following the nomenclature used by [Butler & Tan \(2009\)](#) and [Butler & Tan \(2012\)](#).

2.3 Observations

The N₂D⁺ (2 – 1) observations were carried out throughout August 2009 with the Institut de Radioastronomie Millimétrique 30-m telescope (IRAM-30m) at Pico Veleta, Spain. The large-scale images were obtained in the On-The-Fly (OTF) mapping mode. The central coordinates of the maps are $\alpha(\text{J2000}) = 18^{\text{h}}57^{\text{m}}08^{\text{s}}$, $\delta(\text{J2000}) = 02^{\circ}10'30''$ ($l = 35.517^{\circ}$, $b = -0.274^{\circ}$). The off-source position used was (300'', 0''); in relative coordinates). The EMIR receivers were used. The VErSatile SPectrometer Assembly (VESPA) provided a spectral resolution at 156 kHz (equivalent to 0.3 km s⁻¹) at the frequency of the N₂D⁺(2 – 1) line (main hyperfine component frequency

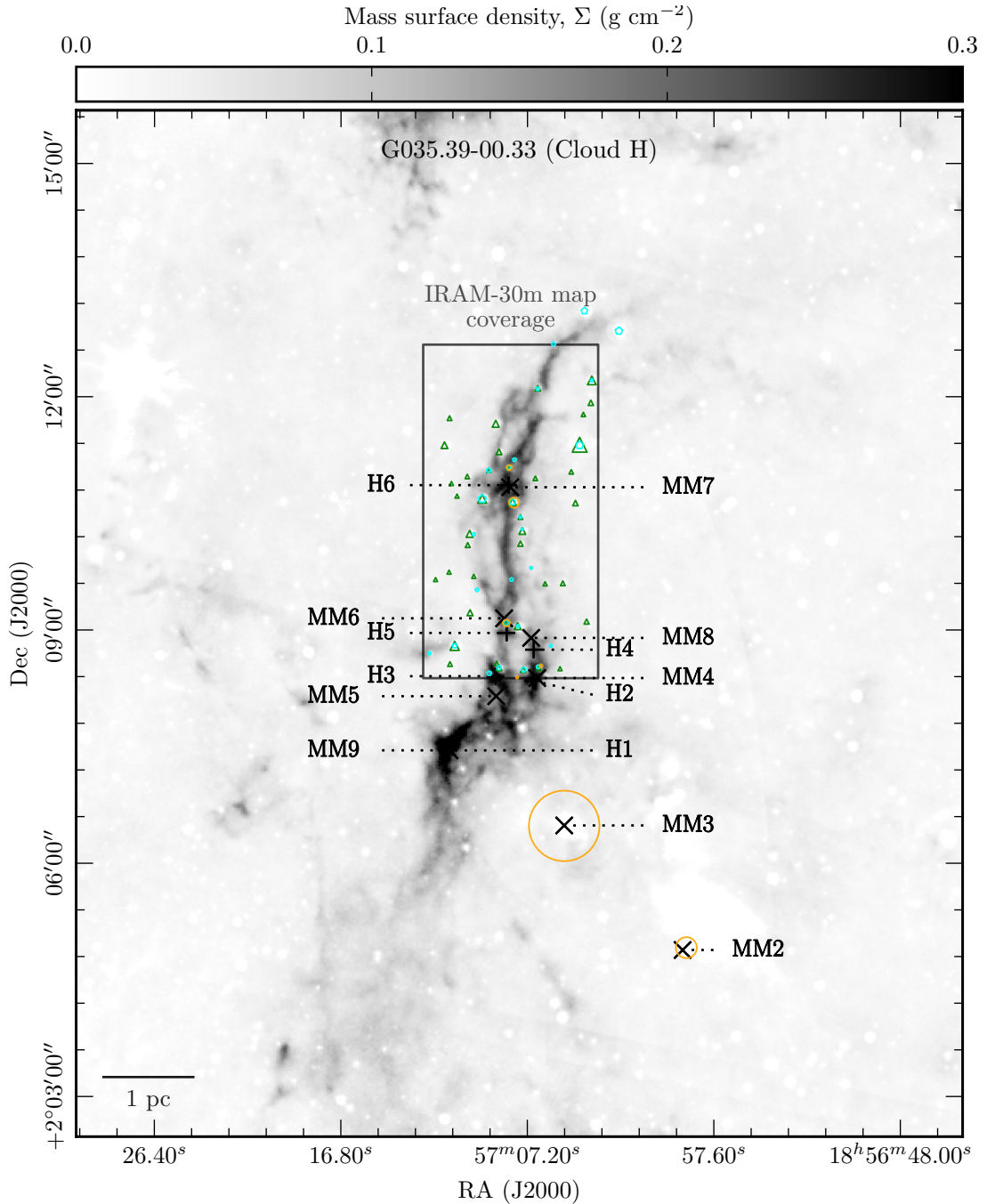


Figure 2.1: Shown in greyscale is the high-resolution, high-dynamic-range mass surface density map of the IRDC G035.39-00.33, produced by combining the dust extinction at the near- and far-infrared wavelengths (Kainulainen & Tan, 2013). Shown with + and × symbols and labeled are the positions of the “core” regions identified by Butler & Tan (2012, with H prefix) and those from Rathborne, Jackson & Simon (2006, with MM prefix), respectively. Shown as green triangles and cyan pentagons indicate the positions of the $8\mu\text{m}$ and $24\mu\text{m}$ sources, respectively (possibly related to heated dust from an embedded proto-stellar source; Carey et al., 2009). Sources with extended, enhanced $4.5\mu\text{m}$ emission, or “green fuzzies”, are plotted as orange circles (possibly related to shocked H_2 gas from an embedded proto-stellar source; Chambers et al., 2009). The size of each source scales linearly with the flux (Jiménez-Serra et al., 2010). The black rectangle shows the coverage of the IRAM-30m observations used in this chapter.

154217.1805 MHz; Dore et al., 2004). The data were converted into main beam brightness temperature, T_{MB} , from antenna temperature, T_{A}^* , by using the beam and forward efficiencies shown in Table 2.1. Saturn was observed to calculate the focus, and pointing was checked every ~ 2 hours on G34.3+0.2. The data were calibrated with the chopper-wheel technique (Kutner & Ulich, 1981), with a calibration uncertainty of ~ 20 per cent. Information on the beam sizes, frequencies, velocity resolutions are summarised in Table 2.1.

The GILDAS² packages CLASS and MAPPING were used to post-process the data. This included subtracting a first-order polynomial function to produce a flat baseline, and convolving the on-the-fly-data (OTF) with a Gaussian kernel, increasing the signal-to-noise ratio, and allowing us to resample the data onto a regularly spaced grid. The absolute angular resolution of the IRAM-30m antenna at the frequency of the $J=2 \rightarrow 1$ transition of N_2D^+ is $\sim 16''$. To allow comparison between the datasets, throughout this chapter all maps are spatially smoothed to an effective angular resolution of $\sim 27''$.

In this chapter we utilise the N_2H^+ ($1 - 0$) map from Henshaw et al. (2013), CO depletion map of Hernandez et al. (2012), and the mass surface density map from Kainulainen & Tan (2013).

2.4 Results

The average N_2D^+ ($2 - 1$) spectrum for the mapped region is presented in Figure 2.2, overlaid with a horizontal dotted line representing the σ_{rms} on the average (i.e. the average σ_{rms} over $N_{\text{sp}}^{0.5}$, where N_{sp} is the number of spectra in the map). Despite the very low σ_{rms} of the observations presented here, the detection of the N_2D^+ ($2 - 1$) is relatively weak. The majority of the emission is found within a velocity range of $40 - 50 \text{ km s}^{-1}$, which is shown as the grey shaded region on Figure 2.2. The emission within the velocity range is thought to be associated with Cloud H, as there are no other dense gas structures known along the line of sight to the source. Furthermore,

²see <https://www.iram.fr/IRAMFR/GILDAS/>

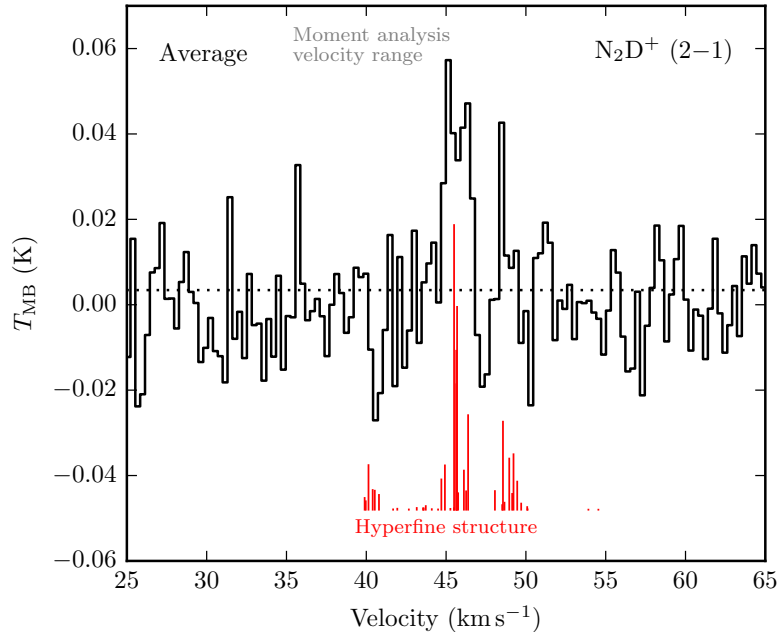


Figure 2.2: The average spectrum of N_2D^+ ($2 - 1$) transition for across the mapped region of Cloud H (boxed region in Figure 2.1). The horizontal dotted line represents the rms level, σ_{rms} , on the average spectrum of ~ 0.004 K. Note, this value is different to the average of the σ_{rms} within individual positions, which is given in Table 2.1. The shaded region shows the velocity range used for the integrated intensity map (zeroth-order moment; see Figure 2.4). The vertical red lines below the spectrum indicate the positions and relative strengths of all the hyperfine components of the N_2D^+ ($2 - 1$) transition (Dore et al., 2004), assuming a rest velocity of 45.5 km s^{-1} .

previous works investigating the molecular line emission from other, more abundant, molecular species found the brightest detections within this velocity range.

The spectra at each position across the mapped region are presented in Figure 2.3, which have been plotted over the same velocity range as the average spectrum and a temperature scale of -0.2 to 0.3 K (or approximately $-5 \sigma_{\text{rms}}$ to $8 \sigma_{\text{rms}}$). A clear detection of the line can be seen along the length of the cloud, particularly towards positions of high mass surface density (shown in the background of this figure). Each spectrum has been inspected by-eye for the presence of multiple velocity components previously identified in N_2H^+ and C^{18}O emission (Henshaw et al., 2013; with mean N_2H^+ emission velocities of $42.95 \pm 0.17 \text{ km s}^{-1}$, $45.63 \pm 0.03 \text{ km s}^{-1}$, and $46.77 \pm 0.06 \text{ km s}^{-1}$). However, evidence of only one component, centred at $\sim 46 \text{ km s}^{-1}$ can be identified. Unlike the N_2H^+ ($1 - 0$) line, however, N_2D^+ ($2 - 1$) possesses no isolated hyperfine components; the line is a blend of 40 hyperfine components, spread across a ve-

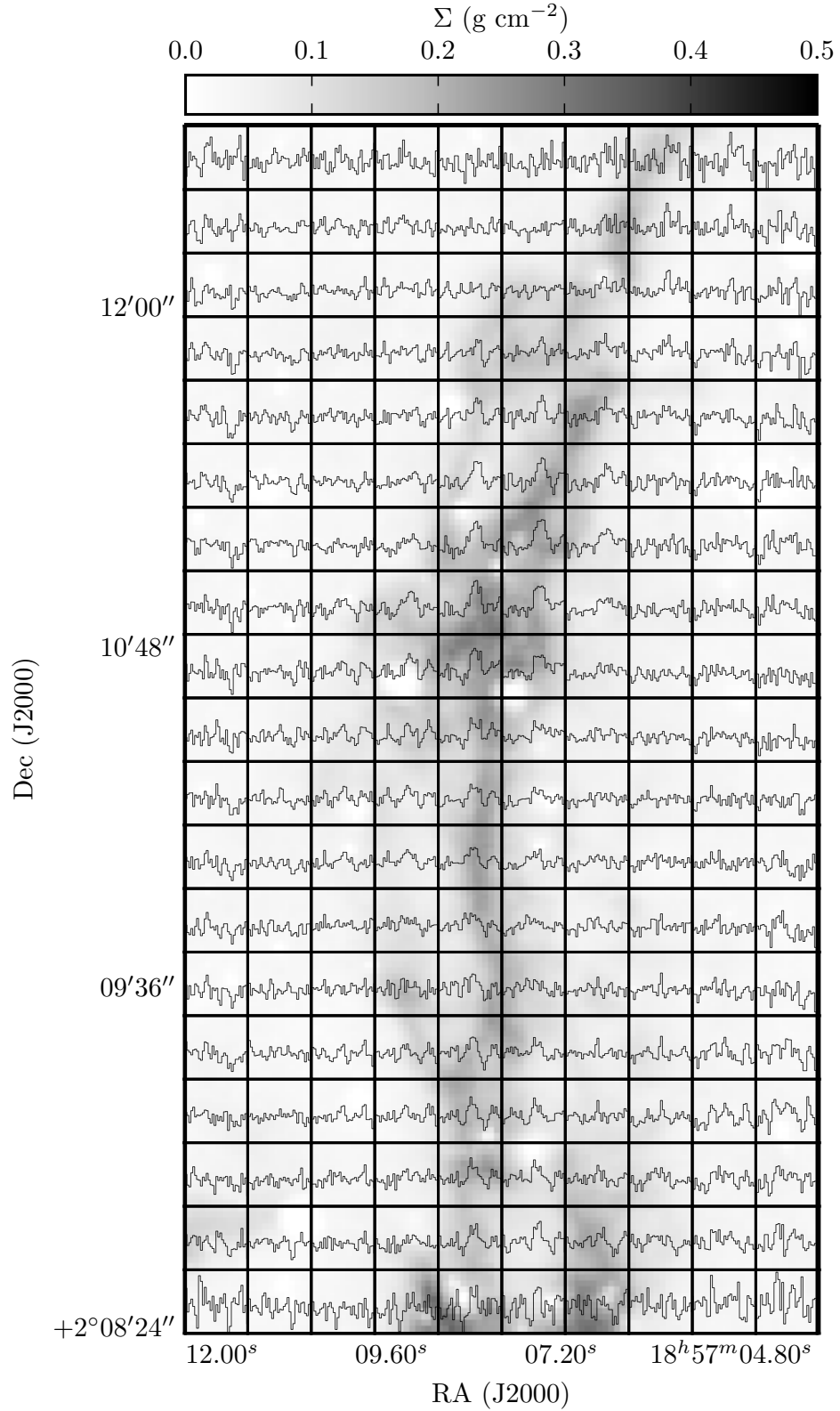


Figure 2.3: Shown are the individual N_2D^+ (2 – 1) spectra across the mapped region of Cloud H. The velocity range of each spectrum is 40 to 50 km s^{-1} , and the intensity range is -0.2 to 0.3 K. The background greyscale is the mass surface density map, determined from near and mid-infrared extinction ([Kainulainen & Tan, 2013](#)).

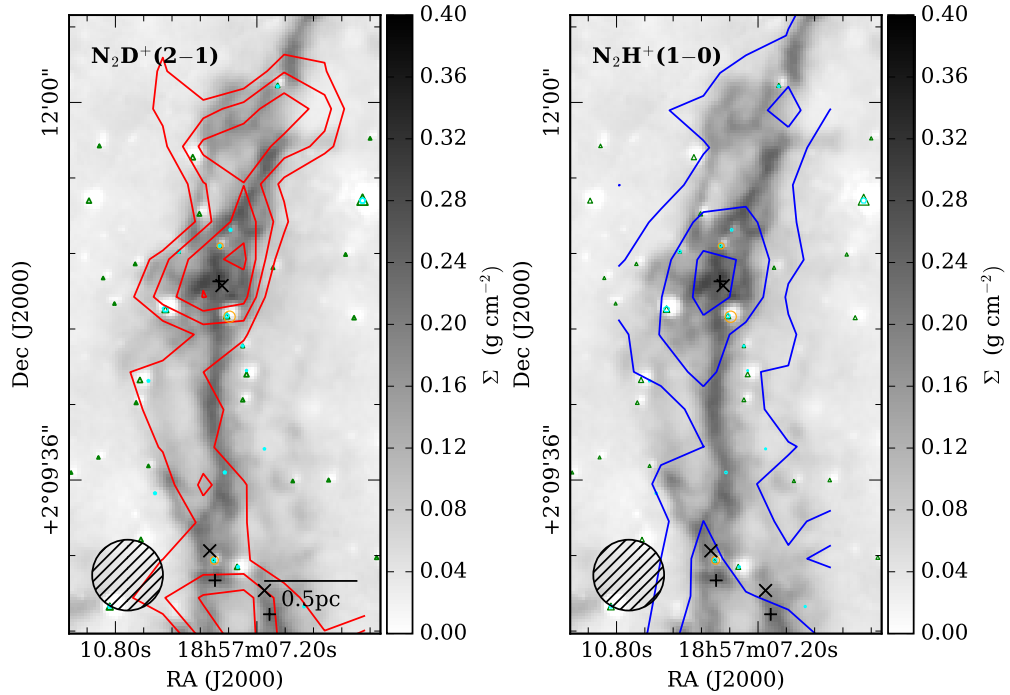


Figure 2.4: [left panel] The integrated intensity map of N_2D^+ ($2 - 1$) emission seen in contours of $2\sigma_W$, $3\sigma_W$, $4\sigma_W$ and $5\sigma_W$; where $\sigma_W = 0.07 \text{ K km s}^{-1}$. [right panel] The integrated intensity contours of the N_2H^+ ($1 - 0$) emission, data taken from [Henshaw et al. \(2013\)](#); contours are 5, 10 and $15\sigma_W$, where $\sigma_W \sim 0.11 \text{ K km s}^{-1}$. Each contour map is overlaid on the mass surface density map ([Kainulainen & Tan, 2013](#)). The over-plotted symbols are identical to those shown in [Figure 2.1](#).

locity range of 14.6 km s^{-1} (as shown in [Figure 2.2](#)). This, as well as line-widths of $\sim 1 \text{ km s}^{-1}$ (i.e. similar to those of N_2H^+ ($1 - 0$); [Henshaw et al., 2013](#)), makes the identification of multiple velocity components very difficult.

[Figure 2.4](#) presents a map of the N_2D^+ ($2 - 1$) emission integrated between $40 - 50 \text{ km s}^{-1}$ (shaded region in [Figure 2.2](#)), where the contours represent levels of $\sigma_W = \Delta v \sigma_{\text{rms}} N_{\text{ch}}^{0.5}$, where Δv is the velocity resolution (see [Table 2.1](#)) and N_{ch} is the number of channels integrated over. The integrated intensity contours are overlaid on the mass surface density map of [Kainulainen & Tan \(2013\)](#), with symbols identical to [Figure 2.1](#). The N_2D^+ emission is concentrated towards the “H6” region, and the south, near H2, H3, H4 and H5 “core” regions. However, when considering the $2\sigma_W$ emission level (most outer contour), there is evidence to suggest that the emission is extended across a large portion of the cloud.

2.5 Analysis

2.5.1 Column density

The column densities are calculated from the integrated intensity of the N_2D^+ ($2 - 1$) line using equation 1.11 (Caselli et al., 2002a). Therefore, the assumption is made that the emission is optically thin ($\tau_\nu \ll 1$), which is reasonable given the relatively faint detection of the line across the cloud. Assuming a constant excitation temperature of $T_{\text{ex}} \sim 4.5$ K, which is equivalent to the mean T_{ex} derived from the N_2H^+ observations (Henshaw et al., 2013), gives a mean beam-averaged column density of $N(\text{N}_2\text{D}^+) = 6.2 \pm 1.4 \times 10^{11} \text{ cm}^{-2}$, when imposing a three sigma threshold on the N_2D^+ ($2 - 1$) emission. The maximum beam-averaged column density of N_2D^+ is found toward the H6 region, with a value of $N(\text{N}_2\text{D}^+) = 8.0 \pm 1.4 \times 10^{11} \text{ cm}^{-2}$. Ranging the T_{ex} between 4 – 20 K would cause the column density to vary by $N(\text{N}_2\text{D}^+)_{-60\%}^{+30\%}$. This is most likely more representative of the physical uncertainty on the column density, rather than the measurement uncertainty shown on the values above (see Caselli et al., 2002a for uncertainty calculation).

2.5.2 Deuterium fraction

The N_2D^+ to N_2H^+ column density ratio is used to define the deuterium fraction across the mapped region, which is shown in Figure 2.5. We find values of the deuteration fractions larger than 0.01 widespread throughout the cloud, with the highest values found towards the north. The mean beam-averaged deuterium fraction across Cloud H is $D_{\text{frac}}^{\text{N}_2\text{H}^+} = 0.04 \pm 0.01$. The maximum value is found north of the ‘‘H6’’ region (at $\alpha(\text{J2000}) = 18^{\text{h}}57^{\text{m}}09^{\text{s}}$, $\delta(\text{J2000}) = 02^\circ 11'39''$), with a value of $D_{\text{frac}}^{\text{N}_2\text{H}^+} = 0.09 \pm 0.02$. Note that varying the excitation temperature for both N_2H^+ and N_2D^+ between 4 – 20 K would cause a change of $D_{\text{frac}}^{\text{N}_2\text{H}^+}{}_{-55\%}^{+15\%}$. Again, this could be seen as more representative of the physical uncertainty (although see below for discussion of beam dilution effects).

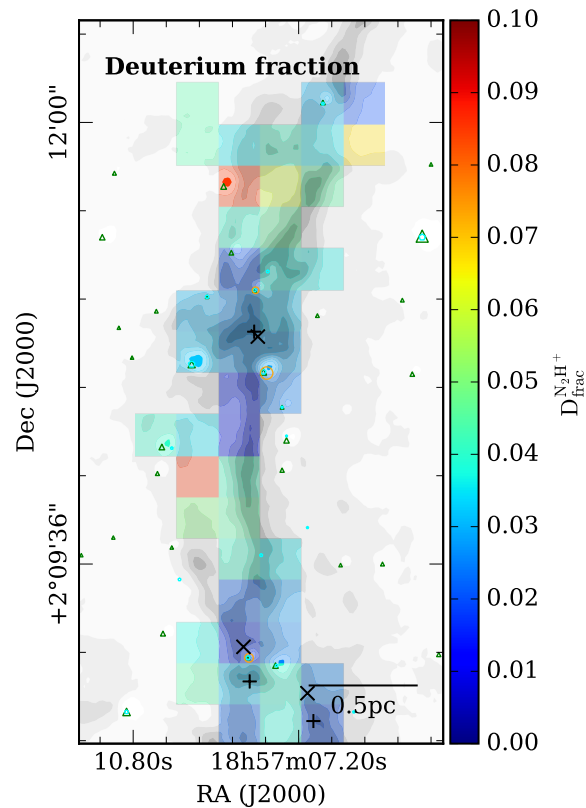


Figure 2.5: A map of the deuterium fraction shown in colour-scale, overlaid with a grey-scale of the mass surface density map (Kainulainen & Tan, 2013). The over-plotted symbols are identical to those shown in Figure 2.1.

2.6 Discussion

2.6.1 Comparison to other star-forming regions

As in low-mass star-forming regions, the deuterium fraction in high-mass star-forming regions is believed to be a good evolutionary tracer (e.g. Fontani et al., 2011). However, the exact boundaries to define an evolutionary state are still poorly understood. To show this, plotted on Figure 2.6 is the column densities of N_2D^+ and N_2H^+ found in this chapter, and for various other high-mass (in blue; Fontani et al., 2006, 2011; Miettinen, Hennemann & Linz, 2011; Gerner et al., 2015; Kong et al., 2016) and low-mass (in red; Crapsi et al., 2005; Friesen et al., 2010; Friesen, Kirk & Shirley, 2013) cores described within the literature. In this figure, the left panel shows a scatter plot of

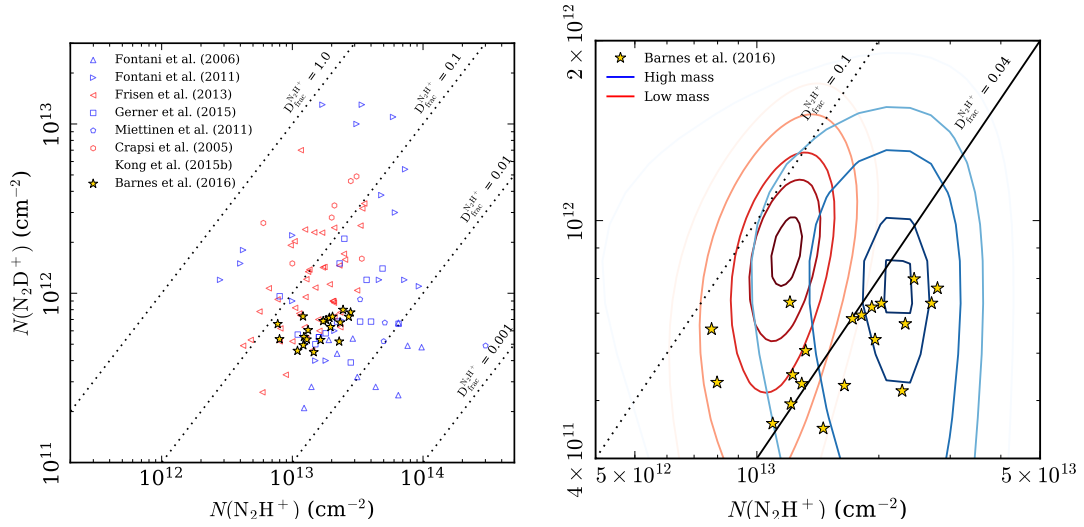


Figure 2.6: Column density of N_2H^+ as a function of the column density of N_2D^+ . The values found in this work are shown as stars. [left panel] Over-plotted are values from the literature, where the red symbols represent the low-mass star forming regions, and the blue represent high-mass star forming regions. [right panel] Red and blue contours representing the number density of low and high mass sources, respectively. The dashed diagonal lines overlaid represent deuterium fractions of $D_{\text{frac}}^{\text{N}_2\text{H}^+} = [0.001, 0.01, 0.04, 0.1, 1.0]$, as labelled.

the deuterium fraction determined within each source taken from the literature, which have been grouped according to their masses and represented as contours in the right panel of this figure.

The deuterium fractions found within Cloud H are most similar to those found in IRDCs by Gerner et al. (2015), who found mean values of $\sim 0.01 - 0.1$ (observed at spatial resolution of a $\sim \text{few } 10''$, at $\sim 4 \text{ kpc}$). However, our values are an order of magnitude lower than the values observed by Fontani et al. (2011) and Kong et al. (2016) towards high-mass starless cores (HMSCs), where $D_{\text{frac}}^{\text{N}_2\text{H}^+} \sim 0.3$. Gerner et al. (2015) suggest that the low deuteration values found in their sample of IRDCs may be due to the presence of unresolved evolved objects ($24 \mu\text{m}$ sources). This could also be the case for Cloud H, as the average deuterium fraction is also close to the values observed towards high-mass protostellar candidates (~ 0.04 ; Fontani et al., 2006, 2011).

2.6.2 Comparison to the physical properties of the cloud

This section aims at investigating how the deuterium fraction may be affected by the physical properties of Cloud H. To do so, the deuterium fraction and the column density of N_2D^+ and N_2H^+ have been plotted against several cloud properties. Shown in Figure 2.7 are several interesting correlations that have been found, which are discussed below.

The column density - mass surface density plots [upper panels], show that both the N_2D^+ and N_2H^+ have an increase with increasing mass surface density. However, this increase is more significant for N_2H^+ (dynamical range of ~ 3), than N_2D^+ (dynamical range of ~ 1.5 ; compare to the uncertainty bar on the upper left of left panel). This is reflected in the deuterium fraction - mass surface density plot [lower left], which shows an overall negative correlation. This, on the face of it, is not expected for the scenario of N_2D^+ having significantly elevated abundances towards the densest (i.e. high mass surface density) regions within the cloud.

It has been previously mentioned that the deuterium fraction is very sensitive to the level of CO depletion (see Section 1.3.1). The CO depletion can be expressed as the factor, f_D , which is defined as the ratio of the observed mass surface density to mass surface density derived from CO emission, assuming a reference CO fractional abundance with respect to H_2 . Here the CO depletion fraction values determined by Hernandez et al. (2012) is used,³ which is plotted against the deuterium fraction in the lower right panel of Figure 2.7. Again, however, an anti-correlation is seen, similar to that of the mass surface density (compare to lower right panel).

The above result is not expected for the scenario of elevated deuteration within densest, coldest cores, which is facilitated by their high levels of CO depletion. However, keeping in mind that everything along the line-of-sight is traced by the column densities determined here, there maybe the scenario that N_2D^+ and N_2H^+ are in-fact tracing

³These authors calculate the CO depletion averaged along each line-of-sight (i.e. each pixel) throughout the cloud, and then normalise these values such that on average pixels with mass surface densities of $0.01 \text{ g cm}^{-2} < \Sigma < 0.03 \text{ g cm}^{-2}$ are unity. This method produces a modified CO depletion factor, f'_D , which is used for the purposes of this chapter.

different material. As assumed, there may be compact core regions, which are traced by both N_2D^+ and N_2H^+ , however, these may be surrounded by an envelope which is traced by only N_2H^+ . Therefore, there would be comparatively more emission along a given line-of-sight from the N_2H^+ with respect to the N_2D^+ , purely due to it tracing more material.

2.6.3 Comparison with chemical models

To determine if the observed levels of deuteration are consistent with the current evolutionary stage of Cloud H, we have conducted a series of chemical models (Kong et al., 2015). The model consists of the Nahoon code and a reduced network extracted from the Kinetic Database for Astrochemistry (KIDA Wakelam et al., 2012),⁴ including the elements H, D, He, C, N, O. The chemical species traced by the code contain up to 3 atoms in size, except for H_3O^+ and its deuterated isotopologues, which significantly improve the consistency with a more complete network (Sipilä, Caselli & Harju, 2013). Spin states of H_2 , H_3^+ and their deuterated isotopologues are included, and the formation of o- H_2 , p- H_2 , HD, o- D_2 , p- D_2 on dust grain surface are considered following Le Petit, Roueff & Le Bourlot (2002). We follow Pagani et al. (2009) in calculating the dissociative recombination rates of all forms of H_3^+ . The initial elemental abundances are listed in Table 2 in Kong et al. (2015). In this paper, we treat the depletion of neutral species by reducing the initial elemental abundances of C, N, O by the depletion factor, f_{D} , and consider a broad combination of physical conditions appropriate for Cloud H.

We explore a grid of models with $A_{\text{v}} = [5, 10, 20, 30]$ mag, $n_{\text{H}} = [0.1, 1, 2, 10] \times 10^4$ cm^{-3} , $T_{\text{kin}} = [10, 15, 20]$ K, $f_{\text{D}} = [1, 2, 3, 5, 10]$, to check the equilibrium $\text{D}_{\text{frac}}^{\text{N}_2\text{H}^+}$ and timescale. We adopt a constant radiation field four times stronger than the standard Habing field (G_0), however because of high visual extinction values considered here, small changes of G_0 do not affect the chemistry. We also explore initial ortho-to-para H_2 ratios of $\text{OPR}_0^{\text{H}_2} = 0.001-3$. A $\text{OPR}_0^{\text{H}_2} = 3$ represents the high temperature statistical ratio limit, as ortho- and para- H_2 are formed at high temperatures on dust grains in

⁴<http://kida.obs.u-bordeaux1.fr>

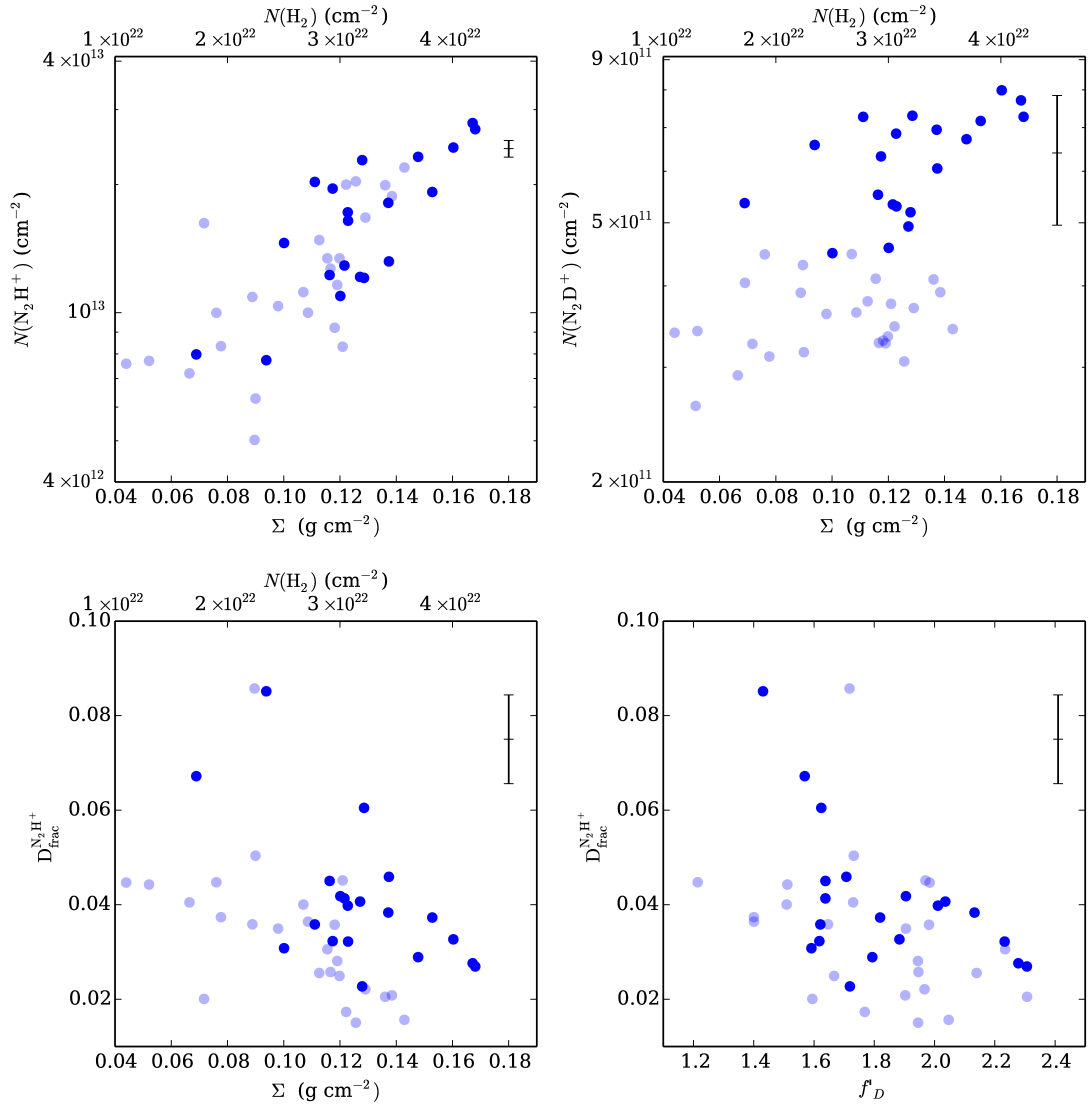


Figure 2.7: Shown in the panels are the N_2H^+ [upper left] and N_2D^+ [upper right] column densities as a function of mass surface density, deuterium fraction as a function of mass surface density [lower left], and deuterium fraction as a function of normalised CO depletion factor [lower right]. Average errors for N_2D^+ column density and $D_{\text{frac}}^{N_2H^+}$ are displayed in the upper right of each plot. Not shown are the errors on the mass surface density and CO depletion, which are $\sim 30\%$ (Kainulainen & Tan, 2013) and $\sim 50\%$ (Hernandez et al., 2012), respectively. The solid and transparent points represent positions where both the N_2H^+ and N_2D^+ emission is above a 3σ and 2σ threshold, respectively.

the ratio of their nuclear spin state statistical weights (3:1; see section 1.3.1). $\text{OPR}_0^{\text{H}_2} = 0.1 - 1$ are values close to those deduced by [Crabtree et al. \(2011\)](#) in translucent clouds with $T = 50 - 70$ K: 0.8 - 0.3. Recently, [Xu et al. \(2016a\)](#) made some rough constraints on the H_2 ortho-to-para ratio for the low density gas within Taurus. These authors estimate $\text{OPR}^{\text{H}_2} \sim 0.2$. Lower values are expected in dark molecular clouds (see [Sipilä, Caselli & Harju, 2013](#)). Therefore, our $\text{OPR}_0^{\text{H}_2}$ exploration covers typical values observed in molecular clouds.

Table 2.2 presents the results of a subset of models with input parameters which best represent the global properties of Cloud H. Shown are the equilibrium deuterium fraction, $D_{\text{frac,eq}}^{\text{N}_2\text{H}^+}$, the time taken to achieve 90% of this value. Variation of the extinction is not displayed in the Table, as ranging A_v between [10, 20, 30] mag does not significantly effect the results, however an extinction of 5 mag tends to decrease the $D_{\text{frac,eq}}^{\text{N}_2\text{H}^+}$ and the time by a factor of a few. This is not thought to be an issue as the mapped region of Cloud H has an average extinction of ~ 20 mag ([Kainulainen & Tan, 2013](#)).

The observed deuterium fractions within Cloud H are generally similar with the model equilibrium values, for kinetic temperatures of 10 K and 15 K. If we assume that the cloud has a mean global density $n_{\text{H}} \sim 10^4 \text{ cm}^{-3}$ ([Hernandez et al., 2012](#)), a mean CO depletion of $f_{\text{D}} = 3$, and assume the mean kinetic temperature is comparable to the ~ 15 K dust temperature found by [Nguyen Luong et al. \(2011\)](#), the model predicted equilibrium value is $D_{\text{frac,eq}}^{\text{N}_2\text{H}^+} = 0.048$, remarkably close to the average observed value of $D_{\text{frac}}^{\text{N}_2\text{H}^+} = 0.04 \pm 0.01$.

Figure 2.8 shows how the ortho-to-para ratio of H_2 and $D_{\text{frac}}^{\text{N}_2\text{H}^+}$ vary as a function of time, for the model parameters of $n_{\text{H}} = 10^4 \text{ cm}^{-3}$, $f_{\text{D}} = 3$, $T_{\text{kin}} = 15$ K and $A_v = 20$ mag. For these properties which best describe Cloud H, we find the time to reach the observed deuterium fraction vary between $\sim 0.2 - 8$ Myrs, where the shortest times are for low initial ortho-to-para ratios (e.g. $\text{OPR}_0^{\text{H}_2} = 0.001$; also see Table 2.2).

Figure 2.9 displays the time needed to reach the observed deuterium fraction of $D_{\text{frac}}^{\text{N}_2\text{H}^+} = 0.04$ from a given initial ortho-to-para ratio of H_2 (shown on the top axis) versus the time needed to reach this initial ortho-to-para ratio if starting from the high

Table 2.2: Equilibrium deuterium fractions for models with an extinction of $A_v = 20$ mag, number densities, n_H , of 10^4 and 10^5 cm^{-3} , and initial ortho-to-para H_2 ratios of 0.001, 0.01, 0.1, and 1. Columns show the model inputs of gas kinetic temperature, T_{kin} , CO depletion, and model outputs of equilibrium value of $D_{\text{frac}}^{\text{N}_2\text{H}^+}$ and the time taken to achieve 90 % of this value, $t_{\text{eq},90}$.

T_{kin} (K)	f_{D}	$D_{\text{frac,eq}}^{\text{N}_2\text{H}^+}$	$t_{\text{eq},90}$ (Myr)			
			$\text{OPR}_0^{\text{H}_2} = 0.001$	$\text{OPR}_0^{\text{H}_2} = 0.01$	$\text{OPR}_0^{\text{H}_2} = 0.1$	$\text{OPR}_0^{\text{H}_2} = 1$
$n_H = 10^4 \text{ cm}^{-3}$						
($t_{\text{ff}} = 4.4 \times 10^5$ yrs)						
10	1	0.021	0.73	3.24	6.19	8.36
10	3	0.044	0.29	2.10	3.61	4.73
10	5	0.057	0.24	1.79	3.01	3.92
10	10	0.076	0.26	1.50	2.45	3.16
15	1	0.022	0.71	3.32	6.32	8.50
15	3	0.048	0.27	2.06	3.52	4.60
15	5	0.062	0.20	1.73	2.90	3.76
15	10	0.083	0.19	1.43	2.32	2.99
20	1	0.015	0.39	2.91	6.48	8.72
20	3	0.025	0.03	1.90	3.57	4.65
20	5	0.029	0.003	1.61	2.91	3.76
20	10	0.034	0.0005	1.32	2.32	2.96
$n_H = 10^5 \text{ cm}^{-3}$						
($t_{\text{ff}} = 1.4 \times 10^5$ yrs)						
10	1	0.026	0.67	2.87	5.23	6.99
10	3	0.076	0.45	1.48	2.35	3.02
10	5	0.111	0.40	1.13	1.75	2.23
10	10	0.17	0.40	0.84	1.28	1.61
15	1	0.027	0.65	2.96	5.44	7.27
15	3	0.079	0.32	1.48	2.37	3.04
15	5	0.115	0.29	1.12	1.74	2.21
15	10	0.175	0.28	0.83	1.26	1.58
20	1	0.017	0.35	2.67	5.69	7.61
20	3	0.033	0.06	1.45	2.49	3.18
20	5	0.04	0.01	1.09	1.81	2.28
20	10	0.048	0.0004	0.79	1.27	1.59

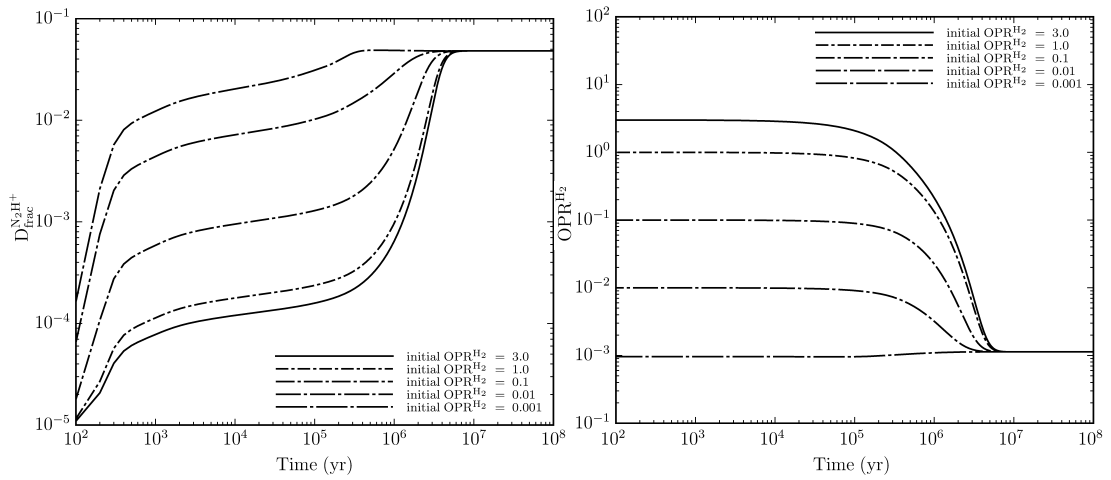


Figure 2.8: Time evolution of the OPR^{H_2} [left panel] and $D_{\text{frac}}^{\text{N}_2\text{H}^+}$ [right panel] under different assumptions of the initial OPR^{H_2} , for $n_{\text{H}} = 10^4 \text{ cm}^{-3}$, $f_{\text{D}} = 3$, $T_{\text{kin}} = 15 \text{ K}$ and $A_{\text{V}} = 20 \text{ mag}$. We explore OPR^{H_2} from 3 down to 0.001.

temperature statistical ratio limit of 3 (Kong et al., 2015). The solid blue line shows this result for the fiducial model parameters, e.g. of density, temperature, depletion factor, cosmic ray ionisation rate. The dashed blue line shows the time to reach $D_{\text{frac}}^{\text{N}_2\text{H}^+} = 0.02$ for the fiducial model.

An estimate of the total age of the molecular cloud is the sum of the ortho-to-para ratio decay timescale and deuteration timescale, i.e. from the initial time when the hydrogen molecules formed with an assumed high temperature statistical ortho-to-para ratio (the diffuse clouds formation), to when they reach the initial ortho-to-para ratio in the model and the deuteration level is allowed to evolve (the IRDC formation), until the time when the observed deuteration level is achieved (current state of IRDC). Shown on Figure 2.9 as dotted black lines are example contours of this sum for 0.3, 1, 3, 10 Myr. The astrochemical model results indicate that a timescale of at least 3 Myrs is needed for the cloud to evolve from its initial state to the present observed deuterated state. Adopting values of CO depletion factor and density of a factor two higher ($f_{\text{D}} = 6$ and $n_{\text{H}} = 2 \times 10^4 \text{ cm}^{-3}$) or a cosmic ionisation rate of a factor two lower ($\zeta = 1.25 \times 10^{-17} \text{ s}^{-1}$) would imply cloud ages of at least 3 – 7 Myrs, shown in left panel of Figure 2.9. We note that decreasing the CO depletion or density, or increasing the cosmic ionisation rate would cause the models to never reach an equilibrium deu-

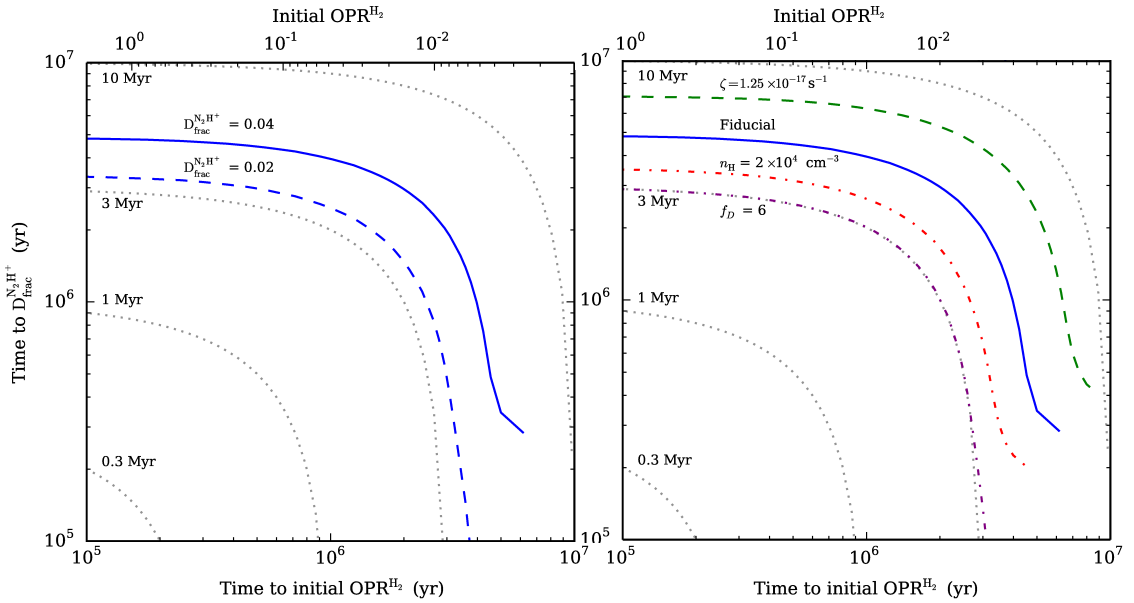


Figure 2.9: Time to reach the observed deuterium fraction ($D_{\text{frac}}^{\text{N}_2\text{H}^+} = 0.04$) from a given initial ortho-to-para ratio of H_2 [shown on the top axis] versus the time to reach this initial ortho-to-para ratio if starting from statistical equilibrium ratio of 3. The solid blue line shows this result for the fiducial model parameters, e.g. of density, temperature, depletion factor, cosmic ray ionisation rate. Grey dotted lines show contours of the sum of the deuteration timescale and ortho-to-para ratio decay timescale to equal 0.3, 1, 3, 10 Myr, as labelled. The dashed blue line [left panel] shows the time to reach $D_{\text{frac}}^{\text{N}_2\text{H}^+} = 0.02$ for the fiducial model. The dashed and dot-dashed lines [right panel] show the effect of varying several of the model parameters, as labelled.

terium fraction of 0.04, hence these are not plotted on Figure 2.8. We thus conclude that the age of Cloud H is at least ~ 3 Myr. This is a lower limit, since the current observed deuteration level is consistent with astrochemical equilibrium.

A lower limit of 3 Myr is equivalent to ~ 8 local free-fall timescales, assuming an average density of 10^4 cm^{-3} (with spherical geometry $\sim 4 \times 10^5$ yrs). This indicates the cloud is dynamically “old” and is thus likely to have had time to achieve approximate virial equilibrium (as was concluded in Hernandez et al., 2012). This timescale is consistent with that estimated from a kinematic analysis in Henshaw et al., 2013.

2.6.4 Caveats of the Kong et al. (2015) chemical model

We do note, however, that the Kong et al. (2015) model used for this investigation of the deuterium fraction in Cloud H does not allow for the full cloud evolution (i.e. it has a constant density and extinction), which could affect the estimated total cloud lifetimes. Including these into the model would cause the deuterium fraction to evolve slower at early times, when the density and extinction is lower, and faster at later times when the cloud has collapsed and dense cores have formed. It is, however, difficult to estimate the precise effect this would have on the results of this work, and we hope to address this in future with a more complete model that takes into account the chemical and physical evolution of the cloud. In the limitations of the current model, for the time being, below we try to place a lower limit of the age of Cloud H by assuming a higher density (i.e. a faster evolving deuterium fraction), which is physically motivated by observed in dense cores within the cloud.

Given that much of the complex structure observed in the mass surface density plot is not seen in the N_2D^+ and N_2H^+ emission maps, we use the core diameters extracted from 3.2 mm continuum observations of Cloud H with the PdBI are typically 0.1 pc (Henshaw et al., 2016a). This implies an approximate beam dilution factor of ~ 0.07 (i.e. the square of the core-to-beam size ratio). To check this, we input typical core properties in the model. Assuming the cores have densities of $\sim 10^5 \text{ cm}^{-3}$ (average “core”; e.g. Butler & Tan, 2012), temperatures of $\sim 10 \text{ K}$, and CO depletions of $\sim 5 - 10$, we find model predicted $D_{\text{frac,eq}}^{\text{N}_2\text{H}^+}$ of 0.11 – 0.17 (see Table 2.2), which are closer to the deuteration values found in high-mass prestellar cores (Fontani et al., 2011). Applying the beam dilution factor to the predicted values, we find deuterium fractions of $\sim 0.007 - 0.01$. Although these values are slightly below what is observed, this could be a plausible explanation for the low observed deuterium fractions in the IRDCs, where unresolved dense cores are present. The timescales to reach these deuteration levels in gas at these higher densities of 10^5 cm^{-3} are shorter: $\sim 1 \text{ Myr}$ (see also Punanova et al., 2015). However, this is still long compared to the local free-fall time of $\sim 0.1 \text{ Myr}$.

Higher angular resolution observations of N_2D^+ are needed to disentangle if Cloud H has reached a deuterium fraction equilibrium in its diffuse gas, $\sim 10^4 \text{ cm}^{-3}$ bulk density, or if the observed deuteration is dominated by a population of denser, currently unresolved cores.

2.7 Summary

The main results of this chapter are summarised below.

- i) The emission from N_2D^+ is extended across Cloud H, and from this emission we calculate a mean beam-averaged column density of $6.2 \pm 1.4 \times 10^{11} \text{ cm}^{-2}$.
- ii) The deuterium fraction across the cloud is $D_{\text{frac}}^{\text{N}_2\text{H}^+} (\text{N}_2\text{D}^+/\text{N}_2\text{H}^+) = 0.04 \pm 0.01$, which is three orders of magnitude higher than the interstellar $[\text{D}]/[\text{H}]$ ratio. This is within the range quoted for other IRDCs (e.g. [Miettinen, Hennemann & Linz, 2011](#); [Gerner et al., 2015](#)), yet it is significantly smaller than the values found toward massive starless cores within quiescent IRDCs ([Fontani et al., 2011](#)).
- iii) Chemical modelling of the deuteration, shows that the observed values are consistent with those of chemical equilibrium. Such an equilibrium would have taken at least $\sim 3 \text{ Myr}$ to be established. This scenario places a lower limit on the cloud age of ~ 8 local free-fall times, which indicates that the IRDC filament is dynamically “old”, with sufficient time to relax to a quasi-equilibrium virialised state. This is consistent with the previous age estimates based on the kinematics ([Henshaw et al., 2013](#)).
- iv) To test if beam dilution of denser unresolved sub-structure is causing the low deuterium fraction, typical core properties are used in the chemical model. The results of these tests show that a core would reach a higher equilibrium value, faster than a lower density cloud ($\sim 1 \text{ Myr}$, or ~ 7 local free-fall times). The typical cores size, of $\sim 0.1 \text{ pc}$, would imply a beam dilution factor of ~ 0.07 .

These results suggest that irrespective of the assumed density, Cloud H appears to be dynamically “old”, i.e. older than several free-fall times. This, therefore, would suggest that this cloud could be a supported, rather than a transient, molecular cloud (see Section 1.2.1). Indeed, [Hernandez et al. \(2012\)](#) and [Hernandez & Tan \(2015\)](#) found that both the IRDC and the larger GMC (around tens of parsec-scale) are close to virial equilibrium, hence could survive for longer than a free-fall time (see Section 1.2). Higher angular resolution observations show that this virial support could also be present on core scales if magnetic field strengths of \sim mG are present within the cloud ([Henshaw et al., 2016b](#); [Sokolov et al., 2018](#)). Magnetic fields strengths of this order would not be uncommon for an IRDC (e.g. [Pillai et al., 2015](#)).

As mentioned in Section 1.2.1, this supported molecular cloud scenario also requires the on-going replenishment of turbulence to prevent collapse. Potential sources of energy injection could be outflows from embedded proto-stellar objects and/or from the energy cascade produced by large-scale gravitational collapse (e.g. [Mac Low & Klessen, 2004](#)). Interestingly, both of these mechanisms have been proposed to explain the widespread, narrow line-width SiO emission (i.e. shocks) observed by [Jiménez-Serra et al. \(2010\)](#).

A potential caveat to the above discussion is that, although the cloud lifetimes determined here appear to be dynamically old (as determined from the local free-fall time), these are not of the order typically quoted for a supported molecular cloud (e.g. on the ambipolar diffusion timescale of $t_{AD} \sim 10$ Myr; [Mac Low & Klessen, 2004](#)). This may be a result of the chemical model from [Kong et al. \(2015\)](#) not taking the evolution of the system density into account. Further work is needed to see if this would increase or decrease the cloud lifetime, allowing for a more accurate probe of the cloud’s age and a more stringent test on the competing predictions.

Chapter 3

Similar complex kinematics within two massive, filamentary infrared dark clouds

3.1 Preface

This chapter presents work which has been published by [Barnes et al. \(2018\)](#). The observations for this work were proposed, collected and reduced by J. D. Henshaw. The data analysis and interpretation were conducted by A. T. Barnes. The initial draft of the publication was written by A. T. Barnes, who then incorporated comments from co-authors and an anonymous referee in the final draft.

3.2 Introduction

As previously discussed, the structures within star-forming regions are thought to play an important role in their evolution. Analysis of these structures is, however, limited, as only the phase-space (i.e. position-position-velocity) representation of their true three-dimensional structure is observable. Moreover, identifying structures within this

phase-space using spectroscopic observations is complicated by the complex kinematic structure of these regions, which can have multiple velocity components within each observed line-of-sight (e.g. [Henshaw et al., 2013](#)). This chapter presents an investigation of the complex kinematic structure within the IRDC, G034.43+00.24 (henceforth Cloud F). This is compared to the kinematic structure within the IRDC discussed in the previous chapter (Cloud H), which shares many similar physical properties. Cloud F is then placed in the context of the larger scale GMC structure.

3.2.1 IRDC G034.43+00.24

This chapter will focus on the IRDC, Cloud F, which was first identified by [Miralles, Rodriguez & Scalise \(1994\)](#) as an unresolved elongated structure in NH_3 emission (a tracer of cold, dense gas) to the north of the bright IRAS source 1807+0121 (see [Figure 3.1](#)). Further investigation of this region was, however, delayed until the advent of higher resolution infrared telescopes, such as the *MSX*, which [Simon et al. \(2006a\)](#) used to identify Cloud F, along with 10,930 other candidate IRDCs, as having an extended structure silhouetted against diffuse background emission. [Simon et al. \(2006b\)](#) then investigated the global properties of the clouds from the [Simon et al. \(2006a\)](#) sample which resided within the Galactic Ring Survey's coverage (a survey of $^{13}\text{CO}(1-0)$ molecular line emission), which were especially extended (major axis >1.53) and had a strong average extinction contrast against the background (with $[\text{background-image}]/\text{background} > 0.25$). Using 1.2 mm continuum observations, [Rathborne, Jackson & Simon \(2006\)](#) then investigated the core properties within 38 of these clouds (the positions of these cores within Cloud F are shown in [Figure 3.1](#)), selecting those which had kinematic distance estimates ([Simon et al., 2006b](#)). [Butler & Tan \(2009, 2012\)](#) and [Kainulainen & Tan \(2013\)](#) studied the core properties within 10 of the [Rathborne, Jackson & Simon \(2006\)](#) sample IRDCs, which were relatively nearby, massive, dark, and showed relatively simple surrounding diffuse emission (positions shown in [Figure 3.1](#)). These maps highlighted Cloud F in particular (along with Cloud H; see [Section 3.7.2](#)), as having a complex filamentary morphology containing several massive cores, and a large amount of dense, quiescent gas (also see [Fontani et al., 2011](#) and

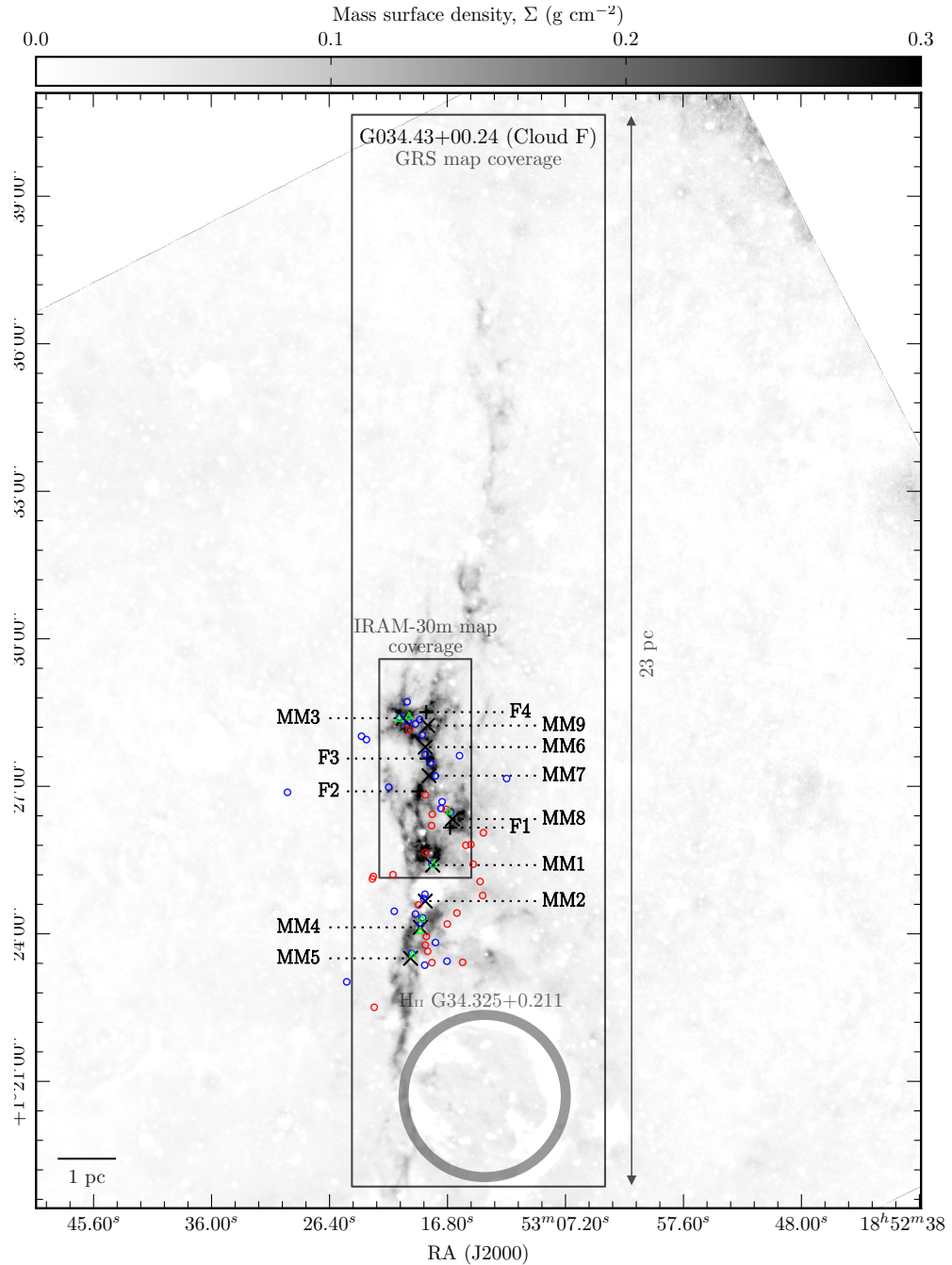


Figure 3.1: Shown in greyscale is the high-resolution, high-dynamic-range mass surface density map of the IRDC G034.43+00.24, produced by combining the dust extinction at the near- and far-infrared wavelengths (Kainulainen & Tan, 2013). The black rectangles show the coverage of the Galactic Ring Survey (Jackson et al., 2006, see Section 3.14) and IRAM-30m observations. Shown with + and × symbols and labeled are the positions of the “core” regions identified by Butler & Tan (2012, with F prefix) and those from Rathborne, Jackson & Simon (2006, with MM prefix), respectively. Shown as coloured circles are the young stellar objects candidates, identified by their spectral energy distribution in the *Spitzer* bands (Shepherd et al., 2007): “good” and “poor” (i.e. those with a poor or no spectral energy distribution fit) detections are shown in blue and red, respectively. Sources with extended, enhanced $4.5\mu\text{m}$ emission, or “green fuzzies”, are plotted as green triangles (Chambers et al., 2009). Shown in the lower right of the map is the approximate shell of the H II region G34.325+0.211, see Xu et al., 2016b for a discussion of its influence on the IRDC.

Table 3.1: Cloud properties within the IRAM-30m mapped region, shown in Figure 3.1. See Section 3.7.2 for comparison to the Cloud H.

Cloud property within IRAM-30 map	Cloud F (G034.43+00.24)	Cloud H (G035.39-00.33)
Distance, d (kpc) ^a	3.7 ± 0.6	2.9 ± 0.4
Map size, R (pc) ^b	3.4 ± 0.5	2.3 ± 0.3
Aspect ratio, A_0	2.4	2.6
Σ (g cm^{-2}) ^c	0.10 ± 0.03	0.09 ± 0.03
f_{D} ^d	1.1 ± 0.6	2.8 ± 1.4
Mass, M (M_{\odot}) ^e	4700 ± 1400	1700 ± 500
T (K) ^f	~ 17	~ 13
m ($M_{\odot} \text{ pc}^{-1}$) ^g	1400 ± 400	740 ± 200

a: Near kinematic distance to the sources (Simon et al., 2006b; Roman-Duval et al., 2009). See Section 3.7.3 for further discussion of the source distance.

b: Calculated from the mean RA and Dec range.

c: Average mass surface density (Kainulainen & Tan, 2013).

d: CO depletion factor presented in Section 3.6 compared to the value measured by Hernandez et al. (2012).

e: Masses calculated for the region covered by the IRAM-30m observations. Total cloud masses calculated by (Butler & Tan, 2012) are 4,460 and 13,340 M_{\odot} for Clouds F and H, respectively.

f: Dirienzo et al. (2015); Pon et al. (2016a); Sokolov et al. (2017)

g: The mass per unit length can be given as $m = M/R$.

Kong et al., 2017 for chemical studies towards the quiescent gas within this cloud). The stringent selection process, through several datasets, summarised here, has singled out Cloud F as an ideal candidate in which to investigate the initial conditions of massive star formation. Table 3.1 presents the physical properties of interest for Cloud F (determined within the area mapped by the IRAM-30m observations), and Figure 3.1 shows the mass surface density map across the cloud region (Kainulainen & Tan, 2013).

3.2.2 Observational tools required to investigate the kinematic structure

To investigate the kinematic structures on various scales within Cloud F, we use emission from the $\text{C}^{18}\text{O}(1-0)$ and $\text{N}_2\text{H}^+(1-0)$ molecular line transitions. Assuming that the $\text{C}^{18}\text{O}(1-0)$ line is thermalised and optically thin, this should trace the more extended gas, as its critical density is comparable to the average volume density expected within IRDCs ($\sim 10^{3-4} \text{ cm}^{-3}$ when observed at scales of $\sim 0.5 \text{ pc}$; e.g. Hen-

shaw et al., 2013). The N_2H^+ (1–0) transition has a significantly higher critical density ($\sim 10^{4-5} \text{ cm}^{-3}$), and therefore is expected to trace the higher density regions. In nearby low-mass star-forming regions N_2H^+ (1–0) typically traces dense cores (e.g. Caselli et al., 2002a; André et al., 2007; Friesen et al., 2010), however, given the significantly higher volume densities seen within some IRDCs, this line is found to be extended (e.g. Tackenberg et al., 2014; Henshaw et al., 2013, 2014).

We note, however, that the transitions from the N_2H^+ molecule contain hyperfine structure, which can complicate the analysis of kinematically complex regions, where the hyperfine components can be merged to form one broad component (e.g. in the case where the line width is larger than the separation of the components). Unlike its higher J-transitions, however, N_2H^+ (1–0) has a hyperfine component (the $F_1, F = 0, 1 \rightarrow 1, 2$ transition) which is “isolated” by $> 7 \text{ km s}^{-1}$ from the main group (i.e. those with a separation of $\sim 1 \text{ km s}^{-1}$; Caselli, Myers & Thaddeus, 1995), and is, therefore, unlikely to merge given the typical line properties observed within IRDCs (e.g. with line-widths of $\sim 1 \text{ km s}^{-1}$; Henshaw et al., 2013). As all the analysis presented in this work will be conducted on the isolated hyperfine component of N_2H^+ (1–0) henceforth, unless otherwise stated, when mentioning the N_2H^+ (1–0) transition we are referring to this hyperfine component. To do so, we will centre on the frequency of the isolated hyperfine component from Pagani, Daniel & Dubernet (2009). We note, however, that slightly different frequencies for the isolated hyperfine component are available in the literature (93176.2637–93176.2650 MHz; Caselli, Myers & Thaddeus, 1995; Cazzoli et al., 2012),¹ yet changing to these will only shift the centroid velocity by $(3.7 - 4.1) \times 10^{-2} \text{ km s}^{-1}$. As this variation is below the spectral resolution of $\sim 6 \times 10^{-2} \text{ km s}^{-1}$ of the N_2H^+ (1–0) observations used throughout this chapter (see Table 3.2), we do not expect this to significantly affect the results presented throughout this chapter (particular importance for Section 3.5.3).

¹See <https://www.astro.uni-koeln.de/cdms>

3.3 Observations

The C^{18}O (1 – 0) and N_2H^+ (1 – 0) observations towards Cloud F were obtained using the Institute for Radio Astronomy in the Millimeter Range 30-m telescope (IRAM-30m) on Pico Veleta, Spain, over the 27th - 28th July 2012.² The data cubes were produced from On-The-Fly (OTF) mapping, covering an area of $\sim 104'' \times 240''$ (corresponding to $2\text{pc} \times 4.8\text{pc}$, at the source distance of 3.7 kpc; [Simon et al., 2006b](#)), using central reference coordinates of RA (J2000) = $18^{\text{h}}53^{\text{m}}19^{\text{s}}$, Dec (J2000) = $01^{\circ}27'21''$,³ which is shown on Figure 3.1. These observations were carried out using the EMIR receivers. The VERSatile Spectrometer Assembly (VESPA) provided spectral resolutions of $\sim 20 - 80$ kHz.

The GILDAS⁴ packages CLASS and MAPPING were used to reduce and post-process the data. This included subtracting a single-order polynomial function to produce a flat baseline and convolving the OTF-data with a Gaussian kernel, thereby increasing the signal-to-noise ratio and allowing us to resample the data onto a regularly spaced grid. All the intensities were converted from units of antenna temperature, T_{A}^* , to main-beam brightness temperature, T_{MB} , using the beam and forward efficiencies shown in Table 3.2. The native angular resolution of the IRAM-30m antenna at the frequency of the C^{18}O (1 – 0) and N_2H^+ (1 – 0) transitions are $\sim 23''$ and $26''$, respectively. Both data sets are smoothed to achieve an effective angular resolution of $\sim 28''$, with a pixel spacing of $14''$, to allow comparison (corresponding to a spatial resolution of ~ 0.5 pc at the source distance of ~ 3.7 kpc; [Simon et al., 2006b](#)).

Table 3.2: Observational parameters.

Observational parameter	$\text{N}_2\text{H}^+(1-0)$	$\text{C}^{18}\text{O}(1-0)$
Frequency (MHz)	93176.7637 ^a	109782.1780 ^b
HPBW (") ^c	26	23
Velocity Resolution (km s^{-1})	6.28×10^{-2}	5.33×10^{-2}
Beam Efficiency	0.81	0.78
Forward Efficiency	0.95	0.94
rms level, σ_{rms} (K)	0.13	0.15

a: Frequency of main hyperfine component, the isolated component N_2H^+ ($J, F_1, F = 1, 0, 1 \rightarrow 0, 1, 2$) has a frequency of 93176.2522 MHz (Pagani, Daniel & Dubernet, 2009).

b: Cazzoli, Puzzarini & Lapinov (2003)

c: Calculated as $\theta_{\text{HPBW}} = 1.16 \lambda / D$, where λ and D are the wavelength and telescope diameter, respectively (see <http://www.iram.es/IRAMES/mainWiki/Iram30mEfficiencies>).

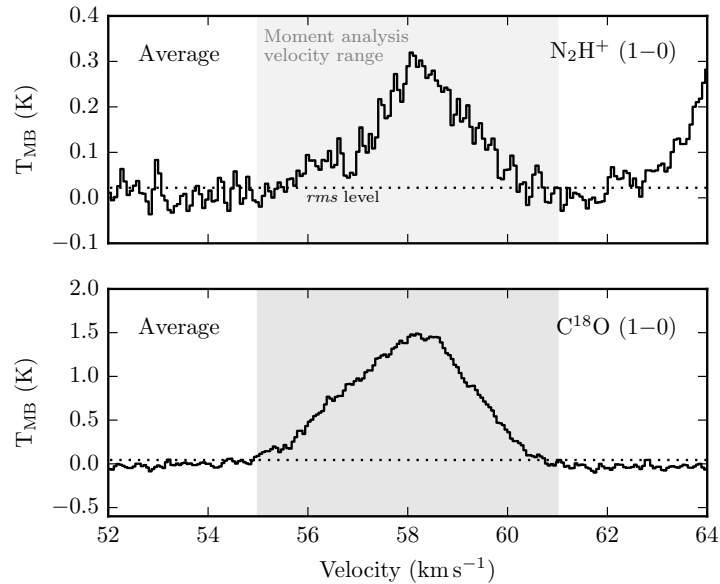


Figure 3.2: Shown are the average spectrum of the $\text{N}_2\text{H}^+(1-0)$ transition [upper panel] and the $\text{C}^{18}\text{O}(1-0)$ transition [lower panel] across the mapped region of Cloud F. The horizontal dotted line represents the rms level, σ_{rms} , on the average spectrum of ~ 0.02 K and ~ 0.04 K for $\text{N}_2\text{H}^+(1-0)$ and $\text{C}^{18}\text{O}(1-0)$, respectively. Note, these values are different to the average of the σ_{rms} within individual positions, which is given in Table 3.2. The shaded region shows the velocity range used for the moment map analysis (see Figure 3.3).

3.4 Results

3.4.1 Moment analysis

To gain an initial insight into the intensity distribution and kinematics of the molecular line emission we conduct a moment analysis, using the SPECTRAL CUBE package for PYTHON.⁵ This analysis has been carried out for a velocity range of 55 – 61 km s⁻¹ for both lines, which was chosen to best incorporate all the significant emission from Cloud F identified in the spectrum averaged across the whole mapped area, shown in Figure 3.2. The average uncertainty on the integrated intensity towards each position for N₂H⁺ (1 – 0) and C¹⁸O (1 – 0) are $\sigma_W \sim 0.08$ K km s⁻¹ and $\sigma_W \sim 0.09$ K km s⁻¹, respectively (the σ_{rms} is shown in Table 3.2, and the uncertainty has been calculated following Caselli et al., 2002b). The pixels below a $3\sigma_W$ threshold have been masked after the moment analysis procedure.

The results of the moment analysis towards Cloud F are presented in Figure 3.3. Shown in greyscale in the first column is the mass surface density map determined from extinction in the near infrared (Kainulainen & Tan, 2013). Shown in the second, third and fourth columns are the integrated intensities (0th order moment), intensity weighted velocity field (1st order moment), and intensity weighted line width (2nd order moment) maps, respectively. For reference, contours of the integrated intensity are overlaid on each panel, and the positions of the Rathborne, Jackson & Simon (2006) and Butler & Tan (2012) core regions are plotted on the mass surface density map.

This analysis shows that both the N₂H⁺ (1 – 0) and C¹⁸O (1 – 0) emission is extended across the length of the IRDC, where only a few (< 10 per cent) of the pixels do not meet the $3\sigma_W$ integrated intensity threshold. The N₂H⁺ (1 – 0) emission traces the mass surface density map morphology relatively well, with peaks towards the MM3 and MM1 core regions. The C¹⁸O (1 – 0) emission also traces the mass surface density

²Project code: 025-12

³In Galactic coordinates $l = 34.441^\circ$, $b = 0.247^\circ$.

⁴see <https://www.iram.fr/IRAMFR/GILDAS/>

⁵<https://spectral-cube.readthedocs.io/en/latest/>.

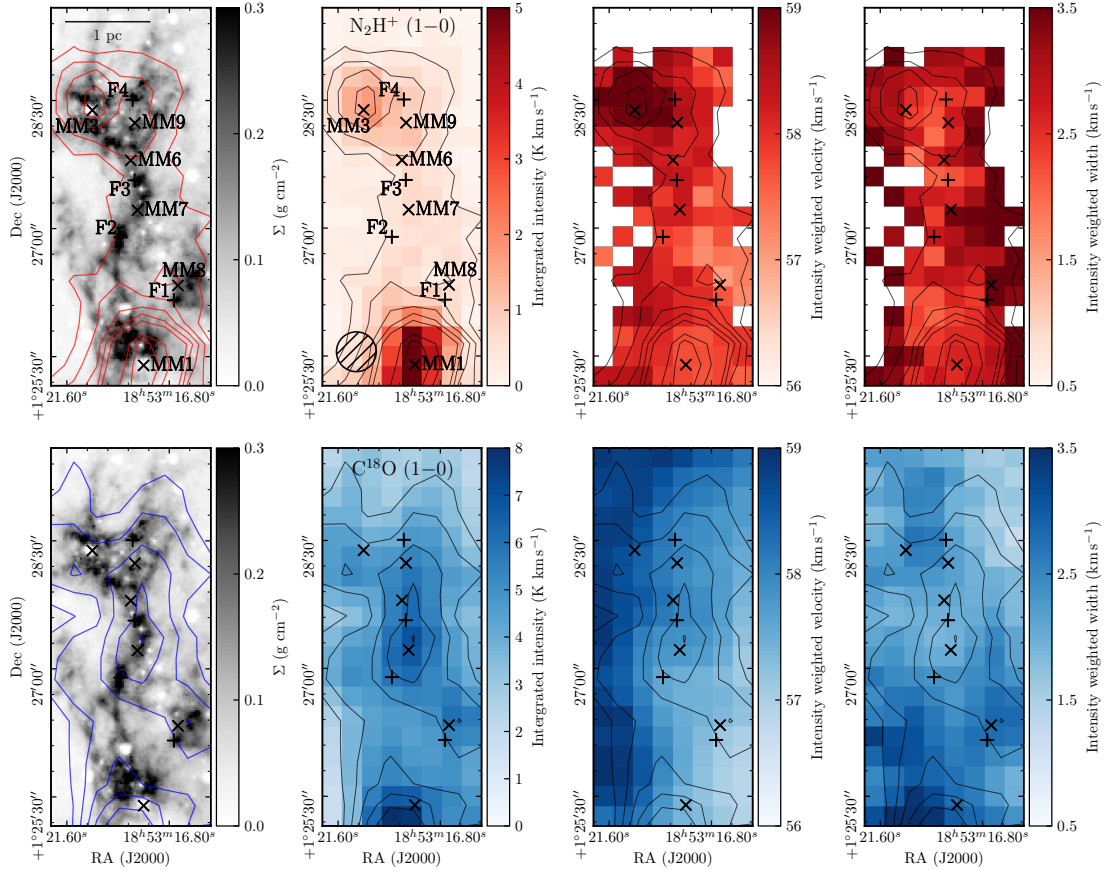


Figure 3.3: Moment map analysis of the Cloud F $\text{N}_2\text{H}^+(1-0)$ [upper row] and $\text{C}^{18}\text{O}(1-0)$ [lower row] observations. Shown in greyscale in the first column is the mass surface density map of Cloud F, determined from near and mid-infrared extinction (Kainulainen & Tan, 2013). Shown with + and \times symbols are the positions of the “core” regions identified by Butler & Tan (2012) and those from Rathborne, Jackson & Simon (2006), respectively, which are labeled in both the upper left and upper centre-left panels. Shown in the second, third and fourth columns are the integrated intensities (0^{th} order moment), intensity weighted velocity field (1^{st} order moment), and intensity weighted line width (2^{nd} order moment) maps. Overlaid as red [first column] and black [second, third and fourth columns] contours in the upper row is the integrated intensity of $\text{N}_2\text{H}^+(1-0)$, in steps of $[5, 10, 15, 20, 25, 45, 55] \sigma_W$; where $\sigma_W \sim 0.08 \text{ K km s}^{-1}$. Overlaid as blue [first column] and black [second, third and fourth columns] contours in the lower row is the integrated intensity of $\text{C}^{18}\text{O}(1-0)$, in steps of $[40, 50, 60, 70, 80] \sigma_W$; where $\sigma_W \sim 0.09 \text{ K km s}^{-1}$. The moment analysis has been performed above $3\sigma_W$ for all transitions. Shown in the lower left corner of the second upper panel is the smoothed angular beam size.

morphology, albeit to a lesser extent than the N_2H^+ (1 – 0) emission, peaking at the position of the MM7 core, to the west of the F1 and MM8 regions, to the south-east of the MM3 region, and towards the MM1 region. A likely cause of the different spatial distributions of the C^{18}O (1 – 0) and N_2H^+ (1 – 0) emission is that C^{18}O traces the extended envelope material, whereas N_2H^+ is expected to trace the dense gas, which follows the continuum cores and mass surface density distribution. Furthermore, towards these densest regions, unlike N_2H^+ , C^{18}O can suffer from freeze-out (see Section 3.6).

The intensity weighted velocity field maps for both transitions show an increasing velocity from the west to east (right to left in Figure 3.3). The total difference of velocity across the mapped region is $\sim 2 - 3 \text{ km s}^{-1}$, which corresponds to a gradient of the order $\sim 0.5 - 0.7 \text{ km s}^{-1} \text{ pc}^{-1}$ for the approximate distance diagonally across the mapped region of 3 – 4 pc, at the assumed source distance (see Table 3.1).

The intensity-weighted line width maps show different morphologies. The C^{18}O (1–0) shows the largest values of the intensity weighted line width towards the MM1 region and the south-east corner of the mapped region ($\sim 3.5 \text{ km s}^{-1}$), with peaks towards the MM3 region ($\sim 2.7 \text{ km s}^{-1}$), and towards the peak in integrated intensity towards the west of the F1 and MM8 regions ($\sim 2.9 \text{ km s}^{-1}$). The N_2H^+ (1 – 0) emission shows narrower line widths towards the centre of the cloud, with values of $\sim 2.5 \text{ km s}^{-1}$ towards the MM1 region, and $\sim 2 \text{ km s}^{-1}$ towards the MM3 region.

3.4.2 Channel map analysis

To investigate the velocity gradients identified in the N_2H^+ and C^{18}O moment map analysis, the emission from these transitions has been integrated across subsets of the total velocity range used to create the moment maps (referred to as channel maps). We integrate the N_2H^+ (1 – 0) and C^{18}O (1 – 0) transitions from 55 – 61 km s^{-1} in steps of 0.5 km s^{-1} (which corresponds to approximately 10 channels for both lines). Figure 3.4 shows contours of the integrated intensity in these steps for N_2H^+ (1 – 0) (in red) and C^{18}O (1 – 0) (in blue), overlaid on the mass surface density map (Kainulainen

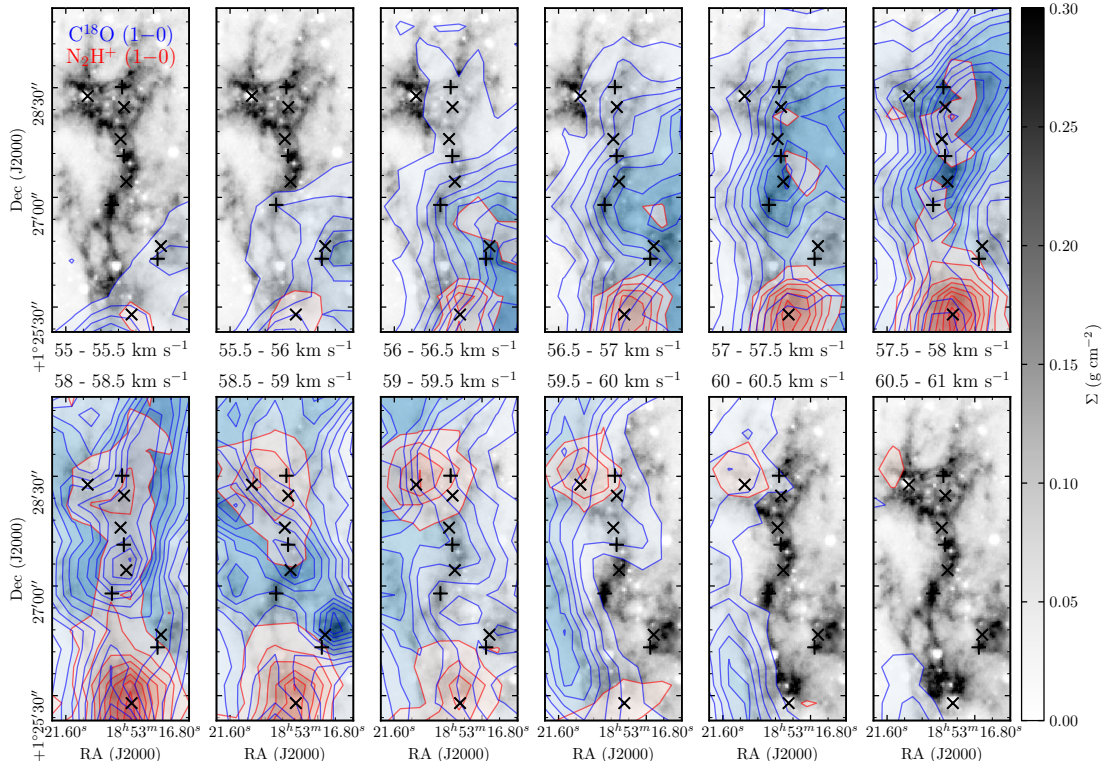


Figure 3.4: Cloud F channel maps of N_2H^+ (1–0) and C^{18}O (1–0) shown in red and blue filled contours, which begin at $5\sigma_W$, and increase in steps of $5\sigma_W$, where $\sigma_W \sim 0.023 \text{ K km s}^{-1}$ and $\sigma_W \sim 0.024 \text{ K km s}^{-1}$, respectively. The intensities are integrated from $55 - 61 \text{ km s}^{-1}$ in steps of 0.5 km s^{-1} , as shown below or above each map. Each map is overlaid on the mass surface density map of [Kainulainen & Tan \(2013\)](#). Shown with + and × symbols are the positions of the “core” regions identified by [Butler & Tan \(2012\)](#) and those from [Rathborne, Jackson & Simon \(2006\)](#), respectively.

& Tan, 2013).

The channel maps show a complex morphology, where both lines appear to peak towards the south for the majority of the velocity range, with several local maxima appearing at different velocities towards the north of the cloud. These suggest that the velocity gradients identified in the moment map analysis are not continuous, but rather that they are due to distinct peaks in velocity across the map, which, when averaged, mimic a smoothly varying centroid velocity. Identifying velocity structures by arbitrarily separating these maxima can be, however, dependent on the applied spatial and/or velocity boundaries.

3.5 Analysis

To determine if multiple velocity components are present across Cloud F, as the various intensity peaks in the channel map analysis would seem to suggest, we check the individual N_2H^+ ($1 - 0$) and C^{18}O ($1 - 0$) spectra. Figures 3.5 and 3.6 show the spectra at each position across the cloud. Multiple distinct velocity components can indeed be clearly identified, predominately in the C^{18}O ($1 - 0$) emission, at several positions across the cloud. A result which is not evident from the average spectra, shown in Figure 3.2. A more reliable method to separate these components than is possible with moment or channel maps is, therefore, required to accurately analyse the kinematics within this complex IRDC. In this Section, we use a semi-automated Gaussian fitting algorithm and automated hierarchical clustering algorithm. These have been chosen such that the identified coherent velocity structures can be tested for robustness against a range of input parameters, within both the fitting and clustering algorithms. This method ensures that the structures are both reliable and reproducible. Importantly, in Section 3.7.2 we investigate an apparently similar IRDC to Cloud H, for which we use this same method to identify the coherent velocity structures, allowing for a systematic comparison of their kinematic properties.

3.5.1 Spectral line fitting and velocity coherent features

To separate the velocity components, we fit Gaussian profiles to the spectra across the cloud using the Semi-automated multi-COMponent Universal Spectral-line fitting Engine (SCOUSE; Henshaw et al., 2016b).⁶ SCOUSE has been chosen over manually fitting each individual spectrum (a total of ~ 300 for both Cloud F maps), as this algorithm was specially produced to efficiently and systematically fit a large number of spectra. To do so, SCOUSE works in several steps. Firstly, the map is split into regions (referred to as “spectral averaging areas”, SAA), within which the data are spatially averaged. For each SAA spectra, the user is instructed to fit the appropriate number

⁶Written in the IDL programming language. See <https://github.com/jdhenshaw/SCOUSE> for more details.

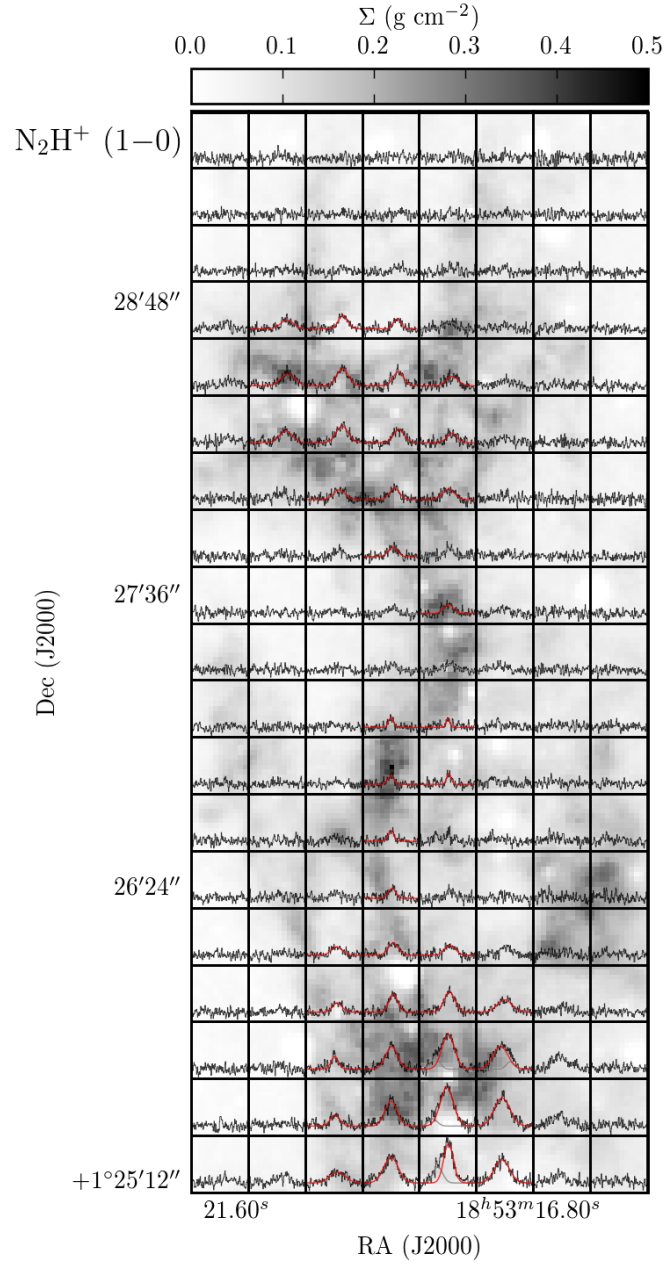


Figure 3.5: Shown are the spectra of the N_2H^+ ($1 - 0$) transition across the mapped region of Cloud F. The velocity ranges are 54 to 62 km s^{-1} , and the intensity ranges are -0.5 to 2.5 K . Overlaid on each spectrum are the results of the line fitting (SCOUSE) and clustering (ACORNS) routines, which are discussed in Section 3.5.1. The colours of these profiles represent the various velocity component associations given in Table 3.3. The background greyscale is the mass surface density map, determined from near and mid-infrared extinction (Kainulainen & Tan, 2013).

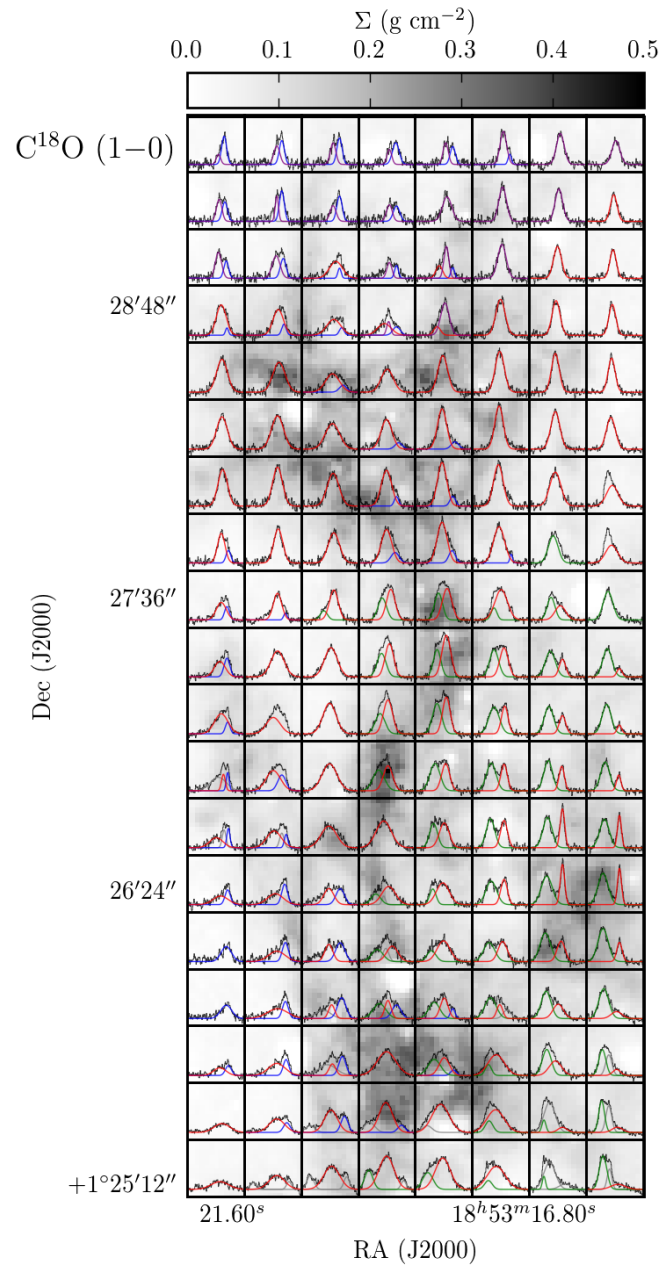


Figure 3.6: Shown are the spectra of the $C^{18}O$ (1 – 0) transition across the mapped region of Cloud F. The velocity ranges are 54 to 62 km s^{-1} , and the intensity ranges are -0.5 to 3.5 K. Overlaid on each spectrum are the results of the line fitting (SCOUSE) and clustering (ACORNS) routines, which are discussed in Section 3.5.1. The colours of these profiles represent the various velocity component associations given in Table 3.3. The background greyscale is the mass surface density map, determined from near and mid-infrared extinction (Kainulainen & Tan, 2013).

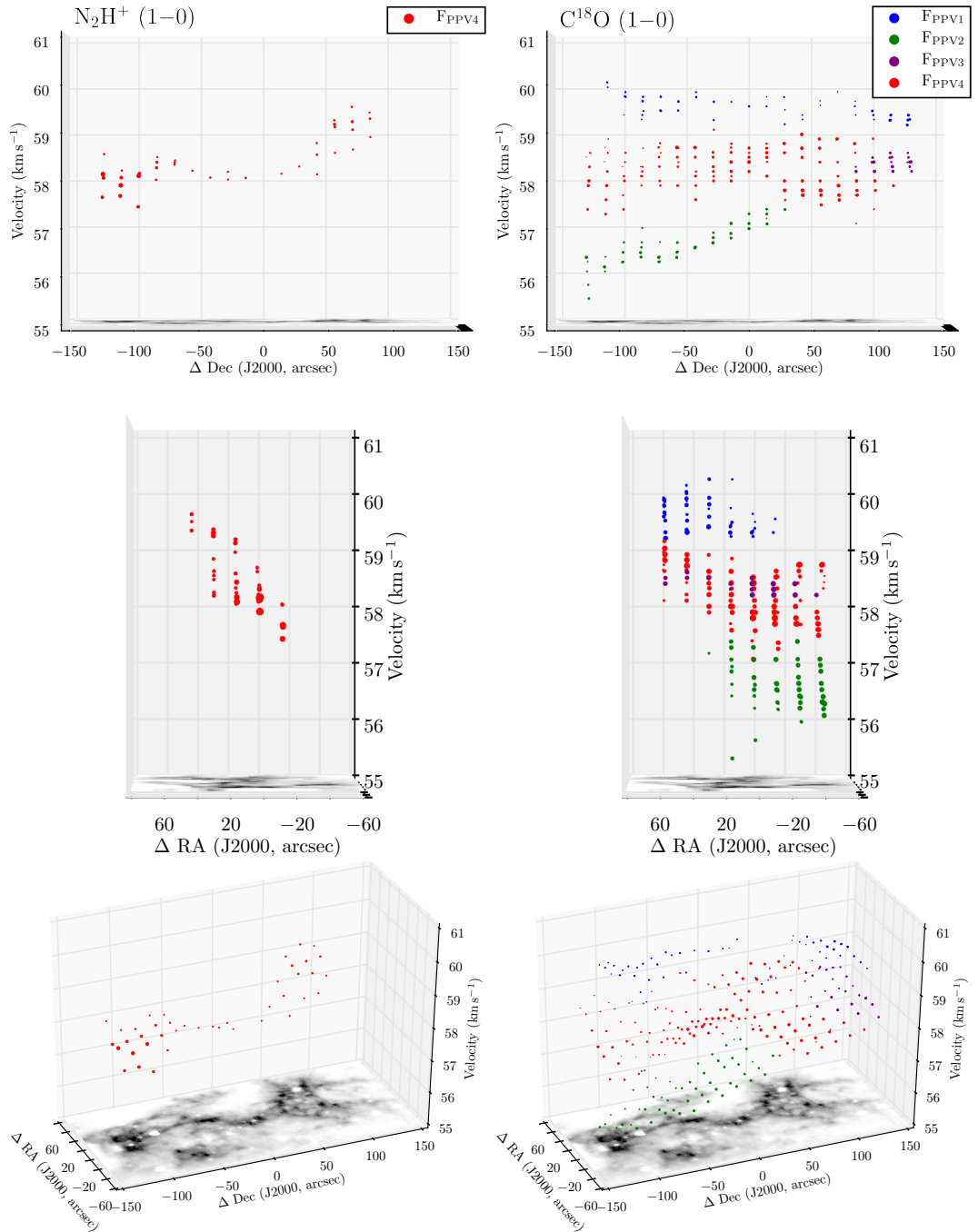


Figure 3.7: Displayed in each panel is the position-position-velocity diagram of Cloud F, shown at three viewing angles for comparison. The left and right panels show N_2H^+ (1 – 0) and C^{18}O (1 – 0) results, respectively. The colour of each point represents its association to one of the coherent velocity components, $\text{F}_{\text{PPV}1}$ in blue, $\text{F}_{\text{PPV}2}$ in green, $\text{F}_{\text{PPV}3}$ in purple, and $\text{F}_{\text{PPV}4}$ in red. The size of each point represents its relative peak intensity. The mass surface density map of [Kainulainen & Tan \(2013\)](#) is shown on the base of each plot. Note that the coordinate offsets of these plots are relative to the centre of the mapped region: RA (J2000) = $18^{\text{h}}53^{\text{m}}19^{\text{s}}$, Dec (J2000) = $01^{\circ}27'21''$ ($l = 34.441^{\circ}$, $b = 0.247^{\circ}$).

Table 3.3: Parameters of the velocity components identified in the IRAM-30m observations towards Cloud F (F_{PPV} , [upper rows]) and Cloud H (H_{PPV} , [lower rows]). Shown are the molecules used to identify the components, and for each component: the name with the colour used for each Figure in parentheses, the total number of points, the average centroid velocity, the average line width, the velocity gradient and the angle of this gradient with respect to East of North. When the uncertainty on the velocity gradient is larger than or equal to the calculated velocity gradient, the velocity gradient angle is unconstrained, and therefore not shown.

Line	Component (colour)	# points	Centroid velocity (V_0) km s ⁻¹	Line width (Δv) km s ⁻¹	Velocity gradient (∇v) km s ⁻¹ pc ⁻¹	Gradient angle ($\theta_{\nabla v}$) degrees
$\text{C}^{18}\text{O}(1-0)$	F_{PPV1} (blue)	54	59.56 ± 0.24	0.96 ± 0.31	0.12 ± 0.03	-38.89 ± 14.81
	F_{PPV2} (green)	53	56.68 ± 0.40	1.48 ± 0.31	0.25 ± 0.08	-31.07 ± 23.86
	F_{PPV3} (purple)	22	58.39 ± 0.12	1.04 ± 0.27	0.16 ± 0.05	-83.77 ± 4.32
	F_{PPV4} (red)	128	58.26 ± 0.43	1.75 ± 0.60	0.28 ± 0.07	-85.83 ± 5.93
$\text{N}_2\text{H}^+(1-0)$	F_{PPV4} (red)	41	58.44 ± 0.51	1.75 ± 0.50	0.75 ± 0.15	70.20 ± 3.20
$\text{C}^{18}\text{O}(1-0)$	H_{PPV1} (orange)	20	46.12 ± 0.11	0.47 ± 0.15	0.12 ± 0.06	76.08 ± 12.41
	H_{PPV2} (purple)	27	46.61 ± 0.20	1.39 ± 0.41	0.38 ± 0.11	61.15 ± 9.66
	H_{PPV3} (green)	26	43.67 ± 0.16	1.33 ± 0.38	0.29 ± 0.09	-87.80 ± 7.77
	H_{PPV4a} (red)	21	45.07 ± 0.06	1.48 ± 0.34	0.01 ± 0.02	...
	H_{PPV4b} (blue)	32	45.52 ± 0.25	1.35 ± 0.47	0.33 ± 0.10	-56.27 ± 11.72
$\text{N}_2\text{H}^+(1-0)$	H_{PPV2} (purple)	14	46.88 ± 0.10	0.74 ± 0.20	0.15 ± 0.08	-29.98 ± 29.89
	H_{PPV4a} (red)	38	45.42 ± 0.10	1.26 ± 0.16	0.02 ± 0.02	...
	H_{PPV4b} (blue)	27	45.99 ± 0.09	1.02 ± 0.35	0.10 ± 0.05	-77.40 ± 10.68

of Gaussian components. The individual spectra contained within the SAAs are then automatically fitted using the parameters from the Gaussian fits of their SAA within given tolerance limits on the peak intensity, line centroid velocity, line width and separation between components. As a final step, the results are checked for anomalies, which can be re-fitted if required.

As discussed in [Henshaw et al., 2016b](#), the size of the SAA selected will be somewhat data dependent. A size of 30'' represented the maximum size for which the spatially averaged spectrum was a good representation of the line profiles of its composite spectra. Changing the SAA size will not significantly affect the final best-fitting solutions across the cloud. Rather, decreasing the size of the SAA will result in an increase in the number of spectral that require manual fitting during the SAA fitting stage (and a reduction of fits that need to be corrected during the later stages). Alternatively increasing the size of the SAA will have the opposite effect. An SAA radius of 30'' for the Cloud F data, such that each SAA contained four to six spectra, therefore, represented the most efficient choice. The tolerance limits were set such that each fit had to have a peak intensity of at least three times the rms level, σ_{rms} , a centroid velocity similar to an SAA fit to within three times the value of the velocity dispersion and a full-width at half-maximum line width to within a factor of two. To be considered a multi-component fit, the components had to be separated by a factor of two times the line width. These parameters gave reasonable fits across the cloud for both N_2H^+ (1 – 0) and C^{18}O (1 – 0), where the mean residual across all positions after fitting was $< 3 \sigma_{\text{rms}}$ and only ~ 10 per cent of the spectra required manual checking. The results of SCOUSE are over-plotted on the spectrum at each position in [Figures 3.5 and 3.6](#).

To identify coherent velocity features within our decomposed data, we use Agglomerative Clustering for ORganising Nested Structures (ACORNS; [Henshaw et al. in prep](#)).⁷ A complete description of the algorithm and the process will be presented in [Henshaw et al. \(in prep\)](#), however, the key details are included below.

⁷Written in the PYTHON programming language, soon available at <https://github.com/jdhenshaw/acorns>.

ACORNS is specifically designed to work on decomposed spectroscopic data, i.e. the output of SCOUSE (or an equivalent algorithm). The algorithm follows the principles of hierarchical agglomerative clustering and searches for a hierarchical system of clusters within the decomposed dataset. In agglomerative clustering, each data point begins its life as a “cluster”. Clusters grow by merging with other clusters provided they satisfy a number of conditions which are supplied by the user (see below). As the algorithm progresses, hierarchies develop. These hierarchical clusters, as in many areas of research, can be visualised graphically as a dendrogram.

The merging process is governed by a series of conditions controlled by the user. These conditions are known as linkage criteria, and can refer to, for example, a Euclidean distance between two clusters or an absolute difference in a variable of the users choice (e.g. velocity or velocity dispersion). If two adjacent clusters satisfy the linkage criteria, they will be merged. In this work, for two data points to be linked, we require several that criteria are satisfied. Namely, adjacent clusters must: i) have a Euclidean separation less than a beam size; ii) have an absolute velocity difference less than twice the spectral resolution of the data; iii) have an absolute difference in velocity dispersion that is less than the thermal velocity dispersion of the gas (estimated to be $c_s = 0.23 \text{ km s}^{-1}$ at 17K, from Table 1, given a mean molecular weight of 2.33 a.m.u).⁸ We consider these criteria to be fairly strict and representative of the limitations of our data (i.e. our spatial and spectral resolution). Once this initial robust hierarchy has been established (i.e. all possible links satisfying these criteria have been exhausted), ACORNS then allows the user to relax these conditions in order to further develop the hierarchy. This can be performed in several ways, in incremental stages, both interactively and non-interactively, or in a single step. In this study we relaxed the conditions in a single step, however, we conducted a parameter space study in order to establish the set of relaxation parameters that produced the most robust hierarchy. These optimal parameters were chosen when a hierarchy appeared most persistent across an

⁸The observed velocity dispersion is given as $\sigma_{\text{obs}} = \Delta v (8 \ln(2))^{-0.5}$, where Δv is the observed full width half maximum (or line width). Here and throughout this work, we use the classical value of the abundance to be consistent with the previous IRDC analyses (e.g. [Henshaw et al., 2013](#); [Jiménez-Serra et al., 2014](#)), and not the value obtained when accounting for heavier elements (2.37; see [Kauffmann et al., 2008](#)). Taking the latter would not significantly affect the results of this work.

area of the parameter space (i.e. when the hierarchy did not significantly change for a range of relaxation parameters), whilst being comparable for both the C^{18}O and N_2H^+ data (assuming that N_2H^+ traces similar, or at least the densest, components traced by C^{18}O). This was achieved with relaxation factors of 2.5, 1.75, and 0.75, for the spatial separation, centroid velocity and line width, respectively, for both transitions.

Figure 3.7 shows the position-position-velocity diagram for the above analysis, where the centroid velocities of the Gaussian profiles at each position have been plotted, and the colours correspond to the identified components (shown in the legend). Four coherent velocity components have been identified in the C^{18}O ($1 - 0$) emission from Cloud F: F_{PPV1} , F_{PPV2} , F_{PPV3} and F_{PPV4} , which are shown in blue, green, purple, and red, respectively, on Figures 3.5, 3.6 and 3.7. We find that the components F_{PPV1} and F_{PPV4} are extended across the length of the cloud, whereas F_{PPV2} and F_{PPV3} are limited to the southern and northern portions of the cloud, respectively. The component F_{PPV4} is also identified in the N_2H^+ ($1 - 0$) transition emission. The basic properties of these components are given in Table 3.3, and they are analysed in the following sections.

3.5.2 Velocity gradients

As previously shown in the moment map analysis, Cloud F appears to have a smooth velocity gradient increasing in velocity from west to east (see Figure 3.3). However, in the kinematic structure identified from the Gaussian decomposition, we do not see such a smooth gradient, instead, we observe the velocity components at distinct velocities across the cloud. We find that the F_{PPV1} is at a high velocity ($\sim 60 \text{ km s}^{-1}$) on the east of the mapped region, and the F_{PPV2} is at a low velocity ($\sim 57 \text{ km s}^{-1}$) on the west of the mapped region (see Figure 3.7). When averaged with F_{PPV4} , as in the case of the moment map analysis, these would mimic a smooth velocity gradient across the cloud. Rather than a primarily west to east velocity gradient, the identified components show large-scale velocity gradients running along the south-north axis of the cloud. Here we determine the magnitude and angle of the larger scale gradients across the cloud following the analysis of [Goodman et al. \(1993\)](#), who assume that the line centroid

velocities can be represented by the linear function,

$$V_{\text{LSR}} = V_0 + A \Delta\text{RA} + B \Delta\text{Dec}, \quad (3.1)$$

where ΔRA and ΔDec are the offset right ascension and declination in radians (i.e. the difference in position over the region of interest), V_0 is the average velocity of the velocity component, V_{LSR} is the centroid velocity of the Gaussian profile fit at each position, and A and B are solved for using the non-linear least squares optimisation routine `SCIPY.OPTIMIZE.CURVE_FIT` in `PYTHON`. The velocity gradient, ∇v , can be calculated with,

$$\nabla v = \frac{(A^2 + B^2)^{0.5}}{d}, \quad (3.2)$$

where d is the source distance. The angle of the gradient, $\theta_{\nabla v}$, can be determined from,

$$\theta_{\nabla v} = \tan^{-1}\left(\frac{A}{B}\right). \quad (3.3)$$

The magnitudes and angles, with respect to East of North, of the velocity gradients for each velocity component, are given in Table 3.3. We find velocity gradients across the cloud in the range of $0.12 - 0.75 \text{ km s}^{-1} \text{ pc}^{-1}$, with an average over all components of $\sim 0.3 \text{ km s}^{-1} \text{ pc}^{-1}$, which is lower than the range determined from the moment map analysis $\sim 0.5 - 0.7 \text{ km s}^{-1} \text{ pc}^{-1}$. This is due to the fact that here we are analysing the gradients of the individual components, rather than the gradient produced by the separation of the components when they are averaged.

3.5.3 Comparing the $\text{N}_2\text{H}^+ (1 - 0)$ and $\text{C}^{18}\text{O} (1 - 0)$ centroid velocities

Comparing the distribution of different molecular species, both spatially and in velocity, within star-forming regions, can provide clues of their formation scenarios (e.g. [Henshaw et al., 2013](#)). To do so within Cloud F, we compare the centroid velocity at each position of the component identified in the $\text{N}_2\text{H}^+ (1 - 0)$ and $\text{C}^{18}\text{O} (1 - 0)$, F_{PPV4} .

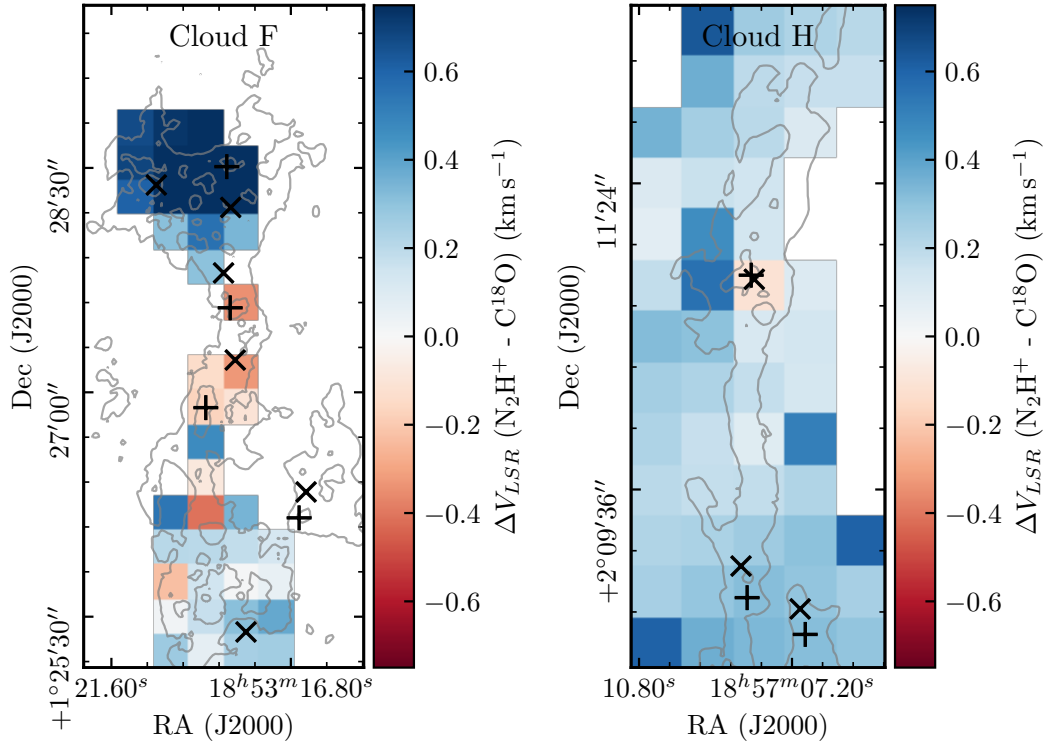


Figure 3.8: The left and right panels are maps of the difference in the centroid velocity, $\Delta V_{LSR}(N_2H^+ - C^{18}O)$, of Clouds F and H (see Section 3.7.2), respectively. Over-plotted as + and × symbols are the positions of the “core” regions identified by Butler & Tan (2012) and those from Rathborne, Jackson & Simon (2006), respectively. For reference, the clouds are labeled at the top of each plot.

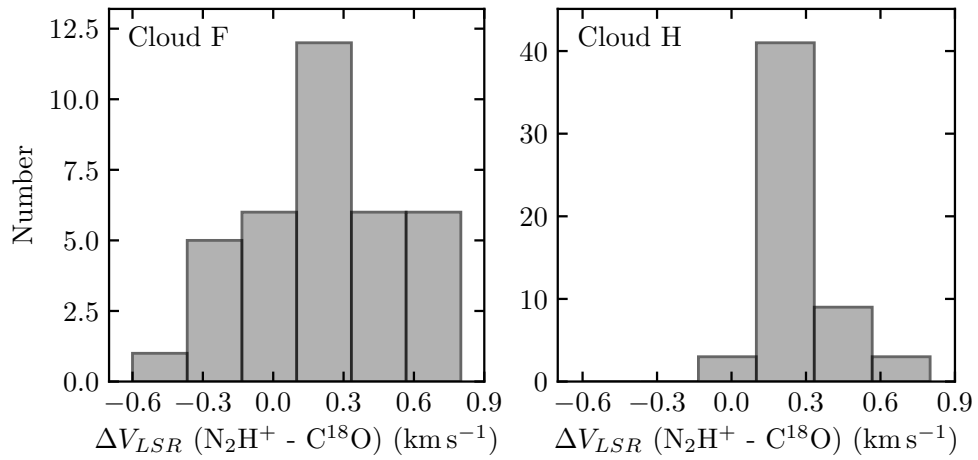


Figure 3.9: Histograms of the difference of the centroid velocity, $\Delta V_{LSR}(N_2H^+ - C^{18}O)$, at each position for [left panel] Cloud F and [right panel] Cloud H (see Section 3.7.2), respectively. For reference, the clouds are labeled at the top of each plot.

The centroid velocity difference,

$$\Delta V_{\text{LSR}}(\text{N}_2\text{H}^+ - \text{C}^{18}\text{O}) = V_{\text{LSR}}(\text{N}_2\text{H}^+) - V_{\text{LSR}}(\text{C}^{18}\text{O}), \quad (3.4)$$

map and histogram are presented in Figures 3.8 and 3.9, respectively. We find that the average difference in velocity is $+0.32 \pm 0.06 \text{ km s}^{-1}$.⁹

A velocity shift between two tracers may, however, be produced when comparing the velocity from emission which is not tracing the same gas; or in other words, here we choose to compare the emission from the F_{PPV_4} component, as this is seen in both C^{18}O and N_2H^+ , however, if some of this emission is actually from a different component that has been wrongly assigned, then an artificial velocity shift would be produced. Such an effect could be plausible towards the north of the cloud, where the $\text{N}_2\text{H}^+(1-0)$ emission appears to originate at a velocity in-between the F_{PPV_1} and F_{PPV_4} components (see Figure 3.7). To investigate this, we temporarily attribute the emission above $\text{Dec (J2000)} = 01^\circ 27' 36''$ to the F_{PPV_1} component, and re-determine the velocity shift between the $\text{N}_2\text{H}^+(1-0)$ and $\text{C}^{18}\text{O}(1-0)$. Doing so, we find an average value towards this northern region is $-0.67 \pm 0.10 \text{ km s}^{-1}$; a negative shift which is a factor of two larger in magnitude than that found when assigning this region to the F_{PPV_4} component. Demonstrating that there is a significant shift in velocity between the $\text{N}_2\text{H}^+(1-0)$ and $\text{C}^{18}\text{O}(1-0)$ emission regardless of which component the $\text{N}_2\text{H}^+(1-0)$ emission within the northern region is assigned, and this result is persistent, regardless of which N_2H^+ and C^{18}O components are compared. We continue with the assumption that components closer in velocity are the most likely to be physically associated, hence keep the original assignment of all the $\text{N}_2\text{H}^+(1-0)$ emission to the F_{PPV_4} component, which provides a smaller, yet still significant, average velocity shift ($+0.32 \pm 0.06 \text{ km s}^{-1}$).

⁹Uncertainty given is the standard error on the mean, where the standard deviation is $\pm 0.40 \text{ km s}^{-1}$.

3.5.4 Velocity dispersions

In order to study the non-thermal motions of the gas from the observed line widths we use the expression from Myers (1983),

$$\sigma_{\text{NT}} = \sqrt{\sigma_{\text{obs}}^2 - \sigma_{\text{T}}^2} = \sqrt{\frac{\Delta v^2}{8 \ln(2)} - \frac{k_{\text{B}} T_{\text{kin}}}{m_{\text{obs}}}}, \quad (3.5)$$

where σ_{NT} , σ_{obs} , and σ_{T} , are the non-thermal, the observed, and the thermal velocity dispersion, respectively. Δv is the observed full width half maximum (or line width), k_{B} is the Boltzmann constant, T_{kin} is the kinetic temperature of the gas and m_{obs} refers to the mass of the observed molecule (30 a.m.u for C^{18}O ; 29 a.m.u for N_2H^+). We assume a constant kinetic gas temperature of 17 K (e.g. Drienzo et al., 2015; Pon et al., 2016a), which gives thermal dispersion contributions of 0.064 km s^{-1} and 0.065 km s^{-1} , for C^{18}O and N_2H^+ , respectively.¹⁰

Figure 3.10 shows the non-thermal component of the velocity dispersion compared to both the gas sound speed [lower axis] and thermal component of the dispersion [upper axis] at each position within Cloud F. Comparison to the gas sound speed has been made assuming a temperature of 17 K and a mean molecular weight of 2.33 a.m.u ($c_s = 0.23 \text{ km s}^{-1}$). We find that the velocity dispersions (or Mach numbers $\mathcal{M} = \sigma_{\text{NT}}/c_s$) averaged over all velocity components are $0.75 \pm 0.03 \text{ km s}^{-1}$ ($\mathcal{M} = 3.2 \pm 0.14$) and $0.63 \pm 0.02 \text{ km s}^{-1}$ ($\mathcal{M} = 2.70 \pm 0.07$) for N_2H^+ (1 – 0) and C^{18}O (1 – 0), respectively. To link these observed non-thermal motions to the turbulent motions (i.e. with corresponding Mach number) within the cloud, we make the assumption that no velocity gradients or substructure are present with size scales less than the beam size. This may, however, not be the case for these IRAM-30m observations presented here given the large physical beam size ($\sim 0.5 \text{ pc}$; cf. Henshaw et al., 2013 and Henshaw et al., 2014), hence the values of the turbulent velocity dispersion calculated here most likely represent upper-limits on the true turbulent motions within the cloud. We find that all the velocity components have non-thermal velocity dispersions factors of several

¹⁰Given the weak dependence on the temperature, varying between the expected limits within IRDCs does not affect the results presented here.

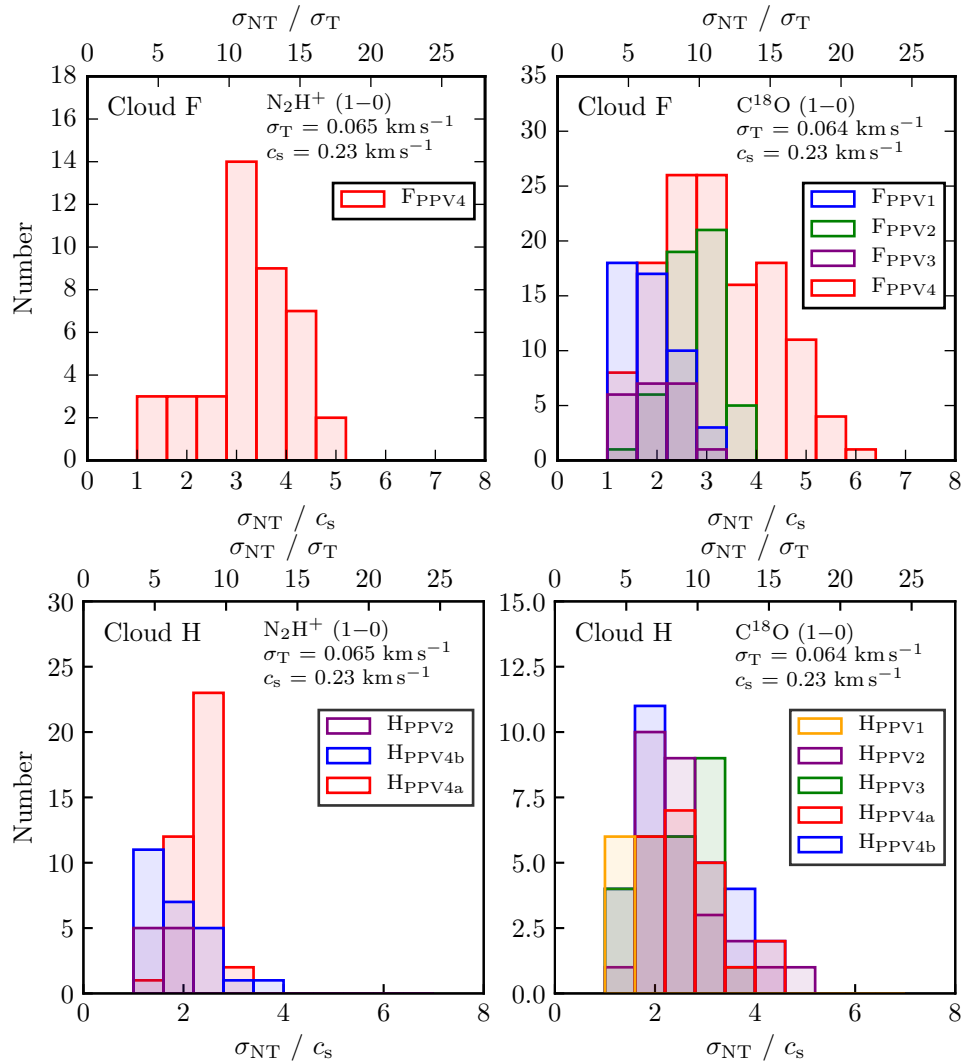


Figure 3.10: Cloud F [upper panels] and Cloud H [lower panels] histograms of the non-thermal contribution to the velocity dispersion over the gas sound speed ([lower axis on each plot]; $c_s = 0.23 \text{ km s}^{-1}$ at 17 K, given a mean molecular weight of 2.33 a.m.u). The upper axis labels on each plot show the non-thermal contribution to the velocity dispersion over the thermal contribution to the velocity dispersion, where $\sigma_T = 0.065 \text{ km s}^{-1}$ and 0.066 km s^{-1} , for $C^{18}O$ (30 a.m.u) and N_2H^+ (29 a.m.u), respectively. Colours represent the various velocity components (see Figures 3.7 and 3.13).

larger than the gas sound speed, which suggests that their internal turbulent motions are (at most) only moderately supersonic over scales of ~ 0.5 pc (traced by these observations).

We note that the calculated average N_2H^+ velocity dispersion is larger than the average C^{18}O velocity dispersion, which is not typically expected if the N_2H^+ is tracing the denser, more compact regions within the cloud, unless the dense gas is associated with embedded young stellar objects. However, when comparing the velocity dispersions for the F_{PPV4} component only, we find comparable values (see Table 3.3). This suggests that both molecular lines are tracing similar gas within this component.

3.6 CO depletion

As previously discussed, CO can become depleted within the coolest, densest regions of IRDCs, and therefore cannot emit. If CO is significantly depleted this lack of emission may be observable within the spectra of CO molecules, such as C^{18}O , as a dip at the centroid velocity of the source. This may wrongly be interpreted as multiple velocity components, and, therefore, before progressing to a discussion of the properties of kinematic features identified in this section, the level of CO depletion within Cloud F is analysed.

The column density, $N(\text{C}^{18}\text{O})$, is calculated using equation 1.11 (Caselli et al., 2002a), and thereby making the assumption that the $\text{C}^{18}\text{O}(1-0)$ emission is optically thin ($\tau_\nu \ll 1$; further discussion on this is given in the following section). The column density of hydrogen is given as $N(\text{H}_2) = \Sigma / \mu_{\text{H}_2} m_{\text{H}}$, where $\mu_{\text{H}_2} = 2.33$ a.m.u is the mean mass per particle, m_{H} is the mass of hydrogen, and Σ is the mass surface density taken from Kainulainen & Tan (2013). The abundance of C^{18}O with respect to H_2 is calculated as $X(\text{C}^{18}\text{O}) = N(\text{C}^{18}\text{O}) / N(\text{H}_2)$. To determine the abundance of CO we use the oxygen isotope ratio $^{16}\text{O}/^{18}\text{O} = 58.5 d_{\text{GC}} + 37.1 \sim 372$ (Wilson & Rood, 1994), given the Galactocentric distance of Cloud F, $d_{\text{GC}} \sim 5.7$ kpc (assuming source distance of 3.7 kpc and a distance to the galactic centre of ~ 8.3 kpc; Simon et al.,

2006b; Reid et al., 2014). We find an average CO abundance across the cloud of $X(\text{CO}) = 1.3 \times 10^{-4}$. Comparing this measured CO abundance to the reference (or “expected”) value, $X^{\text{ref}}(\text{CO})$, gives the CO depletion factor, $f_{\text{D}} = X^{\text{ref}}(\text{CO})/X(\text{CO})$. Using the abundance gradients in the Galactic Disk from Wilson & Matteucci, 1992 and the Solar neighbourhood abundance of CO from Frerking, Langer & Wilson (1982), Fontani et al. (2006) find that the reference abundance of CO is given by $X^{\text{ref}}(\text{CO}) = 9.5 \times 10^{-5} \exp(1.105 - 0.13 d_{\text{GC}})$, which for the Galactocentric distance of Cloud F is $\sim 1.4 \times 10^{-4}$. We find that the average CO depletion factor across Cloud F is ~ 1.2 , which peaks with a value of ~ 2.1 towards the MM3 core region (see Figure 3.1). These values are in the range previously calculated by Hernandez & Tan (2011) using ^{13}CO emission towards Cloud F, albeit these authors used a slightly higher value of the reference abundance of $\sim 2 \times 10^{-4}$. We note Pon et al. (2016b) find higher CO depletion values than observed in this work ($f_{\text{D}} = 5 - 9$), using higher resolution, higher CO J-transition observations with the James Clerk Maxwell Telescope. These observations are, however, more sensitive to the higher density gas, where CO is expected to be more depleted. Therefore, the level of CO depletion within Cloud F is only moderate on the scales probed by the observations used in this chapter, and, therefore, artificially split line profiles are not expected to contaminate the velocity component analysis from the $\text{C}^{18}\text{O}(1 - 0)$ emission.

3.7 Discussion

The kinematic analysis of Cloud F has unveiled a complex structure, consisting of several extended, coherent velocity components. Previous studies of this cloud have shown that it contains a distribution of both quiescent and active star-forming regions, which are discussed in relation to the kinematic structure below, with a particular focus on the Rathborne, Jackson & Simon (2006) and Butler & Tan (2012) core regions shown on Figure 3.1. The kinematic structure of Cloud F is then compared to that within similar IRDCs, and to the larger scale gas kinematics surrounding the cloud.

3.7.1 The kinematic structure of Cloud F

The kinematic structure of Cloud F is discussed in this section with reference to previous work on this source. For reference, the [Rathborne, Jackson & Simon \(2006\)](#) and [Butler & Tan \(2012\)](#) core regions mentioned in the follow section are labeled on [Figure 3.1](#). We also give a note on the physical interpretation of structures identified in molecular line observations.

3.7.1.1 The F1/MM8 region

Towards the south-west of the mapped region, the F1/MM8 core region, we find two distinct velocity components: F_{PPV2} and F_{PPV4} , both seen in the $C^{18}O(1-0)$ emission. As shown in [Figure 3.6](#), the higher velocity of these components shows a factor of two narrower line width, with respect to the mean value of this component (line width towards this region and mean width of the F_{PPV4} component are $\sim 1 \text{ km s}^{-1}$ and $\sim 1.8 \text{ km s}^{-1}$, respectively).

A similar double-peaked line profile may, however, be produced as a result of optical depth. If the emission were optically thick, it would be self-absorbed at the mean centroid velocity of the region (as traced by optically thin emission). Unfortunately, significant $N_2H^+(1-0)$ emission is not observed towards this region, however, another high-density tracing, optically thin molecular line transition, $N_2D^+(3-2)$ has been shown to have emission at velocities coincident with only the lower velocity component ([Tan et al., 2013](#); [Pon et al., 2016a](#)). This is not expected if these components were produced by optical depth, as instead, the optically thin emission would have a centroid velocity at the centre of these components (see [Section 3.7.3](#) for a discussion).

The depletion of CO-bearing molecules, such as $C^{18}O$, onto the dust grains within dense, cold environments, may also artificially produce multiple velocity components. However, a dip in the emission profile of the CO-bearing molecule emission (e.g. $C^{18}O$) would typically be seen at the centroid velocity of the emission from a non-CO bearing molecules (such as N_2D^+), which we again do not see ([Tan et al., 2013](#)).

Furthermore, we calculate the level of CO depletion throughout Cloud F and find an average value towards this region of 1.3 ± 0.1 (no depletion of CO would be represented by a value of unity), which we believe is not significant enough to cause this effect. We, therefore, find that two distinct velocity components with different line profiles are indeed present along the line of sight towards this region, pointing to different internal conditions within these components.

Possible formation scenarios for the interesting structure observed towards this region have been discussed in a series of papers by [Pon et al. \(2015, 2016a,b\)](#). These authors identify both narrow and broad velocity components in JCMT mid-J transition ^{13}CO observations (with a spatial resolution of $\sim 11''$) towards this region, showing similar centroid velocities to the $F_{\text{PPV}2}$ and $F_{\text{PPV}4}$ components identified here. [Pon et al. \(2016a\)](#) suggest that protostars associated with the $24\ \mu\text{m}$ source just to the north of the F1 core have created a wind-blown bubble, where the broader, lower velocity component ($\sim 56\ \text{km s}^{-1}$, $F_{\text{PPV}2}$ here) traces the compressed gas within the bubble wall. This lower velocity component is also seen in high-J CO transitions (e.g. $J = 8 \rightarrow 7$ upwards; [Pon et al., 2015](#)). Comparison between the PDR models and the high-J transition emission shows that there may be a hot gas component (of around $\sim 100\ \text{K}$) within this region, which could have been formed by the dissipation of turbulence as this component is compressed within the shell ([Pon et al., 2015, 2016b](#)). The origin of the narrow velocity component $F_{\text{PPV}4}$ is, however, still unknown.

3.7.1.2 The F4/MM3 region

Initial molecular line studies towards the F4/MM3 region showed it to be cold, dense and quiescent, hence an ideal region to study the initial stages of massive star formation ([Garay et al., 2004](#)). Several more recent studies have, however, found signs that protostars could be already present within this region (e.g. [Foster et al., 2014](#)). For example, there is a clear point source towards this region in the *Spitzer* and *Herschel* images, which can be seen as negative mass surface density values in Figure 3.3. Indeed, [Chambers et al. \(2009\)](#) found two sources within the MM3 region which could be

classified as a “green fuzzie” from their excess of $4.5 \mu\text{m}$ emission, a signpost of heated dust by embedded protostars, and [Cosentino et al. \(2018\)](#) have found bright and broad SiO emission toward this core, indicative of an outflow (also see [Sakai et al., 2013](#); [Yanagida et al., 2014](#)). These authors also detect water and methanol maser emission towards both of these sources, suggesting that massive protostars may be present within this region (e.g. [Walsh et al., 2001](#)). [Wang et al. \(2006\)](#) identified that the water maser emission towards this core has a single component, which is red-shifted by $\sim 20 \text{ km s}^{-1}$ with respect to the molecular gas at $\sim 55 \text{ km s}^{-1}$, suggesting that the embedded protostar(s) within this region have already begun to influence the kinematics of the surrounding gas. [Sanhueza et al. \(2010\)](#) found that the optically thick emission from CO (3 – 2) towards these regions have blue- and red-shifted lobes of $\pm 15 \text{ km s}^{-1}$ around the mean centroid velocity of optically thin lines, such as C^{18}O and CS (similarly broad profiles were found by [Rathborne et al., 2005](#)). These authors suggest that such profiles are the result of a molecular outflow with a total mass of $\sim 40 M_{\odot}$. Using the lower mass limit of the embedded sources within this region from [Shepherd et al. \(2007\)](#),¹¹ and extrapolated with a Kroupa IMF ([Kroupa, 2001](#)), we estimate that the total mass of protostars within this region is comparable to the mass of the molecular outflow.

Towards the F4/MM3 region, we find a relatively simple velocity structure of only a single velocity component, F_{PPV4} . However, in light of the above discussion, it is possible that this kinematic structure has been influenced by protostellar feedback and/or is causing the star formation within this region. Indeed, we find a systematic offset between the N_2H^+ emission towards higher velocities, with respect to the C^{18}O emission (of $\sim 0.2 \text{ km s}^{-1}$; see Section 3.5.3). This red-shift is not, however, as large as the red-shift lobe of the optically thick CO emission from [Sanhueza et al. \(2010\)](#) or the water maser emission from [Wang et al. \(2006\)](#). Interestingly, recent high-resolution N_2D^+ (3 – 2) ALMA observations towards the F4 region show emission at a velocity of $57.10 \pm 0.05 \text{ km s}^{-1}$ ([Kong et al., 2017](#)), which is offset from the N_2H^+ (1 – 0)

¹¹The total mass of the sources with SED fits towards this region – IDs “25”, “26”, “27”, “28”, “29” and “30” – is $\sim 10 M_{\odot}$. We note that the uncertainty on this value, and on the total embedded stellar mass estimate, could be larger than a factor of three (see [Barnes et al., 2017](#) for a discussion of the uncertainties present when determining embedded stellar masses).

and C^{18}O emission by $>0.8 \text{ km s}^{-1}$ for the same position ($58.67 \pm 0.07 \text{ kms}$ and $57.90 \pm 0.02 \text{ kms}$, respectively). Moreover, despite the evidence for an outflow within the region, observations of optically thick molecular lines (HCO^+ , HCN ; Zhang et al., 2017) towards this region show asymmetric line profile characteristic of infall motions (Evans, 1999). This suggests that the active star-forming region within this northern portion of Cloud F, F2/MM3, is currently accreting material from the gas reservoir of the cloud.

3.7.1.3 The MM1 and MM2 regions

We observe the most complex spectra towards the south of the cloud, which at some positions show three velocity components along the line of sight: F_{PPV1} , F_{PPV2} and F_{PPV4} . This region is referred to as the MM1 region (Rathborne et al., 2005; Rathborne, Jackson & Simon, 2006), and is located approximately $40''$ (or $\sim 0.75 \text{ pc}$, assuming a source distance of 3.7 kpc ; Simon et al., 2006b), from the MM2 region, also known as IRAS 18507+0121 (refer to Figure 3.1). The MM1 region is thought to host a young, embedded protostar, with a spectral type B2 (Shepherd, Nürnberg & Bronfman, 2004; Shepherd et al., 2007; Rathborne et al., 2008), whereas the MM2 region is thought to be more massive and evolved, harbouring a B0.5 class star surrounded by an ultracompact H II region (Miralles, Rodriguez & Scalise, 1994; Molinari et al., 1996). These sources are thought to have a combined mass of $\sim 50 M_{\odot}$, and are driving a molecular outflow of $\sim 100 M_{\odot}$ (Shepherd et al., 2007). When extrapolated using a Kroupa IMF the total embedded stellar mass within these regions is $\sim 200 M_{\odot}$. As with the MM3 region, despite the on-going star formation within MM1 and MM2, there is evidence to show large-scale infall motions towards these regions (Ramesh, Bronfman & Deguchi, 1997; Sanhueza et al., 2010; Zhang et al., 2017). Indeed, the spectral profiles of the optically thick ^{13}CO emission towards these regions show asymmetric profiles with enhanced blue-shifted peaks (see Section 3.7.3). Again, this is suggestive that this active star-forming region is accreting material over scales of up to 2 pc , given the approximate extent of the double-peaked, blue-shifted profile seen in the ^{13}CO emission (see Figure 3.14).

3.7.2 Cloud F in the context of other star-forming regions

Galactic Plane surveys, undertaken with infrared space-based telescopes (most recently *Spitzer* and *Herschel*), have shown that filamentary structures appear to be ubiquitous throughout the interstellar medium (e.g. [Molinari et al., 2016](#)). Recently, kinematic analysis of molecular line emission has shown that coherent structures, believed to be the velocity space representation of these filamentary structures, are equally common, appearing in both low- and high-mass star-forming regions (e.g. [Hacar et al., 2013](#); [Henshaw et al., 2014](#); [Hacar et al., 2016c](#); [Henshaw et al., 2017](#)). However, despite these structures being morphologically and qualitatively similar, their physical properties may be very different. Currently, direct comparisons of these structure and thier properties within massive star-forming regions are lacking. To address this, in this section, we discuss how the properties determined for Cloud F compare to a similar IRDC, Cloud H (G035.39-00.33; [Butler & Tan, 2009](#); see Table 3.1), with the aim of highlighting which kinematic properties are shared between these, and potentially other, massive star-forming regions. In the following sections, the details of these observations and the parameters used to determine the kinematic structure are briefly outlined. We then place the structures identified in these massive star forming regions in the context of the structures seen in more local star-forming regions (e.g. Taurus).

3.7.2.1 Observations of Cloud H

Details of the $\text{C}^{18}\text{O}(1-0)$ and $\text{N}_2\text{H}^+(1-0)$ observations towards Cloud H are presented in Table 1 of [Henshaw et al. \(2013\)](#). Here, we smooth these observations to an angular resolution of $36''$, with a pixel spacing of $18''$, such that they have a spatial resolution of ~ 0.5 pc at the source distance of 2.9 kpc ([Simon et al., 2006b](#)). This was done to match the spatial resolution of the Cloud F observations, such that structure identification is not biased to a spatial scale, given the hierarchical nature of the interstellar medium.

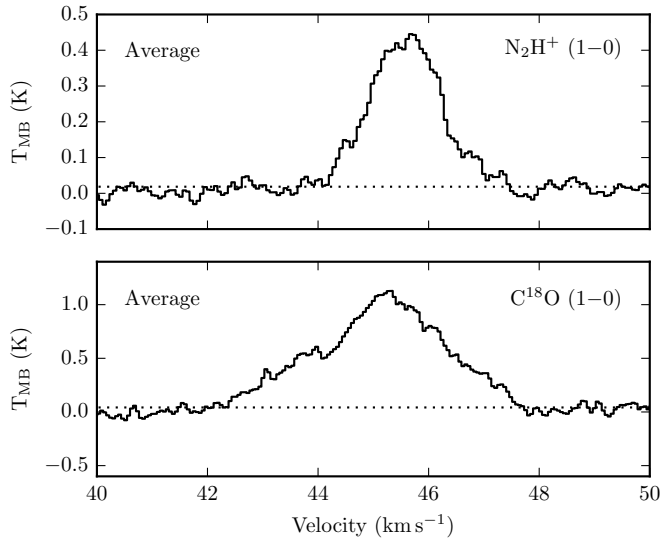


Figure 3.11: Shown are the average spectrum of the $\text{N}_2\text{H}^+(1-0)$ transition [upper panel] and the $\text{C}^{18}\text{O}(1-0)$ transition [lower panel] across the mapped region of Cloud H. The horizontal dotted line represents the σ_{rms} level of ~ 0.02 K and ~ 0.04 K for $\text{N}_2\text{H}^+(1-0)$ and $\text{C}^{18}\text{O}(1-0)$, respectively.

3.7.2.2 Gaussian fitting and hierarchical clustering

Figure 3.11 shows the average spectrum for the $\text{N}_2\text{H}^+(1-0)$ hyperfine component and $\text{C}^{18}\text{O}(1-0)$ transitions across Cloud H. We find that the majority of the emission above the *rms* levels is between approximately $43 - 57 \text{ km s}^{-1}$. Figure 3.12 shows the spectra at each pixel position across the cloud, plotted using the same velocity range as the average spectra. As with Cloud F, several spectra across the mapped region, particularly in $\text{C}^{18}\text{O}(1-0)$, appear to have more than one peak, and show that multiple velocity components are present along the line of sight.

We use the Gaussian profile fitting algorithm *SCOUSE* to separate the velocity components within the spectra, then the hierarchical clustering routine *ACORNS* to identify the coherent velocity structures across the cloud. These same analysis tools were used to determine the kinematic structure (*SCOUSE* and *ACORNS*) of both clouds, such that the systematic comparison is possible, as it has been recently suggested that the results from different structure finding algorithms can vary (e.g. [Chira et al., 2017](#)).

The same spectral averaging area (SAA) radius and threshold values in *SCOUSE* that were used for Cloud F were used for Cloud H. These gave reasonable fits, and < 10 per cent of the data had to be checked and re-fitted. The same input parameters as used in Cloud F were in *ACORNS* for the identification of the initial hierarchy. The parameter space survey of the relaxation factors, however, showed that for values of 0.5, 1.25,

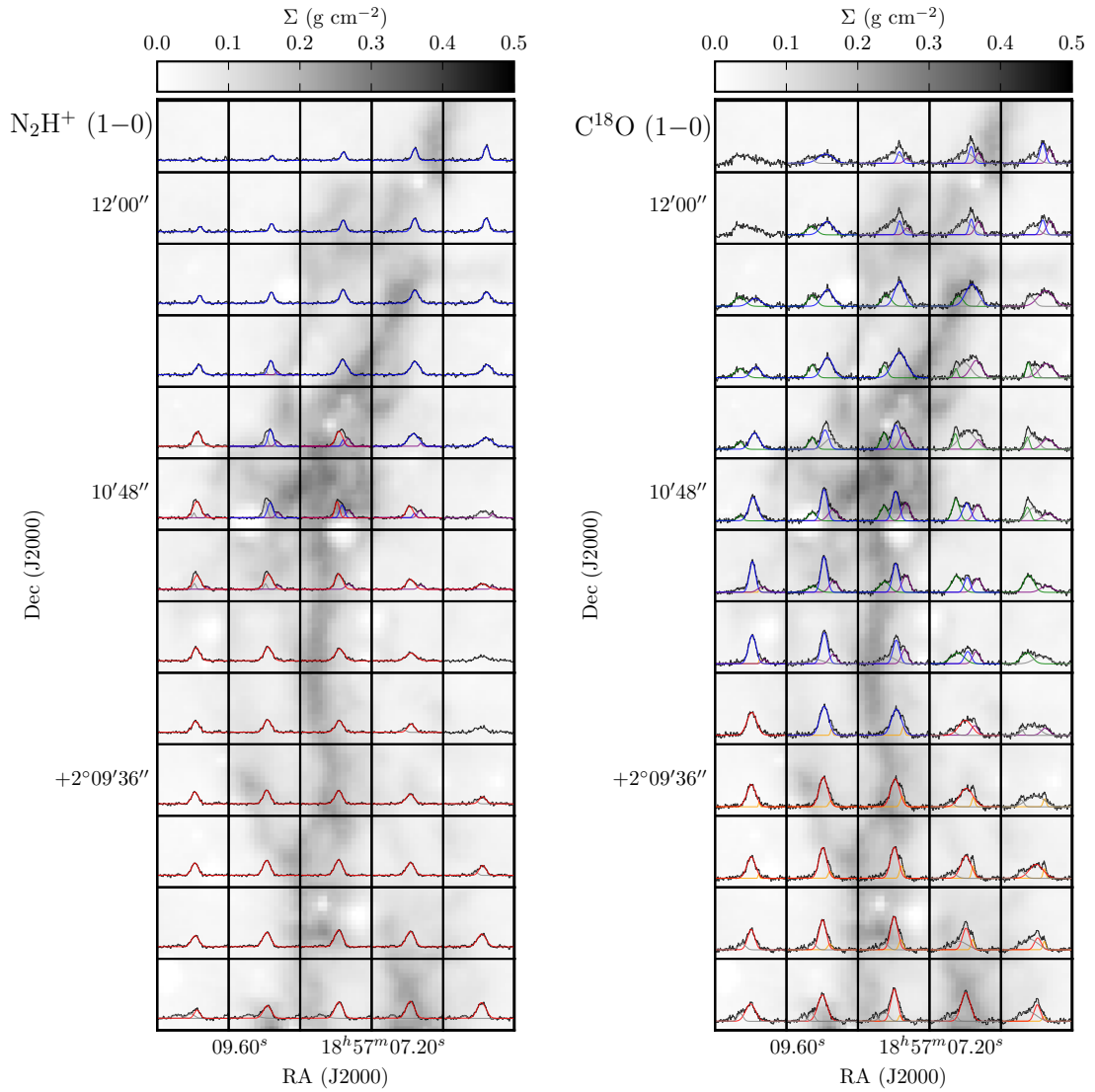


Figure 3.12: The spectra at each each pixel position across the cloud (shown in black). The velocity ranges are 40 to 50 km s^{-1} , and the intensity ranges are -0.5 to 2.5 K for N_2H^+ [left panel] and -0.5 to 3.5 K for C^{18}O [right panel]. Overlaid on each spectrum are the results of the line fitting (SCOUSE) and clustering (ACORNS) routines, which are discussed in Section 3.7.2.2. The colours of these profiles represent the various velocity component associations given in Table 3.3. The background greyscale is the mass surface density map (Kainulainen & Tan, 2013).

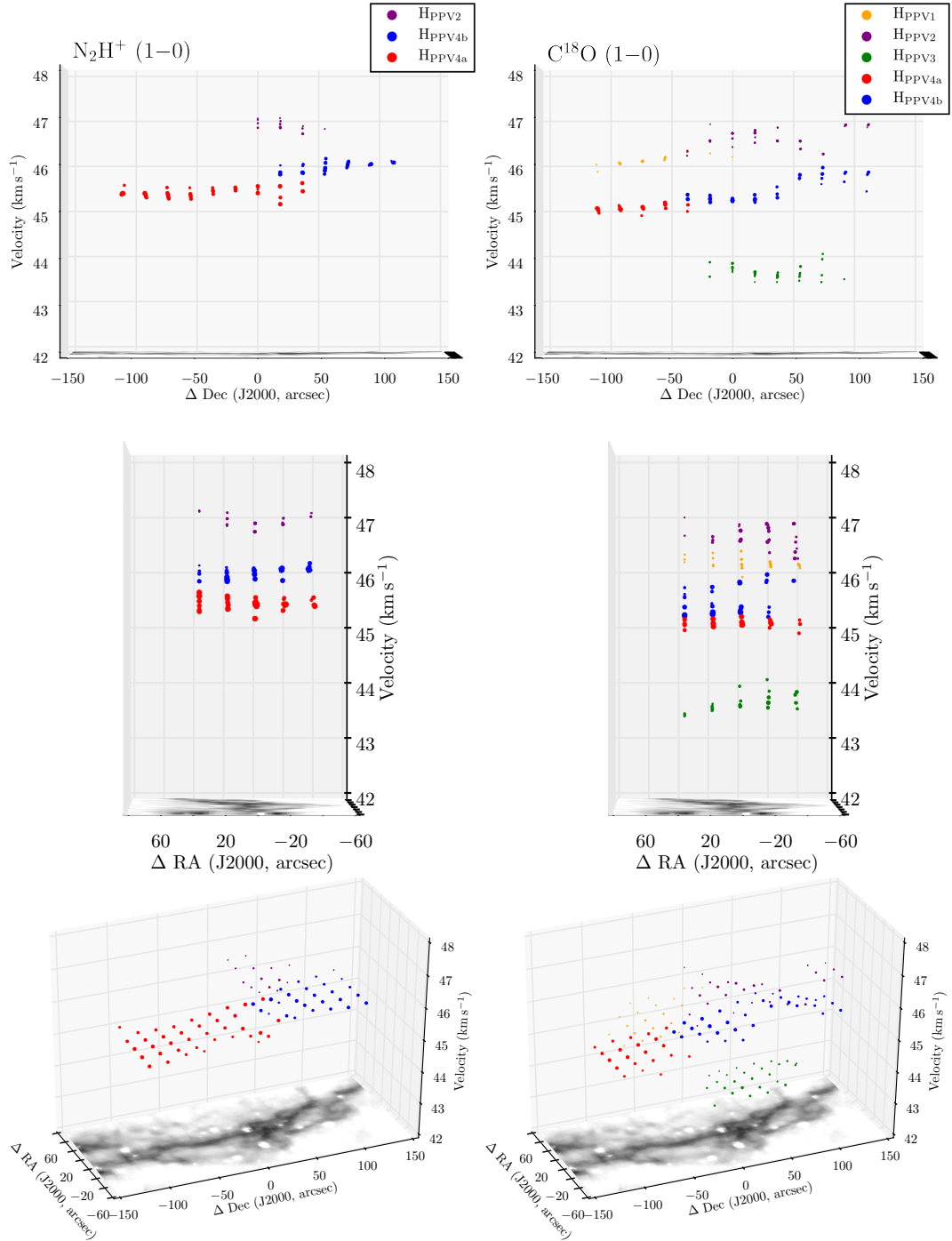


Figure 3.13: Displayed in each panel is the position-position-velocity diagram of Cloud H, shown at various viewing angles. The left and right panels show $\text{N}_2\text{H}^+ (1-0)$ and $\text{C}^{18}\text{O} (1-0)$ results, respectively. The colour of each point represents the association to one of the distinct coherent velocity components identified using the clustering algorithm ACORNS (Henshaw et al. in prep), $\text{H}_{\text{PPV}1}$ in orange, $\text{H}_{\text{PPV}2}$ in purple, $\text{H}_{\text{PPV}3}$ in green, and $\text{H}_{\text{PPV}4a}$ in red and $\text{H}_{\text{PPV}4b}$ in blue. The size of each point represents its relative peak intensity. The mass surface density map of Kainulainen & Tan (2013) is shown on the base of each plot. Note, the coordinate offsets of these plots are relative to the centre of the mapped region: RA (J2000) = $18^{\text{h}}57^{\text{m}}08^{\text{s}}$, Dec (J2000) = $02^{\circ}10'12''$ ($l = 35.512^{\circ}$, $b = -0.277^{\circ}$).

1.0, for the peak intensity, centroid velocity and line width, respectively, were required to identify the most robust structures.¹² The results of the Gaussian fitting and structure finding routines are presented in Figures 3.12 and 3.13.

We identify five structures in the $\text{C}^{18}\text{O}(1-0)$ emission, defined as H_{PPV1} , H_{PPV2} , H_{PPV3} , and H_{PPV4a} and H_{PPV4b} (shown in orange, purple, green, red and blue), three of which are also identified in the $\text{N}_2\text{H}^+(1-0)$ emission. We choose to define H_{PPV4a} and H_{PPV4b} in this way, as, although they have been defined as separate structures (see Henshaw et al., 2014), previous single dish studies have defined them as one (Henshaw et al., 2013; Jiménez-Serra et al., 2014). The basic properties are given in Table 3.3.

We find that Cloud H contains a complex structure, harbouring several coherent velocity components, seen in both the $\text{N}_2\text{H}^+(1-0)$ and $\text{C}^{18}\text{O}(1-0)$ emission, which are in agreement with the results previously found by Henshaw et al. (2013).

3.7.2.3 Similarities between the kinematic structure of the two clouds

Similar to Cloud F, from the measured line width, we have determined the non-thermal velocity dispersions within Cloud H. We find Mach numbers of $\mathcal{M} = 2.00 \pm 0.07$ and $\mathcal{M} = 2.28 \pm 0.08$ using $\text{N}_2\text{H}^+(1-0)$ and $\text{C}^{18}\text{O}(1-0)$ (averaged over all velocity components), respectively; histograms of these results are shown next to those for Cloud F in Figure 3.10. Therefore, we find that the non-thermal contributions are factors of 2 – 3 larger than the sound speed of the gas within both clouds, which sets an upper limit on the turbulent motions being mildly supersonic over the examined physical scale (i.e. the smoothed spatial resolution of ~ 0.5 pc).

We investigate the velocity distribution of the components by comparing the separation of the lowest and highest velocity component within both clouds. We use the components seen in $\text{C}^{18}\text{O}(1-0)$ emission, and find a line-of-sight difference for Cloud F (F_{PPV1} and F_{PPV2}) of $2.9 \pm 0.5 \text{ km s}^{-1}$, and for Cloud H (H_{PPV2} and H_{PPV3}) of $2.9 \pm 0.3 \text{ km s}^{-1}$. Assuming a simple three-dimensional morphology, this result could

¹²We note that, choosing the same relaxation factors as Cloud F did not significantly change the main structures in Cloud H, rather these cause ACORNS to identify additional structures using the lower peak intensity positions throughout the cloud.

indicate that both clouds have kinematic structures that are interacting at a speed of up to 5 km s^{-1} ; accounting for a factor of $\sqrt{3}$, assuming the velocity in the plan of the sky is equivalent in all directions.

A filament merging scenario is in agreement with the wide-spread narrow SiO emission observed within Cloud H, generated by the sputtering of dust grains within large-scale C-shocks (Jiménez-Serra et al., 2010, requiring a shock velocity of $\sim 12 \text{ km s}^{-1}$). It is possible that a similar scenario of filament merging is causing the velocity difference within Cloud F, and indeed Cosentino et al. (2018) also found similarly wide-spread SiO emission throughout this cloud. However, it is difficult to determine if this emission is due to a merging scenario or higher level star-formation within Cloud F, which would have affected the chemistry of the molecular gas as a result of stellar feedback (e.g. towards the F4, or MM3, region). The elevated level of star formation within Cloud F suggest that it is at a later evolutionary stage than Cloud H, which has previously been suggested to be $\sim 3 \text{ Myr}$ old (Henshaw et al., 2013; Jiménez-Serra et al., 2014; Barnes et al., 2016).

We also compare the velocity separation between the coherent velocity components identified in the $\text{N}_2\text{H}^+(1-0)$ and $\text{C}^{18}\text{O}(1-0)$ emission. When doing so within Cloud F we found a significant positive systematic offset of $\Delta V_{\text{LSR}}(\text{N}_2\text{H}^+ - \text{C}^{18}\text{O}) = +0.32 \pm 0.03 \text{ km s}^{-1}$. To conduct a similar analysis within Cloud H, we compare the $\text{H}_{\text{PPV}4\text{a}}$ and $\text{H}_{\text{PPV}4\text{b}}$ structures. These components have been identified simultaneously at three positions within the $\text{N}_2\text{H}^+(1-0)$ map (see Figure 3.12). At these positions, we average the centroid velocity of the components in $\text{N}_2\text{H}^+(1-0)$ and compare this velocity to the component seen in the $\text{C}^{18}\text{O}(1-0)$ emission ($\text{H}_{\text{PPV}4}$).¹³ We note that omitting these positions, which make up only ~ 5 per cent of the total positions used for this comparison, would not significantly affect the result presented here. The centroid velocity difference map and histogram for Cloud H is presented with the Cloud F results in Figure 3.8. We find an average velocity shift of $+0.26 \pm 0.02 \text{ km s}^{-1}$,¹⁴ which is in agreement with the value found by Henshaw et al. (2013). It is intriguing

¹³These positions are towards the complex H6 regions (Henshaw et al., 2014, 2017).

¹⁴Uncertainty given is the standard error on the mean, where the standard deviation is $\pm 0.14 \text{ km s}^{-1}$.

that both clouds share such a similar positive velocity shift between N_2H^+ ($1 - 0$) and C^{18}O ($1 - 0$). Given below are several possible scenarios its formation.

It has been previously proposed that the velocity difference within Cloud H is a result of a filament merging, whereby higher velocity filaments (H_{PPV1} and H_{PPV2} , from this work) are merging with a lower velocity, less massive filament (H_{PPV3}), increasing the density of an intermediate velocity filaments (H_{PPV4a} and H_{PPV4b}). Given the majority of the mass within Cloud H is situated at a higher velocity, the densest gas forming within the intermediate velocity filament, as traced by N_2H^+ , is pushed to a higher velocity with respect to its envelope material traced by C^{18}O , also formed by the merging process (Henshaw et al., 2013; Jiménez-Serra et al., 2014; Henshaw et al., 2014). Indeed, simulations have shown that certain lines-of-sight through density fluctuations and varying velocity fields within collapsing clouds can cause significant velocity difference between molecular tracers (Smith et al., 2013; Bailey, Basu & Caselli, 2015). As previously discussed, such a scenario is plausible for Cloud F, and would also be in agreement with the observed velocity difference between the components. We note, however, a common physical mechanism driving this interaction is not determinable from the data presented here (e.g. cloud-cloud merging or global gravitational collapse).

A second explanation, proposed by Zhang et al. (2017), is that velocity shifts between low and high-density tracers could be a signature of gas that is both expanding and contracting within the core regions of the cloud. This is based on the assumption that the higher critical density molecules, in their case HCO^+ emission, trace the inner dynamics of a core, while lower critical density molecules, C^{18}O , trace the outer, envelope dynamics. These authors find blue-shifted and red-shifted profiles of the high and low-density tracers, respectively, towards a sample of cores, which they suggest shows the different core layers are moving in opposing directions; a scenario of “envelope expansion with core collapse” (e.g. Lou & Gao, 2011). Indeed, these authors proposed such a scenario for a core region within Clouds H (H6/MM7; Rathborne, Jackson & Simon, 2006; Butler & Tan, 2012). We suggest that this could, in theory, be applied to explain the velocity shifts observed across both clouds, yet this would

require the effect being extrapolated over larger scales.

In summary, here we have shown that two massive, morphologically and qualitatively similar IRDCs share several kinematic properties, hinting at similar internal gas conditions. An intriguing result given that they are drawn from different Galactic environments and have differing levels of various internal physical processes (e.g. level of star formation). It would be interesting to examine a larger sample of clouds to determine if these properties are inherent to the wider IRDC population.

3.7.2.4 Unresolved sub-structure within the clouds and comparison to local star forming regions

An interesting result from the study of Cloud F is the observed larger velocity dispersion measurements from the N_2H^+ compared to the C^{18}O , which is not typically expected when N_2H^+ originates from more compact (i.e. less turbulent) regions compare to C^{18}O (see section 3.5.4). One potential cause of this is unresolved velocity components within the N_2H^+ that are not seen in the C^{18}O . It is not clear why such a scenario would arise, nonetheless it is conceivable that this could be the case given the kinematic complexity of these massive star-forming regions. Dense structures within these regions could indeed appear to merge when observed over the relatively large spatial scales probed by the observations used in this chapter (~ 0.5 pc).

Indeed, there have been several high spatial-resolution studies of Cloud H that have shown that this cloud contains much sub-structure (Henshaw et al., 2014, 2016a, 2017; Sokolov et al., 2018). The highest spatial resolution observations to date of this cloud have been carried out with ALMA, and focus on the “H6” core regions (see Figure 2.1). These observations probe scales of ~ 0.01 pc and found that a complex network of dust continuum structures exist with widths of ~ 0.03 pc and masses of $\sim 1 - 10 M_\odot$. Unfortunately, the analysis of the molecular line dataset from these observations is still under analysis, and, therefore, information of the kinematic structure of the dense gas within the regions is not available for comparison (Henshaw et al. in prep). Structures with similar sizes and masses to the ALMA observations have been observed

within several more local star-forming regions (e.g. [Hacar, Tafalla & Alves, 2017](#)). These structures were first referred to “fibres”, as they are suggested to be the smaller scale, subsonic constituents of the larger, supersonic filaments previously observed with lower resolution observations ([Hacar et al., 2013](#)). With the discussion presented here in mind, it seems likely that Cloud F will contain substructure when observed with higher resolution observations, similar to Cloud H, which could potentially be comparable to the fibre structure seen in lower mass star-forming regions.

As an interesting exercise to determine if these fibre structures could make up the filamentary structures identified within Cloud F would be to degrade the spatial resolution of the [Hacar et al., 2013](#) dataset and re-analyse using the methods presented in this work. This, however, is beyond the scope of this thesis, and hence we opt for a simpler comparison of the distribution of centroid velocities of the fibres across the spatial resolution of the IRAM-30m observations (~ 0.5 pc). This would follow the theory outlined by [Hacar et al. \(2016a\)](#), whereby the observed supersonic velocity dispersions towards filaments are just a sum of the relative velocities of their constituent subsonic fibre structures. To conduct this analysis we use the fibre structures presented by [Hacar et al., 2013](#), which were identified using $C^{18}O$ observations towards the L1495/B213 Taurus region (~ 10 pc long filamentary structure). Taking the most kinematically complex region of the cloud, B211-213, as the example for this investigation, we estimate that distribution of centroid velocities on average is ~ 0.5 km s $^{-1}$ (e.g. comparing the B211-213 fibres [3,4,5,7] that are within an area of ~ 0.25 pc 2). Therefore, when observed at the distance of Cloud F, the B211-213 region would appear as a single filament with a velocity dispersion of $\sigma 0.5$ km s $^{-1}$, which would correspond to a Mach number of around 2,¹⁵ i.e. moderately supersonic. This value is very similar to that found for the filaments within Cloud F (and Cloud H): $\mathcal{M} \sim 2 - 3$ (see section 3.5.4).

In summary, we propose that there will most likely be some unresolved substructure within Cloud F, which could explain the the unexpected larger line-width observed for N_2H^+ . It is difficult to estimate with any certainty the scale and properties of these structures, and if they will be in any way similar to those observed within Cloud H.

¹⁵ $\mathcal{M} = \sigma/c_s$, where $c_s = 0.23$ km s $^{-1}$

Nonetheless, we estimate it could be plausible that they resemble the subsonic fibre structures that have been observed within several more local star-forming regions.

3.7.3 Connection between IRDC and GMC scales for Cloud F

As previously mentioned, the interstellar medium is hierarchically structured, with massive star-forming regions hosting a complex sub-structure through various scales (e.g. filaments to cores). However, these regions are by no means at the top of this hierarchy, rather they are believed to be only a small part of larger, Galactic scale structures, which typically have masses and spatial extents one to two orders of magnitude larger than IRDCs (e.g. [Ragan et al., 2014](#); [Hernandez & Tan, 2015](#); [Zucker, Battersby & Goodman, 2015](#)). Indeed, several works have already studied the larger scale environment surrounding both Clouds F and H (as defined here by the IRAM-30m coverage). [Hernandez & Tan \(2015\)](#) find that the larger-scale structures which host Clouds F and H share many similar kinematic properties, such as velocity dispersions ($\sim 3 - 5 \text{ km s}^{-1}$), velocity gradients ($\sim \text{few } 0.1 \text{ km s}^{-1} \text{ pc}^{-1}$) and virial parameters ($\sim \text{unity}$), and [Ragan et al. \(2014\)](#) showed how these IRDCs could be part of “Giant Molecular Filaments” (henceforth, GMFs) structures, which stretch over hundreds of parsecs and have masses of $\sim 10^{5-6} M_{\odot}$. In the following section, the kinematic structure of the region surrounding Cloud F is determined using the same analysis tools used on the IRAM-30m observations.

3.7.3.1 Observations

Observations covering a large scale of Cloud F have been taken as part of the Galactic Ring Survey (GRS; [Jackson et al., 2006](#)). These $^{13}\text{CO}(1-0)$ observations have an angular resolution of $\sim 44''$ and a spectral resolution of $\sim 0.2 \text{ km s}^{-1}$ —factors of ~ 1.5 and ~ 3 larger than the (smoothed) IRAM-30m observations. The data are publicly available at https://www.bu.edu/galacticring/new_data.html, from which we take the data cube over the region $34 < l < 36^{\circ}$, $|b| < 1^{\circ}$, $0 < v < 100 \text{ km s}^{-1}$. This $2^{\circ} \times 2^{\circ}$ image is significantly larger than required, hence we trim the

image to a $\sim 1300'' \times 300''$ region covering the filamentary structure identified in the mass surface density map shown in Figure 3.1.

3.7.3.2 Gaussian fitting and hierarchical clustering

Shown in Figure 3.14 is the spectrum at each position across the map. As with the IRAM-30m observations of this cloud, these spectra are complex, showing multiple velocity components for the majority of positions. We use the SCOUSE and ACORNS algorithms to separate and identify the coherent velocity structures across the cloud. We used the same threshold value in SCOUSE as for the IRAM-30m observations. Given the larger number of pixels present in this dataset compared to the IRAM-30m observations, we choose a larger SAA in SCOUSE of $\sim 145''$ (i.e. each SAA contained 40 positions, given the pixel spacing of $\sim 22''$). Nevertheless, this only resulted in a still manageable ~ 20 per cent of the positions requiring manual inspection. The same input parameters used for the IRAM-30m observations were used in ACORNS for the identification of the initial hierarchy. The parameter space survey of the relaxation values showed that for values of 2.5, 1.75, 0.75, for the peak intensity, centroid velocity and line width, respectively, were required to identify the most robust structures. The results of these analyses are shown in Figures 3.14 and 3.15. Twenty distinct velocity components are identified here, for which the basic properties are presented in Table 3.4. Given that the observation used to identify these components are different in spatial resolution, angular resolution and extent of the IRAM-30m observations, we choose to differentiate these by using a different, “ F_{GRS} ”, nomenclature.

3.7.3.3 The GMC scale structure of Cloud H

The results of this analysis are presented in the upper panel of Figure 3.15, which shows the position-position-velocity diagram with each point coloured to the identified velocity components given in Table 3.4 (features of interest are shown in the figure legend). The most extended and prominent of these structures, $F_{\text{GRS}2}$, is coherent over nearly the entire mapped region, a projected distance of > 20 pc at the assumed source

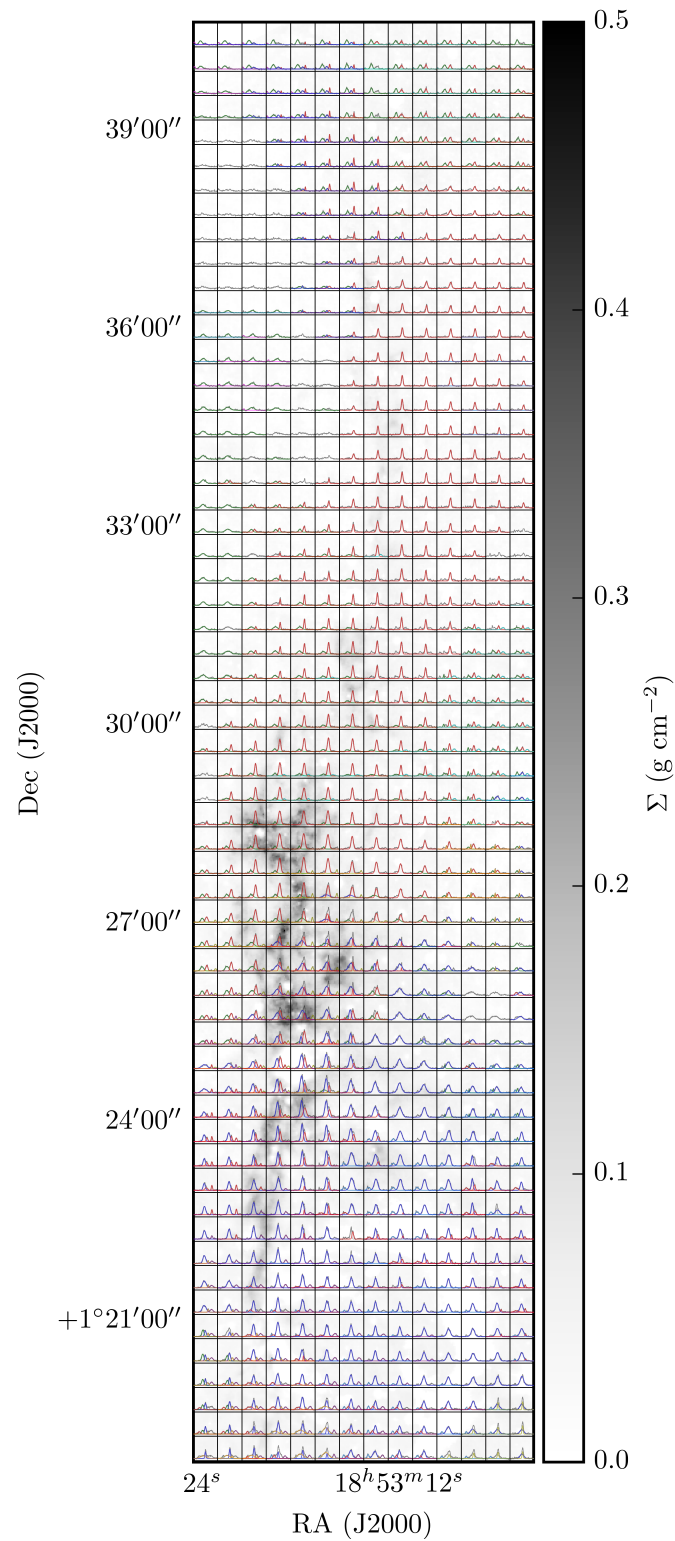


Figure 3.14: The $^{13}\text{CO}(1-0)$ spectra at each pixel position across Cloud F, overlaid with coloured profiles of the various velocity components. The velocity ranges are 45 to 70 km s^{-1} , and the intensity ranges are -0.5 to 5.0 K . The background greyscale is the mass surface density map (Kainulainen & Tan, 2013).

Table 3.4: Parameters of the velocity components identified in the GRS observations towards Clouds F (F_{GRS}). Shown is the molecule used to identify the components, and for each component: the name, the total number of points, the average centroid velocity, the average line width, the velocity gradient and the angle of this gradient with respect to East of North. When the uncertainty on the velocity gradient is larger than or equal to the calculated velocity gradient, the velocity gradient angle is unconstrained, and therefore not shown.

Line	Component	# points	Centroid velocity (V_0) km s ⁻¹	Line width (Δv) km s ⁻¹	Velocity gradient (∇v) km s ⁻¹ pc ⁻¹	Gradient angle ($\theta_{\nabla v}$) degrees
¹³ CO(1 – 0)	F_{GRS1} (blue)	297	56.80 ± 0.39	3.69 ± 1.17	0.02 ± 0.01	-80.85 ± 9.57
	F_{GRS2} (red)	498	58.91 ± 0.71	2.11 ± 0.56	0.14 ± 0.03	82.09 ± 2.55
	F_{GRS3} (green)	357	53.58 ± 1.05	3.89 ± 1.27	0.42 ± 0.07	-86.67 ± 1.02
	F_{GRS4}	60	67.44 ± 0.38	2.11 ± 0.35	0.20 ± 0.07	75.62 ± 6.64
	F_{GRS5}	94	64.31 ± 0.80	3.03 ± 0.75	0.38 ± 0.09	82.56 ± 1.91
	F_{GRS6}	9	46.69 ± 0.21	1.86 ± 0.52	0.51 ± 0.11	-58.46 ± 7.23
	F_{GRS7}	22	44.32 ± 0.18	2.63 ± 0.81	0.11 ± 0.05	83.59 ± 4.60
	F_{GRS8}	92	50.08 ± 0.28	2.28 ± 0.72	0.0 ± 0.0	...
	F_{GRS9}	21	54.73 ± 0.17	0.92 ± 0.19	0.38 ± 0.07	-70.60 ± 2.56
	F_{GRS10}	23	64.11 ± 0.12	1.62 ± 0.26	0.03 ± 0.06	...
	F_{GRS11}	9	55.10 ± 0.57	7.24 ± 0.63	0.29 ± 0.30	83.89 ± 9.12
	F_{GRS12}	9	54.82 ± 0.10	2.60 ± 0.19	0.18 ± 0.15	78.89 ± 13.21
	F_{GRS13}	9	57.71 ± 0.12	1.54 ± 0.27	0.26 ± 0.07	-82.11 ± 2.39
	F_{GRS14}	13	58.83 ± 0.23	1.38 ± 0.88	0.29 ± 0.13	86.05 ± 2.99
	F_{GRS15}	16	45.79 ± 0.23	2.16 ± 0.23	0.41 ± 0.08	-76.43 ± 2.62
	F_{GRS16}	45	62.78 ± 0.31	3.30 ± 0.50	0.18 ± 0.03	-63.14 ± 5.15
	F_{GRS17}	40	41.01 ± 0.18	1.30 ± 0.34	0.03 ± 0.02	85.75 ± 9.67
	F_{GRS18}	51	57.30 ± 0.17	2.21 ± 0.63	0.05 ± 0.04	-82.96 ± 10.16
	F_{GRS19}	77	51.80 ± 1.27	3.40 ± 1.35	0.09 ± 0.10	-82.55 ± 10.78
	F_{GRS20}	29	60.11 ± 0.20	1.66 ± 0.37	0.05 ± 0.05	82.00 ± 11.72

distance of 3.7 kpc (Simon et al., 2006b).

The lower panel of Figure 3.15 shows the structures identified from the IRAM-30m $C^{18}O(1-0)$ observations overlaid on those from the $^{13}CO(1-0)$ GRS observations. We find that the F_{PPV4} structure appears to coincide spatially and in velocity with the F_{GRS2} towards the north of the IRAM-30m mapped region. However, towards the south of the IRAM-30m map, towards the MM1 region, the F_{PPV4} component appears at a velocity in-between the F_{GRS1} and F_{GRS2} components, which suggests that the splitting of these two GRS components is an optical depth effect in the ^{13}CO observations, which would make sense as this is one of the densest regions within the cloud. Furthermore, as discussed in Section 3.7.1, this optically thick emission profile can be linked to the infall motions previously identified towards this region (Ramesh, Bronfman & Deguchi, 1997; Sanhueza et al., 2010).

We find that F_{PPV4} and F_{PPV2} appear to trace F_{GRS1} and F_{GRS2} on the west side of the mapped region, towards the MM8/F1 region. However, given the spatial resolution of the GRS observations (~ 0.8 pc), it is difficult to distinguish the transition to the optically thin regime when inspecting the spectra from the MM1 region to the F1/MM8 regions, hence the ^{13}CO observations towards this region may also be optically thick. Towards the F4/MM3 region, the F_{PPV1} component does not appear to have any associated component in the GRS observations. It is possible that this component has blended in the GRS data, which seems feasible given the broad line width of the F_{GRS2} component within this region (~ 2 km s $^{-1}$), and the close proximity in velocity to the F_{PPV4} component (~ 1 km s $^{-1}$). Despite the caveats discussed here, the brightest and most extended structures in the GRS observations appear to correspond to the structures in the IRAM-30m observations, indicating that Cloud F could be the central, densest part of this larger scale structure.

3.7.3.4 Cloud F as part of a massive inter-arm filament

Ragan et al. (2014) identified a structure within the spatial coverage and velocity range ($50-60$ km s $^{-1}$) of the F_{GRS1}/F_{GRS2} components as the Giant Molecular Filament 38.1-

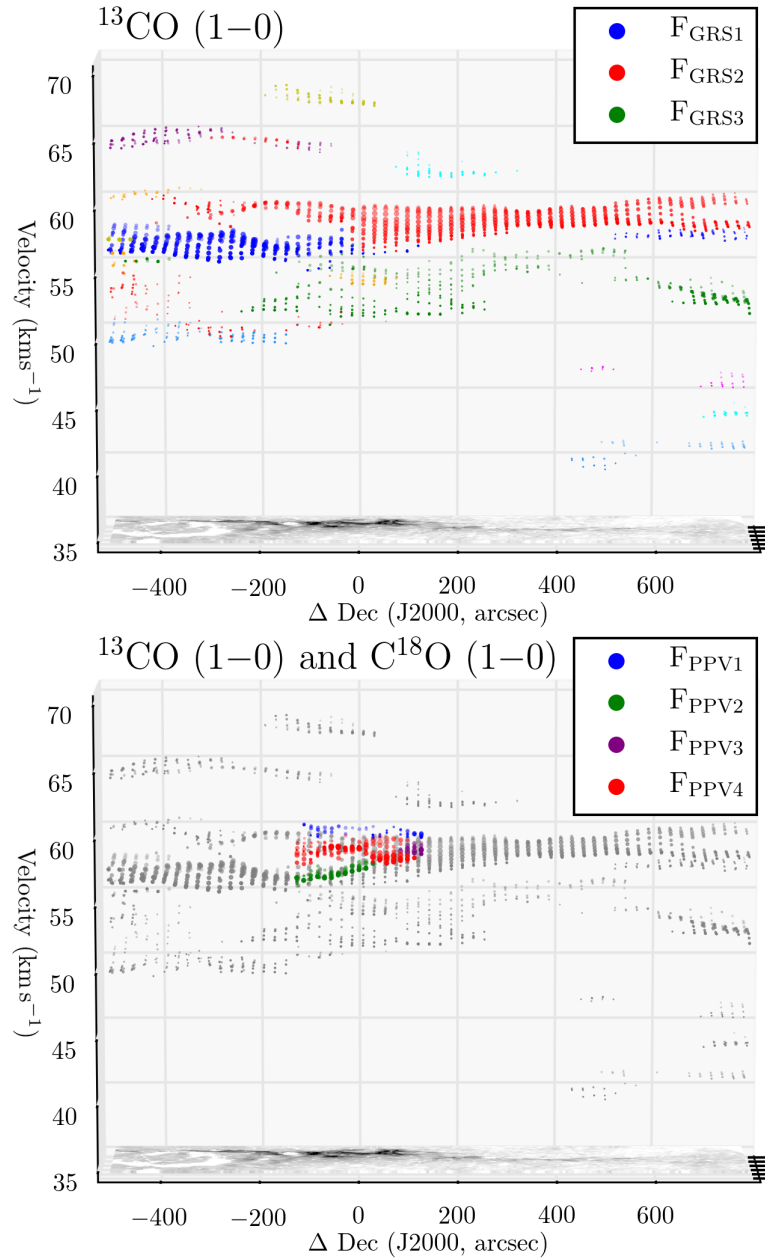


Figure 3.15: Shown are position-position-velocity diagrams covering the large-scale region surrounding Cloud F. The upper panel displays the Gaussian decomposition results for the $^{13}\text{CO}(1-0)$ GRS observations, where the colour of each point represents its association with a coherent velocity component. The three most extended components are shown in the legend in the upper right of the panel. The lower panel displays the same position-position-velocity diagram with the GRS observations shown in grey, overlaid with the structures determined from the IRAM-30m $\text{C}^{18}\text{O}(1-0)$ observations shown in colours identical to Figure 3.7 (see legend in upper right of panel). The size of each point represents its relative peak intensity. The mass surface density map of [Kainulainen & Tan \(2013\)](#) is shown on the base of each plot. Note, the coordinate offsets of these plots are relative to the centre of the mapped region: RA (J2000) = $18^{\text{h}}53^{\text{m}}19^{\text{s}}$, Dec (J2000) = $01^{\circ}27'21''$ ($l = 34.441^{\circ}$, $b = 0.247^{\circ}$).

32.4a, which has the largest mass ($\sim 10^6 M_{\odot}$) and projected length (~ 200 pc) in their sample. It was suggested that this structure resides between the near and far Sagittarius arm, hence could be classified as an “inter-arm cloud” (e.g. Zucker, Battersby & Goodman, 2015). However, the recent Bayesian distance estimator from Reid et al. (2016), which takes into account the kinematic distance, displacement from the plane, and proximity to individual parallax measurements and the probability of residing within a spiral arm (i.e. as priors), places this source in the far Sagittarius arm, at a distance of 10.6 ± 0.3 kpc. This is in disagreement with the kinematic distance analysis from Roman-Duval et al. (2009), which places the cloud at the near distance of 3.7 ± 0.8 kpc based on the absorption of the background HI emission towards this region, the near-infrared extinction distance of ~ 3 kpc (Foster et al., 2012), and the parallax distance of $1.56^{+0.12}_{-1.1}$ kpc (Kurayama et al., 2011; see Foster et al., 2012 and Foster et al., 2014 for discussion of potential issues with this measurement).

We adjust the weighting on the near/far kinematic distance within the Reid et al. (2016) estimator (the only aforementioned prior easily varied). We find that this has to be set to a 1 per cent probability of the source being at the far distance in order to recover a value consistent with the near kinematic distance (3.6 ± 0.7 kpc).¹⁶ Taking this distance estimate for GMF 38.1-32.4a (and Cloud F) places it in-between the near and far Sagittarius arms, as previously suggested by Ragan et al. (2014). This would make this region of particular interest for further study, as one of the most massive and extended inter-arm star-forming complexes in the Milky Way.

3.7.3.5 Could Cloud F be interacting with the supernova remnant W44?

We note that the complication with the source distance may be caused by the higher than average uncertainty in the spiral arm models towards the $33^{\circ} > l > 36^{\circ}$ longitude region, due to the W44 supernova remnant, which has spread the gas over a large velocity range (Dame et al., 1986; Cardillo et al., 2014). A speculative scenario could then

¹⁶See <http://bessel.vlbi-astrometry.org/bayesian>, where the default value that the source is at the far distance is 50 per cent. Adjusting the weighting of the other three priors is possible, yet beyond the scope of this work.

be that the supernova remnant is directly influencing the gas within Cloud F, forcing it to a higher velocity than is predicted for the Sagittarius arm near-arm ($\sim 30\text{km s}^{-1}$; Reid et al., 2014). Assuming that the cloud had an original velocity of $\sim 30\text{km s}^{-1}$, the Reid et al. (2016) estimator places the source at a distance of $2.12 \pm 0.17\text{ kpc}$, which is in better agreement with the parallax distance from Kurayama et al. (2011). This is, however, then significantly closer than the distance to W44 of $\sim 3.2\text{ kpc}$, determined from pulsar timing (Wolszczan, Cordes & Dewey, 1991). Furthermore, the structure of the W44 SNR, observed in the infrared, radio and x-ray, doesn't appear to extend high enough in galactic latitude to be interacting with the Cloud F (or GMF 38.1-32.4a; Castelletti et al., 2007, 2011; Cardillo et al., 2014). It is then not clear if it is possible that these two sources are interacting, nevertheless, such a scenario would further this cloud as an interesting source for future studies.

3.8 Conclusions

This chapter has aimed at investigating the kinematic structures within a relatively quiescent massive IRDC: G034.43+00.24 (or Cloud F; e.g. Butler & Tan, 2009). To do so, we have acquired high-sensitivity, high spectral resolution maps of the $\text{C}^{18}\text{O}(1-0)$ and $\text{N}_2\text{H}^+(1-0)$ molecular line transitions taken with the IRAM-30m telescope. These lines were chosen as they are thought to trace the moderate to high-density gas within quiescent star-forming regions ($\sim 10^{3-5}\text{ cm}^{-3}$). Multiple velocity components are seen in the $\text{C}^{18}\text{O}(1-0)$ spectra at the majority of positions throughout the cloud. To separate and link these into coherent structures, we use semi-automated Gaussian line fitting and hierarchical clustering algorithms (SCOUSE and ACORNS; Henshaw et al., 2016b, in prep). Compared to moment and channel map analysis, which are typically used for kinematic studies, the use of these algorithms removes much of the subjectivity in identifying velocity structures, allowing for a reliable investigation into their properties.

We find four distinct coherent velocity components within Cloud F in $\text{C}^{18}\text{O}(1-0)$ emission, some of which are extended along the majority of the cloud ($\sim 4\text{ pc}$). We

compare the properties of these to the velocity components identified within a similar IRDC, G035.39-00.33 (Cloud H; e.g. [Butler & Tan, 2009](#)). We find that these share many similar properties, such as the components appear to be very dense (approximately $> 10^4 \text{ cm}^{-3}$, as inferred from the extended N_2H^+ emitting area), the components have mildly supersonic velocity dispersions, the components have a similar separation in velocity, and there is a significant (positive) velocity difference between similar components identified in C^{18}O and N_2H^+ emission. The latter two of these could hint at a common scenario of gentle filament merging, although this requires further investigation.

We investigate the large-scale kinematic structure surrounding Cloud F, by using the lower density tracer $^{13}\text{CO} (1 - 0)$ from the Galactic Ring Survey ([Jackson et al., 2006](#)). Several very extended ($> 10 \text{ pc}$) structures are identified throughout the GRS region, some of which may, in fact, be larger if not artificially split in velocity by optical depth effects. We find that the structures identified from the IRAM-30m observations are coincident with the central, brightest and most extended component in the GRS, suggesting that the IRDCs are the densest central parts of less dense, larger scale structures. We find that the structure identified here could be the Giant Molecular Filament 38.1-32.4a found by [Ragan et al. \(2014\)](#), which when taking the kinematic source distance places it as an “inter-arm cloud” (“spur” or “feather”) residing in-between the near and far Sagittarius arm.

Chapter 4

Star formation rates and efficiencies in the Galactic Centre

4.1 Preface

This chapter presents work which has been published by [Barnes et al. \(2017\)](#), which primarily makes use of the datasets from [Churchwell et al. \(2009\)](#), [Carey et al. \(2009\)](#) and [Molinari et al. \(2010\)](#). The data analysis and interpretation were conducted by A. T. Barnes. The initial draft of the publication was written by A. T. Barnes, who then incorporated comments from co-authors and an anonymous referee in the final draft.

4.2 Introduction

It has been previously mentioned that the inner few hundred parsecs of the Milky Way, known as the “Central Molecular Zone” (CMZ), contains an extreme environment compared to that typically seen within the Galactic disc (i.e. compared to the star-forming regions studied in the previous two chapters). However, it has been noted for several decades that despite harbouring a vast reservoir of dense gas, the CMZ appears to be underproducing stars with respect to nearby star-forming regions in the

disc (e.g. [Guesten & Downes, 1983](#); [Caswell et al., 1983](#); [Taylor, Morris & Schulman, 1993](#); [Longmore et al., 2013a](#); see [Figure 1.5](#)). Understanding this dearth of star formation has wider implications, as the extreme properties of the CMZ are similar to those observed in the centres of nearby galaxies, starburst galaxies, and high redshift galaxies at the epoch of peak star formation density at $z \sim 1 - 3$ ([Kruijssen & Longmore, 2013](#)).

There could be several possible explanations for the apparent lack of star formation within the Galactic Centre, which can be split into two categories. Either the low star formation rate is a result of observational bias or uncertainty, or is the product of a physical mechanism.

The first observational explanation, could be that the gas is less dense than commonly assumed, and therefore should not form stars at such a high rate. The gas density is a difficult quantity to determine, as inferences of the three-dimensional structure have to be made in order to convert two-dimensional line-of-sight column density measurements. The measured column density of hydrogen in the CMZ appears to be at least an order of magnitude higher than clouds within the disc ($> 10^{22} \text{ cm}^{-2}$; [Rathborne et al., 2014b](#); [Battersby et al. in prep](#)), implying an average gas volume density above $\sim 10^4 \text{ cm}^{-3}$. However, if the gas is more extended along the line of sight than in the plane of the sky, the density would be overestimated. Surveys using ATCA, APEX, and the SMA have shown that high critical density molecular gas tracers are widespread and spatially trace the peaks in column density (e.g. [Jones et al., 2012](#)). Additionally, these tracers have line of sight velocities which are consistent with being at the distance of the Galactic Centre ([Ginsburg et al., 2016](#); [Henshaw et al., 2016b](#); [Keto et al. in prep](#); [Battersby et al. in prep](#)). Recent radiative transfer modelling of the emission from dense molecular gas have shown that the gas has a density of the order $\sim 10^4 \text{ cm}^{-3}$ ([Armijos-Abendaño et al., 2015](#); [Ginsburg et al., 2016](#)). We conclude it is reasonable to assume that a significant fraction of the gas has a density $> 10^4 \text{ cm}^{-3}$, and therefore remove this as a potential explanation for the apparent dearth of star formation.

The second possible observational explanation for the apparent dearth in star formation

is that methods to determine the star formation rate have systematic differences when applied to the CMZ compared to other environments. Star formation rates within local clouds are primarily determined by counting the embedded young-stellar population (YSO counting; refer to Section 4.4.2.1). However, it is not possible to use this technique in external galaxies, as the individual sites of star formation cannot be resolved. Instead, the star formation rate is determined from integrated light measurements (e.g. infrared and free-free emission; refer to Sections 4.4.2.2 and 4.4.2.3). Our proximity to the centre of the Galaxy means that it is the only *extreme* environment in which comparison between YSO counting and integrated light measurement methods can be made. However, compared to the solar neighbourhood star-forming regions, the visual extinction is orders of magnitude higher (some positions have $A_V > 1000$ mag), and contamination from non-associated (e.g. bulge) stars are more of an issue. This could result in systematic uncertainties in the YSO counting method. Furthermore, as we observe the Galactic Centre through the disc of the Milky Way, contamination of sources along the line-of-sight may also be an issue for the integrated light methods. A combination of these systematic uncertainties could lead to unreliable star formation estimates from any given method.

The first physical explanation for the apparent lack of star formation within the Galactic Centre may be that star formation is episodic (Kruijssen et al., 2014). Krumholz & Kruijssen (2015) and Krumholz, Kruijssen & Crocker (2016) have modelled the dynamics of gas flows funnelled into the CMZ from large radii as acoustic instabilities within the bar's inner Lindblad resonance (Montenegro, Yuan & Elmegreen, 1999). In this model, when the gas reaches a radius of ~ 100 pc, and the rotation curve turns from flat to near-solid body, there is a decrease in shear which stops the inward flow and gas begins to accumulate. This accumulation of mass proceeds until the density is high enough for the gas to become gravitationally unstable, at which point there is an episode of intense star formation. The feedback from the recently formed high-mass stars then begins to drive turbulence and thereby increase the virial ratio of the gas, which quenches the star formation. Then as feedback from these stars fades, gas can again accumulate and the cycle repeats. The estimated cycle timescale for a

Milky Way-like galaxy is $\sim 10 - 20$ Myr. [Emsellem et al. \(2015\)](#) have conducted high-resolution, numerical simulations of the large scale gas motions within a galaxy similar to the Milky Way. These authors also find that gas is funnelled along the bar into the central ~ 100 pc, where transient star-forming complexes are observed, with timescales of a few Myr. [Torrey et al. \(2016\)](#) have tested the stability of feedback-regulated star formation for different environmental properties (e.g. ambient density, pressure) in the centres of galaxies. These authors find that a steady equilibrium state of star formation, where the energy input from feedback (which stops gravitational collapse) is balanced by the energy dissipation (which allows gravitational collapse), cannot be reached within the Galactic Centre, again requiring some degree of episodicity. [Suzuki et al. \(2015\)](#) also predict time-dependent flows, but these are instead driven via magnetic instabilities generated by differential rotation of the galaxy. Although these models and simulations differ in many aspects, the predicted trends in star formation activity are broadly similar in that they follow the scenario proposed by [Kruijssen et al. \(2014\)](#): gas steadily accumulates until a critical point is reached, when it becomes gravitationally unstable, collapses, and rapidly forms stars. Star formation continues until it is quenched by feedback, and the cycle restarts.

[Leroy et al. \(2013\)](#) selected a sample of 30 nearby galaxies from the HERACLES survey to study the distribution of gas and stars on scales of ~ 1 kpc. They find a ~ 1 dex scatter on the gas depletion time (i.e. the time taken for all the gas to be converted to stars at the current star formation rate) towards the central < 0.5 kpc of the galaxies within their sample. This is a ~ 0.3 dex increase when compared to similar measurements in the disc of the same galaxies. This could be suggestive that episodic star formation is not limited to the centre of the Milky Way, but is also present within centres of other galaxies.

The second physical explanation for the apparent lack of observed star formation may be that the comparison to the predictions from star formation models may need revision (see Section 4.4.3 for discussion). These models have been benchmarked against regions in the solar neighbourhood (see [Federrath & Klessen, 2012](#) and references within), so the predictions may not be directly applicable to extreme environments

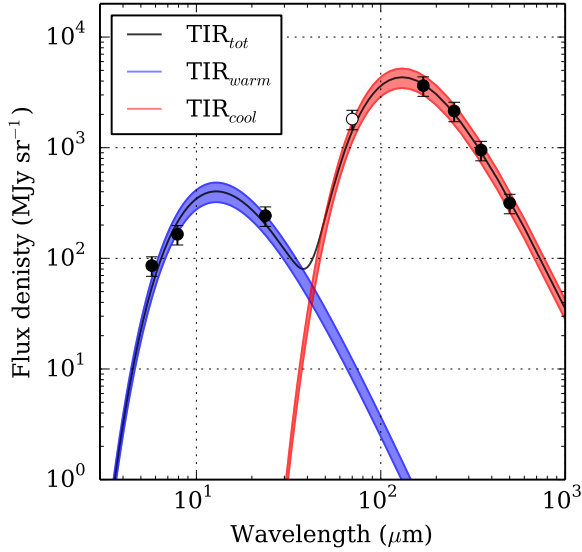


Figure 4.1: The average background subtracted spectral energy distribution for the $|l| < 1^\circ$, $|b| < 0.5^\circ$ region (see Figure 4.2). The points show the flux density for each wavelength (70 μm point is shown but is not used in the fitting), and the lines represent the warm component fit in dashed red (TIR_{warm}), the cool component in dashed blue (TIR_{cool}) and the total fit in solid black ($\text{TIR}_{\text{tot}} = \text{TIR}_{\text{warm}} + \text{TIR}_{\text{cool}}$). Error bars show the estimated ~ 20 per cent uncertainty on each point, and the shaded region represents the uncertainty on each fit.

(e.g. as is found in the Galactic Centre).

In this chapter we investigate the three outstanding (observational and physical) explanations for the low star formation rate observed within the Galactic Centre: 1) inconsistent star formation rate measurements, 2) episodic star formation, 3) inappropriate comparison to the predictions of theoretical star formation models. To do this, we use infrared luminosities to determine the star formation rate over global and local (cloud) scales, and compare these to existing measurements and predictions from star formation models.

4.3 Bolometric luminosity maps of the Galactic Centre

To create the infrared luminosity maps of the Galactic Centre needed to derive the star formation rates, we use *Spitzer* and *Herschel* telescope observations. The wavelengths and resolutions of these observations are presented in Table 4.1. To account for interstellar extinction, we adopt an average K-band extinction of $A_K \sim 2$ mag from Figer et al. (1999), Dutra et al. (2003) and Schödel et al. (2010), who determined the extinction for several objects within the CMZ region. This is applied to the 5.8 – 70 μm wavelength maps using the extinction relations presented by Chapman et al. (2009, see Table 4.1). To apply the extinction to the 70 – 500 μm emission, we use the ex-

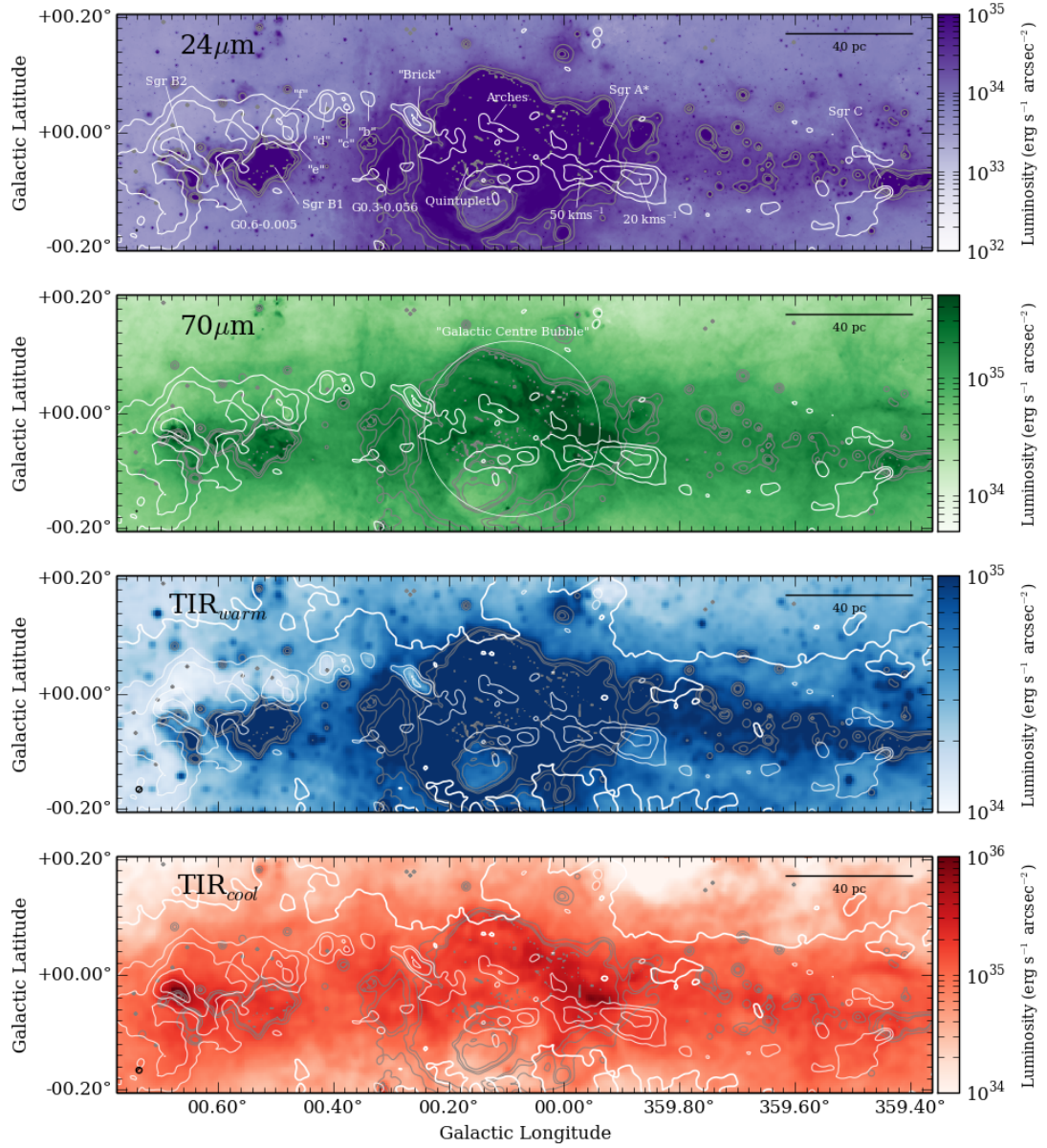


Figure 4.2: Maps of the extinction-corrected $24\ \mu\text{m}$ luminosity [upper panel, purple], $70\ \mu\text{m}$ luminosity [upper middle panel, green], and warm [lower middle panel, blue] and cool [lower panel, red] components of the bolometric luminosity. Overlaid are the warm component column density contours in grey of $N^{\text{warm}}(\text{H}_2) = [1, 1.9, 2.6] \times 10^{17}\ \text{cm}^{-2}$, and cool component contours in white of $N^{\text{cool}}(\text{H}_2) = [5, 10, 24, 75] \times 10^{22}\ \text{cm}^{-2}$. These contours levels are used to define the various sources (see Table 4.5). The thick white contour shown in the lower two panels is of $N^{\text{cool}}(\text{H}_2) = 1 \times 10^{22}\ \text{cm}^{-2}$. This contour highlights the widespread distribution of the cool column density component, which dominates the total column density $N(\text{H}_2) = N^{\text{warm}}(\text{H}_2) + N^{\text{cool}}(\text{H}_2)$. The $24\ \mu\text{m}$ luminosity map [upper panel] has several sources labeled, and the $70\ \mu\text{m}$ map has the “Galactic Centre Bubble” shown [upper middle panel; e.g. [Bally et al., 2010](#)]. Each panel has a scale bar located in the top right which represents 40 pc at a distance of $\sim 8.5\ \text{kpc}$ ([Reid et al., 2014](#)) and a circle in the bottom left which represents the beam size of the observations.

Table 4.1: Summary of survey data. Columns show the wavelength of the band, the beam full width at half maximum (FWHM), the image pixel size, the extinction with respect to the K-band, and the survey from which the observations were taken.

Band (μm)	FWHM ($''$)	R_{pix} ($''$)	A_{λ}/A_{K}	Survey
5.8	2	1.2	0.44^a	GLIMPSE ^c
8	2	1.2	0.43^a	GLIMPSE ^c
24	6	2.4	0.61^a	MIPSGAL ^d
70	5	3.2	0.06^b	Hi-GAL ^e
160	11	4.5	...	Hi-GAL ^e
250	18	6.0	...	Hi-GAL ^e
350	25	8.0	...	Hi-GAL ^e
500	36	11.5	...	Hi-GAL ^e

^a Relations taken directly from [Chapman et al. \(2009\)](#).

^b Calculated using conversion from [Suutarinen et al. \(2013\)](#).

^c The *Spitzer* GLIMPSE is presented by [Churchwell et al. \(2009\)](#).

^d The *Spitzer* MIPS GAL survey is presented by [Carey et al. \(2009\)](#).

^e The *Herschel* Hi-GAL survey is presented by [Molinari et al. \(2010\)](#).

extinction relation $A_{\lambda}/A_{\text{K}} \sim 0.0042 (250/\lambda [\mu\text{m}])^2$ ([Suutarinen et al., 2013](#)). From this, the 70 μm luminosity is corrected by $A_{70\mu\text{m}} = 0.06$ mag, whilst for wavelengths larger than 70 μm the correction is negligible. To remove the background emission from the 70–500 μm data, we follow the method outlined by [Battersby et al. \(2011\)](#), background removal of these data will be presented by [Battersby et al. in prep](#)).

Figure 4.1 displays the extinction corrected average spectral energy distribution for an example region ($|l| < 1^\circ$, $|b| < 0.5^\circ$). This shows that the Galactic Centre shows two distinct temperature components. The first peaks at wavelengths $\sim 100 - 200 \mu\text{m}$, and is thought to originate from the cool dust ($T \sim 30 \text{ K}$). The second peaks at $\sim 10 \mu\text{m}$ ($T \sim 300 \text{ K}$), and becomes prominent towards known star-forming regions, and originates from warm dust. To measure the total column density of hydrogen, the dust temperatures and the total bolometric luminosity, we fit a two component modified Planck function to the spectral energy distribution at each pixel (after smoothing all wavelengths to the largest resolution of $\sim 36''$). Expanding upon equation 1.6, the observed flux-density, S_{ν} , from a source, assuming no background contribution, is given as,

$$S_{\nu} = I_{\nu} \Delta\Omega = \frac{2h\nu^3}{c^2} \frac{1}{\exp(h\nu/k_{\text{B}}T) - 1} [1 - \exp(-\tau_{\nu})] \Delta\Omega, \quad (4.1)$$

where $\Delta\Omega$ is the solid angle subtended by the source. The opacity is defined as (see Section 1.1.1.2),

$$\tau_\nu = \Sigma\kappa_\nu = \mu_{\text{H}_2}m_{\text{H}}\kappa_\nu N(\text{H}_2). \quad (4.2)$$

We assume a mean molecular weight of $\mu_{\text{H}_2} = 2.8$ a.m.u (see [Kauffmann et al., 2008](#) appendix), a dust opacity of $\kappa_\nu = \kappa(\nu/\nu_0)^\beta$ at $\nu = 505$ GHz with a $\kappa_0 = 4.0$ and $\beta = 1.75$ ([Battersby et al., 2011](#)), and a constant gas-to-dust ratio of 100.

To separate the two temperature components, we consider wavelengths between 5.8 - 24 μm for the warm component, and 160 - 500 μm for the cool component (cool component is provided by [Battersby et al. in prep](#)). We do not consider *Spitzer* data with wavelengths shorter than 5.8 μm when fitting the spectral energy distribution, as it is not clear how much flux at these wavelengths is from recently formed stars or the older stellar population in the bulge of the Galaxy. Overlaid on Figure 4.1 are the average warm (TIR_{warm}) and cool component (TIR_{cool}) fits, and the total fit ($\text{TIR}_{\text{tot}} = \text{TIR}_{\text{warm}} + \text{TIR}_{\text{cool}}$).

The shaded region for the average fits represents the instrumental uncertainty, which has been estimated as a conservative ~ 20 per cent on the flux density measurements. However, we expect the absolute uncertainty to be higher than this, due to variations in the dust properties across the region. For example, several authors have shown that there is a gradient of decreasing gas-to-dust ratio with decreasing galactocentric radius ([Schlegel, Finkbeiner & Davis, 1998](#); [Watson, 2011](#)), a trend which has also been observed in several other star-forming galaxies ([Sandstrom et al., 2013](#)). Assuming that the gas-to-dust ratio is inversely proportional to the metallicity, the gas-to-dust ratio within the central kpc of the Galaxy would be ~ 50 (e.g. [Sodroski et al., 1995](#)), which would cause the column densities, and gas mass measurements later in this work (see Section 4.5), to be a factor of two lower. Given this, we estimate the absolute column density measurements should be reliable to within a factor of two.

The flux-densities, S_ν , are converted into fluxes, S (in units of MJy sr^{-1}), by integrating the two component modified black body at each position. To convert these into luminosities (units of erg s^{-1} or L_\odot) requires an accurate measurement of the source

distance. This analysis, therefore, has been restricted to the $|l| < 1^\circ$, $|b| < 0.5^\circ$ region, as parallax measurements (Reid et al., 2009, 2014) and modelling (Molinari et al., 2011; Kruijssen, Dale & Longmore, 2015) have shown that the majority of the dense molecular gas and star-forming regions are close to the Galactic Centre. Additionally, the extreme environment within this region has many identifiable features (e.g. large velocity dispersion), which have been used to show that there is little contamination from non-associated material along the line-of-sight (e.g. Henshaw et al., 2016b). We are, therefore, confident with the distance measurement to the $|l| < 1^\circ$, $|b| < 0.5^\circ$ region of 8.34 ± 0.16 kpc (Reid et al., 2014). The integrated flux, S (MJy sr⁻¹), is converted to luminosity, L (erg s⁻¹), with the units shown in parenthesis using,

$$L(\text{erg s}^{-1}) = 2.8 \times 10^{10} S(\text{MJy sr}^{-1}) R_{\text{pix}}^2(") D^2(\text{pc}), \quad (4.3)$$

where R_{pix} is the pixel size and D is the distance to the region. Figure 4.2 presents the 24 μm , 70 μm , and the warm and cool component bolometric luminosity maps (TIR_{warm} and TIR_{cool} , respectively) for the $|l| < 1^\circ$, $|b| < 0.5^\circ$ region. Over-plotted are grey and white contours of the warm and cool gas column densities, respectively. Labels shows the positions of the main objects of interest. Figure 4.3 shows how the normalised luminosities for these components vary as a function of galactic longitude for the region $|l| < 1^\circ$, $|b| < 0.5^\circ$.

The total luminosities within $|l| < 1^\circ$, $|b| < 0.5^\circ$ are:

$$L(24 \mu\text{m}) = 9.4 \pm 1.9 \times 10^7 L_\odot,$$

$$L(70 \mu\text{m}) = 3.4 \pm 0.7 \times 10^8 L_\odot,$$

$$L(\text{TIR}_{\text{warm}}) = 2.8 \times 10^8 L_\odot,$$

$$L(\text{TIR}_{\text{cool}}) = 2.9 \times 10^8 L_\odot,$$

$$L(\text{TIR}_{\text{tot}}) = 5.7 \pm 1.7 \times 10^8 L_\odot.$$

Table 4.2 displays the infrared luminosities and the fractions of the total luminosity across the $|l| < 1^\circ$, $|b| < 0.5^\circ$ region, for several specific sources of interest that are

Table 4.2: Luminosities, and the fractions of the total luminosity across the $|l| < 1^\circ$, $|b| < 0.5^\circ$ region ($5.7 \times 10^8 L_\odot$), for the sources which have not be previously noted (see Figure 4.2).

Source	$L(\text{TIR}_{tot})$ (L_\odot)	Fraction of total (TIR_{tot}) within $ l < 1^\circ$, $ b < 0.5^\circ$ (per cent)
“Galactic Centre Bubble”	8.9×10^7	20
Sgr A*	3.6×10^6	0.6
Sgr C	3.1×10^6	0.5
Arches cluster	2.7×10^5	0.05
Quintuplet cluster	2.5×10^5	0.04

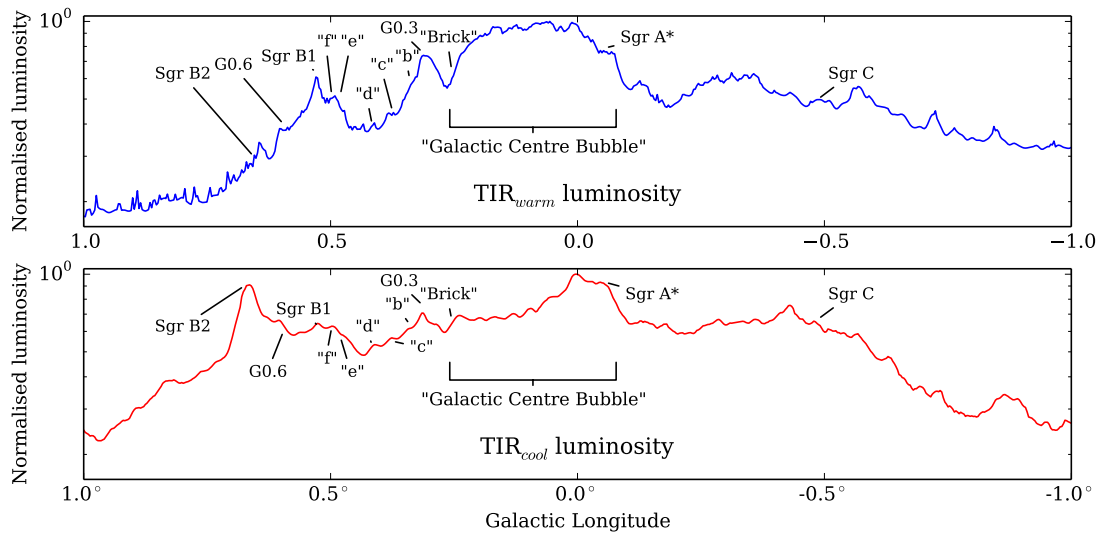


Figure 4.3: Plots the warm [upper panel, blue] and cool [lower panel, red] component luminosities as a function of galactic longitude. Positions of sources interest are shown, see Figure 4.2.

highlighted on Figure 4.2).

Throughout this work, we make the standard assumption that all the emission from the embedded stellar population is reprocessed by the surrounding dust to infrared wavelengths, which is emitted at much shorter wavelengths at the interface where the dust becomes optically thin. In this scenario, the total infrared luminosity directly corresponds to the bolometric luminosity produced by the embedded population. We estimate the measurement uncertainty on the total bolometric luminosity as the maximum variation after changing the flux densities at each wavelength by ± 20 per cent (an upper limit estimate of the flux uncertainties) and re-fitting the spectral energy distribution. These uncertainties are, however, small when compared to the systematic uncertainties, for example: i) leakage of high-energy photons (in which case the in-

frared luminosity is not equal to the total bolometric luminosity), ii) heating of dust via other sources, and iii) emission produced from the older embedded population within the CMZ (e.g. Calzetti et al., 2010). It is difficult to estimate the amount of energy leakage, as this requires an accurate description of the three-dimensional density structure of the individual star-forming regions. Similarly, for the dust heating from other sources, such as from the central super massive black hole (Sgr A*), it is difficult to estimate given our limited knowledge of the radiation field within this region. However, an estimate of the contribution from the older embedded population can be made using the Besançon model (Robin et al., 2003). To estimate the expected bolometric luminosity from the field stellar population we use the online¹ catalogue simulation, which includes all the stellar luminosity classes and ages. Within the region $|l| < 1^\circ$, $|b| < 0.5^\circ$, taking all stars with a distance between 8.4 – 8.6 kpc (i.e. forming a $\sim 200 \times 100 \times 200$ pc box containing the CMZ), we find that the total bolometric luminosity from the population older than 0.15 Gyr is $\sim 2.5 \times 10^8 L_\odot$.²

The Robin et al. (2003) bulge population luminosity of $\sim 2.5 \times 10^8 L_\odot$ is similar to that determined by Launhardt, Zylka & Mezger (2002, see their Table 6, $1.9 \times 10^8 L_\odot$), from 2.2 – 240 μm IRAS and COBE data. The Robin et al. (2003) and Launhardt, Zylka & Mezger (2002) estimates are around half of the total measured luminosity we find within $|l| < 1^\circ$, $|b| < 0.5^\circ$ ($5.7 \pm 1.7 \times 10^8 L_\odot$). However, the spectral energy distribution of old stars will peak at wavelengths $< 5 \mu\text{m}$. To estimate the direct contribution of the old stellar population to the infrared luminosity in the wavelength range between 5.8 – 500 μm we integrate the black-body spectral energy distribution with the average effective temperature of all stars from the Robin et al. (2003) stellar population model (~ 3000 K). We find that the fraction of the luminosity produced by these stars emitted between 5.8 – 500 μm is ~ 3 per cent. This suggests that approximately $\sim 1 - 2$ per cent of the total infrared luminosity within $|l| < 1^\circ$, $|b| < 0.5^\circ$ is directly produced by the old bulge star population. We, therefore, do not remove this contribution from the luminosity and conclude the bolometric luminosity between 5.8 – 500 μm is dominated

¹<http://model.obs-besancon.fr>

²We note that Robin et al. (2003) do not fit the model to the observed stellar density within $|l| < 1^\circ$. Rather the stellar densities are predicted by extrapolating a power-law, from the DENIS survey within $-8^\circ < l < 12^\circ$, $|b| < 4^\circ$ (see Epchtein et al., 1997).

by the emission from young stars.

4.4 Global (~ 100 pc) scale star formation

4.4.1 Determining the global star formation rate

In order to estimate the total star formation rate across the CMZ, we apply several infrared luminosity-to-star formation rate (luminosity-SFR) relations to the bolometric and monochromatic infrared luminosities (see [Kennicutt & Evans, 2012](#) and references therein). These relations are based on the assumption that high-mass “young stellar objects” (YSOs) classified as having ages in the range $\sim 0.1 - 5$ Myr (see Section 4.4.2), are still heavily embedded within their parent molecular clouds when they first reach the zero age main sequence (ZAMS). Therefore, the majority of their prodigious short wavelength (e.g. ultra-violet) emission is absorbed by dust within their surrounding medium, and re-emitted at longer infrared wavelengths ($\sim 1 - 1000$ μm). Hence, the infrared luminosity can be used, similar to a calorimeter, to estimate the underlying embedded population. Given that high-mass stars have a characteristic age of a few Myr, the star formation rate can then be estimated. One advantage of this method is that it does not require the individual sites of star formation to be resolved (< 0.05 pc). By using the integrated luminosity of an entire stellar population, over scales of > 100 pc, the luminosity-SFR relations can be used to determine the star formation rates within extragalactic sources for which it is impossible to resolve individual forming stars. A sample of the most widely used monochromatic and bolometric luminosity-SFR relations are summarised in Table 4.3, with the luminosity limits over which they are considered to be reliable. Table 4.3 also shows the global star formation rates within the region $|l| < 1^\circ$, $|b| < 0.5^\circ$ derived using these relations. We find that the average star formation rates derived from the 24 μm , 70 μm , and TIR luminosities are 0.09 ± 0.02 , 0.10 ± 0.02 , and $0.09 \pm 0.03 M_\odot \text{ yr}^{-1}$, respectively. The uncertainties shown here are from the measurement uncertainties on the luminosity (see Section 4.3). We note, however, that the systematic uncertainty on the luminosities are significantly larger, and

the luminosity-SFR relations have an uncertainty of around a factor two. Taking these uncertainties into account, we estimate that the measured star formation rates are reliable to within a factor of two. Hence the average global star formation rate within the $|l| < 1^\circ$, $|b| < 0.5^\circ$ region derived from the luminosity-SFR relations has a mean of $0.09 \pm 0.02 M_\odot \text{ yr}^{-1}$.

4.4.2 Comparison to star formation rates within the literature

In this section, we discuss the methods which have been previously used to determine the total star formation rate within the Galactic Centre, and compare to the values determined in Section 4.4.1.

4.4.2.1 YSO counting

The first method uses infrared emission to measure the masses of individual high-mass YSOs (ages $\sim 0.1 - 1$ Myr; $M > 10 M_\odot$). As previously mentioned, high-mass stars reach the ZAMS whilst they are still heavily embedded within their parent molecular cloud (and are most likely still accreting material). They inject a significant amount of energy into their surrounding environment, and can therefore be identified from their strong, compact near/mid infrared emission. Once identified, their masses can be estimated from their bolometric luminosity. The total embedded stellar population mass of a region can then be inferred by extrapolating the stellar initial mass function down to lower masses assuming an appropriate initial mass function (IMF). Using this method, [Yusef-Zadeh et al. \(2009\)](#) identified potential YSOs as sources which show excess $24 \mu\text{m}$ emission with respect to $8 \mu\text{m}$ emission within the region $|l| < 1.3^\circ$, $|b| < 0.17^\circ$. By modelling the spectral energy distributions, they distinguish which are the young sources, and measure their luminosities to estimate the masses. They find the total embedded stellar population after IMF extrapolation is $\sim 1.4 \times 10^4 M_\odot$. These authors assume a YSO lifetime of 0.1 Myr, which they use to estimate a global star formation rate of $\sim 0.14 M_\odot \text{ yr}^{-1}$ ($|l| < 1.3^\circ$, $|b| < 0.17^\circ$).

Table 4.3: Summary of various SFR conversion factors. Columns show the wavelengths to which the conversions apply, the conversion reference, the conversion factors (where $L(\lambda)$ is the luminosity at wavelength λ), the reliability limits, and the calculated star formation rate within within $|l| < 1^\circ$, $|b| < 0.5^\circ$.

Wavelengths for conversion (μm)	Conversion ($\text{erg s}^{-1} M_\odot^{-1} \text{ yr}$)	Luminosity range ^a (erg s^{-1})	Reference for conversion	SFR within $ l < 1^\circ$, $ b < 0.5^\circ$ ($M_\odot \text{ yr}^{-1}$)
24	$2.75 \times 10^{-43} L(24 \mu\text{m})$	$(0.01 - 1) \times 10^{44}$	Wu et al. (2005)	0.10
	$2.46 \times 10^{-43} L(24 \mu\text{m})$	$(0.004 - 2) \times 10^{44}$	Zhu et al. (2008)	0.09
	$2.04 \times 10^{-43} L(24 \mu\text{m})$	$(0.4 - 5) \times 10^{43}$	Rieke et al. (2009)	0.07^b
	$9.01 \times 10^{-34} L(24 \mu\text{m})^{0.768}$	$(0.001 - 3) \times 10^{41}$	Pérez-González et al. (2006)	0.07
	$5.83 \times 10^{-38} L(24 \mu\text{m})^{0.871}$	$(0.0001 - 3) \times 10^{44}$	Alonso-Herrero et al. (2006)	0.09
	$1.31 \times 10^{-38} L(24 \mu\text{m})^{0.885}$	$(0.0001 - 3) \times 10^{44}$	Calzetti et al. (2007)	0.08
	$5.66 \times 10^{-36} L(24 \mu\text{m})^{0.826}$	$(0.000001 - 3) \times 10^{44}$	Relaño et al. (2007)	0.12
70	$5.88 \times 10^{-44} L(70 \mu\text{m})$	$> 1.4 \times 10^{42}$	Calzetti et al. (2010)	0.07
	$9.37 \times 10^{-44} L(70 \mu\text{m})$	$(0.005 - 5) \times 10^{43}$	Li et al. (2010)	0.12
	$9.70 \times 10^{-44} L(70 \mu\text{m})$...	Lawton et al. (2010)	0.12
TIR	$4.50 \times 10^{-44} L(\text{TIR})$...	Kennicutt (1998a)	0.10^c
	$3.88 \times 10^{-44} L(\text{TIR})$	$(0.02 - 2) \times 10^{43}$	Murphy et al. (2011)	0.09

^a Note, most of the authors do not specify a luminosity range of the validity of the SFR conversion. Therefore, following Calzetti et al. (2010), we define the luminosity range as the limits of the sample in each work.

^b Yusef-Zadeh et al. (2009) estimate a star formation rate of $0.07 M_\odot \text{ yr}^{-1}$, using this conversion with a $24 \mu\text{m}$ luminosity over an area of $|l| < 1.3^\circ$, $|b| < 0.17^\circ$.

^c Crocker et al. (2011) estimate a star formation rate of $0.08 M_\odot \text{ yr}^{-1}$, using this conversion with a bolometric luminosity found from $2.2 - 240 \mu\text{m}$ IRAS data.

There are several inherent difficulties with the YSO counting method. For example, it is not trivial to determine the YSO ages from either the infrared excess, or the spectral energy distributions. Furthermore, dusty, bright, asymptotic giant branch stars are also known to emit at infrared wavelengths with similar colours to YSOs (Habing, 1996). Therefore, YSO identification can be plagued with source contamination. In light of this, Koepferl et al. (2015) re-examined the Yusef-Zadeh et al. (2009) YSO sample, comparing in-depth radiative transfer modelling of both embedded YSOs and embedded older main sequence stars (ages of > 1 Myr). These authors conclude the Yusef-Zadeh et al. (2009) sample suffers from significant contamination from embedded main sequence stars (which produce very similar emission profiles within the wavelengths used by Yusef-Zadeh et al., 2009). They propose the star formation rate is factors of several lower: $\sim 0.06 M_{\odot} \text{ yr}^{-1}$. Immer et al. (2012b) used infrared spectral features to attempt to disentangle the young and more evolved stars. These authors initially identified candidate YSOs as compact sources with excess $7\mu\text{m}/15\mu\text{m}$ emission, which are verified by examining the infrared spectral features of a test sample. Within $|l| < 1.5^{\circ}$, $|b| < 0.5^{\circ}$, Immer et al. (2012b) estimate a total embedded stellar population mass of $\sim 7.7 \times 10^4 M_{\odot}$. Given the slightly different selection criteria used by Immer et al. (2012b), these authors assume a longer YSO lifetime of ~ 1 Myr compared to Yusef-Zadeh et al. (2009) and Koepferl et al. (2015), yet calculate a comparable average SFR of $\sim 0.08 M_{\odot} \text{ yr}^{-1}$.

4.4.2.2 Free-free emission

The second method to determine star formation rates involves using cm-(mm)-continuum emission to measure the mass of the YSO population. Along with heating the surrounding environment, YSOs with ages of ~ 3 Myr and masses $> 8 - 10 M_{\odot}$ emit a significant amount of high-energy ionising radiation (i.e. photons with $h\nu > 13.6 \text{ eV}$), which produces H II regions. The free-free emission from the ionised gas (i.e. bremsstrahlung radiation) can be observed at cm-wavelengths, when the medium is optically thin. Cm-continuum emission observations, therefore, provide a reliable way to determine the rate at which ionising photons are produced from massive stars

within a region, which in turn can be used to estimate their mass. The total embedded stellar population can then be extrapolated using an IMF, from which the star formation rate can be estimated (e.g. Murray & Rahman, 2010). Lee, Murray & Rahman (2012) used *Wilkinson Microwave Anisotropy Probe* (*WMAP*) continuum observations at wavelengths of $\sim 3 - 150$ mm, to identify and measure sources of free-free emission within the Milky Way. Longmore et al. (2013a) used this catalogue and the free-free-to-SFR conversion presented by Murray & Rahman (2010), to estimate a global star formation rate of $\sim 0.06 M_{\odot} \text{ yr}^{-1}$ within the region $|l| < 1^{\circ}$, $|b| < 0.5^{\circ}$ (the same region adopted by this work).

4.4.2.3 Infrared luminosities

The third method to estimate star formation rates involves using the bulk infrared emission and the luminosity-SFR relations. This method follows a similar basis to the YSO counting method, where the near/mid infrared dust emission is modelled to determine the embedded population. The key difference is that the luminosity-SFR relations use the integrated emission from entire stellar populations, hence sample star formation rates over larger times, which usually translates to larger spatial scales, than to YSOs counting (see Table 4.4).

Launhardt, Zylka & Mezger (2002) fit the spectral energy distribution of $2.2 - 240 \mu\text{m}$ *IRAS* and *COBE* data, and estimate the total infrared bolometric luminosity within $|l| < 0.8^{\circ}$, $|b| < 0.3^{\circ}$ is $L(\text{TIR}_{\text{tot}}) = 4.2 \times 10^8 L_{\odot}$. Crocker et al. (2011) use this, with the relation of Kennicutt (1998a, see Table 4.3) to calculate a SFR of $\sim 0.08 M_{\odot} \text{ yr}^{-1}$. Yusef-Zadeh et al. (2009) have used the $24 \mu\text{m}$ monochromatic luminosity from *Spitzer*, of $L(24 \mu\text{m}) = 9 \times 10^7 L_{\odot}$ within $|l| < 1.3^{\circ}$, $|b| < 0.17^{\circ}$, with the luminosity-SFR relation presented by Rieke et al. (2009, also see Table 4.3), to estimate a star formation rate of $\sim 0.07 M_{\odot} \text{ yr}^{-1}$.

4.4.2.4 Comparison of star formation rates

In Table 4.4 we tabulate the measurements of the star formation rate within the Galactic Centre. Apart from the YSO counting measurement of Yusef-Zadeh et al. (2009)³, we find agreement to within ~ 35 per cent between the various measurements. To attempt a fairer comparison between these star formation rates and those found in this work, we re-determine the star formation rates within the areas adopted by the works listed in Table 4.4, when using the total bolometric luminosity and using a single luminosity-SFR relation (Kennicutt, 1998a). These measurements are shown in Table 4.4. As the total bolometric luminosity measurements are self-consistent, they exclusively reflect the effect of changing the considered area. Given this, we can conclude that there is no systematic uncertainty in any one measurement method which is causing an underestimation of the star formation rate.

4.4.3 Comparison to star formation rates predicted from theoretical models

Given that we now have a set of consistent measurements for the global star formation rate within the Galactic Centre, comparison can be made to different star formation theories within the literature (as outlined in Section 1.4). Previously, Longmore et al. (2013a) used two models to determine the predicted global star formation rate within the CMZ ($|l| < 1^\circ$, $|b| < 0.5^\circ$): the column density threshold relation of Lada, Lombardi & Alves (2010), and the model of Krumholz, Dekel & McKee (2012), which is an evolution of the Krumholz & McKee (2005) model. For the column density limit model, they estimate that ~ 95 per cent of the gas within the CMZ lies above the threshold for collapse, which gives a predicted star formation rate of $0.78 M_\odot \text{ yr}^{-1}$. For the volumetric model, they then calculate the volume density by assuming that the gas at $|l| < 1^\circ$ deg is distributed in a ring-like stream with a radius of ~ 100 pc (Molinari et al., 2011). This structure has a mass of $1.8 \pm 0.9 \times 10^7 M_\odot$, which gives a predicted star formation

³This likely suffers from contamination, see Section 4.4.2.1.

Table 4.4: Summary of star formation rate measurements within the literature. Shown is the measurement method, the characteristic age range traced by the method, the CMZ area over which the star formation rate has been measured, the measured star formation rate, the star formation rate determined using the infrared bolometric luminosity within the different areas of the CMZ and the luminosity-star formation-rate relation from (Kennicutt, 1998a).

Method used to determine the SFR	Characteristic age probed by method (Myr)	Area of CMZ over which the SFR is calculated	SFR determined from the corresponding method and area ($M_{\odot} \text{ yr}^{-1}$)	SFR determined using the infrared bolometric luminosity with the Kennicutt (1998a) relation from the corresponding area ($M_{\odot} \text{ yr}^{-1}$)
YSO counting	~ 0.1	$ l < 1.3^{\circ}, b < 0.17^{\circ}$	0.14^b	0.07
YSO counting	~ 0.1	$ l < 1.3^{\circ}, b < 0.17^{\circ}$	0.06^c	0.07
Infrared luminosities	0-5-100 ^a	$ l < 1.3^{\circ}, b < 0.17^{\circ}$	0.07^b	0.07
Infrared luminosities	0-5-100 ^a	$ l < 0.8^{\circ}, b < 0.3^{\circ}$	0.08^d	0.07
YSO counting	~ 1	$ l < 1.5^{\circ}, b < 0.5^{\circ}$	0.08^e	0.12
free-free emission	$\sim 0.3-10^a$	$ l < 1^{\circ}, b < 0.5^{\circ}$	0.06^f	0.10

^a The second number indicates the mean age of the stellar population contributing to the emission, the third number shows the age below which 90 per cent of emission is contributed (Kennicutt & Evans, 2012).

^b Yusef-Zadeh et al. (2009).

^c Koepferl et al. (2015).

^d Crocker et al. (2011).

^e Immer et al. (2012b).

^g Longmore et al. (2013a).

rate of $0.4 \pm 0.2 M_{\odot} \text{ yr}^{-1}$. These predictions are significantly higher than the average observed star formation rate of $\sim 0.09 M_{\odot} \text{ yr}^{-1}$. Table 4.4 shows the conclusion of Longmore et al. (2013a) holds no matter which method is used to determine the star formation rate.

4.4.4 Implications for the global star formation rate

In summary, we find that the star formation rates for the CMZ measured from the infrared luminosity, YSO counting, and free-free emission have a mean value across all measurements of $0.09 \pm 0.02 M_{\odot} \text{ yr}^{-1}$, given their uncertainties are in agreement to within around a factor two. Furthermore, in agreement with the conclusion of Longmore et al. (2013a), we find that this is factors of a few to more than an order of magnitude smaller than is predicted from star formation models. In Section 4.2 we speculated three possible causes for this apparent dearth in star formation within the Galactic Centre: 1) inaccurate star formation rate measurements, 2) episodic star formation, or 3) inappropriate comparison to the predictions from star formation relations/models. The results found in this section have shown:

- i) The star formation rates determined from the infrared luminosity-SFR relations are within a factor two of previous measurements. This allows us to rule out that systematic uncertainties in the measurements are causing the apparent low star formation rate, unless this uncertainty affects all the methods in the same way, which seems unlikely.
- ii) The luminosity-SFR relations, which use the integrated light from the whole stellar population, and YSO counting methods, which require the sites of star formation to be resolved, are consistent in the Galactic Centre. As the Galactic Centre is the most extreme environment for which it is possible to resolve individual forming stars and make this measurement, the results here provide confidence that the luminosity-SFR relations reliably trace the star formation rate over kpc scales within similar environments present in starburst galaxies, and high-redshift galaxies.

- iii) The various methods to determine the star formation rates are in agreement, despite being sensitive to star formation over different time scales over the past few Myr. Therefore, the global star formation rate has not changed over this time by more than a factor of two to three of its current rate. This is consistent with recent theoretical models predicting that the star formation rate in the CMZ is episodic on a timescale of $\sim 10 - 20$ Myr, much longer than the mean timescales covered by the adopted star formation rate tracers of $\sim 0.1 - 5$ Myr.

Returning to the discussion in the introduction, we have ruled out the first of the possibilities for the apparent low star formation rate within the Galactic Centre, that it results from inaccurate star formation rate measurements. Furthermore, in agreement with recent theoretical work, we find that the Galactic Centre could be in a low point in a star formation cycle. [Kruijssen et al. \(2014\)](#) have suggested that the majority of gas within the CMZ is not bound by self-gravity, rather it is bound by the potential produced from the embedded bulge stars. Therefore, despite the gas being very dense, it will not gravitationally collapse to form stars as it would in the Galactic disc, and the CMZ is therefore at a star formation minimum. This idea has been quantified further by [Krumholz & Kruijssen \(2015\)](#) and [Krumholz, Kruijssen & Crocker \(2016\)](#), who predict that significant star formation should take place once the gas becomes self-gravitating. To investigate this, we examine the star formation rates on parsec scales (rather than global scales) within molecular clouds and star formation regions which are believed to be bound by self-gravity.

4.5 Local (~ 1 pc) scale star formation

4.5.1 Determining the gas and embedded stellar masses from infrared observations

It is clear from [Figure 4.2](#) that the luminosity in the Galactic Centre varies significantly over scales as little as a few parsecs, implying that the instantaneously measured lo-

cal star formation rate and efficiency also vary over similar scales. However, as the individual clouds only harbour specific stages of star formation, we can not apply the SFR-luminosity relations, as these require continuous star formation over $\gg 5$ Myr (Kruijssen & Longmore, 2014). In this section we therefore propose an alternative method to measure the embedded stellar masses, which will be used in the following sections to estimate the star formation rate.

Firstly, the individual clouds which are believed to be bound by self-gravity are identified, and their boundaries are determined. Next, we measure the enclosed infrared bolometric luminosity. This is used to estimate the mass of the most massive star, from which the total embedded population can be extrapolated using a stellar initial mass function. We choose to limit the sources to those within the region $0.18 < l < 0.76^\circ$, $-0.12 < b < 0.13^\circ$, as this region has both significant cool and warm gas emission, and is known to contain both quiescent (the so called “dust-ridge”) and actively star-forming regions (e.g. Sgr B2), whilst not suffering significant line-of-sight confusion from prominent sources within the Galactic Centre (e.g. Sgr A*). Despite being limited to this “simple” region of the Galactic Centre, a certain level of ambiguity is present when identifying the extent for the sources. The interstellar medium is intrinsically hierarchical and the three-dimensional structure of the gas within the Galactic Centre is complex (e.g. Rathborne et al., 2015; Walker et al., 2015; Henshaw et al., 2016b; see Section 4.5.3.1). It is therefore difficult to impose physically meaningful cloud boundaries in the same way one can separate individual stars.

We define the boundaries using various warm and cool column density contours (see Figure 4.2), which have been chosen by-eye to best separate different sources. The column density limits, radii and enclosed gas masses for each source is displayed in Table 4.5. These masses are within a factor of two to those presented by Immer et al. (2012a), Longmore et al. (2012), Walker et al. (2015) and Federrath et al. (2016). The moderate difference is a result of our higher column density boundaries. We investigate the effect of changing the source boundaries in Section 4.5.3, and show that this does not affect the results of this work.

To estimate the embedded population within each cloud, we first assume that the total infrared luminosity represents the bolometric luminosity from a single massive embedded star. This is a reasonable assumption since the most massive star should dominate the luminosity of a simple stellar population ($M \propto L^x$, where $x \sim 1 - 3.5$; e.g. Mould, 1982; Salaris & Cassisi, 2005). To estimate the mass of this embedded object ($M_{*,\max}$), we adopt the bolometric luminosity-mass conversions presented by Davies et al. (2011). The total embedded population mass ($M_{*,\text{tot}}$), is extrapolated by solving the following two equations (see Section 1.2.3):

$$1 = \int_{M_{*,\max}}^{\infty} m^{-\alpha} dm, \quad (4.4)$$

where $\alpha = 2.3$, and,

$$M_{*,\text{tot}} = \int_{0.001 M_{\odot}}^{\infty} m^{1-\alpha} dm, \quad (4.5)$$

where $\alpha = 0.3$ for $0.001 < m/M_{\odot} < 0.08$, $\alpha = 1.3$ for $0.08 < m/M_{\odot} < 0.5$, and $\alpha = 2.3$ for $m > 0.5 M_{\odot}$ (Kroupa, 2001). Figure 4.4 presents a red-green-blue map of the region containing the sources, where the quiescent clouds are in red and proto-clusters in blue, over which the embedded and gas masses are labeled. The calculated masses are summarised in Table 4.5, which are used to determine star formation rates and efficiencies in Section 4.5.4.

4.5.2 Determining the embedded stellar masses from additional observations

In addition to measurements from infrared observations, the embedded stellar mass can be inferred from cm/mm wavelengths observations. Walker et al. (2015) have determined the embedded stellar mass within the Sgr B2 region which encompasses the Sgr B2 “main”, “north” and “south” H II region complexes. These authors estimate the mass of high-mass stars embedded within the ultra compact H II regions within these complexes (UCH II from their 1.3 cm continuum emission (Gaume et al., 1995 identified ~ 40 regions). Given that the cm-observations are only sensitive to high-

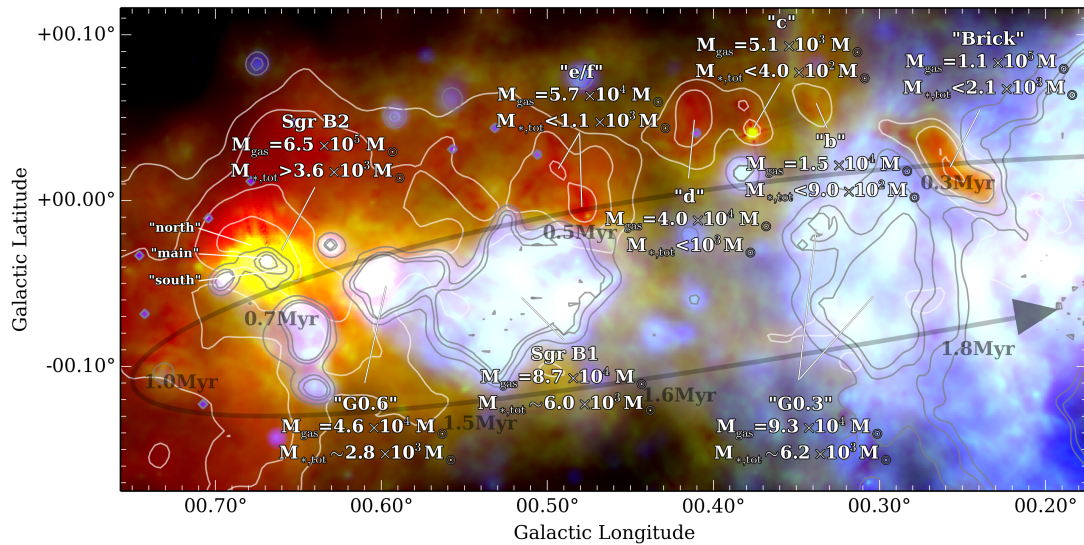


Figure 4.4: Three colour zoom-in of the “dust-ridge”, shown in blue and red are the warm and cool component luminosities, and in green is the $70\ \mu\text{m}$ emission. Over-plotted are contours identical to Figure 4.2. Labeled are the sources with their total gas and embedded masses determined from infrared measurements (see Table 4.5 from embedded masses determined via additional methods). The transparent curved arrow represents the path of the orbital model of Kruijssen, Dale & Longmore (2015), with labels of time since pericentre passage according to this model.

mass stars, the full population is extrapolated using a Kroupa IMF. Walker et al. (2015) estimate a total embedded stellar population mass of $\sim 3500 M_{\odot}$. Belloche et al. (2013) determined a similar mass of $\sim 3900 M_{\odot}$ when using this same method, with the data of Gaume et al. (1995). More recently, Schmiedeke et al. (2016) have compiled all the available cm-continuum data from the literature (Mehringer et al., 1993; Gaume et al., 1995; De Pree, Goss & Gaume, 1998; ~ 70 regions identified) and follow the above method to determine the total embedded stellar population mass. These authors estimate a mass of $\sim 3.3 \times 10^4 M_{\odot}$ (shown in parentheses in Table 4.5), which is an order of magnitude larger than the previously derived values.

To determine the embedded stellar masses within G0.6-0.005 (henceforth G0.6) and Sgr B1, we follow the method used by Walker et al. (2015), Belloche et al. (2013), and Schmiedeke et al. (2016), and the spectral classifications of the UCH II regions as determined by Mehringer et al. (1992). To convert these into masses, we use the spectroscopic masses of zero age main sequence stars given by Vacca, Garmany & Shull (1996). We obtain the total mass using a Kroupa IMF. We find that the total

embedded masses within G0.6 and Sgr B1 are $3300 M_{\odot}$ and $7200 M_{\odot}$, respectively.

Along with the above VLA observations, we use *WMAP* observations to calculate the stellar mass within Sgr B1.⁴ *WMAP* data has better absolute flux precision, suffers less from spatial filtering and covers a larger frequency range than the VLA observations. From these data an accurate spectral index of the emission can be calculated allowing accurate determination of the relative contributions from free-free, non-thermal and spinning dust emission. From the *WMAP* source catalogue presented by [Lee, Murray & Rahman \(2012\)](#), we find that Sgr B1 has an inferred ionising flux of $Q = 0.5 \pm 0.19 \times 10^{53} \text{ s}^{-1}$. [Murray & Rahman \(2010\)](#) showed that the ionising flux per stellar mass averaged over the initial mass function is $\langle q \rangle / \langle m_* \rangle = 6.3 \times 10^{46} M_{\odot}^{-1} \text{ s}^{-1}$. Using this, we find that the total embedded stellar mass within Sgr B1 is $\sim 8000 M_{\odot}$.

4.5.3 Uncertainties

This section includes a discussion of the uncertainties present when estimating the embedded young stellar mass and gas mass.

4.5.3.1 Source boundaries

In Section 4.5.1 we attempted to determine the boundaries of sources within the region $0.18 < l < 0.76^{\circ}$, $-0.12 < b < 0.13^{\circ}$, using several column density contours. This is not trivial as the interstellar medium is intrinsically fractal and hierarchically structured. A similar difficulty in defining the sources was noted by [Walker et al. \(2015, 2016\)](#), who showed that the properties of sources vary depending on the choice of boundary. To test the effect of changing the boundaries, Figure 4.5 shows how the enclosed gas and embedded stellar masses vary as a function of radius (assuming a spherical geometry). Varying the radius of each cloud by approximately ± 30 per cent gives on average a difference of $M_{\text{gas}}^{+90\%}_{-40\%}$, and $M_{*,\text{tot}}^{+50\%}_{-20\%}$.

⁴*WMAP* observations can only be used for Sgr B1, as this is the only source identified by [Lee, Murray & Rahman \(2012\)](#).

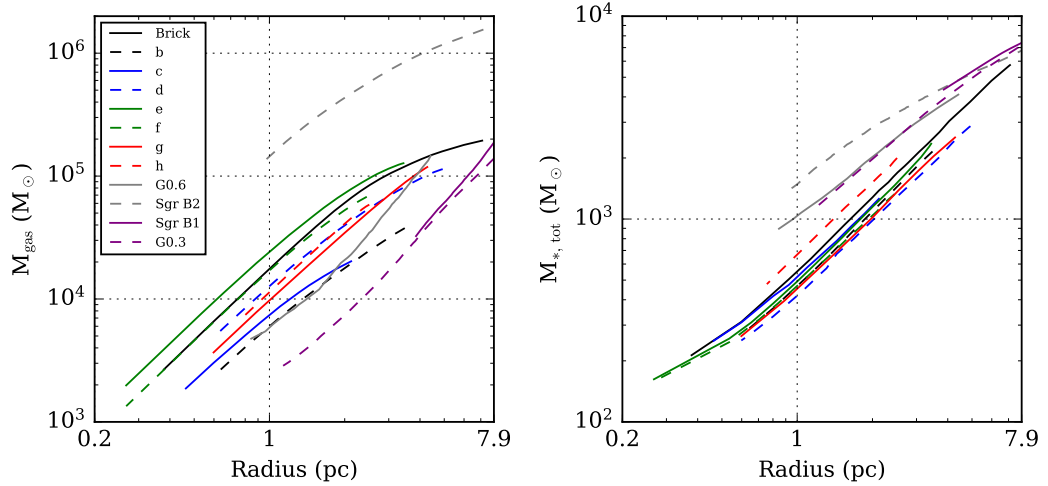


Figure 4.5: Plots of radius against the total mass of the gas [left panel] and embedded young stellar population [right panel]. The radial profiles of the CMZ sources are shown by the coloured solid and dashed lines [see the legend in the left panel].

We find the Sgr B2 region is particularly difficult to define with a single column density contour, as it is thought to contain both dense gas and actively star forming regions (also see [Schmiedeke et al., 2016](#)). We choose to define the Sgr B2 region by a cool component column density of $7.5 \times 10^{23} \text{ cm}^{-2}$, as this contour separates it from neighbouring sources (see Section 4.5.1). However, this contour does not contain the warm luminosity component to the south-west ($l \approx 0.64^\circ$, $b \approx -0.8^\circ$) or the extended cool envelope to the north ($l \approx 0.6^\circ$, $b \approx 0.0^\circ$), which have both been previously attributed to Sgr B2 (e.g. [Yusef-Zadeh et al., 2009](#)). Increasing the column density limit to include these would increase the gas and embedded stellar masses by factors of two to three.

Changing the source boundaries varies both the gas mass and embedded young stellar mass on average by a factor of two, however the gradient of both parameters as a function of radius are similar. As the star formation efficiencies per free-fall time that are calculated in the later sections of this work (Section 4.5.4), are essentially ratios of the gas mass and embedded young stellar mass, these are not sensitive to the choice boundary over a few parsecs.

4.5.3.2 Field Star contribution

The sample of clouds within $0.18 < l < 0.76^\circ$, $-0.12 < b < 0.13^\circ$ are thought to reside ~ 100 pc from the centre of the galaxy. There is a high number density of old population bulge stars within this region, which may contribute to the measured infrared luminosity and cause an overestimation of mass of the embedded stellar population. To investigate this, we use the Besançon model (Robin et al., 2003). We use the same catalogue simulation from Section 4.4.1, with a distance range of 8.3 – 8.5 kpc and a step of 50 pc, towards the coordinates of the clouds within the $0.18 < l < 0.76^\circ$, $-0.12 < b < 0.13^\circ$ region. This gives an average bolometric luminosity density of $28 \pm 5 L_\odot \text{pc}^{-3}$ (~ 15 stars pc^{-3}). Therefore, we find that the old stellar population stars will contribute to < 1 per cent of the total bolometric luminosity measured for each cloud.

4.5.3.3 Background contribution

There is a smoothly varying infrared component to the diffuse Galactic emission along the line-of-sight to the CMZ, which contributes to the luminosity. This has been subtracted for the emission at wavelengths $> 70 \mu\text{m}$ using the method presented in Battersby et al. (2011), which causes an average decrease of ~ 20 per cent in the measured bolometric luminosity at each pixel. There may be some residual diffuse emission that varies on small scales associated with the CMZ itself, which has not been removed when using the background subtraction routine and could contaminate the bolometric luminosity measurements for each cloud. We, however, do not expect this to be a significant effect.

We have not taken into account background subtraction for the line-of-sight emission at wavelengths $< 70 \mu\text{m}$, which could lead to an overestimation of the luminosity. This is expected to be more of a problem for the sources which have less emission at these wavelength, such as those in the dust-ridge. We estimate the magnitude of this to be on the order of the $> 70 \mu\text{m}$ Galactic diffuse emission: ~ 20 per cent. On the other hand, we do not believe this will be a significant effect to the brighter star-forming clouds

(e.g. Sgr B2), as their luminosities are clearly dominated by the embedded young stellar population.

4.5.3.4 Luminosity from external heating

The dust ridge clouds are thought to be externally heated (Longmore et al., 2013a,b; Ott et al., 2014; Rathborne et al., 2014a), therefore we consider that some fraction of their luminosity may be produced by the heating from bright nearby sources. As an example, we estimate how much luminosity would be produced by the heating from the two brightest clusters within the Galactic Centre, the Arches and Quintuplet clusters. Using the three-dimensional structure of the Galactic Centre determined by Kruijssen, Dale & Longmore (2015, see Section 4.5.4), we estimate that the “Brick” is the closest cloud, residing at a distance of ~ 25 pc from these clusters, hence use this as the example subject. Figer, McLean & Morris (1999); Figer et al. (2002) estimate that the luminosity within the Arches and Quintuplet clusters is $10^{7.8}$ and $10^{7.5} L_{\odot}$, respectively. Assuming that the luminosity is isotropically radiated from each cluster, and is completely absorbed and re-emitted by the “Brick” (assuming a circular geometry with a radius of ~ 3.1 pc), the luminosity contribution from the Arches and Quintuplet clusters is $\sim 2 \times 10^5 L_{\odot}$ and $10^5 L_{\odot}$, respectively. This is ~ 30 per cent of the total luminosity of the “Brick”. We suggest that this is an upper limit to the affect of external radiation on the measured luminosity of the sources considered here.

4.5.3.5 Accretion luminosity

We consider that some fraction of the bolometric luminosity from these clouds may be caused by the accretion of material onto the embedded stars. It is thought that the accretion luminosity for low-mass young stars can be around an order of magnitude higher than the intrinsic stellar luminosity, whereas for high-mass stars the stellar luminosity dominates over the accretion luminosity for all reasonable accretion rates ($> 10 M_{\odot}$; e.g. Hosokawa & Omukai, 2009). In this work we assume that the infrared luminosity from each of the embedded stellar populations is dominated by high-mass

stars, so assume the contribution of the accretion luminosity should be insignificant.

4.5.3.6 Variation in the embedded stellar population

We calculate the total embedded stellar population mass within each source in the Galactic Centre by extrapolating from a high-mass sample of the population. The three caveats which may affect our measurement of the embedded stellar population mass are the choice of the initial mass function, the sampling of the initial mass function and the upper mass limit of the initial mass function (i.e. the maximum stellar mass of the population), and are discussed below.

Throughout this work we estimate the embedded stellar population assuming a Kroupa IMF (Kroupa, 2001). However, many IMFs are used in the literature, which despite years of major scrutiny, share broadly similar properties: a power-law at the high-mass end with a slope of roughly -2.3, and a turnover (Kroupa) or Gaussian (Chabrier, 2003) low-mass end. These give broadly the same result, and therefore the choice of the initial mass function is not considered an issue. Furthermore, these turn out to be broadly universal across a range of environments (Bastian, Covey & Meyer, 2010) although recent claims have claimed otherwise (but these are still disputed; Bartko et al., 2010; Conroy & van Dokkum, 2012; Cappellari et al., 2012), hence any variation in the IMF is also not considered further.

When using IMFs it is important to consider their stochastic nature, particularly for stellar populations with low number statistics - i.e. in regions where star formation has recently begun. When stars form they stochastically populate the IMF, such that each star has finite probability of having any mass between a given mass range. More massive stellar populations will in general have more stars, and hence will have a higher chance of being fully populated (e.g. Gilmore, 2001; Fumagalli, da Silva & Krumholz, 2011). Populations with masses of $\sim 10^4 M_{\odot}$ should fully sample the initial mass function (Bruzual & Charlot, 2003). In this work we estimate embedded stellar masses significantly less than this, for example dust-ridge clouds have $M_{*,\text{tot}} \sim 10^3 M_{\odot}$ ($\sim 400 - 1000$ stars). The initial mass function for these sources will, therefore,

most likely not be fully sampled, and stochastic effects may be significant. Elmegreen (1999) have shown that low number sampling (1000 stars) of an IMF could cause the power-law slope to vary by ± 0.1 . This effect is inherently “random” and is therefore difficult to quantify for each source. Nevertheless, changing a single power-law slope of $\alpha = 2.3$ by ± 0.1 , would vary the total embedded mass by a factor of two to three.

The final caveat in calculating the total embedded stellar population mass for each source is that the bolometric luminosity is produced solely by the most massive star in the population. There may be, however, a non-negligible contribution by the second, and progressively lower massive stars to the measured bolometric luminosity, which could cause an overestimation of the most massive star in the population. To investigate how this affects the total mass of the embedded population, we plot the bolometric luminosity as a function of total embedded stellar population mass, with the assumption that all the luminosity is produced by the most massive star. On the same axis we plot the bolometric luminosity as a function of total embedded stellar population mass produced from the synthetic stellar population model STARBURST99 (see Figure 4.6).⁵ The model input parameters are an instantaneous star formation burst populating a Kroupa IMF with total cluster masses ranging from 1000 to 100,000 M_{\odot} . We note that, the STARBURST99 is unable to produce stellar populations with masses below 1000 M_{\odot} . We find that the STARBURST99 mass-luminosity relation has a power-law slope which is shallower than if we assume all the luminosity is produced from the most massive star, with the intersection between the two relations at $\sim 5000 M_{\odot}$. As the star-forming sources G0.6, Sgr B1 and G0.3-0.056 (henceforth G0.3) have masses close to this value, these should not be significantly affected by this uncertainty. However, the dust ridge clouds have embedded masses much lower than this. The STARBURST99 modelling shows that stochastic sampling may lead to an overestimation of the total embedded stellar mass by up to factor of three.

In summary, we estimate that the main sources of uncertainty on the embedded population within the Galactic Centre clouds are the stochastic nature of the IMF and the form of the adopted IMF. This leads to an uncertainty in the embedded stellar mass

⁵<http://www.stsci.edu/science/starburst99/docs/default.htm>

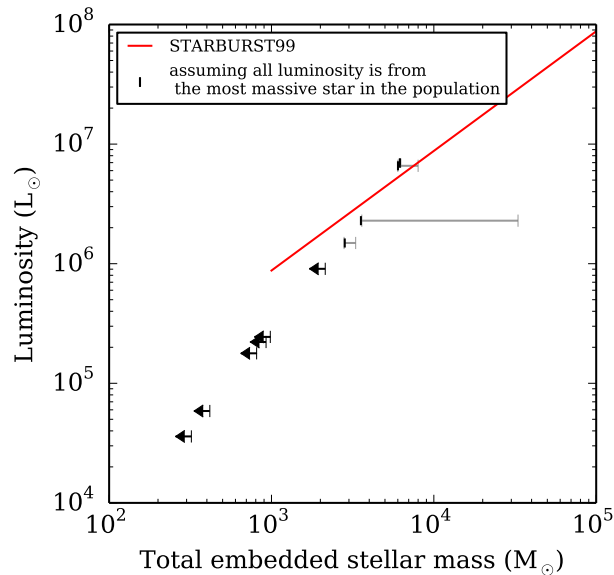


Figure 4.6: Plot displaying the luminosity as a function of mass for the sources in this work when assuming all the luminosity originates from only the most massive embedded star (black lines). The grey error bars indicate the ranges of embedded masses determined from alternative measurements (see Section 4.5.2). Also shown is the results of the STARBURST99 stellar population model (red line). From this, we conclude that the contribution from lower mass stars to the total bolometric luminosity is insignificant for the larger star-forming sources of our sample (Sgr B2, G0.6, Sgr B1 and G0.3). However, their contribution to the luminosity of the more quiescent clouds (“dust-ridge” clouds), may result in over estimation of their embedded stellar mass by factors of a few.

estimate of at least a factor of two.

4.5.3.7 Saturation

Several of the *Spitzer* and *Herschel* maps used in this work contain saturated pixels, which we treat as having the maximum observed value within each map. This was not considered a problem when determining the global star formation rates as these pixels did not significantly contribute to the total luminosities. However, this is not the case for the individual clouds, where the majority of saturated pixels are located. We find that 8, 5, 40,⁶ and 3 per cent of the pixels within Sgr B2, G0.6, Sgr B1, and G0.3, respectively, are saturated. The luminosity towards these saturated pixels is considered a

⁶We highlight that the high fraction of saturated pixels in the bolometric luminosity maps towards the Sgr B1 region is a result of saturation in the *Spitzer* 24 μ m map.

lower limit, and therefore contributes to an underestimation of the measured embedded stellar mass of each source. We expect that this will cause a more severe underestimation of the embedded stellar mass when a high concentration of the embedded sources are within the saturated pixels. Despite Sgr B1 having the majority of saturated pixels, we find only eight H II regions towards these pixels (Mehring et al., 1992), whereas the saturated pixels towards Sgr B2 contain more than sixty H II regions (Schmiedeke et al., 2016). We therefore expect pixel saturation to cause a significant underestimation of the embedded stellar mass towards the Sgr B2 region.

4.5.3.8 Summary of embedded stellar population mass uncertainties

To summarise, several of the uncertainties discussed above can significantly affect the estimate of the embedded stellar population masses for all the sources. Some are only applicable to either the quiescent clouds (high gas mass/low embedded stellar mass), or the star-forming clouds (low gas mass/high embedded stellar mass). The uncertainties which affect all the sources are the choice of arbitrary boundary (± 50 per cent) and the contribution from accretion luminosity (negligible). The uncertainties which primarily affect the quiescent clouds are the contribution of CMZ diffuse background luminosity and the stochasticity in the IMF, as their low masses do not enable full/significant sampling of the IMF. As the diffuse background luminosity will cause the stellar mass to be overestimated, we conclude that the embedded stellar mass estimates for the quiescent clouds (“Brick”, “b”, “c”, “d”, “e” and “f”) should be considered as upper limits. On the other hand, the main uncertainty on the bolometric luminosity, hence the embedded stellar mass, which affects the star-forming clouds is pixel saturation, yet it is difficult to quantify the magnitude of the uncertainty this induces. To approximate the severity of this, we compare the embedded stellar masses determined from the infrared bolometric luminosity and cm-continuum observations (Section 4.5.2 and Table 4.5). We find that the discrepancy in embedded stellar mass determined from these observations for G0.6 and Sgr B1 is small (20–30 per cent). Therefore, given the other uncertainties on the embedded stellar mass discussed in this section, we conservatively estimate that the embedded stellar masses determined for these two sources are reliable to within a

factor of 2 – 3. As no previous measurements of embedded stellar mass toward G0.3 are available, we suggest that this is also reliable to within a factor of 2 – 3. We find that the embedded stellar mass determined from infrared measurements of Sgr B2 is an order of magnitude below the value determined by [Schmiedeke et al. \(2016\)](#), which we expect is due to the high concentration of UCH II regions towards the saturated pixels within this source. We suggest that this has caused a significant underestimation of the embedded stellar mass within the Sgr B2, hence this infrared measurement should be considered a lower limit.

4.5.4 Deriving the star formation efficiency and star formation rates

Having measured the embedded stellar populations and gas masses for each of the regions we now seek to determine the efficiency with which gas is converted into stars in the Galactic Centre. We are interested in deriving two numbers in particular: (i) the ratio of a cloud’s gas mass, M_{gas} , to the mass in stars, $M_{*,\text{tot}}$, which is defined as the star formation efficiency, $\epsilon \equiv M_{*,\text{tot}}/(M_{\text{gas}} + M_{*,\text{tot}})$; (ii) the fraction of the cloud’s gas mass which is converted into stars per free-fall time, $\epsilon_{\text{ff}} = \epsilon \times (t_{\text{ff}}/t_0)$, where t_0 is the time since the onset of star formation.

Table 4.5 summarises the properties of gas and young stars in several of the most massive and dense clouds and proto-clusters within the Galaxy. Figure 4.4 shows the cool molecular gas (red) and hot (ionised) gas (blue and green) towards the region containing these sources of interest; $0.18 < l < 0.76^\circ$, $-0.12 < b < 0.13^\circ$. Over-plotted are contours of cool and warm gas column densities in white and grey, respectively (see Section 4.3). Labeled on this plot are the sources and their respective gas and embedded stellar population masses within the radius defined in Table 4.5.

From the observed M_{gas} and $M_{*,\text{tot}}$ it is straightforward to derive and compare the ϵ for each region. We know that all the regions lie in the same environment, hence we can remove a major source of uncertainty that has hampered previous comparisons of SFEs for sources that may have formed in (potentially very) different environments.

Table 4.5: The properties of the sources within the $0.18 < l < 0.76^\circ$, $-0.12 < b < 0.13^\circ$ region. These do not depend on any relationship between these regions, other than that they all reside at the same distance. The columns show the column density limits used to define the sources, the masses and the radii, bolometric luminosities, maximum embedded object mass, total embedded stellar mass, the free-fall time and the star formation efficiency¹. Shown in parentheses are the embedded stellar masses, and the resulting cloud properties, determined from VLA, and WMAP observations (see corresponding footnotes for references).

Source	$N(\text{H}_2)$ boundary (cm^{-2})	M_{gas}^1 ($10^4 M_\odot$)	R (pc)	L_{bol}^1 ($10^5 L_\odot$)	$M_{*,\text{max}}$ (M_\odot)	$M_{*,\text{tot}}^1$ (M_\odot)	t_{ff}^1 (Myr)	ϵ^1 (per cent)
““Brick””	$N^{\text{cool}}(\text{H}_2) = 8 \times 10^{22}$	11	3.1	9.1	80	$< 2.1 \times 10^3$ (8.8×10^2) ^a	0.27	2
“b”	$N^{\text{cool}}(\text{H}_2) = 5 \times 10^{22}$	1.5	1.8	2.2	40	$< 9.3 \times 10^2$	0.31	6
“c”	$N^{\text{cool}}(\text{H}_2) = 10 \times 10^{22}$	0.51	0.8	0.59	20	$< 4.2 \times 10^2$	0.16	8
“d”	$N^{\text{cool}}(\text{H}_2) = 10 \times 10^{22}$	4	2.0	2.4	40	$< 9.8 \times 10^2$	0.23	2
“e”	$N^{\text{cool}}(\text{H}_2) = 24 \times 10^{22}$	4.8	1.5	1.8	40	$< 8.1 \times 10^2$	0.13	2
“f”	$N^{\text{cool}}(\text{H}_2) = 24 \times 10^{22}$	0.9	0.7	0.36	20	$< 3.2 \times 10^2$	0.10	3
Sgr B2	$N^{\text{cool}}(\text{H}_2) = 75 \times 10^{22}$	65	2.7	23	120	$> 3.6 \times 10^3$ (3.3×10^4) ^b	0.09 (0.09)	1 (5)
G0.6	$N^{\text{warm}}(\text{H}_2) = 2.6 \times 10^{17}$	4.6	2.8	15	100	2.8×10^3 (3.3×10^3) ^c	0.35 (0.35)	6 (7)
Sgr B1	$N^{\text{warm}}(\text{H}_2) = 2.6 \times 10^{17}$	8.7	5.8	66	180	6.0×10^3 (7.2×10^3 , 8.0×10^3) ^{c,d}	0.77 (0.77)	6 (8)
G0.3	$N^{\text{warm}}(\text{H}_2) = 1.9 \times 10^{17}$	9.3	6.5	69	180	6.2×10^3	0.86	6

^a Kauffmann et al. (2016)

^b Mass determined from high-resolution VLA observations Schmiedeke et al. (2016).

^c Mass determined from medium-resolution VLA observations Mehringer et al. (1992).

^d Mass determined from WMAP observations Lee, Murray & Rahman (2012).

¹ These values represent the instantaneous source properties: M_{gas} , $M_{*,\text{tot}}$, t_{ff} , SFE (see Section 4.5.4).

As shown in Table 4.5, we find that the “dust-ridge” clouds have $\epsilon < 4$ per cent (upper limits), and the star-forming sources have $\epsilon \sim 7$ per cent. Taking these numbers at face value it appears that, despite these regions containing some of the most vigorous star formation activity in the Galaxy, only a small fraction of their total gas mass has so far been converted to stars (see chapter 6.1 for a comparison to Galactic disc clouds).

4.5.5 Deriving the star formation efficiency per free-fall time assuming a model of tidally triggered star formation

Other than assuming all the sources lie at the same distance and in the same general environment, all of the analysis until this point has implicitly treated all regions as independent. We now attempt to infer the possible relationship between gas clouds and proto-clusters by interpreting pertinent observational facts.

Firstly, observations of dense gas molecular line tracers (e.g. HNC, N_2H^+) towards the region from Figure 4.4, clearly show the quiescent clouds (red) and proto-clusters (blue) are all linked along a coherent velocity structure, or “stream”, in position-position-velocity (PPV) space (e.g. Kruijssen, Dale & Longmore, 2015; Henshaw et al., 2016b). The quiescent clouds found towards the north of this region lie at one end of the PPV stream. These clouds show very little signs of star formation, despite their similarly large gas masses and small radii (e.g. Lis et al., 1999; Immer et al., 2012b; Longmore et al., 2013b; Walker et al., 2015; Ginsburg et al., 2015). Following the stream to higher galactic longitudes and velocities, and lower latitudes lies the mini-starburst complex Sgr B2 (e.g. Bally et al., 1988; Hasegawa et al., 1994; Sato et al., 2000). Continuing on the stream from Sgr B2 to lower longitudes, latitudes and velocities, the H II region complexes G0.6, Sgr B1 and G0.3 are found (e.g. Mehringer et al., 1992; Lang et al., 2010). The first assumption we make is that as the quiescent clouds and proto-clusters are all part of the same stream.

Secondly, the quiescent gas clouds all have very similar masses and radii, and are close to virial equilibrium and therefore likely to collapse (Walker et al., 2015). Thirdly, the gas column density probability distribution functions of the quiescent gas clouds are

indicative of imminent star formation (Rathborne et al., 2014b; Battersby in prep.), and the radial distributions of the mass surface densities suggest that collapse of these clouds could produce Arches or Quintuplet-like clusters in the future (Walker et al., 2016). Lastly, there is a general progression of star formation along the stream from quiescent gas clouds to proto-clusters.

If the clouds and proto-clusters within the $0.18 < l < 0.76^\circ$, $-0.12 < b < 0.13^\circ$ region do represent an evolutionary sequence, one has an estimation of the initial conditions for star formation within the Galactic Centre. With a measure of ϵ from Section 4.5.4 and t_{ff} , the only thing needed to derive ϵ_{ff} is an absolute timescale linking the clouds and proto-clusters.

Kruijssen, Dale & Longmore (2015) have developed a dynamical orbital solution to interpret the PPV structure of the molecular emission throughout the central ~ 200 pc of the Galaxy, from which “Streams 2 and 3” have been over-plotted in Figure 4.4. The focal point of this open, elliptical orbit coincides with the position of the supermassive black hole at the centre of the Galaxy, Sgr A*, and all the sources within the $0.18 < l < 0.76^\circ$, $-0.12 < b < 0.13^\circ$ region are downstream past pericentre passage on this orbit.

The observed star formation activity increases with time past pericentre (shown as the increasing spatial extent of the hot gas component in Figure 4.4). In the scenario presented by Longmore et al. (2013b), Kruijssen, Dale & Longmore (2015), and Longmore et al. (2016), gas clouds will experience strong tidal forces close to pericentre passage, which will compress the gas along the vertical direction. This adds turbulent energy into the gas which can be quickly radiated away by shocks due to the high density. In the model, this implies the clouds become self-gravitating and allows them to initiate gravitational collapse, eventually triggering star formation. Further downstream, as star formation continues, feedback from massive embedded stars begins to blow cavities in the surrounding environment, and eventually cause the dissipation of the host cloud (Barnes et al. in prep).

Assuming that star formation within each cloud was triggered at peri-

centre passage, we can calculate the time-averaged star formation rate as $\text{SFR} (\text{M}_{\odot} \text{yr}^{-1}) = M_{*,\text{tot}}(\text{M}_{\odot}) / t_{\text{p,last}} (\text{yr})$, where $t_{\text{p,last}}$ is the time since the last pericentre passage. In Figure 4.4 we label the time since pericentre passage for the orbital model presented by Kruijssen, Dale & Longmore (2015), where the pericentre of the orbit is located just upstream from the ‘‘Brick’’. We find the star formation rates of these clouds are in the range $0.001 - 0.045 \text{ M}_{\odot} \text{yr}^{-1}$. The total star formation rate within these clouds sums to $0.03 - 0.071 \text{ M}_{\odot} \text{yr}^{-1}$. These clouds, therefore, contribute a quarter to three-quarters of the total star formation within the CMZ ($|l| < 1^{\circ}$, $|b| < 0.5^{\circ}$; $\sim 0.09 \text{ M}_{\odot} \text{yr}^{-1}$). The values for the individual clouds are presented in Table 4.6, and are in agreement with those determined through independent methods by Kauffmann et al. (2016, also see Table 4.6) and Lu et al. (in prep).

The calculated star formation rates are used to determine the fraction of the cloud’s mass which is converted into stars per free-fall time. This can be described as $\epsilon_{\text{ff}} = \epsilon \times (t_{\text{ff}} / t_{\text{p,last}})$. We find star formation efficiencies per free-fall time in the range of 1 – 5 per cent,⁷ which are again listed in Table 5.

4.5.6 Comparison to theoretical models

We now compare these measurements of the star formation rate to the predictions of star formation theories within the literature. The comparison to the column density threshold relation and volumetric models for star formation is limited to those discussed in Section 1.4 (see reviews by Federrath & Klessen, 2012 and Padoan et al., 2014). The column density threshold relation predicts the star formation rate solely from the dense gas mass (Lada, Lombardi & Alves, 2010; Lada et al., 2012). On the other hand, the volumetric models predict the dimensionless star formation efficiency per free-fall time, ϵ_{ff} , from the physical global properties of the cloud: the sonic Mach number, Alfvénic Mach number, virial parameter, and the turbulence driving parameter. Padoan et al. (2014) show that a comparison between the predictions from these

⁷Note that these values change by less than a factor of two when using typical timescales for star formation in young massive clusters (e.g. the free-fall time; see the review by Longmore et al., 2014), rather than the timescales from the Kruijssen, Dale & Longmore (2015) orbital model.

Table 4.6: The source properties based on the assumptions adopted in Section 4.5.5. The first assumption is that the “dust-ridge” clouds are representative of the early evolutionary stages of the star-forming clouds, Sgr B2, G0.6, Sgr B1 and G0.3. The second assumption is that the clouds are on an elliptical orbit around the CMZ, which tidally triggers star formation at the point of pericentre passage. Tabulated in the first column are the times since pericentre passage (i.e. triggering of star formation) as defined from the orbital model of (Kruijssen, Dale & Longmore, 2015), which have been used to determine the star formation rates and star formation efficiencies per free-fall time. Shown in parentheses are the properties determined when using the embedded stellar masses calculated from VLA and WMAP observations (see Table 4.5).

Source	$t_{p,\text{last}}$ (Myr)	SFR ($M_{\odot} \text{ yr}^{-1}$)	ϵ_{ff} (per cent)
““Brick””	0.3	0.007	2
“b”	0.4	0.002	5
“c”	0.4	0.001	3
“d”	0.5	0.002	1
“e”	0.5	0.002	0.5
“f”	0.5	0.001	1
Sgr B2	0.7	0.005 (0.045)	0.1 (1)
G0.6	1.4	0.002 (0.002)	1 (2)
Sgr B1	1.6	0.004 (0.005)	3 (4)
G0.3	1.8	0.004	3

relations/models and observations is not trivial. Scatter of more than an order of magnitude exists in the observed star formation rate for a given gas mass, due to the range of environments, evolutionary stages, and spatial scales probed by observations of different clouds.

In Section 4.5.5 we discussed several means by which we hope to overcome several of these limitations: i) directly determining the gas mass and embedded stellar population mass within several sources in the same environment and at the same spatial resolution, ii) using the Kruijssen, Dale & Longmore (2015) orbital model to estimate the absolute time which has passed since star formation within each source was plausibly triggered, and iii) limiting our study to sources within the extreme environment of the Galactic Centre, which may be representative of the environment in which the majority of stars have formed (Kruijssen & Longmore, 2013).

Lada, Lombardi & Alves (2010); Lada et al. (2012) propose that the gas above a column density of $6.7 \times 10^{21} \text{ cm}^{-2}$ has a universal depletion timescale of ~ 20 Myr ($\sim 50 t_{\text{ff}}$). They propose that the star formation rate can be predicted using equa-

tion 1.33. We find that the constraints on the star formation rate within the dust-ridge clouds “d”, “e”, and “f” are too poor to test the Lada, Lombardi & Alves (2010) and Lada et al. (2012) predictions with any significance. Kauffmann et al. (2016) have inferred an upper limit of the star formation rate within the “Brick” of $< 0.0008 M_{\odot} \text{ yr}^{-1}$, from the non-detection of the star formation tracers (e.g. H II regions and masers). This is an order of magnitude below the upper limit found here, and is most likely more representative of the true star formation rate within this source. The star formation rate predicted by the column density limit relation for the “Brick” is $\sim 0.006 M_{\odot} \text{ yr}^{-1}$, which is significantly higher than measured by Kauffmann et al. (2016). The predictions for the star-forming sources Sgr B2, G0.6, Sgr B1 and G0.3 show better agreement with the observed star formation rates.

Predictions from volumetric star formation models within the Galactic Centre have been previously determined, however their comparison to observations have been limited. Rathborne et al. (2014b) and Rathborne et al. (2015) used the Atacama Large Millimeter/submillimeter Array to measure 3 mm continuum dust emission at high-spatial resolution towards the “Brick”. These authors measure a column density probability function dispersion of $\sigma_N = 0.34$, and place lower limits on the critical over-density of collapse of $x_{\text{crit}} > 100$ (see equation 1.35). Although the star formation rate was not calculated, these results are consistent with an environmentally dependent *absolute* density threshold for star formation, which is orders of magnitude higher than that derived for clouds within the disc of the Milky Way. Recently, Federrath et al. (2016) have conducted a further analysis of these continuum data, with the addition of molecular line observations from Rathborne et al. (2015) and dust polarisation observations from Pillai et al. (2015). These observations were used to determine the dimensionless parameters required for the volumetric star formation models: the three-dimensional turbulent Mach number, the virial parameter including both turbulence and shear, the turbulent magnetic field parameter, and the turbulence driving parameter (see Section 4.4.3). These authors used the multi-free-fall model of Krumholz & McKee (2005), with the fiducial parameters determined by Federrath & Klessen (2012), to predict a star formation efficiency per free-fall time within the brick of $\epsilon_{\text{ff}} = 4 \pm 3$ per

cent. This is consistent with our measurement of $\epsilon_{\text{ff}} \sim 2$ per cent towards the “Brick” (see Table 4.5). We note, however, that the observed ϵ_{ff} within the “Brick” should be considered an upper limit. Taking the embedded stellar population inferred by [Kauffmann et al. \(2016\)](#) would give $\epsilon_{\text{ff}} \sim 1$ per cent, which is only just within the lower uncertainty range of the value predicted by [Federrath et al. \(2016\)](#). Here we attempt to expand on this comparison by testing all the volumetric star formation models presented by [Federrath & Klessen \(2012\)](#) against the observed star formation within a number of Galactic centre clouds.

To compare the measured star formation rates to the volumetric models, we first need to determine the initial conditions for star formation for each source. As discussed in Section 4.5.5 we assume that the “dust-ridge” clouds should represent the early evolutionary stages of the star-forming sources. The “Brick” is the most recent of the “dust-ridge” clouds to pass pericentre, hence its properties should best represent the initial conditions for star formation within this region. This cloud has the benefit of being the most well studied of the dust-ridge clouds (i.e. its properties are the most well constrained), and is known to contain little-to-no active star formation (e.g. [Kauffmann, Pillai & Zhang, 2013](#); [Johnston et al., 2014](#); [Rathborne et al., 2014b](#); [Kauffmann et al., 2016](#)).

However, we note that the volumetric models are limited to predicting the ϵ_{ff} over the next free-fall time. In the orbital model of [Kruijssen, Dale & Longmore \(2015\)](#), the “Brick” and Sgr B2 are separated by a time along the orbit that is similar to the free-fall time of the “Brick” (see Tables 4.5 and 4.6), and thus the comparison for these regions should be robust. Given that there are several free-fall times between the “Brick” and G0.3, using the initial conditions present within the “Brick” to predict ϵ_{ff} in the more evolved sources (G0.6, Sgr B1 and G0.3) may not be ideal. Nevertheless, given the relatively small range in gas properties of the “dust-ridge” clouds and of the progenitor condensations upstream from pericentre ([Henshaw, Longmore & Kruijssen, 2016](#)), the conditions within the “Brick” should provide at least approximate predictions for these more evolved sources, which can be compared to the observations.

The star formation rates determined for the quiescent clouds are not considered for

the comparison to the volumetric models, as their embedded masses measured from infrared observations (and hence ϵ_{ff}) are considered as upper limits (see Section 4.5.3). We, therefore, limit our analysis to the star-forming sources (Sgr B2, G0.6, Sgr B1, and G0.3), for which we are confident in the measurement of the embedded stellar mass.

We use the volumetric models given in the form presented by the Federrath & Klessen (2012) review (Padoan et al., 2014). This includes the derivation of the log-normal volume density probability distribution function ($p(s)$; equation 1.36), and the critical density for collapse (x_{crit}) and solution to the ϵ_{ff} for each model (equation 1.34). These models by KM05, PN11 and HC13, and their multi-free-fall counterpart (i.e. those that allow for the density dependence of the free-fall time in their calculation), have been introduced in Section 1.4.2 and summarised in Table 1.1. As discussed in Section 1.4.2, the key physical variables in these models are the three-dimensional turbulent sonic Mach number, \mathcal{M} , the (turbulence+shear) virial parameter, α , and the parameter which describes the strength of the turbulent magnetic field, β (the purely hydrodynamical scenario is retrieved by setting $\beta \rightarrow \infty$), and the mode of turbulence driving, b (for solenoidal turbulence $b = 0.33$, for mixed turbulence $b = 0.4$, and for compressive turbulence $b = 1.0$).

Figure 4.7 shows how the predicted star formation efficiency per free-fall time varies as a function of the key physical variables when assuming a constant value of $b = 0.33$, which represents a purely solenoidal turbulent driving mode, as Krumholz & Kruijssen (2015) suggest that shear is the typical driving mode of turbulence within the dust-ridge clouds, and within clouds at the centres of other galaxies. The vertical dash lines shows the result of varying either $\mathcal{M} = 11 \pm 3$, $\alpha = 4.3 \pm 2.3$, and $\beta = 0.11 - 0.61$,⁸ which are representative of the conditions derived for the ‘‘Brick’’ (Federrath et al., 2016). Each model line (shown in colour) is plotted as a function of one of the above three parameters, where the shaded region around each line indicates the uncertainty on the predicted ϵ_{ff} when varying the two remaining parameters over the ranges specified above. The horizontal dotted lines show the calculated ranges of ϵ_{ff} ,

⁸The probability distribution function of β within the ‘‘Brick’’ is asymmetric, with a mean value and standard deviation of $\beta = 0.34$ (0.35) (Federrath et al., 2016). Here we use the 16th and 84th percentiles of this distribution ($\beta = 0.11 - 0.61$; C. Federrath, private communication).

within star-forming regions Sgr B2, G0.6, Sgr B1, and G0.3.⁹ ϵ_{ff} determined using the VLA embedded stellar mass (Schmiedeke et al., 2016). Models passing through the shaded region enclosed by the dotted and dashed lines correctly predict the star formation rate per free-fall time in the star-forming clouds, when assuming that their initial conditions were similar to the current properties of the “Brick”. We find that both single-free-fall and multi-free-fall models of PN11 and HC13 enter the shaded region on Figure 4.7.

When testing the volumetric star formation theories, we need to choose the value for several of their free parameters (ϵ_{core} , ϕ_t , ϕ_x , θ , and y_{cut}). Table 1.1 shows how each of these free parameters is included into the calculation of x_{crit} and ϵ_{ff} for each model. In Figure 4.7 we adopted the fiducial parameters from the original papers, which have been summarised in Table 4.7. Federrath & Klessen (2012) have constrained these parameters in a different way, by fitting them to magneto-hydrodynamical turbulent box simulations, resulting in the substantially different values, which are also shown in Table 4.7. We note that the Federrath & Klessen (2012) determine values of $y_{\text{cut}} > 1$, however a physical interpretation of y_{cut} can only be made for $0 > y_{\text{cut}} > 1$ (HC13).

The result of using the Federrath & Klessen (2012) parameters is shown in Figure 4.8, where we find *all* of the volumetric models appear to overpredict the star formation rate by factors of several. Recently, Federrath et al. (2016) used the Federrath & Klessen (2012) fiducial values and a turbulent driving parameter of $b = 0.22$ ¹⁰ in the KM05 multi-free-fall model to predict the ϵ_{ff} within the “Brick”. Figure 4.9 shows the result of using these values for all the volumetric star formation theories. Here we find that both the single-free-fall and multi-free-fall models of KM05 and PN11 enter the shaded region, and are therefore consistent with the observed star formation rate.

This analysis shows that varying the turbulent driving parameter in the range determined for the “Brick” ($b = 0.10 - 0.34$; Federrath et al., 2016), and adopting either the

⁹ As ϵ_{ff} measured from infrared observations for Sgr B2 is a lower limit, henceforth we use only the more accurate

¹⁰ The idealised case presented by Federrath, Klessen & Schmidt (2008), $b = 0.33$ represents purely isotropic solenoidal turbulence driving. However, lower values of b may be possible when the driving is anisotropic, whereby a particular vortex direction is continuously driven (e.g. by anisotropic shear).

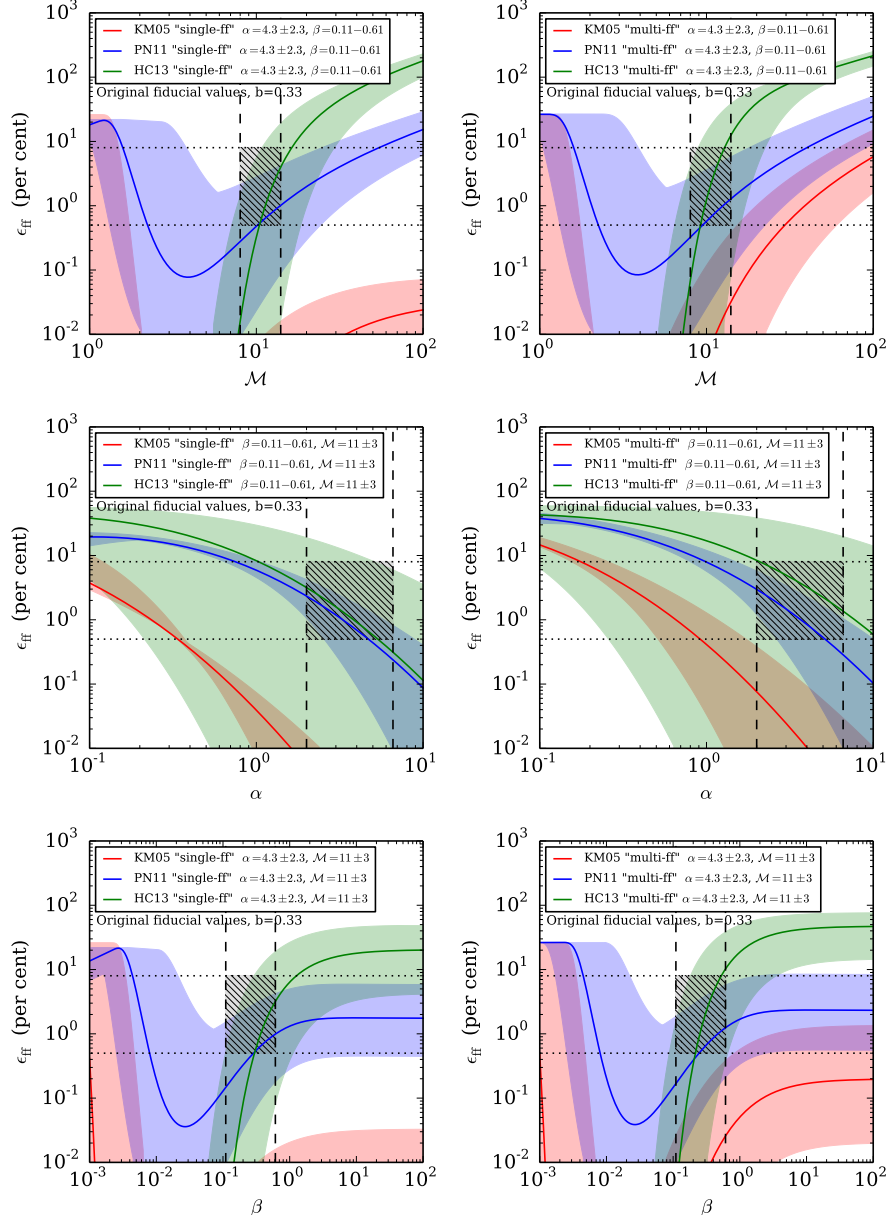


Figure 4.7: Plots of the star formation efficiency per free-fall time, ϵ_{ff} , as predicted from the single-free-fall [left panels] and multi-free-fall [right panels] models, as a function of the Mach number [upper panels], the virial parameter [middle panels], and the magnetic field strength [lower panels]. The purely hydrodynamical scenario is retrieved by setting $\beta \rightarrow \infty$. These are calculated using the fiducial values of $\phi_x \approx 1.12$ (Krumholz & McKee, 2005, KM05), $\theta \approx 0.35$ (Padoan & Nordlund, 2011, PN11), and $y_{\text{cut}} \approx 0.1$ (Hennebelle & Chabrier, 2013, HC13). The coloured lines represent the model predictions. The shaded coloured regions represent the upper and lower limits within the range of our adopted initial conditions (as shown in the legend of each plot). The vertical dashed lines show the result of varying the variable on the x-axis by the range assumed to represent the properties present within the “Brick”, i.e. the initial conditions for star formation within this region: $\beta = 0.11 - 0.61$, $\mathcal{M} = 11 \pm 3$, $\alpha = 4.3 \pm 2.3$ (Federrath et al., 2016) and $b = 0.33$ (see text). Here we adopt values of $\epsilon_{\text{core}} \approx 0.5$ and $\phi_t \approx 1.91$ for each model (Federrath & Klessen, 2012). The horizontal dotted regions represent the range of ϵ_{ff} for the star-forming sources within the $0.18 < l < 0.76^\circ$, $-0.12 < b < 0.13^\circ$ region (determined from both infrared and VLA embedded stellar mass estimates, see Table 4.6),⁹ accounting for the approximate factor of two uncertainty in ϵ_{ff} (i.e. $\epsilon_{\text{ff}} = 0.5 - 8$ per cent; see Section 4.5.3).

fiducial values from the original papers or those determined by Federrath & Klessen (2012) gives a range of predicted star formation rates which span several orders of magnitude (see Figure 4.10). In view of the above discussion, we point out that the verification or falsification of these star formation theories is fundamentally obstructed by the lack of consensus on the values of these free parameters.

4.6 Discussion and conclusions

In this work, we have utilised infrared *Spitzer* and *Herschel* observations, with the aim of investigating the lack of star formation within the extreme environment of the Galactic Centre (see Longmore et al., 2013a). To do this we have determined the star formation rate for the Galactic Centre as a whole (defined as $|l| < 1^\circ$ and $|b| < 0.5^\circ$), by using a variety of extra-galactic luminosity-star formation-rate conversions (which trace star formation within the last ~ 5 Myr). From the $24\ \mu\text{m}$, $70\ \mu\text{m}$, and the total infrared bolometric luminosity (determined from two component modified Planck function fits between $5.8 - 500\ \mu\text{m}$), we find average global star formation rates of $\sim 0.09 \pm 0.02\ M_\odot\ \text{yr}^{-1}$. These are comparable to previous measurements made from YSO counting and the free-free emission, which are sensitive to star formation over the last $\sim 0.1 - 3$ Myr. The conclusions that can be drawn from this analysis, are discussed below.

- i) We can rule out that systematic uncertainties in the star formation rate measurements are causing the apparent low star formation rate, unless this uncertainty affects all the methods in the same way, which seems unlikely.
- ii) The luminosity-SFR relations and YSO counting methods are consistent in the Galactic Centre. As the Galactic Centre is the most extreme environment for which it is possible to resolve individual forming stars and make this measurement, the results here provide confidence that the luminosity-SFR relations reliably trace the star formation rate over kpc scales within similar environments present in starburst galaxies, and high-redshift galaxies.

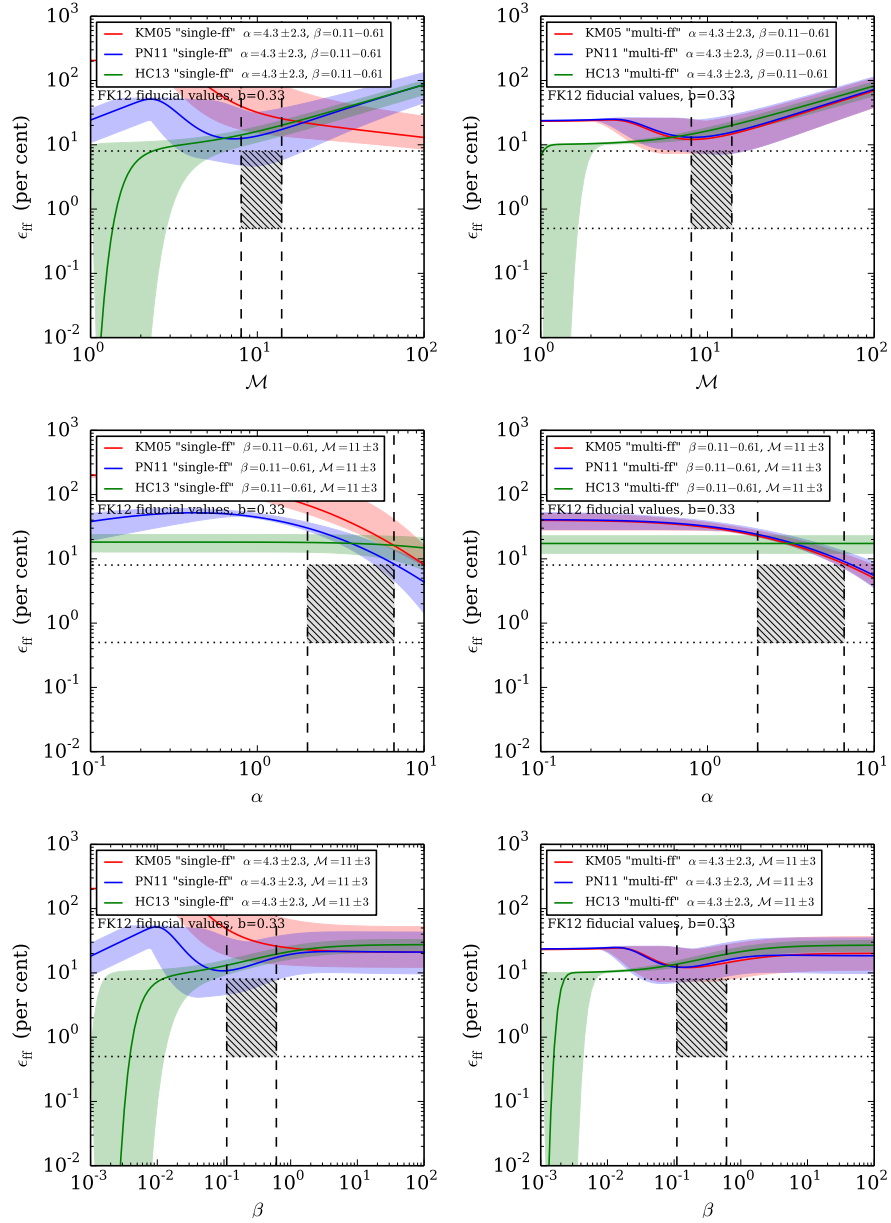


Figure 4.8: This figure is identical to Figure 4.7, however here we use the fiducial values determined by Federrath & Klessen (2012). For the single-free-fall models these are of $\phi_x \approx 0.17$ and $\phi_t = 0.2$ for KM05, $\theta \approx 0.7$ and $\phi_t = 0.7$ for PN11, and $y_{\text{cut}} \approx 4.5$ and $\phi_t = 4.8$ for HC13. For the multi-free-fall models these are of $\phi_x \approx 0.17$ and $\phi_t = 2.2$ for KM05, $\theta \approx 1.0$ and $\phi_t = 2.1$ for PN11, and $y_{\text{cut}} \approx 5.9$ and $\phi_t = 5.0$ for HC13.

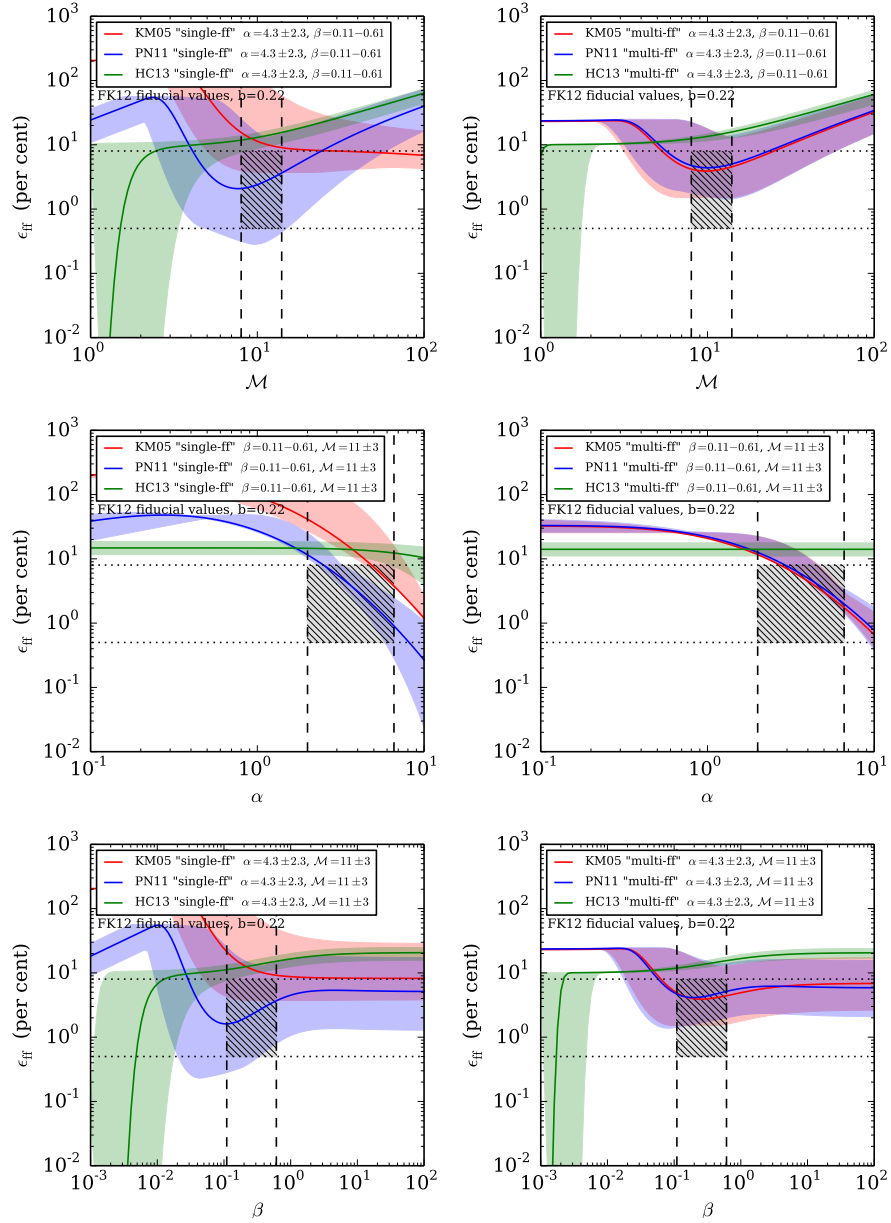


Figure 4.9: This figure is identical to Figure 4.7, however here we use the fiducial values determined by Federrath & Klessen (2012) and $b = 0.22$. For the single-free-fall models these are of $\phi_x \approx 0.17$ and $\phi_t = 0.2$ for KM05, $\theta \approx 0.7$ and $\phi_t = 0.7$ for PN11, and $y_{\text{cut}} \approx 4.5$ and $\phi_t = 4.8$ for HC13. For the multi-free-fall models these are of $\phi_x \approx 0.17$ and $\phi_t = 2.2$ for KM05, $\theta \approx 1.0$ and $\phi_t = 2.1$ for PN11, and $y_{\text{cut}} \approx 5.9$ and $\phi_t = 5.0$ for HC13.

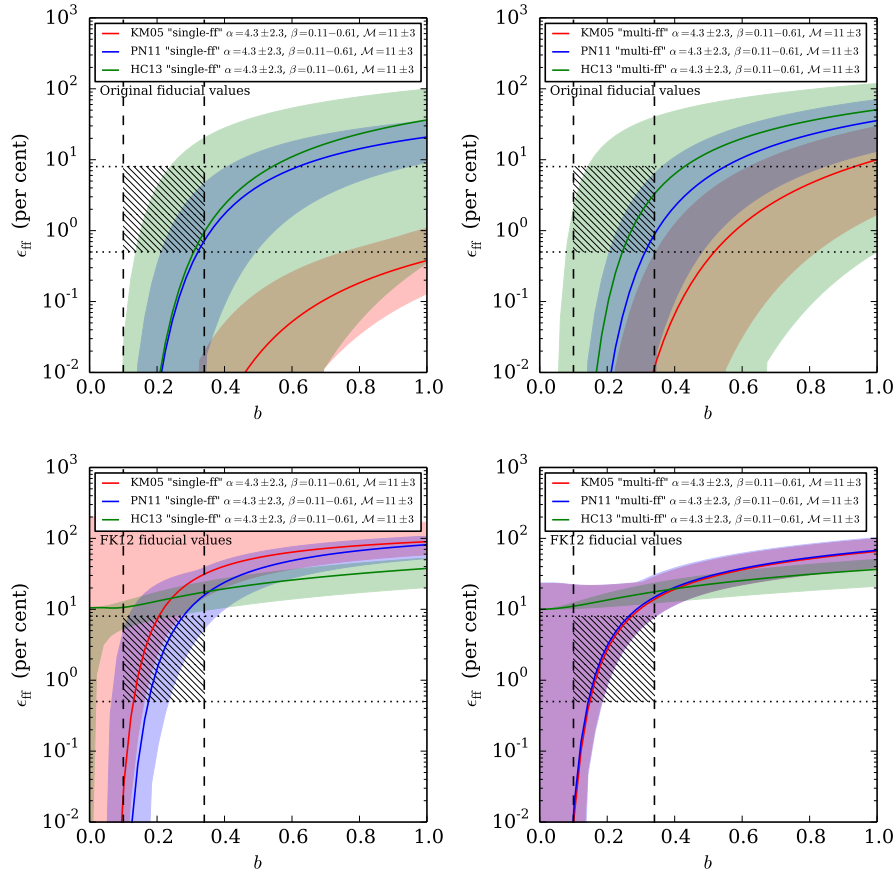


Figure 4.10: Plots of the star formation efficiency per free-fall time, ϵ_{ff} , as predicted from the single-free-fall [left panels] and multi-free-fall [right panels] models, as a function of turbulence driving parameter. In the upper panels we assume the fiducial values found by [KM05](#), [PN11](#) and [HC13](#), as in Figure 4.7. In the lower panels we assume fiducial values determined by [Federrath & Klessen \(2012\)](#), which are used in Figures 4.8 and 4.9. The fiducial values are summarised in Table 4.7. The coloured lines represent the model predictions. The shaded coloured regions represent the upper and lower limits within the range of our adopted initial conditions (as shown in the legend of each plot). The vertical dashed lines show the result of varying the variable on the x-axis by the range assumed to represent the turbulent driving parameter within the “Brick” of $b = 0.22 \pm 0.12$ ([Federrath et al., 2016](#)). The horizontal dotted regions represent the range of ϵ_{ff} for the star-forming sources within the $0.18 < l < 0.76^\circ$, $-0.12 < b < 0.13^\circ$ region (determined from both infrared and VLA embedded stellar mass estimates, see Table 4.6),⁹ accounting for the approximate factor of two uncertainty in ϵ_{ff} (i.e. $\epsilon_{\text{ff}} = 0.5 - 8$ per cent; see Section 4.5.3).

Table 4.7: Summary of parameters used for in the volumetric models shown in Figures 4.7, 4.8, and 4.9.

Figure	All models		KM05		PN11		Fiducial values		KM05		PN11		HC13	
	b	ϵ_{core}	single-free-fall		single-free-fall		single-free-fall		multi-free-fall		multi-free-fall		multi-free-fall	
			ϕ_t	ϕ_x	ϕ_t	θ	ϕ_t	y_{cut}	ϕ_t	ϕ_x	ϕ_t	θ	ϕ_t	y_{cut}
4.7	0.33	0.5	1.19	1.12	1.19	0.35	1.19	0.1	1.19	1.12	1.19	0.35	1.19	0.1
4.8	0.33	0.5	0.2	0.17	0.7	0.7	4.8	4.5	2.2	0.17	2.1	1.0	5.0	5.9
4.9	0.22	0.5	0.2	0.17	0.7	0.7	4.8	4.5	2.2	0.17	2.1	1.0	5.0	5.9

- iii) The global star formation rate has not changed by more than a factor of two to three from its current rate over the past few Myr. This is quantitatively consistent with models predicting that the star formation rate is episodic (Kruijssen et al., 2014), with a timescale of $\sim 10 - 20$ Myr (Krumholz & Kruijssen, 2015; Krumholz, Kruijssen & Crocker, 2016).

In an attempt to better understand the origin of the presently low star formation within the Galactic Centre, we have investigated the properties of several individual clouds and H II region complexes. These are thought to be at differing evolutionary stages and connected along a coherent gas stream within Galactic Centre (e.g. Henshaw et al., 2016b). In order to interpret the observations, two assumptions are made about how the gas clouds are related, and how star formation proceeds in this environment.

We make the assumption that the sources are orbiting along a coherent gas stream with known orbital parameters (Kruijssen, Dale & Longmore, 2015), and that star formation within these sources is triggered at the pericentre of the orbit (i.e. when compressive tidal forces are strongest; see Longmore et al., 2013b; Kruijssen, Dale & Longmore, 2015). The direct consequence of this scenario is that the regions reside on a common evolutionary timeline, which allows us to derive their star formation timescales and efficiencies. We estimate that the dense molecular clouds remain relatively quiescent for $0.3 - 0.5$ Myr after star formation is triggered, as these contain a stringent upper limit of few hundred solar masses of embedded stars (see Table 4.6, “Brick” to cloud “f”, i.e. the “dust-ridge” clouds). These then transition to very actively star-forming clouds, which contain a few thousand solar masses of stars, within only $0.2 - 0.4$ Myr (as seen towards Sgr B2). The feedback from these stars provides sufficient pressure to remove the remaining dense gas over a timescale of ~ 0.9 Myr (Barnes et al. in prep), which reveals the later stages of star formation (e.g. diffuse H II regions). We note that this division in phases represents the broad brush strokes according to which star formation proceeds in this region, and that the detailed physical picture will be considerably more complex. Nevertheless, this serves as a general model which can be refined in the future.

We take this simple star formation model for the CMZ and determine star formation rates for the sources in the $0.18 < l < 0.76^\circ$, $-0.12 < b < 0.13^\circ$ region. We find that on average the quiescent “dust-ridge” clouds have stringent upper limits of $< 0.007 M_\odot \text{ yr}^{-1}$, whereas the “star-forming clouds”, Sgr B2, G0.6, Sgr B1 and G0.3, have star formation rates in the range $\sim 0.002 - 0.045 M_\odot \text{ yr}^{-1}$. We find that $\sim 1 - 5$ per cent of a clouds gas mass is converted to stellar mass per free-fall time.

We use this Galactic Centre gas cloud data to quantitatively test the predictions of different star formation models/relations. We find that the [Lada, Lombardi & Alves \(2010\)](#) and [Lada et al. \(2012\)](#) column density limit relations significantly over predict the observed star formation rate in the quiescent clouds. The predictions for the star-forming sources (Sgr B2 etc), are in better agreement with the observed values.

As a first comparison to the volumetric models, we take the predictions presented by [Federrath et al. \(2016\)](#). These authors use the multi-free-fall model of [KM05](#) with the fiducial values of [Federrath & Klessen \(2012\)](#) to predict $\epsilon_{\text{ff}} = 4 \pm 3$ per cent within the “Brick”, which is consistent with the observed value of $\epsilon_{\text{ff}} \sim 2$ per cent.

Expanding on this, we compare our observed star formation rates to all the volumetric relations. Figure 4.7 shows that the [KM05](#) model does not accurately predict the star formation rate for any set of initial conditions, when using the fiducial values from the original models.

The middle row of Figure 4.7 shows that the [HC13](#) model is much more sensitive to variations in \mathcal{M} and β than the other models (i.e. turbulence and magnetic fields), which is a key signature of the [HC13](#) theory (and highlights the role of (shock)-turbulence in star-formation). The observational uncertainty in these properties for the “Brick”, therefore produce a large range of predicted ϵ_{ff} values for a fixed α . This makes verifying/falsifying the [HC13](#) model predictions more difficult than for the other models.

Figures 4.8 and 4.9 show the effect of using the fiducial values of [Federrath & Klessen \(2012\)](#), and choosing a value for the turbulent driving parameter of 0.33 and 0.22, respectively. The former value represents total solenoidal turbulent driving, whilst the

latter value is that determined for the “Brick” by [Federrath et al. \(2016\)](#). The ϵ_{ff} typically changes by an order of magnitude when adopting this range of the turbulent driving parameter. This again highlights the importance for self-consistently determining the values of the model free parameters.

In general, we find better agreement with the multi-free-fall models (i.e. those that allow for the density dependence of the free-fall time in their calculation) over the single-free-fall models, which could ultimately reflect their more accurate description of the hierarchical collapse of star-forming regions. In the future, we aim to use the unique laboratory of the Galactic Centre environment to test additional star formation models.

To summarise, we suggest that the total global (hundred parsec) scale star formation rate for the Galactic Centre appears to be over-predicted by the star formation models ([Longmore et al., 2013a](#)), as the majority of the gas is unbound (super-virial), despite it being very dense ([Kruijssen et al., 2014](#)). When investigating local (parsec) scales within gravitationally bound clouds, we find that several of the models accurately predict the star formation rate. However, a consensus on the free parameters of these models is required before reliable comparison to observations are possible.

Chapter 5

Investigating the Galactic Centre clouds with ALMA

5.1 Preface

This chapter presents work that is currently on-going, and will form the basis of future projects presented in Section 6.2. The observations for this chapter were originally proposed by S. Longmore, and collected by the staff at the ALMA telescope. The data reduction, analysis and interpretation were conducted by A. T. Barnes.

5.2 Introduction

This chapter presents high angular resolution observations of several Galactic Centre “dust-ridge” clouds; Clouds D and E/F.¹ As was highlighted in the previous chapter, these are thought to be still in the early stages of star/cluster formation; before the formation of any H II regions (e.g. Immer et al., 2012a), and reside within the high \mathcal{M} ,

¹The clouds covered were referred to following the nomenclature of Lis et al. (1999), who separated structures based on dust continuum emission, in the previous Chapter (i.e. “D”, “E” and “F”). However, recent analysis of molecular line observations suggest Clouds E and F may be physically linked (e.g. Henshaw et al., 2016b). Therefore, as they are covered by the same mosaic in the observations presented in this chapter, these are henceforth as a single cloud, “E/F”.

high β , and low ϵ_{ff} end of the parameter space. These are, therefore, the most promising regions within the Galactic Centre to potentially verify or falsify the volumetric star formation models.

The specific aim of these observations is to constrain the physical properties of these clouds, and through comparison with detailed hydrodynamic simulations of gas clouds on the known orbit in the Galactic Centre environment (Kruijssen, Dale et al. in prep.), also get a better handle on them, as well as accounting for a more detailed propagation of the observational uncertainties on the dimensionless ratios (taking into account the covariance of uncertainties; e.g. see Federrath et al., 2016). Ultimately, the goal is to be able to unambiguously distinguish between the star formation models. This chapter presents the reduction, both of the continuum and molecular lines, and initial investigation of the observations.

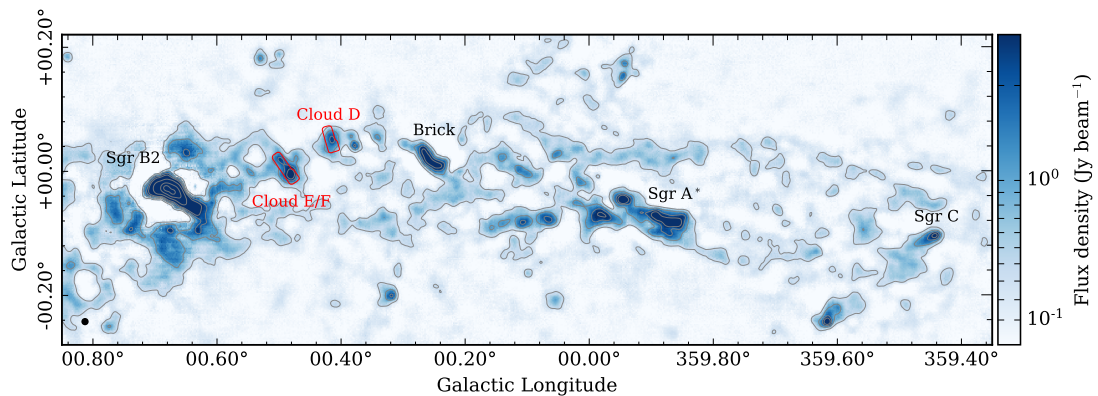


Figure 5.1: Map of the CMZ taken with the 10.4-meter diameter Caltech Submillimeter Observatory (CSO), as part of the BOLOCAM Galactic Plane Survey (BGPS; Ginsburg et al., 2013). Labeled are sources of interest within this region. Shown in red is the coverage of the ALMA Cloud D and Cloud E/F observations. Contours are of 0.3, 1, 2, 3, 7, 20 and 50 Jy beam⁻¹, which have been chosen to best highlight the sources of interest.

5.3 Observations

5.3.1 ALMA interferometric observations

To investigate the early stages of star formation within these regions on proto-stellar core scales, high spatial resolution dust continuum and molecular line ob-

servations have been taken with the Atacama Large Millimetre/sub-millimetre array (ALMA) as part of a Cycle 2 project (Project code: 2013.1.00617; Principal investigator: S.N.Longmore). The observations made use of the Band 6 receiver, with the correlator configured to use dual polarisation within four sidebands centred at approximately 250.5 GHz, 252.5 GHz, 265.5 GHz, and 267.5 GHz, each with a bandwidth of ~ 1875 MHz and a individual channel spacing of ~ 1050 kHz (equivalent to ~ 1.25 km s $^{-1}$; see Figure 1.8). These were carried out in April, August and September 2015 (see Table 5.1). During these dates, the configurations of 12 m and 7 m arrays had projected baseline ranges of 15.0 – 348.5 m and 8.9 – 48.9 m, respectively, which, at the average observed frequency of ~ 259 GHz, gives an combined approximate angular resolution of 1'' and a recoverable size scale up to $\sim 50''$. At this frequency, the primary beam sizes of the 12 m and 7 m dishes are $\sim 25''$ and $\sim 42''$ respectively. Given these, the mosaic covering Cloud D required 67 pointings with the 12 m array, and 36 pointings with the 7 m array, and the mosaic covering Cloud E/F required 88 pointings with the 12 m array, and 41 pointings with the 7 m array. More information regarding the on-source integration time for each array configuration, the observation date, and the bandpass, phase and amplitude calibrators are given in Table 5.1.

The observations were given a Quality-Assurance stage 0 “SemiPass” classification, as only around half of the 7m scheduling blocks were observed due to scheduling constraints. Cloud D had 3 out of 6 scheduling blocks completed, whilst Cloud E/F had 6 out of 8 scheduling blocks completed. These scheduling blocks are designed to be self-contained, such that all the calibrators are observed and the whole region is covered when the block is begun. The resultant maps, therefore, have the complete coverage, but are lacking in total integration time.² Given their “SemiPass” classification, these data were not subject to the pipeline reduction and QA2 stage, hence the raw data had to be manually calibrated. The calibration was done in the Common Astronomy Software Applications package CASA³ version 4.4.0 with assistance from the ALMA support scientist at the UK ALMA regional centre.

²The noise level of the final images were not greatly affected, however, as all the 12m scheduling blocks were taken and the 7m observations are down-weighted during the imaging process.

³see <https://casa.nrao.edu>

Table 5.1: Observations log. Shown are the sources, observation date, array configuration, total on-source integration time, and the sources used for the band pass, flux and phase calibrations.

Cloud	Date	Array	On-source time (hour:min:sec)	Band Pass calibrator	Flux calibrator	Phase calibrator
D	26/04/2015	12 m	01:10:39	J1733-1304, 1924-2914	Titan, Neptune	J1744-3116
D	13/08/2015	7 m	00:35:20	J1733-1304	Titan	J1744-3116
D	14/08/2015	7 m	00:41:59	J1733-1304	J1733-1304	J1744-3116
D	15/08/2015	7 m	00:28:41	1733-1304	J1733-1304	J1744-3116
E/F	26/04/2015	12 m	02:07:09	J1517-242, J1733-1304	Titan	J1744-3116
E/F	27/04/2015	12 m	00:46:26	J1733-1304	Titan	J1744-3116
E/F	18/08/2015	7 m	01:04:31	J1733-1304	Titan, Neptune	J1744-3116
E/F	03/09/2015	7 m	00:28:09	J1924-2914	Titan	J1744-3116
E/F	04/09/2015	7 m	00:14:51	J1924-2914	Titan	J1744-3116
E/F	20/09/2015	7 m	00:21:30	J1517-2422	Titan	J1744-3116

Table 5.2: Observational parameters.

Observational parameter	Cloud D	Cloud E/F
Synthesised beam:		
major axis, θ_{major} (")	1.47	1.27
minor axis, θ_{minor} (")	0.90	0.90
beam position angle, θ_{PA} (°)	-23.19	-00.01
Velocity Resolution (km s^{-1})	1.25	1.25
Continuum rms level, σ_{rms} (mJy beam^{-1}) ^a	0.4	0.6
Line rms level, σ_{rms} (K) ^b	0.1 [9 mJy beam ⁻¹]	0.07 [4 mJy beam ⁻¹]

a: The rms level determined across the full ~ 8 GHz bandwidth.

b: The rms level determined within a single 1.25 km s^{-1} channel.

As is common practice, after calibration we created rough images of the dataset for checking. Upon comparison with observations made with the SMA towards these sources (Walker et al., 2018), a clear offset of several arc seconds,⁴ between the bright, compact sources were noticed in both the clouds. This was a known problem with around 80 projects observed as part of Cycles 1 to 3, of which 2013.1.00617 is included. The problem was produced by the ALMA online system, which introduced a small mislabelling of the position of each field. This was due to an inconsistency between the procedure for computing the coordinates that are stored in the field table of the data by the online software, and the procedure for computing the delay propagation and antenna pointing coordinates. The issue only affected programs that intended to either map extended areas around a reference (mosaics) or used offset pointings from a reference position. For such maps, this problem would result in a distortion of the final image, which was dependent on the distance from the reference position, the coordinates of the reference position and the size of the area mapped (for mosaics). Therefore, in addition to the normal astrometric uncertainty, the positions derived from these images have a systematic error whose magnitude depends on the above factors (see ALMA User Support Ticket ID: 6347). This issue was corrected by the European ALMA Regional Centre, and the raw data was again downloaded and reduced following the scripts previously produced. Several pointings on the upper right side of the 12m mosaic of both clouds were not observed, as a consequence of this issue. These result in the irregular final mosaic coverages shown in Figures 5.2 and 5.3.

As with the previous calibration, rough images of the final calibrated dataset were produced for checking abnormalities. Given that none were then present, the next step was to identify the channel ranges which contain strong line emission (see Figures 5.8 and 5.9). These channels were then masked and a first-order polynomial was fit to the remaining channels using the task UVCONTSUB⁵. This task produces a “model” continuum dataset, which is subtracted from the original dataset to produce a continuum subtracted dataset. The latter of these is used for molecular line imaging, and the

⁴The magnitude of this systematic offset was 3.6'' and 2.2'' for Cloud D and Clouds E/F, respectively.

⁵It is preferable to do this at this stage, rather than post imaging with the IMCONTSUB routine.

former for continuum imaging.⁶

The calibrated continuum and line emission data sets were imaged with clean process TCLEAN in CASA-4.7.0. This was chosen over the standard CLEAN function for its increased functionality and improved stability. For example, testing showed that CLEAN would begin to diverge from a solution at much lower cleaning cycles compared to TCLEAN. This would be particularly evident towards sources of bright emission at the edge of the mapped region, where large negative bowls would spread across the map with increasing severity at progressively higher clean cycles.

Initially, a “basic” set of parameters (i.e. a “hogbom” deconvolver and a single run with large iterations) was used in clean. The produced images, however, contained many artefacts and had high noise levels (i.e. significantly higher than the theoretical noise limits). To produce the best image quality (e.g. with minimal side-lobe structure), the cleaning was done in an iterative process. The data were cleaned down to a given noise level (with a “multiscale” deconvolver), and then the image checked. If required, the mask is then adjusted, and the clean is continued down to a lower noise threshold. The steps of this process are:

- i) The “dirty” image is produced by setting the number of clean cycle iterations to zero. On which, an initial image mask corresponding to some high multiple of the noise is produced (typically $\sim 10 \sigma_{\text{rms}}$). The mask is then pruned such that structures smaller than a given multiple of the beam size are removed (typically ~ 3 beams), hence removing any noise spikes taken into the mask.
- ii) The initial mask is applied in the TCLEAN function, which effectively informs clean where to find the brightest, and therefore most likely real, structures within the map. This is allowed to iterate until a threshold is reached. At the first pass of this stage, the threshold should be reasonably high (typically $\sim 10 \sigma_{\text{rms}}$), such that only the bright structures are cleaned, and to make sure clean doesn’t

⁶Using the model continuum dataset for continuum imaging is, however, not advised in the imaging guidelines. To test this, the cleaned maps produced using the continuum “model” output – used throughout this work – and produced when masking the line channels in the whole cube in TCLEAN, are compared. The results for both clouds are practically identical in structure, and have only a < 10 per cent difference in fluxes, which is within flux calibration uncertainty limit.

begin to diverge early. This should leave the weaker (presumably more extended) emission in the residual image produced after this cleaning stage.

- iii) A new mask is then made from the residual image produced in stage ii), which has a lower multiple of the noise and a higher multiple of the beam size for pruning than used in the previous masking stage (typically around a factor of two lower threshold and a factor of two larger in beam size than previously used). This mask should then encompass more of the larger scale, weaker emission.
- iv) The mask from step iii) is then used in clean, with the image from step ii) as the starting model. Using the image as the starting model allows clean to continue from step ii), taking into account the information of the bright emission (i.e. effectively removing it before clean begins), such that clean can focus on the lower level, larger scale emission.

The steps iii) and iv) are then repeated until an acceptable image is reached, or the deconvolved image begins to unavoidably diverge from a sensible solution (e.g. producing large negative bowls in the image). Cleaning the images via this method of dynamically altering the mask, rather than directly cleaning the image down to a threshold of a given sigma level, enhances the lower level, diffuse emission, whilst suppressing artefacts commonly seen in interferometric images, which have a similar structure to the emission we believe is real (e.g. large-scale striping across the image).

The final images produced for Cloud D have angular beam sizes of [θ_{major} : 1.47", θ_{minor} : 0.90", θ_{PA} : -23.19°],⁷ a $1 \sigma_{\text{rms}}$ continuum sensitivity in the combined single dish image of $\sim 0.4 \text{ mJy beam}^{-1}$, and a $1 \sigma_{\text{rms}}$ sensitivity within a 1.25 km s^{-1} channel of $\sim 0.1 \text{ K}$ ($\sim 9 \text{ mJy beam}^{-1}$).⁸ The final images produced for Cloud E/F have angular beams sizes of [θ_{major} : 1.27", θ_{minor} : 0.90", θ_{PA} : -00.01°], a $1 \sigma_{\text{rms}}$ continuum sensitivity in the combined single dish image of $\sim 0.6 \text{ mJy beam}^{-1}$, and a $1 \sigma_{\text{rms}}$ sensitivity within a 1.25 km s^{-1} channel of $\sim 0.07 \text{ K}$ ($\sim 4 \text{ mJy beam}^{-1}$). These values are summarised in Table 5.2.

⁷[major axis, minor axis, beam position angle]

⁸The total power array was not included in these observations, hence the line data are the combined ALMA 12m and 7m only.

5.3.2 Combination of the ALMA and single dish continuum observations

Single dish continuum observations taken with the 10.4-meter diameter Caltech Submillimeter Observatory (CSO), as part of the BOLOCAM Galactic Plane Survey (BGPS; Ginsburg et al., 2013), were used to recover the zero-spacing (i.e. the missing uv -coverage of the interferometer). The BGPS is a publicly available,⁹ 1.1 mm survey of dust emission in the Northern Galactic plane, covering longitudes $-10^\circ < l < 90^\circ$ and latitudes $|b| < 0.5^\circ$ with a typical rms sensitivity of 30 – 100 mJy in a $\sim 33''$ beam. These observations were chosen as they closely match the frequency and coverage of the ALMA observations, whilst having a moderate crossover between CSO dish size (10.4 m) and the smallest baseline of the ALMA observations (8.9 m). Crossover in dish size is important for the combination of the single dish and interferometric observations, such that the absolute flux scaling of the images can be determined (i.e. such that the flux in the single dish image is conserved).

Before combining the single dish and interferometric observations, the single dish observations were modified. Firstly, as the BOLOCAM observations are at a slightly different frequency to the ALMA dish observations, the flux was scaled in accordance with,

$$\frac{F_{\text{ALMA}}}{F_{\text{BOLOCAM}}} = \left(\frac{\nu_{\text{ALMA}}}{\nu_{\text{BOLOCAM}}} \right)^{\alpha_\nu} \approx \left(\frac{259}{272} \right)^{3.7} \approx 0.8 \quad (5.1)$$

where F (units of Jy beam $^{-1}$) and ν (units of GHz) are the continuum intensities and approximate central frequencies of the ALMA and BOLOCAM observations, which are denoted in the subscript. Ginsburg et al. (2013) found that the spectral index from the BOLOCAM to higher frequency *Herschel* observations is approximately $\alpha_\nu \sim 3.7$, which is consistent with typical dust emissivity index measurements in the range $1.5 < \beta (= \alpha - 2) < 2$. The BOLOCAM image was then regridded and cropped to the same pixels grid and coverage of the ALMA observations. The “feathering” is used to combine the prepared BOLOCAM image and ALMA image. This works by taking the Fourier transforms of both images, summing them with a weighting factor

⁹http://irsa.ipac.caltech.edu/data/BOLOCAM_GPS/

applied to each image, and taking the inverse transform to produce a combined image (see Cotton, 2017). During this, the weighting is adjusted such that the flux of the single dish observations is conserved. For this, the FEATHER function from CASA-version 4.7.0 is used with the default parameter set for effective dish size, single dish scaling and low pass filtering of the single dish observations. Before this combination procedure, the ALMA image was corrected for the primary beam response, which has the effect of pronouncing emission towards the edge of the mosaic, where the antenna response (or sensitivity) is lower.

Shown in Figures 5.2 and 5.3 are the BGPS single dish only, and 12m and 7m from ALMA, and the 12m, 7m and single-dish maps towards Clouds D and E/F, respectively.

5.3.3 ALMA line observations

To identify the lines across both of the clouds, spectra were extracted from the cleaned and continuum subtracted data cube at several positions across the map. These positions were chosen to include both the peaks and the more diffuse continuum emission, and thereby not limited by any a priori assumption on where lines would be detected. Doing so was important, as Rathborne et al. (2015) found that molecular line emission with ALMA Band 3 observations were typically not well correlated with the continuum emission towards another molecular cloud within the dust-ridge; the Brick (see Figure 5.1). To identify molecular transitions responsible for any detected emission peak, the frequency was firstly adjusted to the source velocities of $\sim 29 \text{ km s}^{-1}$, and then compared to the rest frequency of the lines within the Splatalogue spectral line database.¹⁰ When multiple line transitions are present in the database with frequencies in agreement with that observed, the emission was attributed to the transition with the lowest upper state energies (usually in the range of 10 - 300 K). The lines detected within each cloud are presented in Tables 5.3, 5.7 and 5.8, with their rest frequencies and upper state energies (also see Figure 5.8 and 5.9 for example spectrum). For comparison, in Tables 5.3, 5.7 and 5.8 are the lines which are detected towards the Brick

¹⁰<http://www.splatalogue.net>

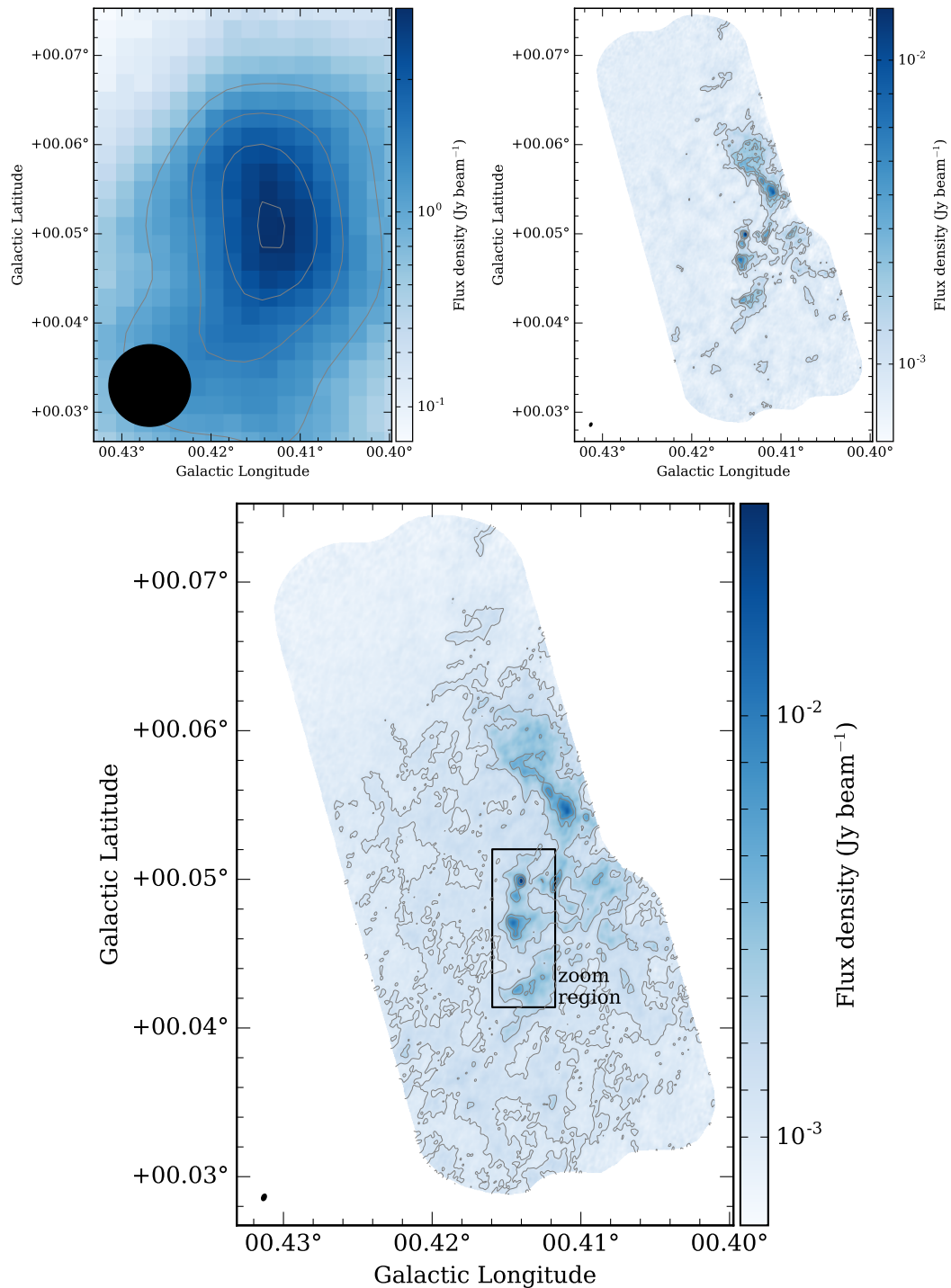


Figure 5.2: Continuum observations towards Cloud D. The upper left panel shows the single dish observations from the BGPS (Ginsburg et al., 2013), overlaid with contours of [1, 1.5, 2, 2.5] Jy beam $^{-1}$. The upper right panel shows the combined 12m and 7m map from ALMA, overlaid with contours of [6, 15, 20, 30] σ_{rms} , where $\sigma_{\text{rms}} \sim 0.2$ mJy beam $^{-1}$. The lower panel shows the combined (or “feathered”) 12m, 7m and single dish map, overlaid with contours of [4, 6, 15, 20, 30] σ_{rms} , where $\sigma_{\text{rms}} \sim 0.4$ mJy beam $^{-1}$. Contours for each panel have been chosen to best highlight the structure in the map, and the lower left of each panel shows the beam size. The rectangle shows the “zoom region” used for the moment maps in the Appendix.

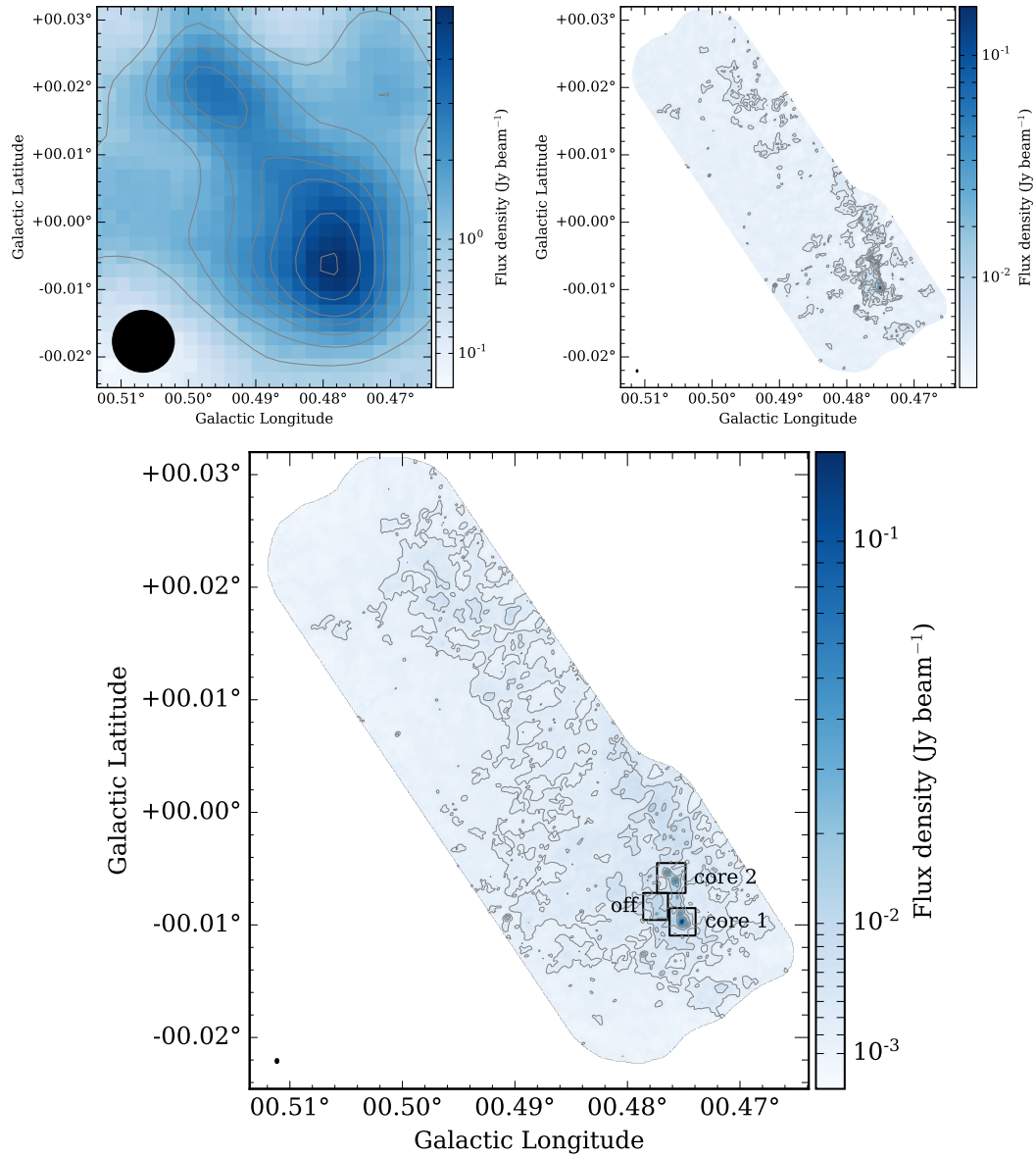


Figure 5.3: Continuum observations towards Cloud E/F. The upper left panel shows the single dish observations from the BGPS (Ginsburg et al., 2013), overlaid with contours of [1, 1.5, 2, 2.5, 3, 4, 5] Jy beam^{-1} . The upper right panel shows the combined 12m and 7m map from ALMA, overlaid with contours of [6, 15, 30, 50, 150] σ_{rms} , where $\sigma_{\text{rms}} \sim 0.2 \text{ mJy beam}^{-1}$. The lower panel shows the combined (or “feathered”) 12m, 7m and single dish map, overlaid with contours of [4, 8, 15, 30, 50] σ_{rms} , where $\sigma_{\text{rms}} \sim 0.6 \text{ mJy beam}^{-1}$. Contours for each panel have been chosen to best highlight the structure in the map, and the lower left of each panel shows the beam size. The rectangles show the “core 1”, “core 2” regions used for the moment maps and spectra in Figures 5.8, 5.9, 5.10 and 5.11. Also shown is the “off”-position used in Figure 5.13.

molecular cloud, from complementary Band 6 ALMA observations (to be presented by Contreras et al. in prep). Table A.1 gives frequencies of lines that were detected yet not identified. These have been adjusted for the assumed source velocity, such that they represent the rest frequency of the associated transition.

5.4 Results

An in-depth kinematic and chemical analysis of these clouds using all the detected lines would require a significant amount of work, which will be split over several future papers (see Section 6.2). As the reduction of these observations has only recently been completed, this section presents only some very preliminary analysis of these regions.

5.4.1 Preliminary results: moment maps analysis

Moment map analysis has been used to investigate the kinematic structure of both clouds. As previously discussed in Section 3.5, there are issues in using the moment map technique within kinematically complex regions, however this is used here to gain a very basic picture of the structures within both clouds. A range of structures are observed within the both clouds, which appear to be very similar to those seen in disc IRDCs: extended, filamentary and core structures. It is found that each of the molecular transitions appear to typically trace one of these structures, and, therefore, the transitions are grouped into the following categories: “extended” across the entire mapped region (i.e. across 2 – 8 pc); “moderately extended” up to a contour level of $\sim 10\sigma_{\text{rms}}$ (or $\sim 5 \text{ mJy beam}^{-1}$; i.e across 1 – 2 pc); “compact” within a contour level of $\sim 20\sigma_{\text{rms}}$ (or $\sim 10 \text{ mJy beam}^{-1}$; i.e. $< 1 \text{ pc}$). These are shown in Table 5.3.

The moment maps for HCN $v=0(3-2)$ and HCO⁺ $(3-2)$ across Cloud D are shown in Figure 5.4, and across Cloud E/F are shown in Figure 5.5. These are both the brightest, with peak intensities of 3 – 15 K, and most extended of the observed molecular transitions across both clouds. For comparison, the emission from a less extended molecule c-HCCCH $v=0(7(0,7)-6(1,6))$ towards both clouds is shown in Figure 5.6.

Table 5.3: Table of the molecules identified in Cloud D and EF. Also show are those identified within the Brick using a similar spectral set-up with ALMA (Contreras et al. in prep). Columns show the molecule name, the transition, the frequency, the upper energy level of the transition, and the extent of the emission within each of the clouds.

Molecule	Transition	Rest frequency (GHz)	Upper energy (K)	Cloud D	Cloud E/F	Brick
HCN $v=0$	(3 – 2)	265.8864	25.5	extended	extended	extended
HCO ⁺	(3 – 2)	267.5576	25.7	extended	extended	extended
c-HCCCH $v=0$	7(0,7) – 6(1,6)	251.3143	50.7	compact	moderately extended	not detected
CH ₂ NH	4(1,3) – 3(1,2)	266.27	39.8	compact	moderately extended	not detected
CH ₂ NH	6(0,6) – 5(1,5)	251.4212	64.1	not detected	compact	not detected
CH ₂ NH	7(1,6) – 7(0,7)	250.1617	97.2	not detected	compact	not detected
CH ₃ NH ₂	J = 6 – 5, K = 0 – 0, A1 – A2	265.7572	44.7	not detected	moderately extended	not detected
NO	J = 5/2 – 3/2, $\Omega = 1/2$, F = 5/2+– 3/2–	250.4407	19.2	not detected	moderately extended	not detected
NO	J = 5/2 – 3/2, $\Omega = 1/2$, F = 7/2– 5/2+	250.7964	19.3	not detected	moderately extended	not detected
NO	J = 5/2 – 3/2, $\Omega = 1/2$, F = 5/2– 3/2+	250.8156	19.3	not detected	moderately extended	not detected
NH ₂ CHO	12(2,11) – 11(2,10)	253.1658	91.1	not detected	compact	not detected
NH ₂ CHO	13(0,13) – 12(0,12)	267.0626	90.9	not detected	compact	not detected
t-CH ₃ CH ₂ OH	4(4, 1) – 3(3, 0)	252.9514	28.5	not detected	compact	not detected
t-HCOOH	3(2, 2) – 3(0, 3)	265.2353	19.2	not detected	compact	not detected
HDCO	4(1, 3) – 3(1, 2)	268.292	40.2	not detected	compact	not detected
SO $^3\Sigma v=0$	5(6) – 4(5)	251.8258	50.7	not detected	moderately extended	core
SO $^3\Sigma v=0$	3(4) – 4(3)	267.1978	28.7	not detected	compact	not detected
¹³ CH ₃ CN	14(1) – 13(1)	250.0882	97.2	not detected	compact	not detected
¹³ CH ₃ CN	15(1) – 14(1)	267.9453	110.0	not detected	compact	not detected
¹³ CH ₃ CN	15(3) – 14(3)	267.9051	167.3	not detected	compact	not detected
¹³ CH ₃ OH $vt=0$	15(4,11) – 16(3,13)	252.3666	368.1	not detected	compact	not detected
CH ₃ COH $vt=0$	15(0,15) – 14(1,14) A ++	267.7251	109.2	not detected	compact	not detected
CH ₃ OCH ₃	15(1,14) – 14(2,13) EE	249.9245	112.6	not detected	compact	not detected
SO ₂ $v=0$	13(1,13) – 12(0,12)	251.1997	82.2	not detected	compact	not detected
SO ₂ $v=0$	8(3,5) – 8(2,6)	251.2106	55.2	not detected	compact	not detected

Table 5.4: Continued from Table 5.3.

Molecule	Transition	Rest frequency (GHz)	Upper energy (K)	Cloud D	Cloud E/F	Brick
$^{13}\text{CH}_3\text{CH}_2\text{CN}$	30(2,28) – 29(2,27)	265.9686	202.8	not detected	not detected	core
$^{13}\text{CH}_3\text{CH}_2\text{CN}$	32(1,32) – 31(1,31)	267.6009	214.2	not detected	not detected	core
$\text{CH}_3^{13}\text{CH}_2\text{CN}$	30(8,23) – 29(8,22)	267.6089	268.3	not detected	not detected	core
$^{13}\text{CH}_3\text{CH}_2\text{CN}$	32(0,32) – 31(0,31)	267.6489	214.2	not detected	not detected	core
$^{13}\text{CH}_3\text{CN}$	15(8) – 14(8)	267.6288	557.9	not detected	not detected	core
$\text{CH}_3\text{OH vt}=0$	13(3,10) – 13(2,11) – +	250.2912	261.0	not detected	compact	not detected
$\text{CH}_3\text{OH vt}=0$	11(0,11) – 10(1,10) + +	250.507	153.1	not detected	moderately extended	not detected
$\text{CH}_3\text{OH vt}=0$	12(3,9) – 12(2,10) – +	250.6352	230.8	not detected	compact	not detected
$\text{CH}_3\text{OH vt}=0$	11(3,8) – 11(2,9) – +	250.9244	203.0	not detected	compact	not detected
$\text{CH}_3\text{OH vt}=0$	10(3,7) – 10(2,8) – +	251.1641	177.5	not detected	compact	not detected
$\text{CH}_3\text{OH vt}=0$	9(3,6) – 9(2,7) – +	251.3599	154.2	not detected	compact	not detected
$\text{CH}_3\text{OH vt}=0$	7(3,4) – 7(2,5) – +	251.6417	114.8	not detected	compact	not detected
$\text{CH}_3\text{OH vt}=0$	6(3,3) – 6(2,4) – +	251.7385	98.5	not detected	compact	not detected
$\text{CH}_3\text{OH vt}=0$	5(3,2) – 5(2,3) – +	251.8119	84.6	not detected	moderately extended	not detected
$\text{CH}_3\text{OH vt}=0$	4(3,1) – 4(2,2) – +	251.8666	73.0	not detected	compact	not detected
$\text{CH}_3\text{OH vt}=0$	5(3,3) – 5(2,4) + –	251.8909	84.6	not detected	compact	not detected
$\text{CH}_3\text{OH vt}=0$	6(3,4) – 6(2,5) + –	251.8957	98.5	not detected	compact	not detected
$\text{CH}_3\text{OH vt}=0$	4(3,2) – 4(2,3) + –	251.9005	73.0	not detected	compact	not detected
$\text{CH}_3\text{OH vt}=0$	3(3,0) – 3(2,1) – +	251.9058	63.7	not detected	compact	not detected
$\text{CH}_3\text{OH vt}=0$	3(3,1) – 3(2,2) + –	251.917	63.7	not detected	compact	not detected
$\text{CH}_3\text{OH vt}=0$	7(3,5) – 7(2,6) + –	251.9236	114.8	not detected	compact	not detected
$\text{CH}_3\text{OH vt}=0$	8(3,6) – 8(2,7) + –	251.9847	133.4	not detected	compact	not detected
$\text{CH}_3\text{OH vt}=0$	9(3,7) – 9(2,8) + –	252.0904	154.2	not detected	compact	not detected
$\text{CH}_3\text{OH vt}=0$	10(3,8) – 10(2,9) + –	252.2528	177.5	not detected	compact	not detected
$\text{CH}_3\text{OH vt}=0$	11(3,9) – 11(2,10) + –	252.4856	203.0	not detected	compact	not detected
$\text{CH}_3\text{OH vt}=0$	12(3,10) – 12(2,11) + –	252.8034	230.8	not detected	compact	not detected

Table 5.5: Continued from Table 5.3.

Molecule	Transition	Rest frequency (GHz)	Upper energy (K)	Cloud D	Cloud E/F	Brick
CH ₃ OH vt = 0	13(3,11) – 13(2,12) +	253.2214	261.0	not detected	compact	not detected
CH ₃ OH vt = 0	5(2,3) – 4(1,3)	266.8381	57.1	not detected	extended	core
CH ₃ OH vt = 0	9(0,9) – 8(1,7)	267.4034	117.5	not detected	compact	not detected
CH ₃ OH vt = 1	5(1,4) – 6(2,5) -	265.2244	360.0	not detected	compact	not detected
CH ₃ OH vt = 0	14(3,11) – 14(2,12) -+	249.8874	293.5	not detected	compact	not detected
CH ₃ OCHO v = 0	20(3,17) – 19(3,16) E	250.2465	134.3	not detected	compact	not detected
CH ₃ OCHO v = 0	20 (3,17) – 19 (3,16) A	250.2584	134.3	not detected	compact	not detected
¹³ CH ₂ CHCN	28(1,28) – 27(1,27)	250.2648	176.9	not detected	compact	not detected
¹³ CH ₃ CN	14(3) – 13(3), F = 13 – 12	250.0506	154.4	not detected	compact	not detected
¹³ CH ₃ CN	14(2) – 13(2), F = 13 – 12	250.0741	118.7	not detected	compact	not detected
CH ₃ CH ₂ CN v = 0	28(7, 22) – 27(7,21)	251.0378	229.1	not detected	compact	not detected
¹³ CH ₃ CN	14(0) – 13(0), F = 13 – 12	250.0929	90.0	not detected	compact	not detected
CH ₃ CHO vt = 0	13(6,8) – 12 (6,7) A -	250.5991	165.4	not detected	compact	not detected
CH ₃ CHO vt = 1	13(-5, 9) – 12(-5,8) E	250.6804	345.6	not detected	compact	not detected
CH ₃ CHO vt = 0	13(4,9) – 12 (4, 8) E	250.8292	120.3	not detected	compact	not detected
CH ₃ CHO vt = 0	13(-4,10) – 12(-4,9) E	250.8532	120.3	not detected	compact	not detected
CH ₃ CH ₂ CN v = 0	28(10,18) – 27(10, 17)	250.8828	285.6	not detected	compact	not detected
CH ₃ CH ₂ CN v = 0	28(11,17) – 27(11,16)	250.8904	308.9	not detected	compact	not detected
CH ₃ CH ₂ CN v = 0	28(9,20) – 27(9,19)	250.8972	264.5	not detected	compact	not detected
CH ₃ CHO vt = 0	13(3,11) – 12(3,10) A ++	250.9346	104.6	not detected	compact	not detected
CH ₃ CH ₂ CN v = 0	28(8,21) – 27(8,20)	250.9433	245.7	not detected	compact	not detected
CH ₃ OCHO v = 0	31(3,28) – 31(3,29)E	250.9664	298.5	not detected	compact	not detected
CH ₃ OCHO v = 0	31(3,28) – 31(2,29)E	250.9718	298.5	not detected	compact	not detected
CH ₃ CHO vt = 0	13(-3, 11) – 12(-3, 10) E	251.0954	104.6	not detected	compact	not detected
CH ₃ NH ₂	8(2) E 1 – 1 – 8(1) E 1–1	251.1287	92.2	not detected	compact	not detected
CH ₃ OCH ₃	21(5,16) – 21(4,17) EE	251.1425	245.8	not detected	compact	not detected

Table 5.6: Continued from Table 5.3.

Molecule	Transition	Rest frequency (GHz)	Upper energy (K)	Cloud D	Cloud E/F	Brick
CH ₃ CH ₂ CN v=0	32(6, 27) – 32(5,28)	251.19	267.2	not detected	compact	not detected
CH ₃ OCHO v=1	20(6,14) – 19(6,13) E	251.2644	148.9	not detected	compact	not detected
CH ₃ OCHO v=1	20(6,14) – 19(6,13) A	251.2857	148.8	not detected	compact	not detected
t-CH ₃ CH ₂ OH	7(3,5) – 6(2,4)	251.3017	34.8	not detected	compact	not detected
CH ₃ CH ₂ CN v=0	28(5,23) – 27(5,22)	251.6071	202.6	not detected	compact	not detected
NH ₂ CHO	19(3,16) – 19(2,17)	251.6275	221.8	not detected	compact	not detected
CH ₃ CH ₂ CN v=0	28(4, 25) – 27(4,24)	251.6688	192.7	not detected	compact	not detected
¹³ CH ₃ OH	17(3,14) – 17(2,15) -+	251.7961	396.5	not detected	compact	not detected
NH ₂ D	9(1,9)0a – 8(3,6)0a	252.4456	644.6	not detected	compact	not detected
CH ₃ CHO vt=1	13(-2,11) – 12(-2,10) E	252.6812	299.8	not detected	compact	not detected
CH ₃ SH v=0	10(2) – 9(2) A	252.7877	85.9	not detected	compact	not detected
CH ₃ NH ₂	2(2)B1 – 2(1)B1	252.8122	22.6	not detected	compact	not detected
CH ₃ SH v=0	10(4) – 9(4)A	252.8415	136.2	not detected	compact	not detected
CH ₃ SH v=0	10(4) – 9(4)E	252.8438	138.3	not detected	compact	not detected
CH ₃ SH v=0	10(-4) – 9(-4)E	252.8484	139.5	not detected	compact	not detected
¹³ CH ₃ OH vt=0	15(3,12) – 15(2,13) -+	252.8702	321.8	not detected	compact	not detected
CH ₃ SH v=0	10(3) – 9(3) E	252.8805	107.4	not detected	compact	not detected
CH ₃ CH ₂ CN v=0	28(4,24) – 27(4,23)	252.896	192.9	not detected	compact	not detected
CH ₃ NH ₂	6(2)E1+1 – 6(1) E 1 – 1	252.9088	60.7	not detected	compact	not detected
³⁴ SO	6(6) – 5(5)	253.207	55.7	not detected	compact	not detected
¹³ CH ₃ OH vt=0	14(3,11) – 14(2,12)	253.3102	287.8	not detected	compact	not detected
NH ₂ CHO	18(1,17) – 18(0,18)	253.3742	181.2	not detected	compact	not detected
HCCCHO	6(2,5) – 6(0,6)	253.4494	21.6	not detected	compact	not detected
¹³ CH ₃ OH vt=0	20(3,17) – 20(2,18)	249.6889	525.5	not detected	compact	not detected
CH ₃ CH ₂ CN v=0	26(6,20) – 26(5,21)	252.9669	191.0	not detected	compact	not detected
CH ₃ SH v=0	10(2) – 9(2) E	252.984	86.6	not detected	compact	not detected

Table 5.7: Continued from Table 5.3.

Molecule	Transition	Rest frequency (GHz)	Upper energy (K)	Cloud D	Cloud E/F	Brick
t-CH ₃ CH ₂ OH	16(0,16) – 15(1,15)	264.662	110.3	not detected	compact	not detected
g-CH ₃ CH ₂ OH	16(0,16) – 15(0,12) v _t = 0–0	264.6763	166.4	not detected	compact	not detected
HNCO v = 0	12(1,11) – 11(1,10)	264.6937	125.8	not detected	compact	not detected
CH ₃ CH ₂ CN v = 0	30 (1,29) – 29(1,28)	264.7479	201.8	not detected	compact	not detected
g-CH ₃ CH ₂ OH	16(0,16) – 15(0,15), v _t = 1–1	264.9156	171.1	not detected	compact	not detected
CH ₃ OCHO v = 1	21(6,15) – 20(6,14) E	265.0026	161.6	not detected	compact	not detected
H ₂ NCH ₂ CN	5(2,3) – 4(1,4)	265.094	24.2	not detected	compact	not detected
CH ₃ OCH ₃	13(7,6) – 12(7,5), F = 13 – 12	265.1527	1266.7	not detected	compact	not detected
g-CH ₃ CH ₂ OH	26(4,22) – 26(3,23)	265.4924	363.1	not detected	compact	not detected
t-DCOOH	12(4,8) – 11(4,7)	265.6835	118.5	not detected	compact	not detected
CH ₃ CH ₂ CN v = 0	32(6,26) v = 0 – 31(7,25) v = 0	265.6959	282.3	not detected	compact	not detected
CH ₃ OCHO v = 1	23(19,5) – 22(19,4)	265.7523	372.3	not detected	compact	not detected
CH ₃ ¹³ CHCN	2(2,0) – 3(1,3)	266.162	157.2	not detected	compact	not detected
CH ₂ CHCN v ₁₁ =1	22 – 21	266.6688	147.2	not detected	compact	not detected
CH ₃ OH vt=0	5(3,3) – 4(3,2), J = 9/2 – 7/2, F ₁ = 4 – 3, F = 7/2 – 5/2	266.704	43.3	not detected	compact	not detected
CH ₃ OCHO v = 0	30(3,27) – 30(2,28), F = 57/2 – 59/2	266.8194	465.2	not detected	compact	not detected
CH ₃ OH vt=1	19(13,7) – 18(16,2)	266.8719	405.7	not detected	compact	not detected
CH ₃ OCHO v = 1	48(13, 35) – 48(12,36)	267.0111	761.4	not detected	compact	not detected
CH ₃ ¹³ CH ₂ CN	51(7,44) – 51(6,45)	267.0307	621.5	not detected	compact	not detected
CH ₃ OCH ₃	16(7,9) – 16(4,12) EE	267.1694	103.7	not detected	compact	not detected
¹³ CH ₃ CN	15(5) – 14(5), F = 14 – 14	267.8256	281.7	not detected	compact	not detected
CH ₂ CH ¹³ CN	15(3,13) – 15(2,14)	267.8602	131.8	not detected	compact	not detected
¹³ CH ₃ CN	20(3,18) – 19(2,17)	267.8698	98.1	not detected	compact	not detected
¹³ CH ₃ CN	15(2) – 14(2), F = 14 – 15	267.9302	131.5	not detected	compact	not detected
¹³ CH ₃ CN	15(0) – 14(0), F = 16 – 15	267.9503	102.9	not detected	compact	not detected

Table 5.8: Continued from Table 5.3.

Molecule	Transition	Rest frequency (GHz)	Upper energy (K)	Cloud D	Cloud E/F	Brick
N ₂ HCHO	22(17,6)– 21(17,5) E	267.9635	529.3	not detected	compact	not detected
CH ₃ CH ₂ CN v = 0	30(6,24) – 29(6,23)	268.0025	238.1	not detected	compact	not detected
CH ₃ C ³ N	8(1,7) – 7(1,6)	268.0138	71.1	not detected	compact	not detected
g-CH ₃ CH ₂ OH	13(9,5) – 14(8,6)	268.0612	128.9	not detected	compact	not detected
CH ₃ CHO	19(14,5) – 18(14,4)	268.3066	363.6	not detected	compact	not detected
CH ₃ OCHO v = 0	57(5,53) – 57(4,54)	268.3167	736.6	not detected	compact	not detected
CH ₃ ¹³ CH ₂ CN	30(5,26) – 29(5,25)	268.3457	226.3	not detected	compact	not detected
t-HCOOH	7(2,6) – 7(0,7)	268.4132	42.9	not detected	compact	not detected
CH ₃ OCHO v = 1	21(6,15) – 20(6,14) A	265.0248	161.6	not detected	compact	not detected
CH ₃ NH ₂	22(4,19) – 21(4,18) A	264.8557	346.6	not detected	compact	not detected
CH ₂ CH ¹³ CN	22(4,19) – 21(4,18) A	264.8704	346.6	not detected	compact	not detected
CH ₃ OCH ₃	28(5,24) – 28(4,25) EE	264.8097	405.9	not detected	compact	not detected
CH ₃ OCHO v = 1	24(1,23) – 23(1,22) E	267.7802	355.1	not detected	compact	not detected
¹³ CH ₃ CN	14(5) – 13(5), F = 13 – 12	249.9755	268.9	not detected	compact	not detected
CH ₃ CHO vt=1	13(10,4) – 12(10,3) A	249.9893	514.0	not detected	compact	not detected
¹³ CH ₃ CN	14(4) – 13(4), F = 15 – 14	250.0177	204.5	not detected	compact	not detected
CH ₃ OCHO v = 0	12(5, 8) – 12(3,9)	250.147	179.2	not detected	compact	not detected
t-CH ₃ CH ₂ OH	18(2,16) – 17(3,15)	250.3618	152.0	not detected	compact	not detected
g-CH ₃ CH ₂ OH	12(2,11) – 11(1,10)	250.4898	70.2	not detected	compact	not detected
CH ₃ CHO vt=1	33(2,31) – 32(3,30)	250.5245	253.2	not detected	compact	not detected
CH ₃ CHO vt=1	13(6,8) – 12(6,7) A -	250.5591	165.4	not detected	compact	not detected
CH ₃ CH ₂ CN v = 0	13(-5,8) – 12(-5,7) E	250.6722	140.6	not detected	compact	not detected
CH ₃ CHO vt=1	30(6,24) – 30(5,25)	251.2752	239.1	not detected	compact	not detected

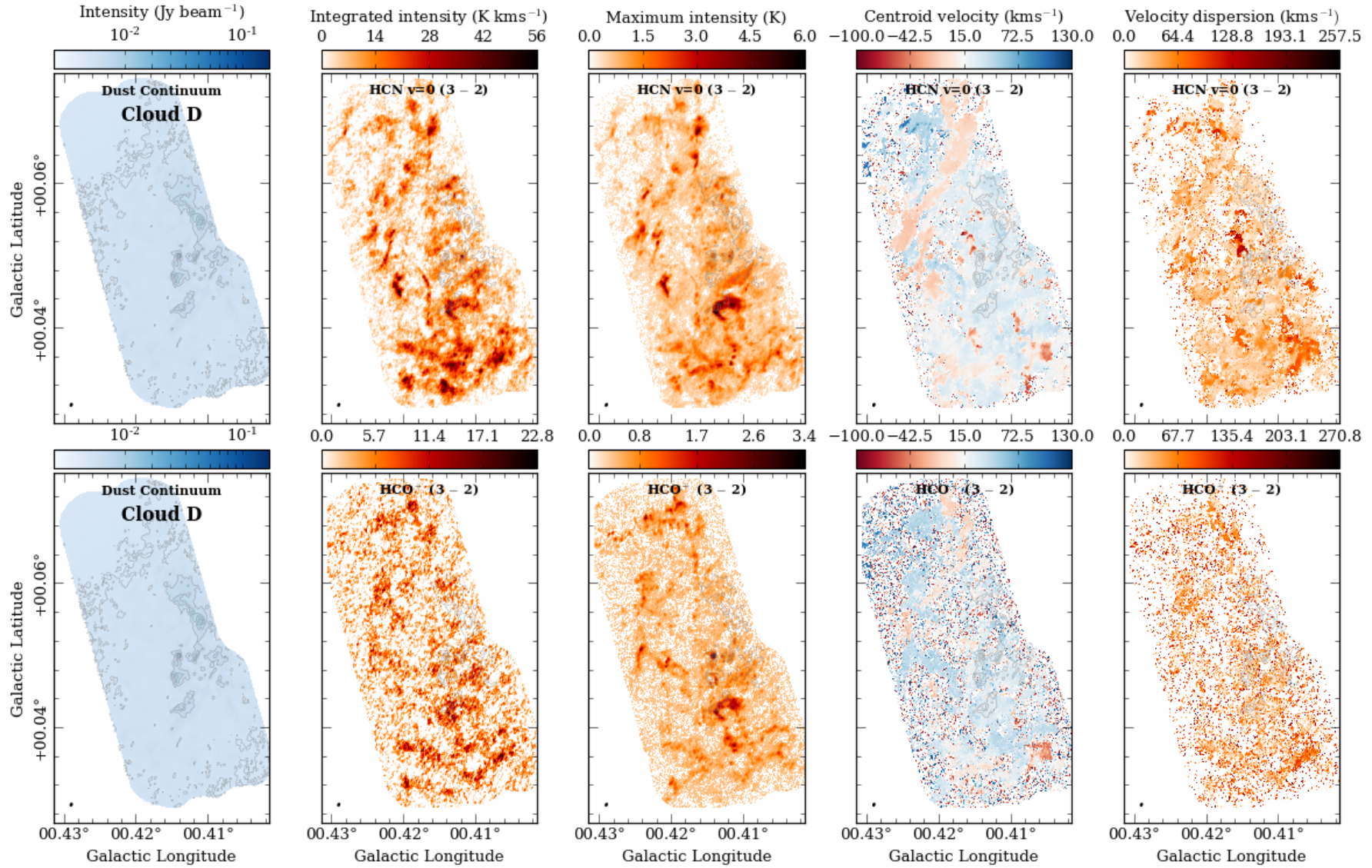


Figure 5.4: Moment maps of HCN $v=0(3-2)$ [upper row] and $\text{HCO}^+(3-2)$ [lower row] towards Cloud D (see table 5.3), with the molecule labeled at the top of each map. Shown from left to right for each molecule are the combined 12m, 7m and single dish continuum map, and moment maps of the integrated intensity, peak intensity, intensity weighted centroid velocity, and intensity weighted velocity dispersion. Contours on each map are of the continuum shown in levels of $[8, 15, 20, 30] \sigma_{\text{rms}}$, where $\sigma_{\text{rms}} \sim 0.4 \text{ mJy beam}^{-1}$.

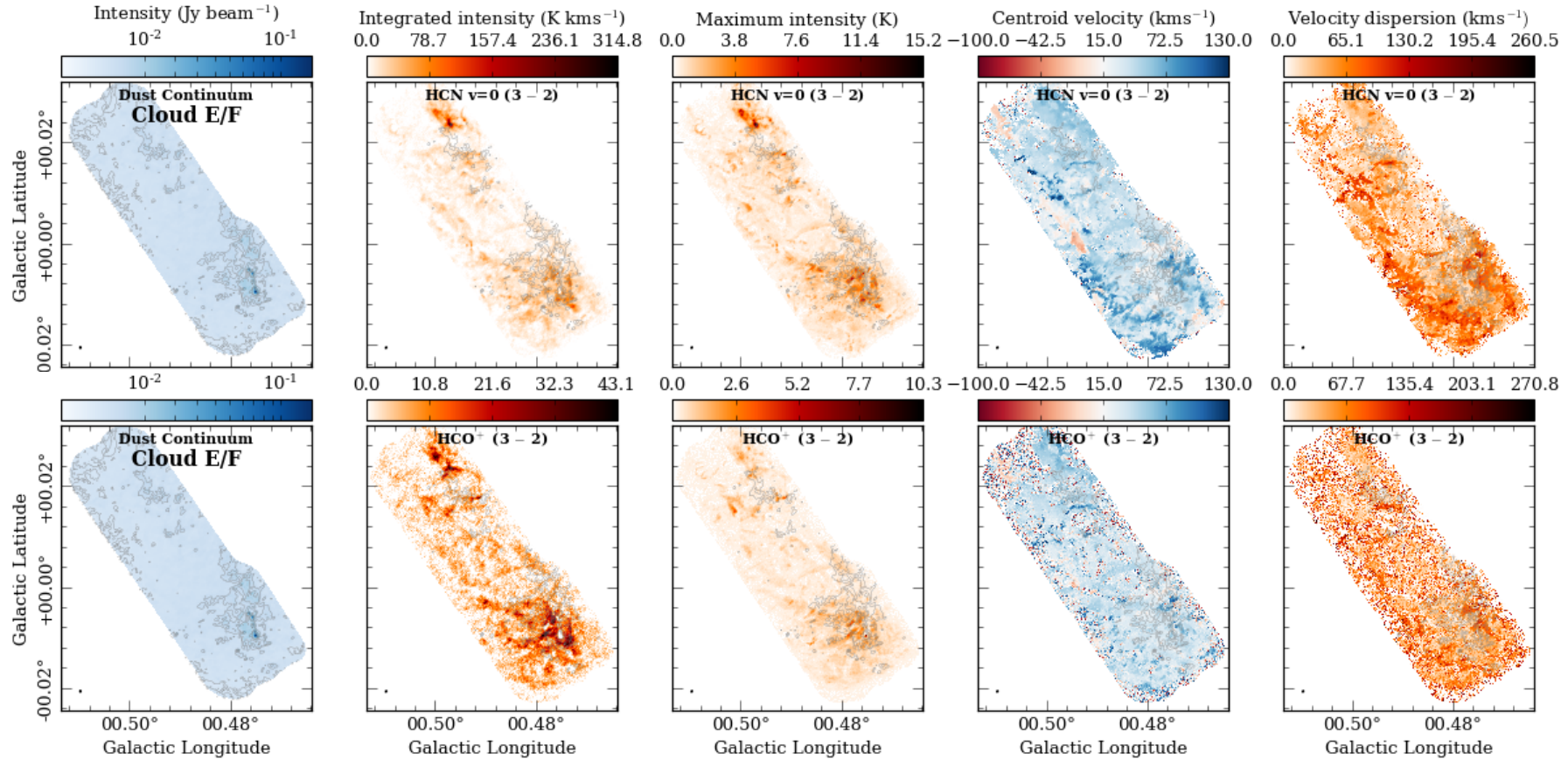


Figure 5.5: Moment maps of HCN $v=0(3-2)$ [upper row] and $\text{HCO}^+(3-2)$ [lower row] towards Cloud E/F (see table 5.3), with the molecule labeled at the top of each map. Shown from left to right for each molecule are the combined 12m, 7m and single dish continuum map, and moment maps of the integrated intensity, peak intensity, intensity weighted centroid velocity, and intensity weighted velocity dispersion. Contours on each map are of the continuum shown in levels of $[8, 15, 30, 50] \sigma_{\text{rms}}$, where $\sigma_{\text{rms}} \sim 0.6 \text{ mJy beam}^{-1}$.

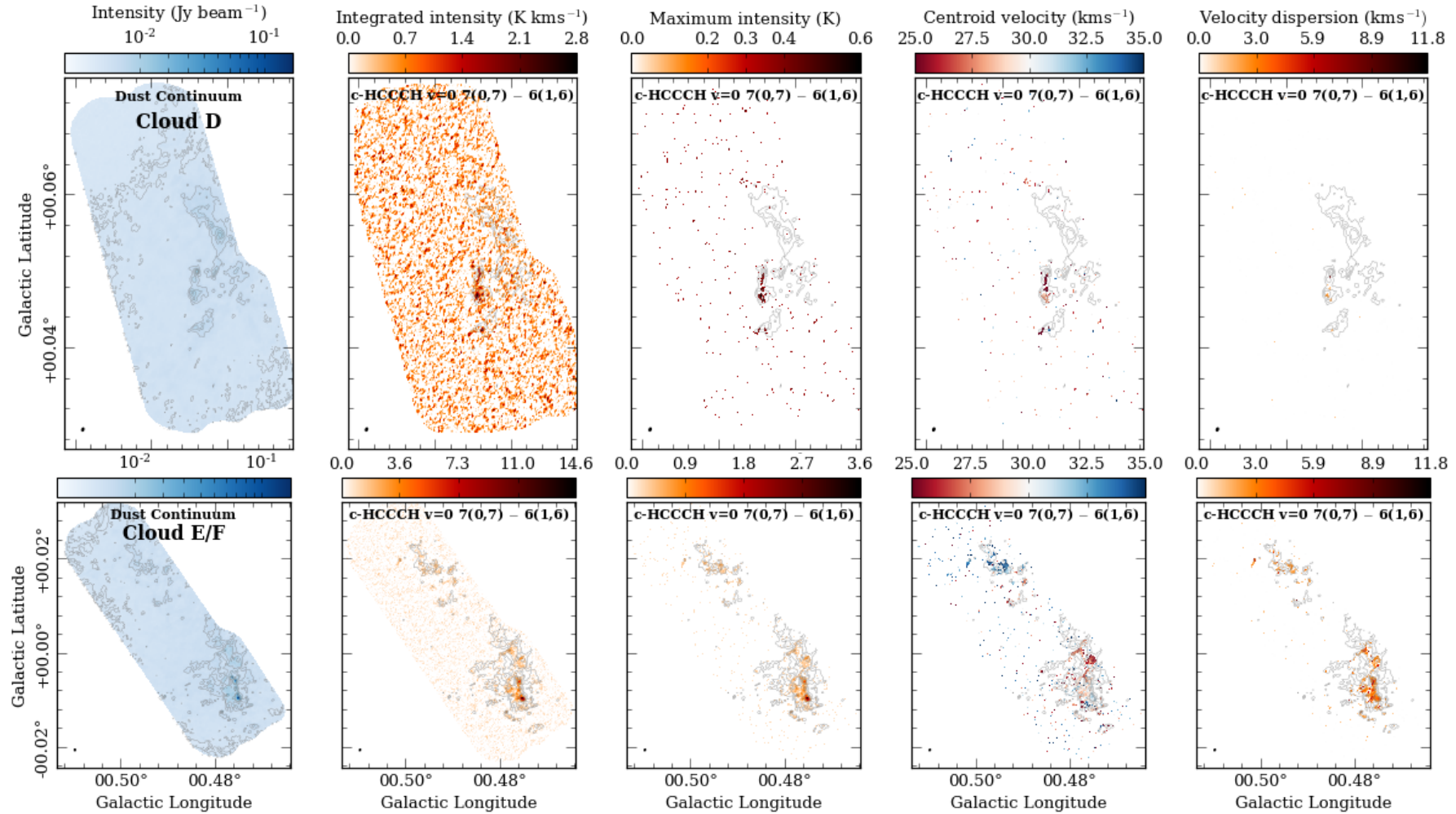


Figure 5.6: Moment maps of c-HCCCH $v=0$ $7(0,7) - 6(1,6)$ towards Clouds D [upper row] and Cloud E/F [lower row]. Shown from left to right for each molecule are the combined 12m, 7m and single dish continuum map, and moment maps of the integrated intensity, peak intensity, intensity weighted centroid velocity, and intensity weighted velocity dispersion. Contours on each map are of the continuum shown in levels of $[8, 15, 30, 50] \sigma_{\text{rms}}$, where $\sigma_{\text{rms}} \sim 0.6 \text{ mJy beam}^{-1}$.

Table 5.9: The properties of the cores within Cloud E/F (see Figure 5.3), assuming temperatures that are respective of the observed gas temperatures within the Galactic Centre (Krieger et al., 2017). Columns show measured radius and calculated gas mass and number density of molecular hydrogen for both cores.

Source	T K	R (pc)	M_{gas} (M_{\odot})	n_{H_2} (10^6 cm^{-3})
“core 1”	20	0.044	260.0	10.7
“core 2”	20	0.029	70.0	9.8
“core 1”	100	0.044	40.0	1.6
“core 2”	100	0.029	10.0	1.5

The remaining moment maps are presented in Appendix A. It is clear from this analysis that both clouds have a very complex velocity structure, showing many discrete intensity peaks (ranging in peak intensity 0.1 – 15 K) and a broad range of centroid velocities and velocity dispersions (both ranging from a few km s^{-1} to over a hundred km s^{-1}).

5.4.2 Preliminary results: examination of the cores

As previously discussed, the clouds observed in this chapter are thought to reside within the same extreme environment, have similar gas masses and ages (see Chapter 4). Therefore, these should harbour similar evolutionary stages of star formation. To investigate this, shown in Figure 5.7 is the combined 12 m, 7 m and single-dish maps towards both clouds plotted on the same colour-scale, overlaid with the same contour levels, and plotted such that the spatial scales are comparable. This figure highlights that, for the most part, these two clouds are indeed very similar in terms of their structure and intensity of emission (linearly convertible into a column density; see Section 1.1). However, one immediately obvious difference is the presence of several compact cores towards the south of Cloud E/F. These have been identified as “core 1” and “core 2” here, which are shown as squares on Figure 5.3. Table 5.9 presents the measured radius, R , and gas mass, M_{gas} , and number density of molecular hydrogen, n_{H_2} , calculated for two gas temperature estimates (Krieger et al., 2017), for each core region.

Along with showing a peak in continuum intensity, these cores also show strong line emission. The whole spectral coverage of the observations towards the two core regions is shown in Figures 5.8, 5.9, 5.10 and 5.11. Overlaid lines show adjusted frequency of all the spectral lines; those in blue have been identified, whereas those in red (also represented by the question mark) are those that are currently unidentified. Moments maps of these lines for both cores regions are presented in Appendix A.

Out of the two cores, core 1 is the brightest and shows the most line emission within the spectrum, with over 100 detected molecular transitions. One detection of interest is NH_2CHO (formamide), for which the following four transitions are detected: $12(2,11) - 11(2,10)$, $13(0,13) - 12(0,12)$, $19(3,16) - 19(2,17)$, $18(1,17) - 18(0,18)$. The strongest two of these detections are shown as moment maps and spectra in Figure 5.12. Formamide is an amide derived from formic acid, and has the potential to form guanine (one of the nucleic acids in DNA and RNA). This detection, therefore, shows that prebiotic molecules can be present even within the extreme environment of the Galactic Centre outside of Sgr B2 and Sgr A* (e.g. Rubin et al., 1971; Gottlieb et al., 1973; Lazareff, Lucas & Encrenaz, 1978).

A further interesting result towards this core region are the strong features seen the $\text{HCN } v=0(3-2)$ and $\text{HCO}^+(3-2)$ emission (see Figures 5.5). To better show this, Figure 5.13 present moment maps towards this compact regions, with spectra of both transitions also shown. For comparison, also shown are spectra towards the “off-position” shown in Figure 5.3. These lined both show strong absorption features at the rest velocity of the source (shown by the vertical dashed line), and at lower velocities (around 0 km s^{-1}). These could indicate that these transitions are very optically thick within this region, potentially due to the high density ($\sim 10^{6-7} \text{ cm}^{-3}$; see Table 5.9). Optically thick lines can be used to trace infall motions within core regions, where an asymmetry double peaked profile is produced due to cores geometry (Evans, 1999; Myers, Evans & Ohashi, 2000). Typically the asymmetry is such that the blue-shifted peak is brighter than the red-shifted peak of the profile, as is observed towards the off-position spectra. This, however, is not seen in the core 1 region spectra, where a blue-shifted peak appears to be weaker than the red-shifted peak for $\text{HCN } v=0(3-2)$,

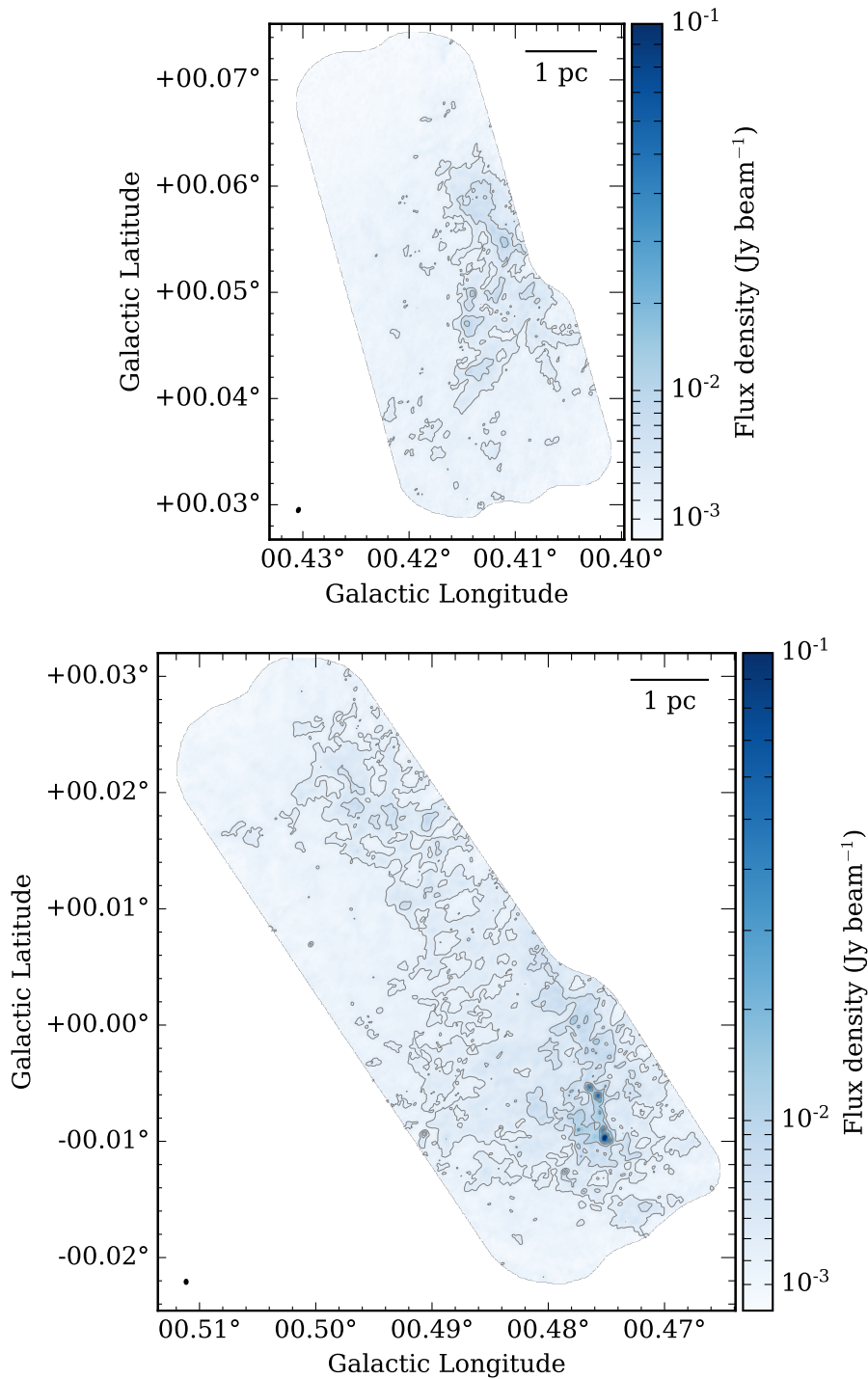


Figure 5.7: The combined 12m, 7m and single dish continuum maps towards Cloud D and Cloud E/F, shown in the upper and lower panels, respectively. These have been plotted on the same colour-scale and overlaid with the same contour levels of [2.4, 4.8, 9, 18, 30] mJy beam $^{-1}$, to highlight the comparative brightness of the core regions within Cloud E/F. Furthermore, these have been plotted on the same size scale, as shown by the scale bar in the upper right of each panel.

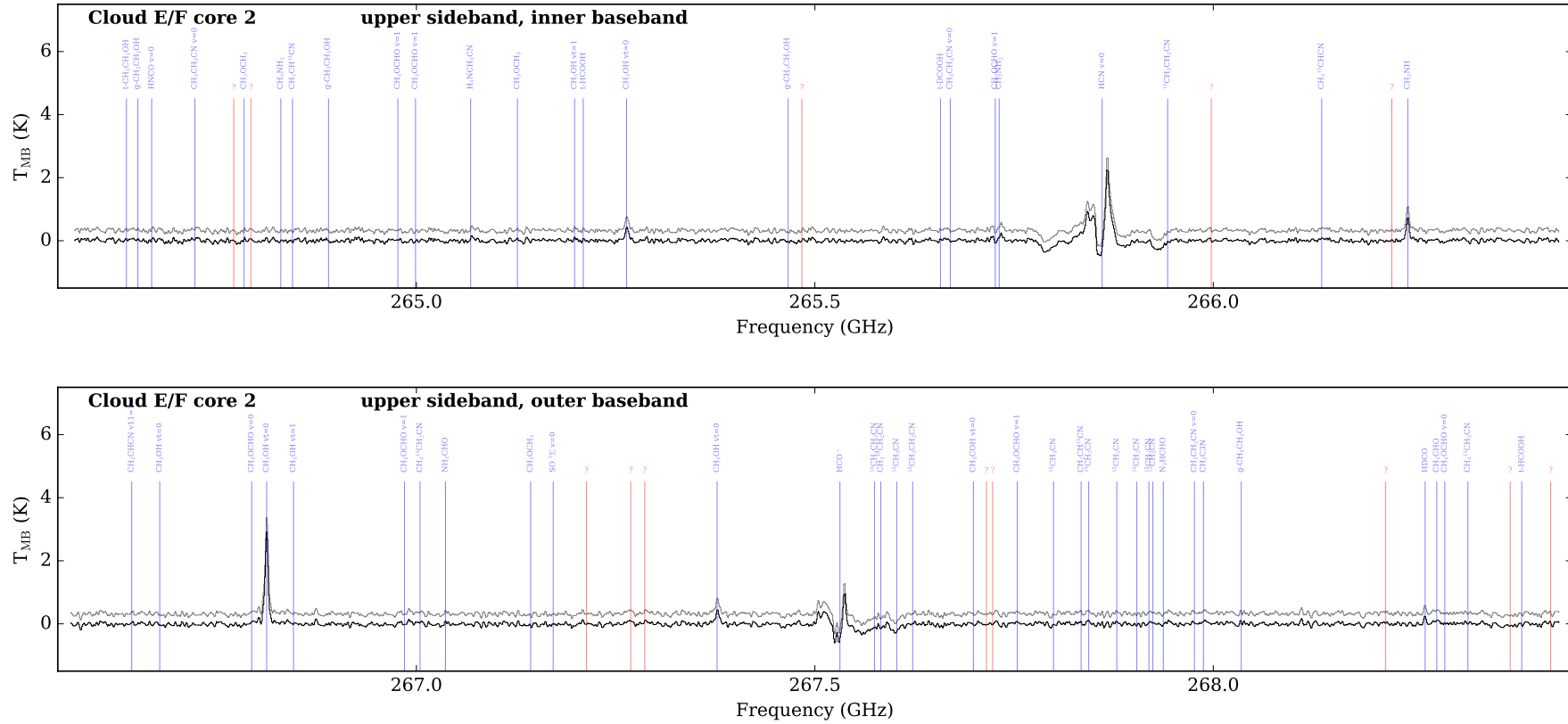


Figure 5.11: The upper sideband, inner [upper panel] and outer [lower panel] basebands, spectra towards the Cloud E/F core 2 for the, both with and without the continuum level subtracted [lower and upper line, respectively]. Labeled are the detected molecules [shown in blue], where the question marks show those which have not been identified [shown in red]. Moment maps and spectra of the individual lines are given in the Appendix.

and almost completely missing for HCO^+ (3 – 2). An explanation for this is currently unclear.

5.5 Summary

This chapter presents the early results from high angular resolution observations of the Galactic Centre “dust-ridge” clouds, Clouds D and E/F. These are thought to be still in the early stages of star/cluster formation; before the formation of any H II regions (e.g. [Immer et al., 2012a](#)), and reside within the high \mathcal{M} , high β , and low ϵ_{ff} end of the parameter space. These are, therefore, the most promising regions within the Galactic Centre to potentially verify or falsify the volumetric star formation models.

The ultimate aim of these observations is to constrain the physical properties of these clouds, and through comparison with detailed hydrodynamic simulations of gas clouds on the known orbit in the Galactic Centre environment ([Kruijssen, Dale et al. in prep.](#)), also get a better handle on them, as well as accounting for a more detailed propagation of the observational uncertainties on the dimensionless ratios (taking into account the covariance of uncertainties; e.g. see [Federrath et al., 2016](#)).

Preliminary analysis of these observations shows that these clouds appear to share similar structures to those observed within disc IRDCs, such as filamentary and core structures. They also appear to have a very complex kinematic structure, harbouring velocity dispersions an order of magnitude higher than disc IRDCs (i.e. hundreds of km s^{-1} compared to a few km s^{-1} , c.f. [Figures 5.4 and 5.5](#) to [Figure 3.3](#)). One particularly interesting result is the identification of a dense core region within Cloud E/F, which appears to contain a rich chemistry (with more than 100 molecular line transitions identified across the ~ 8 GHz bandwidth). Of these, four transitions from the prebiotic molecule formamide, a precursor to the DNA and RNA constituent guanine, have been identified. Furthermore, strong absorption features in $\text{HCN } v=0(3-2)$ and $\text{HCO}^+(3-2)$ have been identified towards this region. An explanation for this is currently unclear, however, they could be suggestive of infall motions towards this core

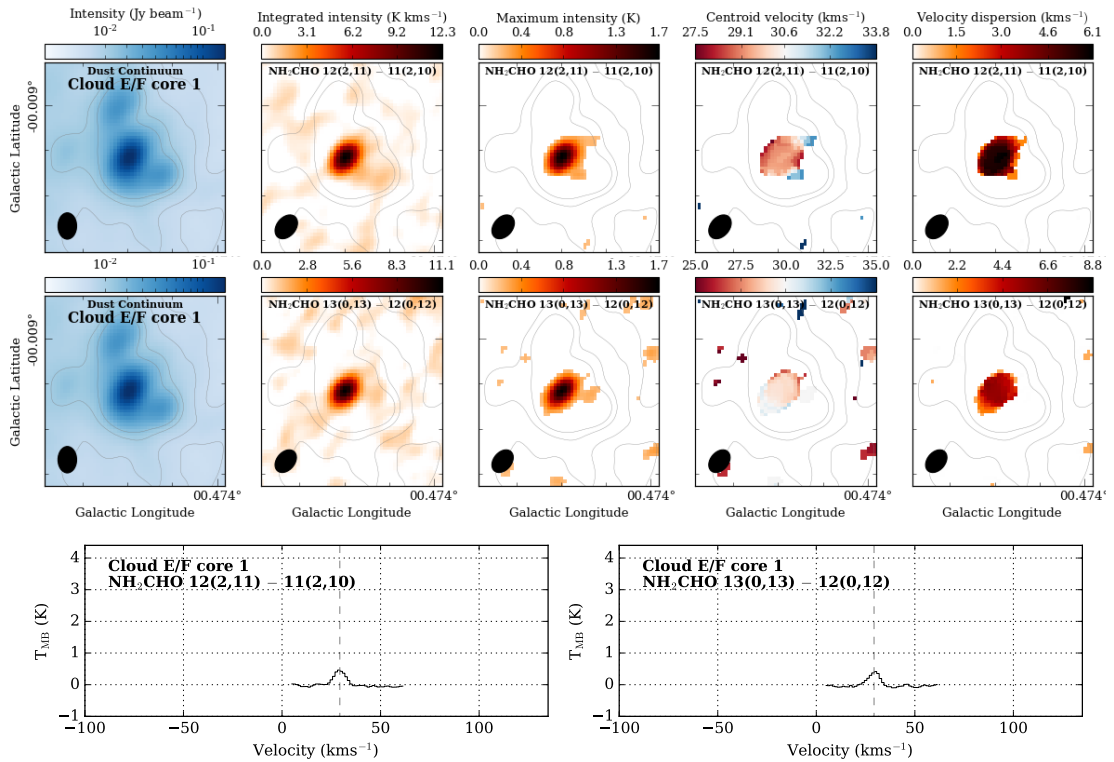


Figure 5.12: [upper two rows] Moment maps of NH_2CHO (formamide) towards Cloud E/F core 1. The analysis for the different molecular transitions are presented in each row, with the molecule labeled at the top of each map. Shown from left to right for each molecule are the combined 12m, 7m and single dish continuum map, and moment maps of the integrated intensity, peak intensity, intensity weighted centroid velocity, and intensity weighted velocity dispersion. Contours on each map are of the continuum shown in levels of [8, 15, 30, 50] σ_{rms} , where $\sigma_{\text{rms}} \sim 0.6 \text{ mJy beam}^{-1}$. [lower row] Spectra of the molecules towards the cores, where the vertical dashed line shows the assumed source centroid velocity.

region. Given that this core region could already contain $\sim 300 M_{\odot}$ of gas, this has the potential to form a very high-mass star in future.

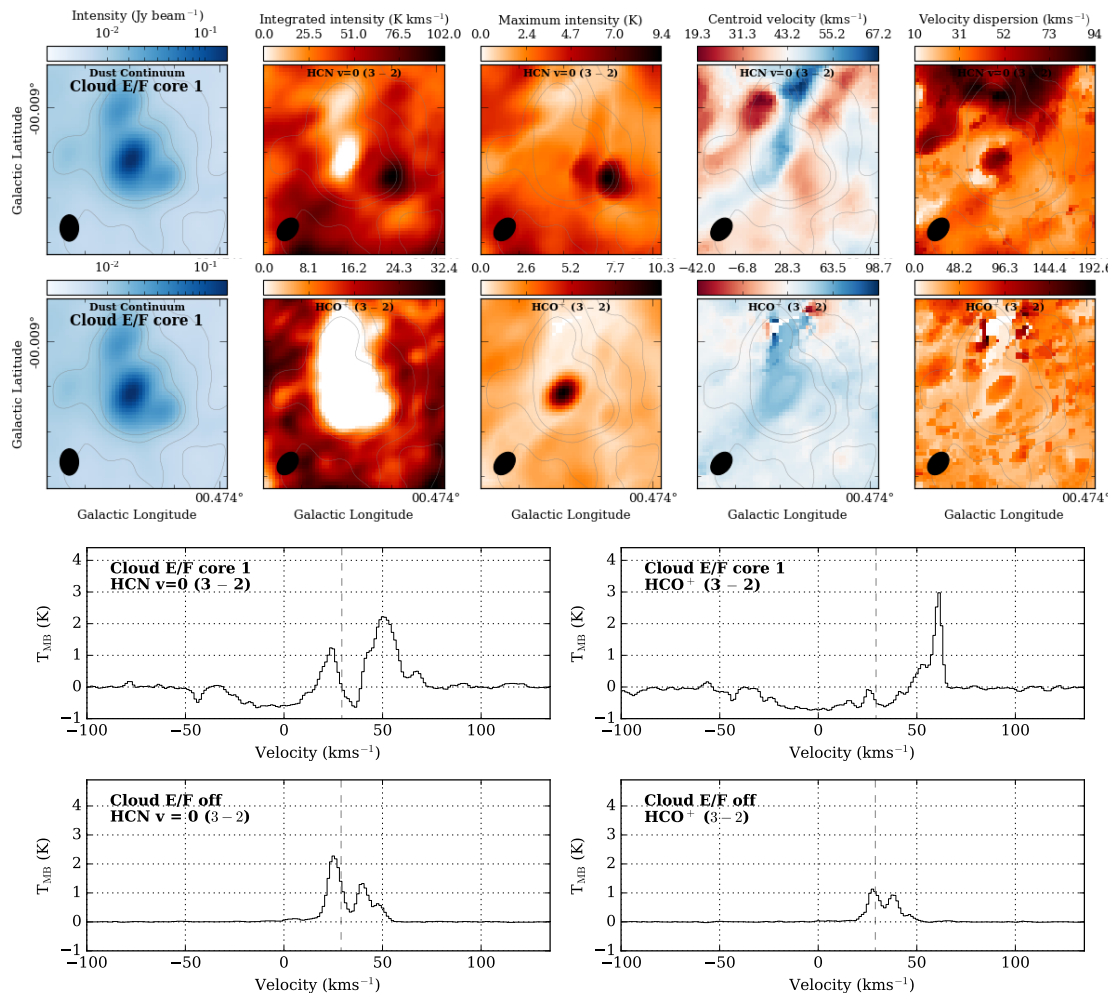


Figure 5.13: [upper two rows] Moment maps of HCN $v=0(3-2)$ and HCO⁺ $(3-2)$ towards Cloud E/F core 1 (see table 5.3). The analysis for the different molecular transitions are presented in each row, with the molecule labeled at the top of each map. Shown from left to right for each molecule are the combined 12m, 7m and single dish continuum map, and moment maps of the integrated intensity, peak intensity, intensity weighted centroid velocity, and intensity weighted velocity dispersion. Contours on each map are of the continuum shown in levels of $[8, 15, 30, 50] \sigma_{\text{rms}}$, where $\sigma_{\text{rms}} \sim 0.6 \text{ mJy beam}^{-1}$. [lower row] Spectra of the molecules towards the cores, where the vertical dashed line shows the assumed source centroid velocity. For comparison, also shown are the spectra towards the “off-position” (see Figure 5.3).

Chapter 6

Conclusions

How do the initial conditions of star-forming regions vary across environments, and do these influence the process of star formation? The aim of this thesis has been to investigate this question for a sample of massive star-forming regions within the Disc and Centre of the Milky Way; two *very* different environments. Specifically, this thesis focuses on regions that are thought to contain the early stages of massive star formation: Infrared Dark Clouds (IRDCs). These are cold ($T_{\text{kin}} \approx 10 - 60 \text{ K}$; e.g. [Ragan, Bergin & Wilner, 2011](#); [Krieger et al., 2017](#)) and dense ($n_{\text{H}_2} \approx 10^{2-6} \text{ cm}^{-3}$; e.g. [Huettemeister et al., 1995](#); [Butler & Tan, 2012](#)) regions, which are present within both the aforementioned environments. The following section summarises the main results from this thesis, before a future project is discussed.

6.1 Summary

The conclusions drawn from this research are summarised as follows –

The Galactic Disc

- (i) Studies of local molecular clouds have revealed that deuterated species are enhanced in the earliest phases of star formation. In [Chapter 2](#), this is tested for a massive star-forming region within the Disc of the Galaxy, IRDC G035.39-

00.33. To do so, a cloud-scale (i.e. over several parsecs) map of the deuterium fraction is produced from N_2D^+ ($2 - 1$) and N_2H^+ ($1 - 0$) observations taken with the IRAM-30m telescope (deuterium fraction defined as $D_{\text{frac}}^{N_2H^+} \equiv N(N_2D^+)/N(N_2H^+)$). Unlike low-mass star-forming regions, where the deuterium fraction is concentrated to the dense cores, the deuterium fraction in G035.39-00.33 is widespread throughout the cloud, with a mean value of $D_{\text{frac}}^{N_2H^+} = 0.04 \pm 0.01$, with a maximum ($D_{\text{frac}}^{N_2H^+} = 0.09 \pm 0.02$) around three orders of magnitude greater than the interstellar $[D]/[H]$ ratio. Given the general cloud properties, chemical modelling suggests that the observed $D_{\text{frac}}^{N_2H^+}$ could be produced if the cloud has reached a chemical equilibrium. To do so would imply that the IRDC is at least ~ 3 Myr old, which is ~ 8 times longer than the mean free-fall time of the observed deuterated region; i.e. the cloud is “dynamically old”. The [Kong et al. \(2015\)](#) chemical model does not, however, take into account the physical evolution of the cloud (i.e. density and extinction), which could cause this estimate of the timescale to change. To put an upper limit on the age of the cloud, the a constant high density is used in the model, which should represent the deuterium fraction within a population of compact cores that are unresolved by the beam of the IRAM-30m observations. This produces higher values of the equilibrium deuterium fraction that are more comparable to deuterium fraction observed towards low-mass star-forming regions.

- (ii) The accurate determination of the kinematic structure of IRDCs is very difficult, due to their complex network of velocity components. It is, however, important to investigate how these contribute to the process of mass concentration within these regions. Chapter 3 presents an in-depth kinematic analysis of the IRDC, G034.43+00.24, using high sensitivity and high spectral resolution IRAM-30m N_2H^+ ($1 - 0$) and $C^{18}O$ ($1 - 0$) observations. Gaussian decomposition and hierarchical clustering algorithms are used to disentangle the complex velocity structure within this cloud. This procedure allowed the identification of four distinct coherent velocity components within G034.43+00.24. These were compared to components found within G035.39-00.33 ([Henshaw et al., 2013](#)),

which is thought to have similar physical properties to G034.43+00.24. The components in both clouds have: high densities (inferred by their identification in N_2H^+), trans-to-supersonic non-thermal velocity dispersions with Mach numbers of $\sim 1.5 - 4$, a separation in velocity of $\sim 3\text{ km s}^{-1}$, and a mean red-shift of $\sim 0.3\text{ km s}^{-1}$ between the N_2H^+ (dense gas) and C^{18}O emission (envelope gas). The latter of these could suggest that these clouds share a common formation scenario. The kinematics of the larger-scale G035.39-00.33 structures are then investigated using lower-density-tracing $^{13}\text{CO}(1-0)$ observations, from the Galactic Ring Survey. A good correspondence is found between the components identified in the IRAM-30m observations and the most prominent component in the ^{13}CO data. This would suggest that the dense IRDC part of G035.39-00.33 is only a small part of a much larger structure, which potentially could be linked to an even larger inter-arm filament structure (Ragan et al., 2014).

The Galactic Centre

The inner few hundred parsecs of the Milky Way harbours gas densities, pressures, velocity dispersions, an interstellar radiation field and a cosmic ray ionisation rate orders of magnitude higher than the Disc, akin to the environment found in star-forming galaxies at high-redshift. Previous studies have shown that this region is forming stars at a rate per unit mass of dense gas which is at least an order of magnitude lower than in the Disc, potentially violating theoretical predictions.

- (iii) Is this low level of star formation an effect of systematic uncertainties in the observed physical properties or measurements of the star formation rate within this region? If not, could this potentially hint at a different mechanism for star formation within this extreme environment? To investigate this on a *global* ($\sim 100\text{ pc}$) scale, in Chapter 4 all the available observational star formation diagnostics – both direct counting of young stellar objects and integrated light measurements – are used to determine the star formation rate over a fixed region (the Central Molecular Zone; CMZ). These are found to be in agreement to within a factor two, hence the low star formation rate is not deemed to be the result

of the systematic uncertainties that affect any one measurement method. Furthermore, as these methods trace the star formation over different timescales, from 0.1 – 5 Myr, it appears that the star formation rate has been constant to within a factor of a few within this time period (i.e. in agreement with a cycle of star formation within the Galactic Centre; [Kruijssen et al., 2014](#)). The progression of star formation on a *local* (~ 1 pc) scale, within gravitationally bound clouds on the “dust-ridge”, are then investigated, with use of the orbital model of [Kruijssen, Dale & Longmore \(2015\)](#). It is found that these clouds are converting around 1 – 4 per cent of their gas masses into stars per free-fall time. This is consistent with a subset of the considered “volumetric” star formation models ([Krumholz & McKee, 2005](#); [Padoan & Nordlund, 2011](#); [Hennebelle & Chabrier, 2013](#)). However, discriminating between these models is obstructed by the current uncertainties on the input observables and by their dependence on ill-constrained free parameters. The lack of empirical constraints on these parameters, therefore, represents a key challenge in the further verification or falsification of current star formation theories.

- (iii) The investigation of the star formation rate on local scales within the Galactic Centre highlighted the high \mathcal{M} , high β , and low ϵ_{ff} end of the parameter space as the most promising for the verification or falsification of the volumetric star formation models. In light of this, [Chapter 5](#) presents high spatial resolution (~ 0.05 pc), continuum and molecular line ALMA observations of two clouds that reside within this part of the parameter space. The aim of these observations is to assess how the extreme environment of the Galactic Centre can affect their fragmented structure (e.g. through analysis of their power-law spectrum, and density probability distribution function), level of complex chemistry (e.g. through modelling), core dynamics (e.g. through virial analysis) and the large-scale kinematics of the clouds (following the procedure within [Chapter 3](#)). Ultimately, these observations will be used to constrain the physical parameters of these clouds, such that they can be used to accurately test the volumetric star formation models. As the reduction of these observations has only recently been

completed, Chapter 5 presents only some very preliminary analysis on the structure of these regions. One particularly interesting result is the identification of a dense core region within one of the clouds, which appears to contain a rich chemistry (with more than 100 molecular line transitions identified). Of these, four transitions from the prebiotic molecule formamide (NH_2CHO), a precursor to the DNA and RNA constituent guanine, have been identified.

An overview of the properties that have been determined for four IRDCs, two of which are from the Galactic Disc and two from the Galactic Centre, studied here in this thesis is presented in Table 6.1. This comparison highlights that despite the similar spatial size of these two sets of molecular clouds, and the fact that they are all gravitationally bound (virial parameter around unity), their *cloud scale* physical properties are very different: the properties of the Galactic Centre clouds are around an order of magnitude higher than those in the Disc (e.g. in gas mass, density, Mach number).

The cloud lifetimes, as determined from the deuterium fraction for the Disc IRDC, and from the orbital model for the Galactic Centre sample, are also shown in Table 6.1. When these are compared to the local free-fall time, the Galactic Disc cloud appears to be dynamically old ($t_{\text{SF}} > t_{\text{ff}}$), whereas the Galactic Centre clouds are dynamically young ($t_{\text{SF}} < t_{\text{ff}}$). This could potentially suggest that both short and long-lived clouds can be present across the Galaxy.

Shown in the table are the embedded stellar mass and star formation efficiency estimates for both sets of clouds. These have been calculated for the Disc clouds using the total number of embedded stellar objects found by Shepherd et al. (2007) and Carey et al. (2009) (see Figures 3.1 and 2.1), and an initial mass function median mass of $M_{\text{IMF}} \sim 0.5 M_{\odot}$ (e.g. Muench et al., 2007). Together with the cloud lifetimes, these then can be used to infer a star formation efficiency per free-fall time, ϵ_{ff} . Interestingly, despite the significantly lower embedded stellar masses of the Disc clouds compared to Galactic centre clouds, their star formation efficiencies per free-fall time are relatively similar (i.e. of the order of a few per cent). Therefore, despite the very different cloud scale properties (such as density and Mach number) once the clouds in the Disc and

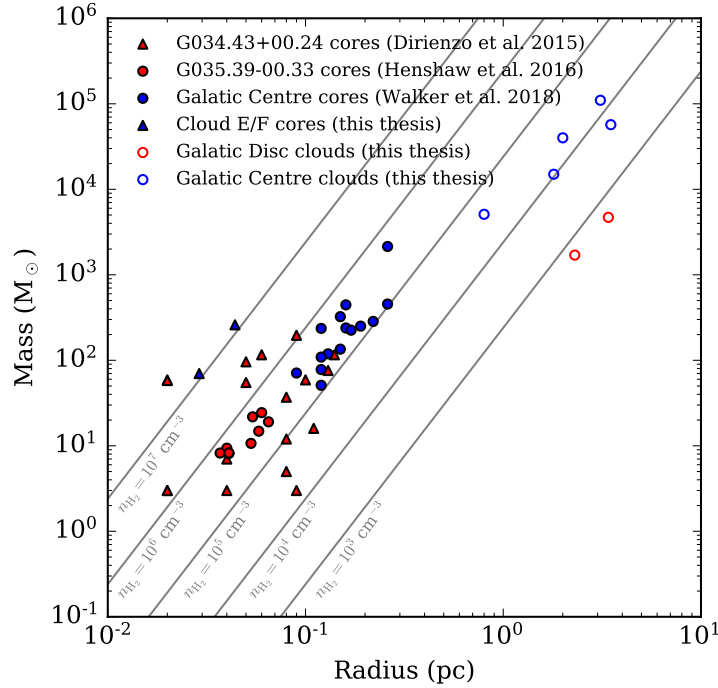


Figure 6.1: The mass as a function of radius for both Galactic Centre [shown in blue] and Disc [shown in red] clouds and cores discussed throughout this thesis. The clouds scale properties shown here are given in Table 6.1 and 4.5, and the Galactic Centre core properties in Table 5.9. Additional Galactic Centre cores properties have been taken from Walker et al. (2018). Core properties for the G034.43+00.24 and G035.39-00.33 Disc clouds were taken from Dirienzo et al. (2015) and Henshaw et al. (2016a), respectively.

centre of the Galaxy become gravitationally bound, they appear to forming stars at a similar rate relative to their cloud-scale densities.

A possible explanation for this is that the individual sites of star formation are not concerned with the cloud scale properties, and are forming stars at a rate that is universal across environments. To investigate this, shown in Figure 6.1 is a plot of the mass as a function of radius for both the Galactic Centre (shown in blue) and the Disc (shown in red) clouds. This plot makes use of data taken from this thesis and works by Dirienzo et al. (2015), Henshaw et al. (2016a) and Walker et al. (2018). This clearly shows that on the larger (> 1 pc) scales, there appears to be a significant difference in density (i.e. mass over radius cubed) for the two environments. On core (< 1 pc) scales, however, they appear to be similar within the large scatter in mass estimates (potentially caused by the different measurement methods used to calculate the mass). The Galactic Centre

cores are generally more massive, but this is most likely an observational and statistical effect. The clouds are farther away and more massive so are statistically more likely to contain higher mass cores, and the observations of these clouds are not sensitive to the lower mass cores.

The cloud scale physical properties and kinematics of these regions must then be governing their level of star formation by determining the number of gravitationally bound core structures that can form. Indeed, in Chapter 5 it was shown that changes in the global properties of these regions could have a significant impact on the star formation, and, in particular, the mode of turbulence driving is found to be a significant limiting factor in the star formation rate (see Figure 4.10). As star formation cannot efficiently proceed within regions that contain solenoidal driven turbulence (i.e. $b < 0.4$), where gas motions are divergence-free and collisions between parcels of gas within the turbulent medium that produce gravitationally bound structures are less likely. Whereas, regions that contain compressively driven turbulence (i.e. $b > 0.4$), the gas motions are curl-free. Therefore, density enhancements caused by collisions are more likely to become gravitationally bound, and star formation can proceed at a higher rate (Federrath, Klessen & Schmidt, 2008; also see Section 1.4.2 of the introduction).

Observations and simulations of Galactic Centre clouds suggest that they are driven by solenoidal turbulence (Federrath et al., 2016), which is most likely a result of the strong shear-driven velocity differential imparted on these clouds (i.e. angular momentum) during their orbit around the CMZ (Kruijssen, Dale & Longmore, 2015). In absence of such strong shear, it is most likely that Galactic Disc molecular clouds have more compressively driven turbulence (Federrath et al., 2016). Indeed, in Chapter 3, the kinematics of two Disc IRDCs were found to be suggestive of a filament merging scenario (also inferred from the presence of narrow line-width SiO emission; Jiménez-Serra et al., 2010; Cosentino et al., 2018), which would cause a more compressive mode of turbulence within these clouds.

The results of this thesis, therefore, suggest an environmentally dependent process of high-mass core formation. This process then indirectly governs the rate of star formation, due to a similar evolutionary time scale for high mass cores once they have formed

(governed by their free-fall time). In this scenario, a high star formation rate within the Galactic Centre, caused by the elevated average gas density compared to Disc clouds, is being suppressed by the inability of the gas to form gravitationally bound cores. The cloud scale properties within these two environments are then governing the rate of core formation in such a way that, despite their very different properties, the resultant star formation rate per free fall time is similar.

In light of the above discussion, the following section presents a future investigation into this discontinuity between the cloud (> 1 pc) and core (< 1 pc) scale properties in governing the level of star formation within molecular clouds. To do so, the structural and kinematic properties of a sample of Galactic Centre and Disc molecular clouds will be analysed. There are also several gaps and uncertain values within the Table, which need to be filled in the future to allow a meaningful comparison between these, and other, molecular clouds in these two environments. This is discussed further in the following section.

6.2 Future work

This section presents potential future work, which expands upon the work summarised above. The project I propose has been split into two parts: a primary project focussing on the properties of the dense gas within potential massive star-forming regions, and a secondary project focussing on the properties of the ionised gas within regions of on-going massive star formation.

6.2.1 Primary objective

To address the currently open questions in the field of star formation, I aim to systematically determine the cloud-to-core scale kinematic and physical properties of IRDCs within contrasting environments: Galactic Disc and Centre. This will allow me to i) when taken individually, assess what scales (both in terms of structure morphologies – i.e. filaments or fibres – and their properties) are influencing the dynamics at the in-

Table 6.1: Properties of Disc and Galactic Centre IRDCs.

Cloud property	The Galactic Disc		The Galactic Centre	
	G034.43+00.24	G035.39-00.33	Cloud D	Cloud E/F
Distance, d (kpc)	3.7 ± 0.6 [1,2]	2.9 ± 0.4 [1,2]	8.34 ± 0.16 [3]	8.34 ± 0.16 [3]
Size, R (pc)	3.4 ± 0.5	2.3 ± 0.3	2.0 ± 0.5	3.5 ± 1.0
Gas mass, M_{gas} ($\times 10^3 M_{\odot}$)	4.7 ± 1.4	1.7 ± 0.5	40 ± 20	57 ± 29
Linear mass, m ($\times 10^3 M_{\odot} \text{pc}^{-1}$)	1.4 ± 0.4	0.7 ± 0.2	20 ± 10	16 ± 8
Density, n_{H_2} ($\times 10^3 \text{cm}^{-3}$)	~ 0.5	~ 0.6	~ 20	~ 6
Gas temperature, T_{gas} (K)	17 ± 5 [4,5]	13 ± 4 [6]	60 ± 20 [7]	60 ± 20 [7]
Dust temperature, T_{dust} (K)	19 ± 3 [8]	15 ± 2 [6]	20 ± 5 [9]	20 ± 5 [9]
CO depletion, f_{D}	1.1 ± 0.6 [10]	2.8 ± 1.4
Deuterium fraction, $D_{\text{frac}}^{\text{N}_2\text{H}^+}$...	0.04 ± 0.01
Mach number, \mathcal{M}	~ 2	~ 3	~ 11 [11,12,13]	~ 11 [11,12,13]
Virial parameter, α	~ 0.5	~ 1	~ 1 [14]	~ 1 [14]
Magnetic field parameter, β	...	~ 0.13 [17]	~ 0.34 [13]	~ 0.34 [13]
Turbulence driving parameter, b	~ 0.22 [13]	~ 0.22 [13]
Free-fall time, t_{ff} (Myr)	~ 1.5	~ 1.4	~ 0.23	~ 0.5
Star formation timescale, t_{SF} (Myr)	...	~ 3	~ 0.5	~ 0.5
Embedded stellar mass, $M_{*,\text{tot}}$ (M_{\odot})	$\sim 20^a$	$\sim 20^b$	< 980	< 1100
Observed Star formation efficiency, ϵ (per cent)	...	~ 1	< 2	< 2
Observed Star formation rate, SFR ($\times 10^{-3} M_{\odot} \text{yr}^{-1}$)	...	$\sim 0.007^b$	< 3	< 2
Observed ϵ per free-fall time, ϵ_{ff} (per cent)	...	$\sim 0.5^b$	< 1	< 1
Predicted SFR $_{\Sigma}$ [15,16] ($\times 10^{-3} M_{\odot} \text{yr}^{-1}$)	~ 0.2	~ 0.1	~ 2	~ 3
Predicted ϵ_{ff} (per cent)	~ 4 [13]	~ 4 [13]

Numbers in square parentheses are the following references: [1] [Simon et al. \(2006b\)](#), [2] [Roman-Duval et al. \(2009\)](#), [3] [Reid et al. \(2014\)](#), [4] [Dirienzo et al. \(2015\)](#), [5] [Pon et al. \(2016a\)](#), [6] [Sokolov et al. \(2017\)](#), [7] [Krieger et al. \(2017\)](#), [8] [Foster et al. \(2014\)](#), [9] Battersby et al. (in prep), [10] [Hernandez et al. \(2012\)](#), [11] [Rathborne et al. \(2015\)](#), [12] [Henshaw et al. \(2016b\)](#), [13] [Federrath et al. \(2016\)](#), [14] [Walker et al. \(2015\)](#), [15] [Lada, Lombardi & Alves \(2010\)](#), [16] [Lada et al. \(2012\)](#), [17] [Liu et al. \(2018\)](#)

a) $M_{*,\text{tot}} = N_{\text{YSO}} M_{\text{IMF}}$ has been determined using the total number of embedded stellar objects found by [Shepherd et al. \(2007\)](#) as N_{YSO} (see Figure 3.1), and an initial mass function median mass of $M_{\text{IMF}} \sim 0.5 M_{\odot}$ (e.g. [Muench et al., 2007](#)).

b) $M_{*,\text{tot}}$ has been determined using the same method as for a), with N_{YSO} as the total number of $8 \mu\text{m}$ and $24 \mu\text{m}$ sources (; [Carey et al., 2009](#); see Figure 2.1). The shown t_{SF} has been used to determined the SFR and ϵ_{ff} .

dividual sites of core/star formation (e.g. in terms of mass flows); ii) when compared, determine the effect of their host environment on the core/star formation process, potentially unveiling variable modes of star formation across the Universe (e.g. comparing turbulence driving). The implications of this affects many fields in astronomy, such as models for star and planet formation to galaxy evolution and large-scale cosmology simulations (via parameters such as the global star formation/feedback efficiency of molecular clouds).

6.2.1.1 A sample of IRDCs within the Milky Way’s disc

The sample of IRDCs from the [Butler & Tan \(2009\)](#) survey is perfect for an expansive study of high-mass star-forming regions within the Galactic Disc. The ten sources within this survey are all massive ($10^{2-5} M_{\odot}$), nearby ($\sim 2 - 6$ kpc), and quiescent (determined from their high extinction against background near-infrared emission and, for some of the sample, from chemical evolutionary tracers). I have recently led a successful proposal (project number: 2017.1.00687.S) to observe the dense, star-forming gas within these sources at high-spatial resolution with ALMA (~ 0.05 pc). [Figure 6.2](#) shows each of these IRDCs overlaid with the coverage of the observations. Moreover, I am the PI of an ATCA (project number: C3091) project, aimed at studying several dense cores within the “Nessie” molecular cloud ([Jackson et al., 2010](#)), the data for which are already reduced and ready for analysis. These observations are ideal for the analysis of the gas dynamics from large, cloud scales, down to the sites of individual star formation.

To overcome the bottleneck of manually disentangling the complex kinematic structure from these observations I will use the SCOUSE and ACORNS routines (see [Chapter 3](#)). This analysis will allow me to (i) reliably determine the coherent kinematic structures within these IRDCs, (ii) investigate the properties of these structures both individually and in the context of those identified over the much larger giant molecular cloud scales (1 to 200 pc, e.g. from in-hand IRAM-30m and Galactic Ring Survey observations; see [Chapter 3](#)). Comparing the structural properties at these various scales will allow me

to test the observable predictions of various cloud structure formation theories, such as those relating to the transonic, sub-parsec, filamentary structures, so-called fibres (e.g. fray-and-fragment or fray-and-gather; [Hacar et al., 2013](#); [Tafalla & Hacar, 2015](#); [Smith et al., 2016](#)), and the larger scale giant molecular clouds, which host IRDCs (e.g. cloud-cloud merging), (iii) establish the dynamical state of both the filaments and the cores to determine which structures are susceptible to gravitational collapse, (iv) produce velocity vector maps and estimate the mass flows onto cores. If the cores gather less than their own mass per free-fall time, this will provide strong evidence for long-lived structures (cores/fibres/filaments) supported by, for example, magnetic fields (see [Hacar et al., 2013](#)). Here I have given examples of several of the key analysis that can be conducted with the available data on the IRDCs within the Disc alone, which, in itself, is important for the progression of the field of high-mass star formation.

6.2.1.2 A sample of IRDCs in an extreme environment

As presented in Chapter 5, I have led the reduction, calibration and analysis of ALMA observations (PI: S. Longmore, Project number: 2013.1.00617) towards two of the most high-mass and dense IRDCs within the extreme environment of the Galactic Centre. A direct comparison of the properties over the same physical scales for these IRDCs to those in Galactic Disc can be made, as the observations have a comparable spatial resolution (~ 0.05 pc) and contain similar dense gas tracers, and, key to my systematic approach, the same analysis tools will be used for both data sets. Furthermore, I am also part of a large survey with the SMA, which aims at uncovering the dense gas properties across the entire Galactic Centre, down to scales of around ~ 0.1 pc (the “CMZoom” survey). Along with the science listed below, this will provide a guide for future broadband observations, particularly towards chemically complex regions, such as the “core 1” within Cloud E (see Chapter 5). I will use these observations, to qualitatively and quantitatively compare the gas kinematic, core properties and chemistry of extreme IRDCs to those in the Disc to address several additional key questions: i) do similar structures exist within this extreme environment (filaments, fibres)? ii) Are the cores within this regions more/less massive than in the Disc, potentially pointing to a

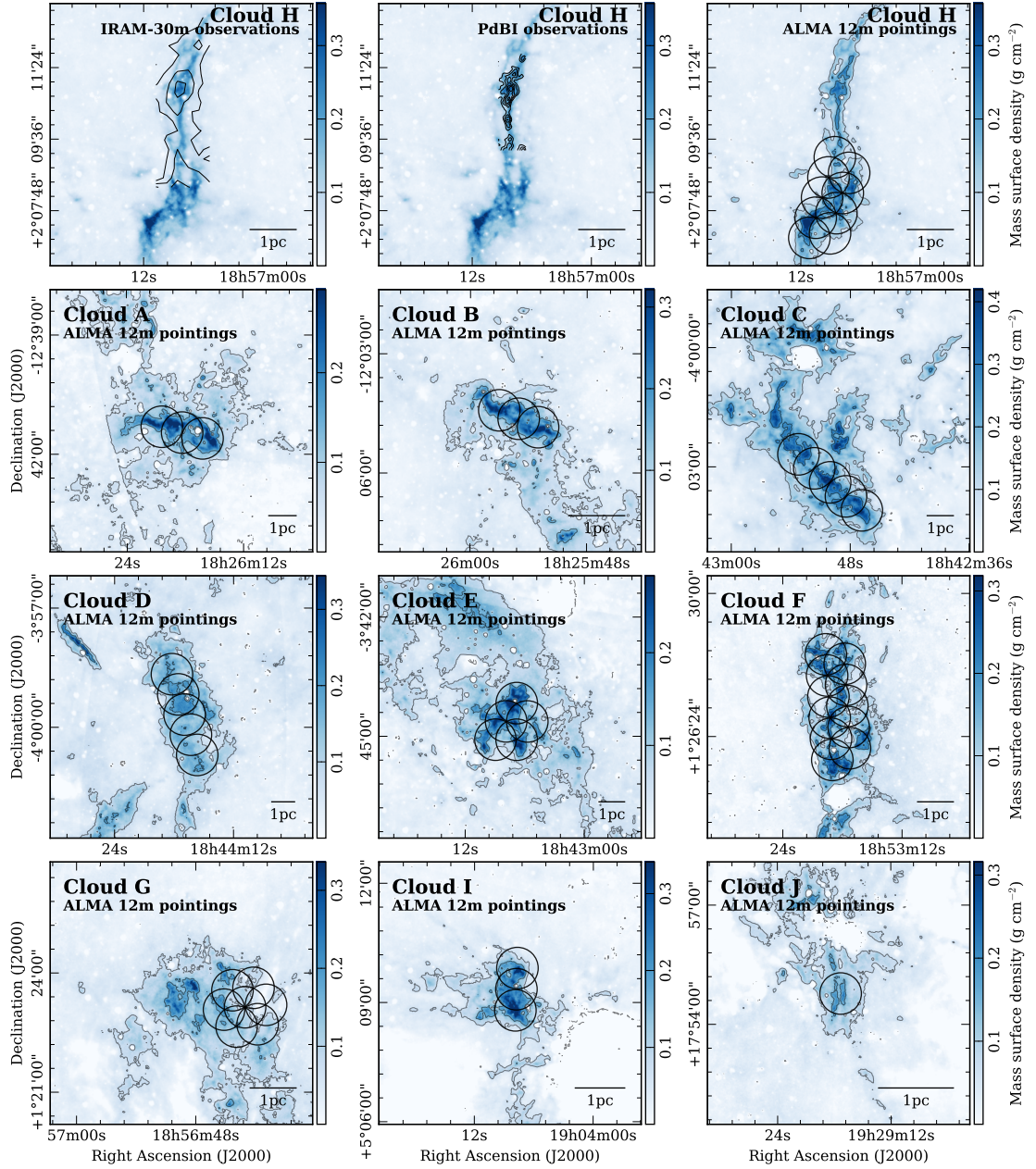


Figure 6.2: Mass surface density maps of the selected IRDC sample [Kainulainen & Tan \(2013\)](#) in colour scale. [Upper left two panels] Overlaid are contours of the N_2H^+ ($1 - 0$) integrated intensity observed with the IRAM-30m telescope (see Chapter 3), and the Plateau de Bure interferometer (PdBI; taken from [Henshaw et al., 2014](#)). As the PdBI has comparable angular resolution to the proposed ALMA observations, this is used to demonstrate the improvement in detail of the proposed observations. [Upper right and lower panels] Overlaid are the proposed mosaic pointings for the ALMA 12 m array primary beam at 93 GHz ($\sim 63''$).

different initial mass function within high-pressure environments (see Chapter 1)? iii) Do the different global turbulent properties of these regions provide a potential explanation for the order of magnitude lower observed star formation rate (see Chapter 4)?

6.2.2 Secondary objective

High-mass stars inject a huge amount of energy and momentum into the interstellar medium in their earliest stages through proto-stellar feedback. Large-scale simulations have shown that without stellar feedback, baryonic matter cools too rapidly and forms stars at a rate of an order of magnitude higher than is observed (e.g. [White & Rees, 1978](#); [Kereš et al., 2009](#)). The process of stellar feedback, and how it spans such a dynamical range of scales is, however, still poorly understood. Recent progress has been made in measuring the injection rates of momentum and energy during the violent pre-main sequence evolution stage of stars (when the star is still heavily embedded and still actively accreting material) in the environment similar to the Galactic Disc (e.g. [Lopez et al., 2011, 2014](#)). However, as previously mentioned, this environment is not representative of that in which most stars in the universe have formed. Given the predicted strong influence of the local environment on the end products of star formation and feedback, it is clear that our understanding of these processes in the solar neighbourhood is not adequate ([Scannapieco et al., 2012](#); [Krumholz, Kruijssen & Crocker, 2016](#)), and observations of the feedback processes in extreme environments, such as the Galactic Centre, are required.

6.2.2.1 The dynamics of ionised gas within the Galactic Centre

I have applied for, and have recently received, C array configuration VLA observations at 5 GHz towards three H II region complexes in the extreme Galactic Centre environment (Project number: 17A-321). These moderate spatial resolution, high sensitivity continuum maps will provide a census of the young high-mass stars in compact and diffuse H II regions down to masses of $\sim 8 M_{\odot}$. The bolometric luminosity and total Lyman continuum flux of the selected H II regions suggest that they should comprise

of $10^{3-4} M_{\odot}$ of newly-formed stars, hence should statistically contain over 50 high-mass stars. Simultaneous observations of hydrogen and helium recombination lines will allow us to determine how these high-mass stars are influencing (and being influenced by) the Galactic Centre environment. Crucial to this investigation, these H II region complexes are all of a similar total mass, have formed in the same extreme environment of the Galactic Centre and are at different evolutionary stages. This dataset will, therefore, allow us to: (i) determine the kinematics of how these young high-mass stars are interacting with the Galactic Centre environment; (ii) place constraints on the efficiency with which these stars are injecting pressure, energy and momentum into the surrounding environment; (iii) test the theories of star-formation within this region. The reduction of these observations is still in its early stages, nevertheless presented in Figure 6.3 is the preliminary continuum image of one of the H II region complexes (in collaboration with N. Butterfield at the VLA headquarters).

To achieve the above results, I will use the previously mentioned analysis tools to reliably map the ionised gas kinematics across these extreme H II regions, which has so far not yet been possible (Mehring et al., 1993), due to previous limitations of the VLA). The kinematic structure of the ionised gas will give a measurement of the pressures within these regions via pressure line broadening (Keto, Zhang & Kurtz, 2008), which will be compared to the higher ambient pressure within the Galactic Centre ($P/k_B = 10^7 \text{ K cm}^{-3}$), to determine if the expansion is being suppressed. Furthermore, I will be able to determine the complete kinematic structure of ionised shells, from which I can directly measure the expansion of the ionised gas. This, for the first time, will allow me to accurately determine the energy and moment injection efficiencies from high-mass stars which are embedded within an environment similar to high-z galaxies. Lastly, these observations of this ionised gas kinematics will provide important constraints on the next iteration of evolutionary models for the Galactic Centre (see Figure 6.3; e.g. Kruijssen, Dale & Longmore, 2015).

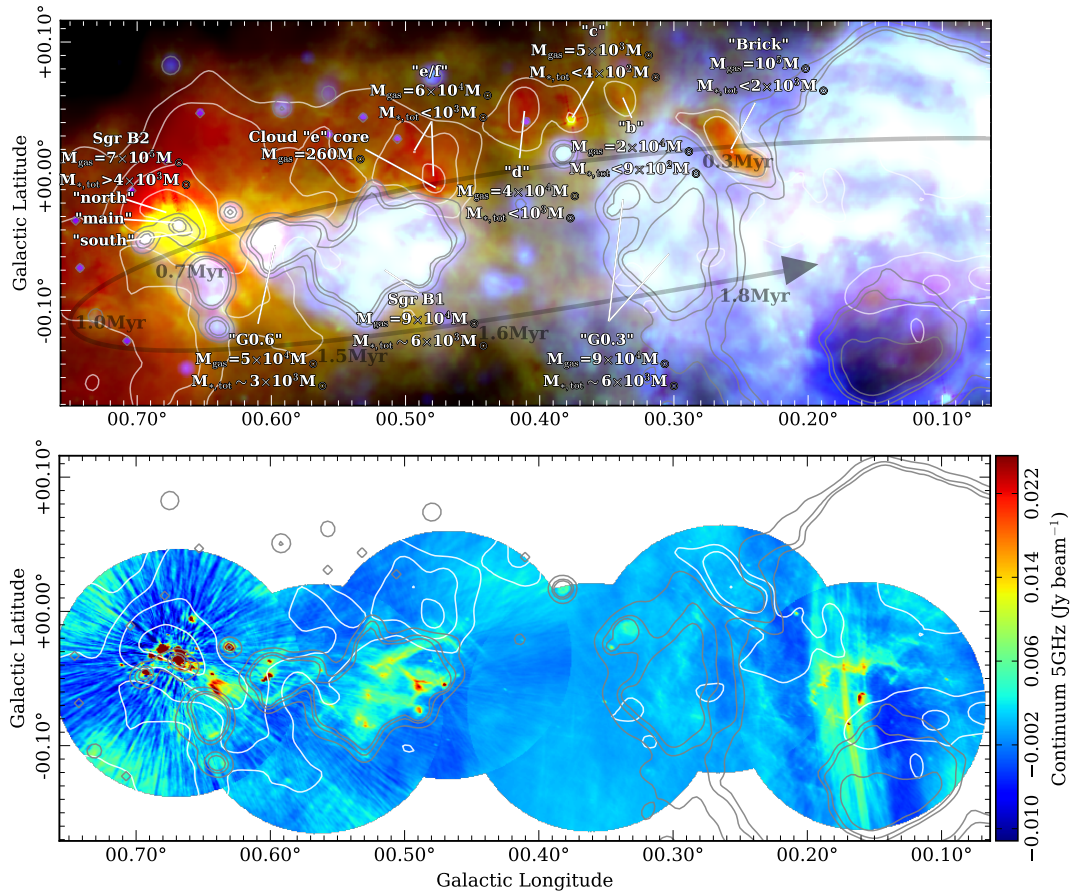


Figure 6.3: [upper panel] The three colour image identical to Figure 4.4. [lower panel] The 5 GHz VLA continuum image, overlaid with identical contours to the upper panel for reference. Note that this is part of a *very* preliminary analysis, hence still contains several image artefacts.

6.2.2.2 The dynamics of ionised gas as a function of the environment

Linking this investigation back to the primary science goal, these results will be compared to star-forming regions within different environments throughout the Galaxy (and within other galaxies). Doing so will show how the process of feedback is altered by the surrounding environment, allowing me to better quantify factors such as the stellar feedback/environment coupling (important for e.g. galaxy evolution simulations).

Appendix A

ALMA observations

Table A.1: Table of the rest frequencies of the unidentified line transitions from Cloud E/F core 1. These have been adjusted for the approximate core velocity of $\sim 29 \text{ km s}^{-1}$.

Rest frequency (GHz)
242.506
250.126
250.649
250.733
250.862
250.914
251.385
252.463
252.508
252.975
252.992
264.797
264.818
265.51
266.023
266.25
267.239
267.295
267.313
267.741
267.749
268.242
268.399
268.45

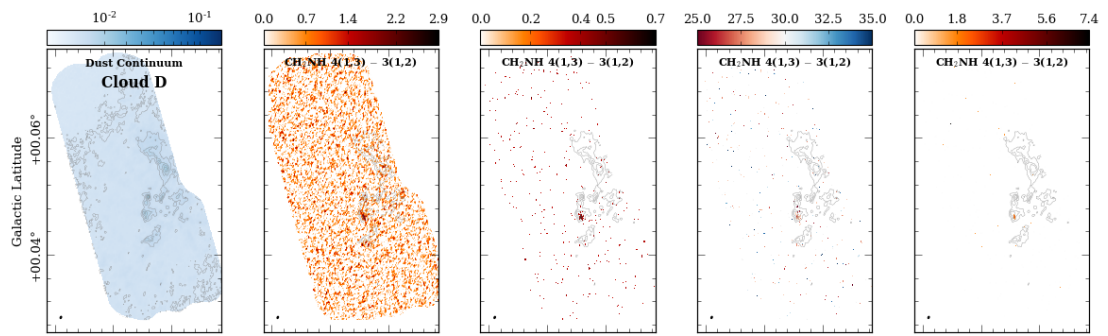


Figure A.1: Moment maps of a molecule towards Cloud D (see table 5.3). The analysis for the different molecular transitions are presented in each row, with the molecule labeled at the top of each map. Shown from left to right for each molecule are the combined 12m, 7m and single dish continuum map, and moment maps of the integrated intensity, peak intensity, intensity weighted centroid velocity, and intensity weighted velocity dispersion. Contours on each map are of the continuum shown in levels of $[8, 15, 20, 30] \sigma_{\text{rms}}$, where $\sigma_{\text{rms}} \sim 0.4 \text{ mJy beam}^{-1}$.

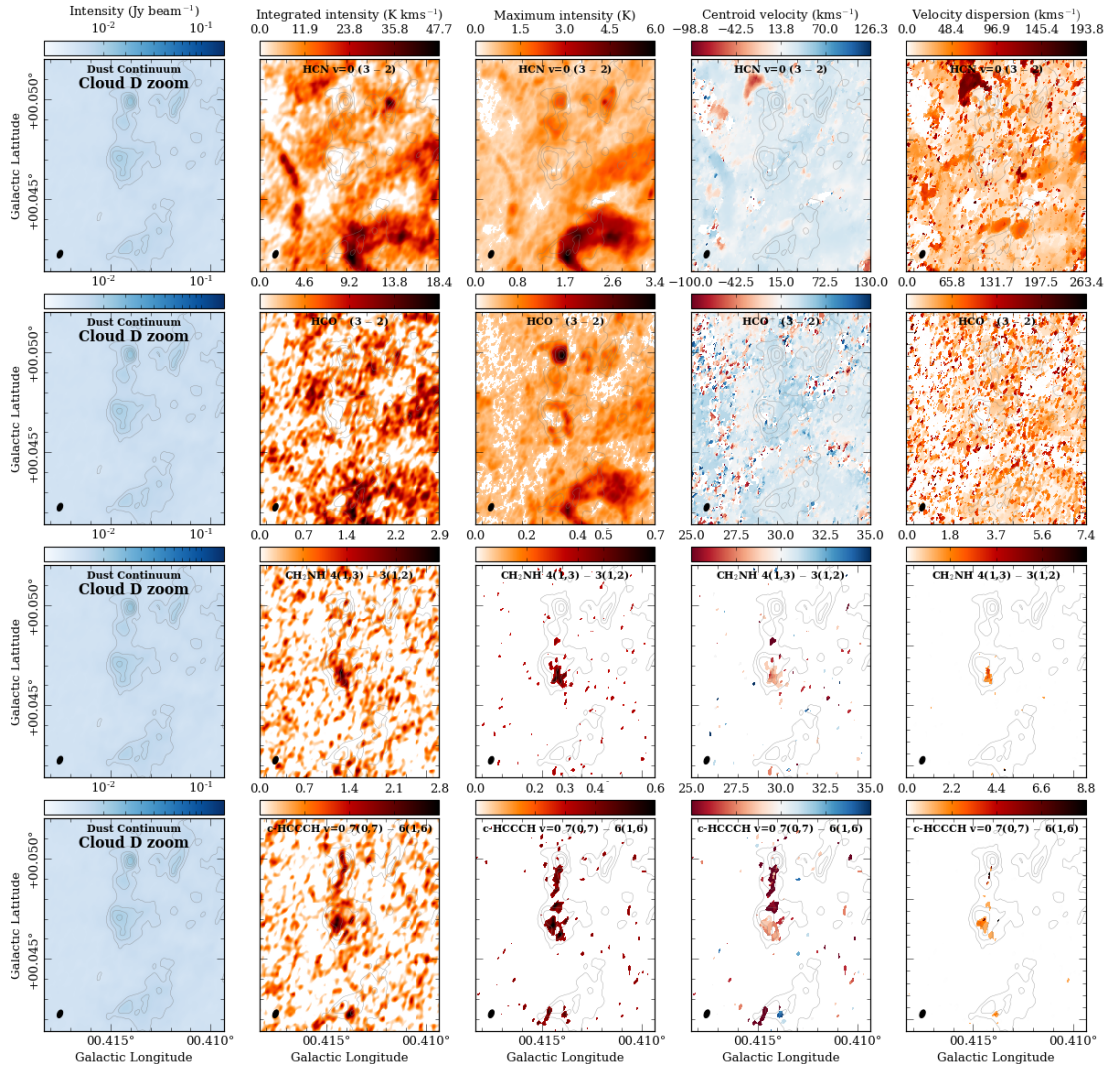


Figure A.2: Moment maps of the extended (upper two rows) and core (lower two rows) molecules towards the zoom region within Cloud D (see table 5.3). The analysis for the different molecular transitions are presented in each row, with the molecule labeled at the top of each map. Shown from left to right for each molecule are the combined 12m, 7m and single dish continuum map, and moment maps of the integrated intensity, peak intensity, intensity weighted centroid velocity, and intensity weighted velocity dispersion. Contours on each map are of the continuum shown in levels of [8, 15, 20, 30] σ_{rms} , where $\sigma_{\text{rms}} \sim 0.4$ mJy beam⁻¹.

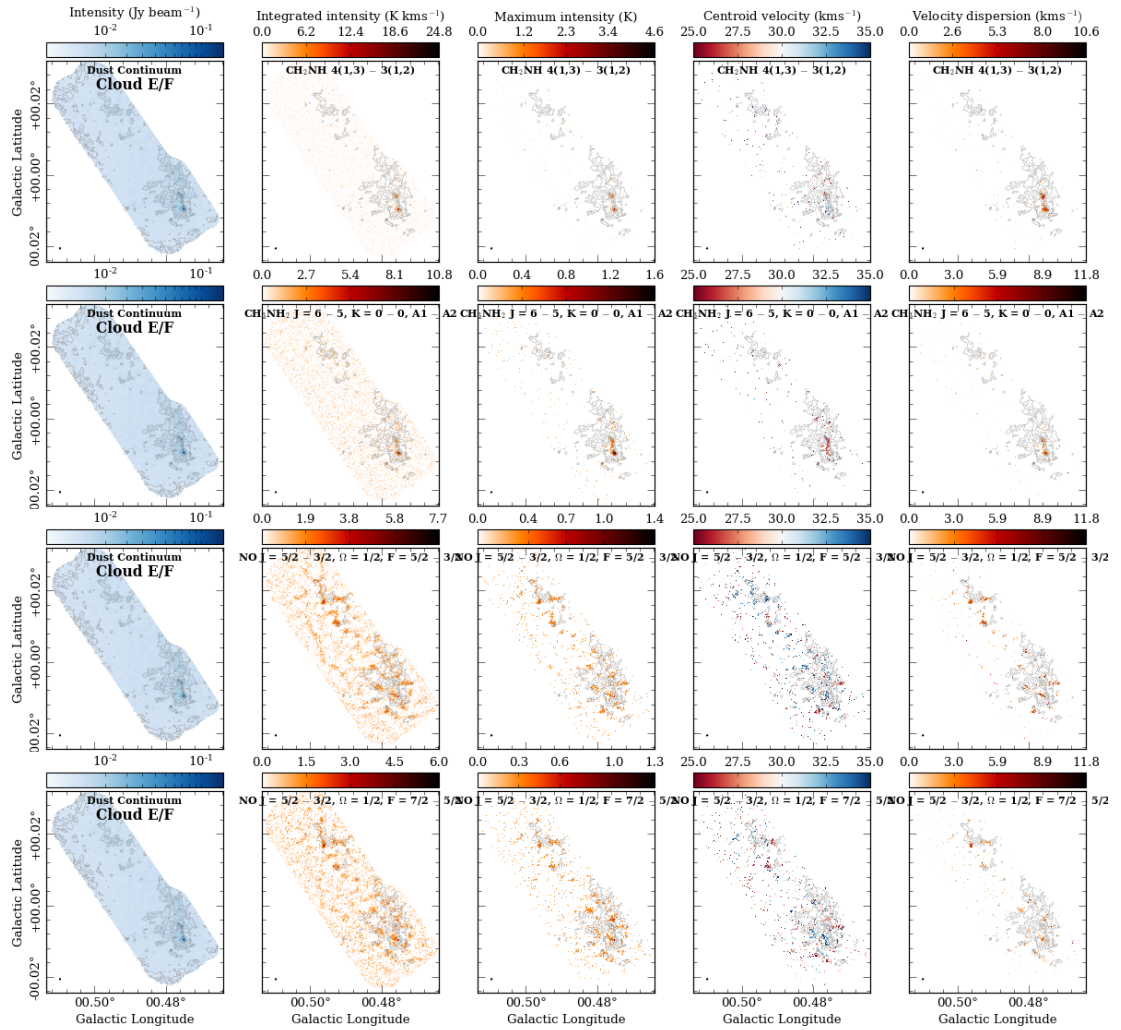


Figure A.3: Moment maps of the moderately extended molecules towards Cloud E/F (see table 5.3). The analysis for the different molecular transitions are presented in each row, with the molecule labeled at the top of each map. Shown from left to right for each molecule are the combined 12m, 7m and single dish continuum map, and moment maps of the integrated intensity, peak intensity, intensity weighted centroid velocity, and intensity weighted velocity dispersion. Contours on each map are of the continuum shown in levels of [8, 15, 30, 50] σ_{rms} , where $\sigma_{\text{rms}} \sim 0.6 \text{ mJy beam}^{-1}$.

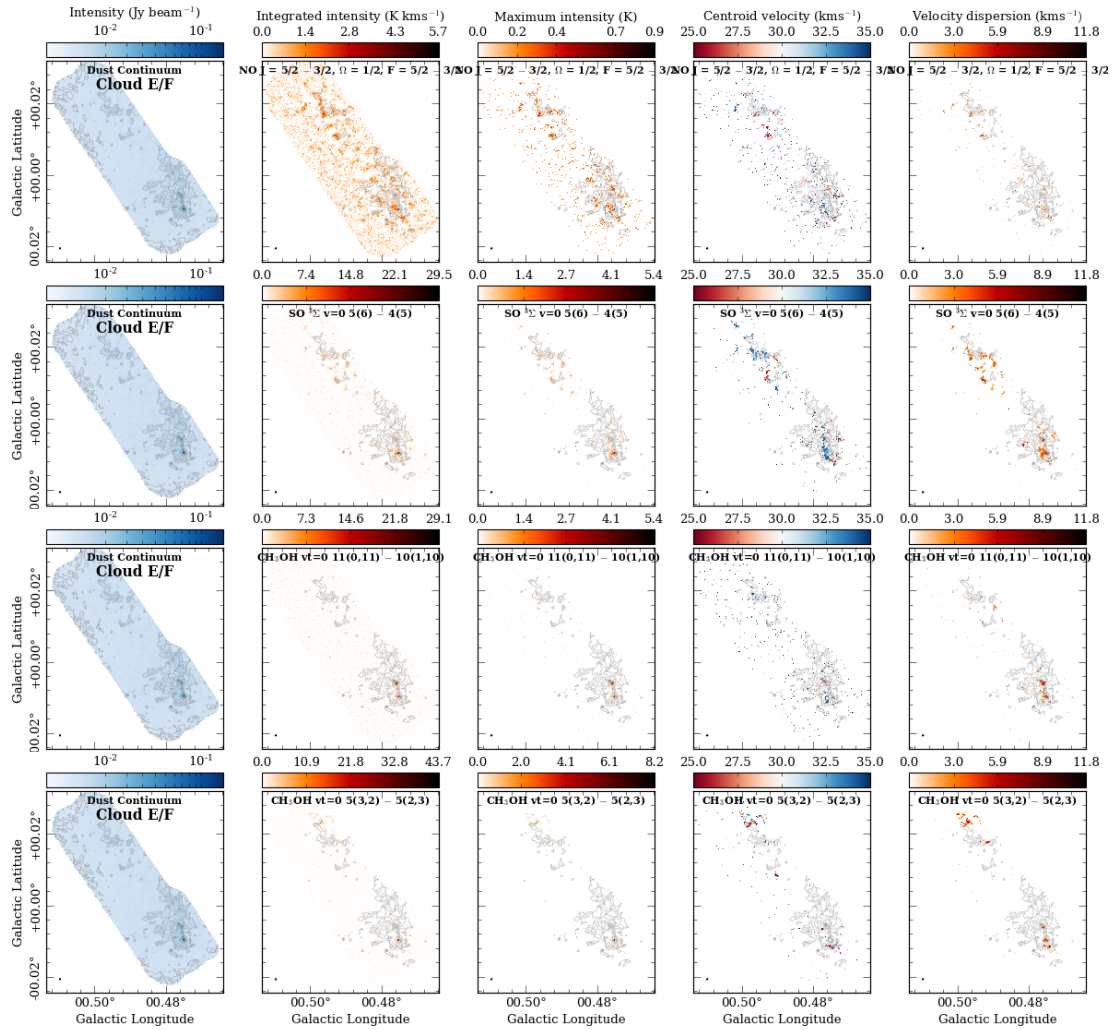


Figure A.4: Moment maps of the moderately extended molecules towards Cloud E/F (see table 5.3). The analysis for the different molecular transitions are presented in each row, with the molecule labeled at the top of each map. Shown from left to right for each molecule are the combined 12m, 7m and single dish continuum map, and moment maps of the integrated intensity, peak intensity, intensity weighted centroid velocity, and intensity weighted velocity dispersion. Contours on each map are of the continuum shown in levels of [8, 15, 30, 50] σ_{rms} , where $\sigma_{\text{rms}} \sim 0.6 \text{ mJy beam}^{-1}$.

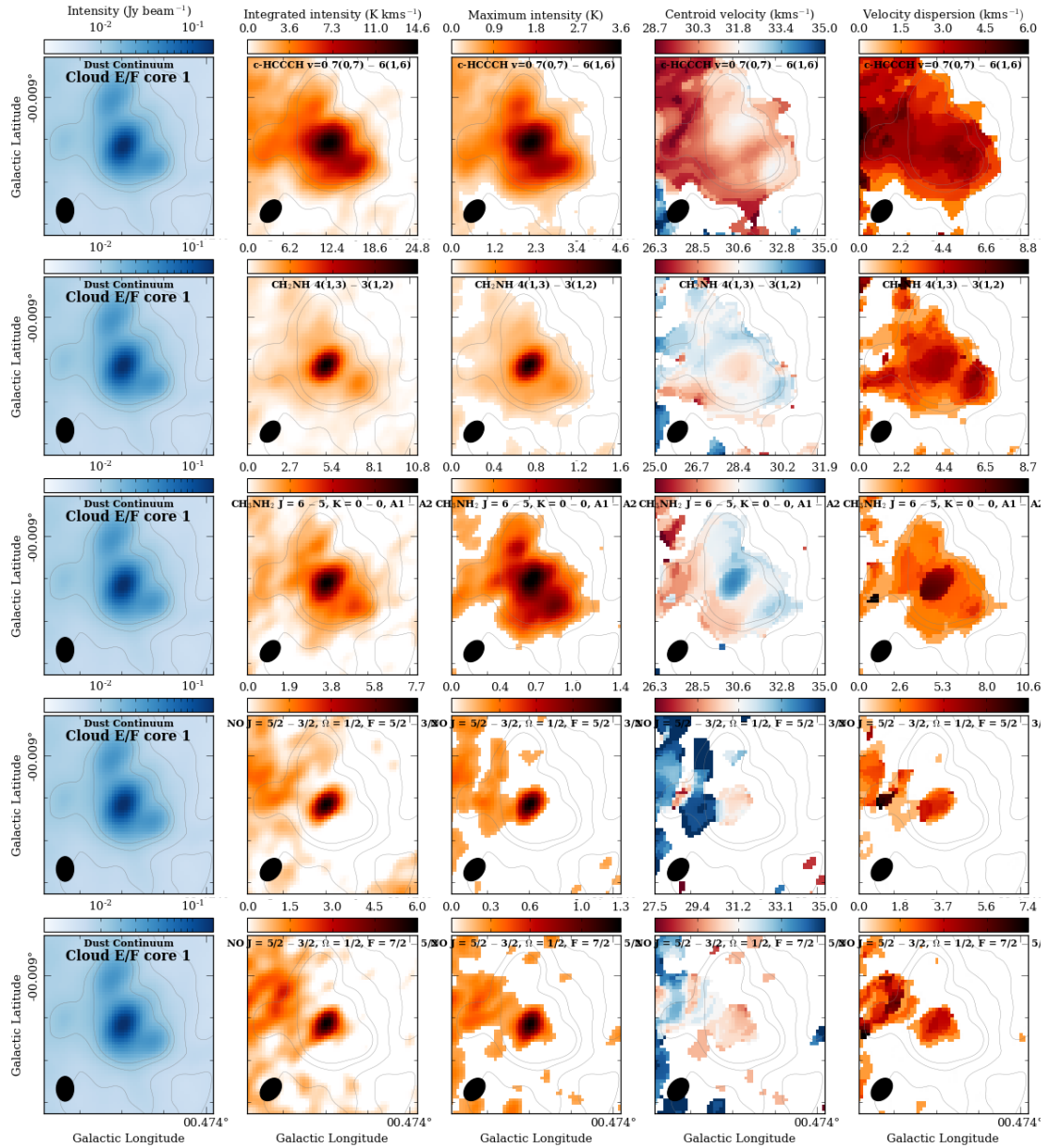


Figure A.5: Moment maps of the moderately extended molecules towards Cloud E/F core 1 (see table 5.3). The analysis for the different molecular transitions are presented in each row, with the molecule labeled at the top of each map. Shown from left to right for each molecule are the combined 12m, 7m and single dish continuum map, and moment maps of the integrated intensity, peak intensity, intensity weighted centroid velocity, and intensity weighted velocity dispersion. Contours on each map are of the continuum shown in levels of [8, 15, 30, 50] σ_{RMS} , where $\sigma_{\text{RMS}} \sim 0.6 \text{ mJy beam}^{-1}$.

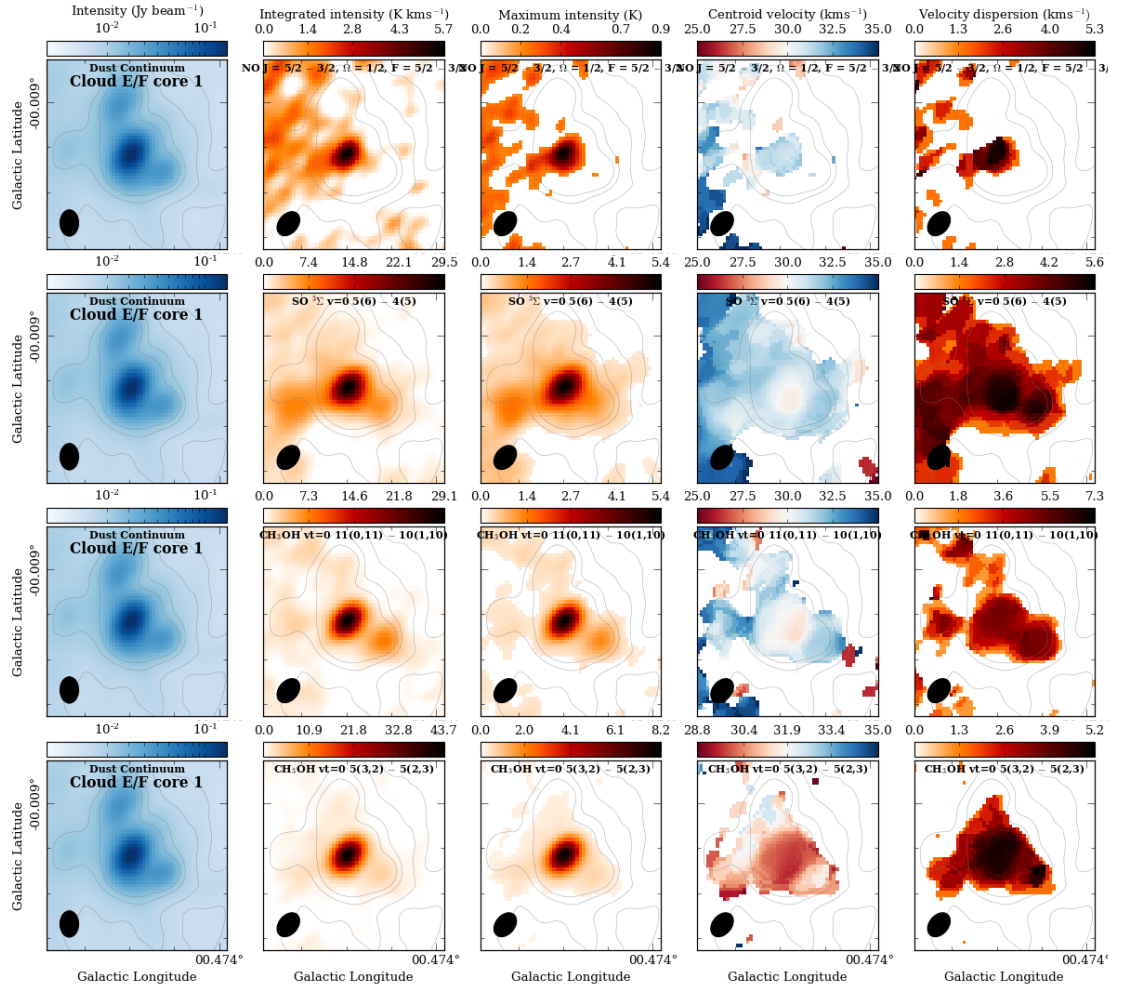


Figure A.6: Moment maps of the moderately extended molecules towards Cloud E/F core 1 (see table 5.3). The analysis for the different molecular transitions are presented in each row, with the molecule labeled at the top of each map. Shown from left to right for each molecule are the combined 12m, 7m and single dish continuum map, and moment maps of the integrated intensity, peak intensity, intensity weighted centroid velocity, and intensity weighted velocity dispersion. Contours on each map are of the continuum shown in levels of [8, 15, 30, 50] σ_{rms} , where $\sigma_{\text{rms}} \sim 0.6$ mJy beam⁻¹.

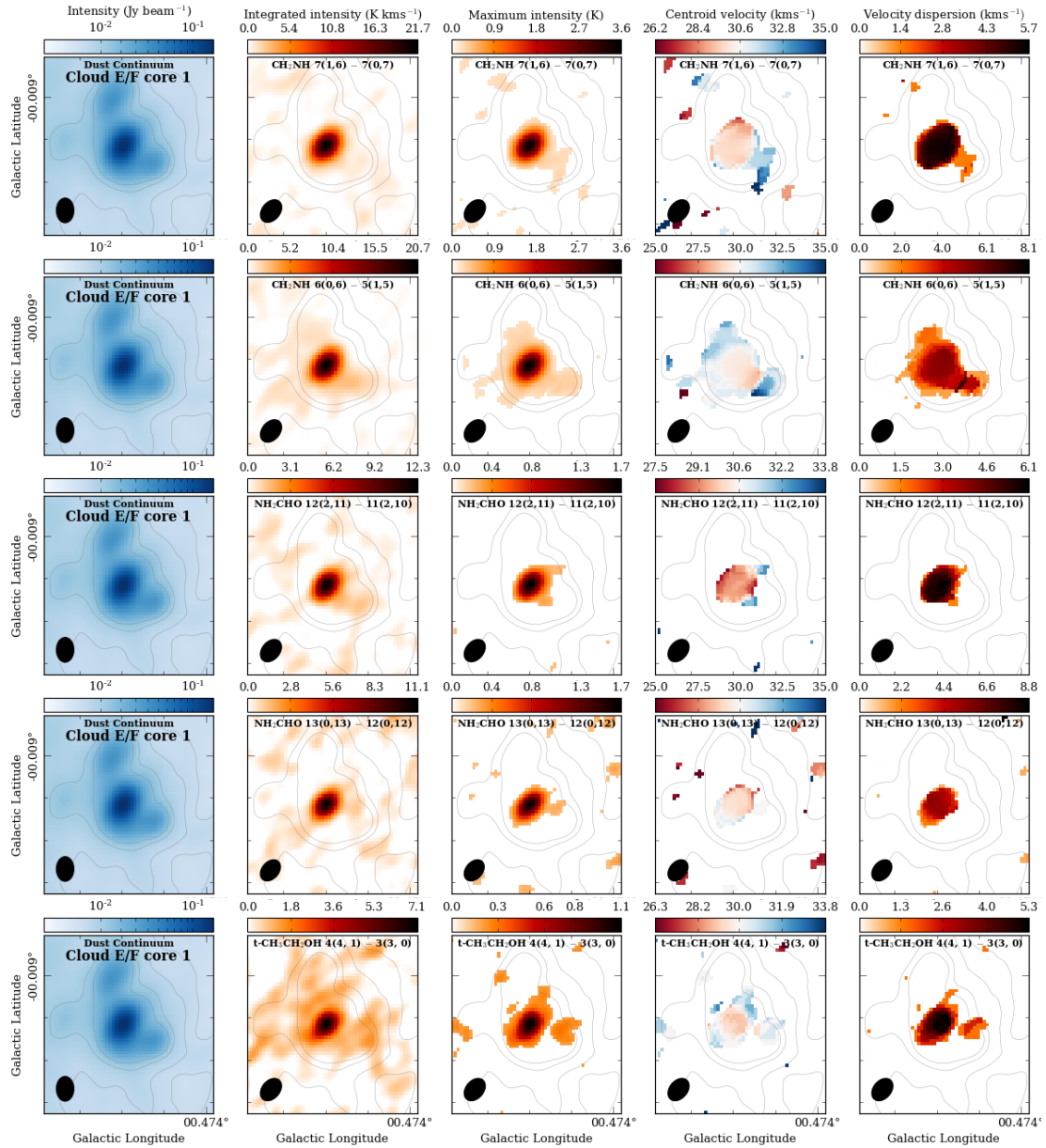


Figure A.7: Moment maps of the core molecules towards Cloud E/F core 1 (see table 5.3). The analysis for the different molecular transitions are presented in each row, with the molecule labeled at the top of each map. Shown from left to right for each molecule are the combined 12m, 7m and single dish continuum map, and moment maps of the integrated intensity, peak intensity, intensity weighted centroid velocity, and intensity weighted velocity dispersion. Contours on each map are of the continuum shown in levels of [8, 15, 30, 50] σ_{rms} , where $\sigma_{\text{rms}} \sim 0.6 \text{ mJy beam}^{-1}$.

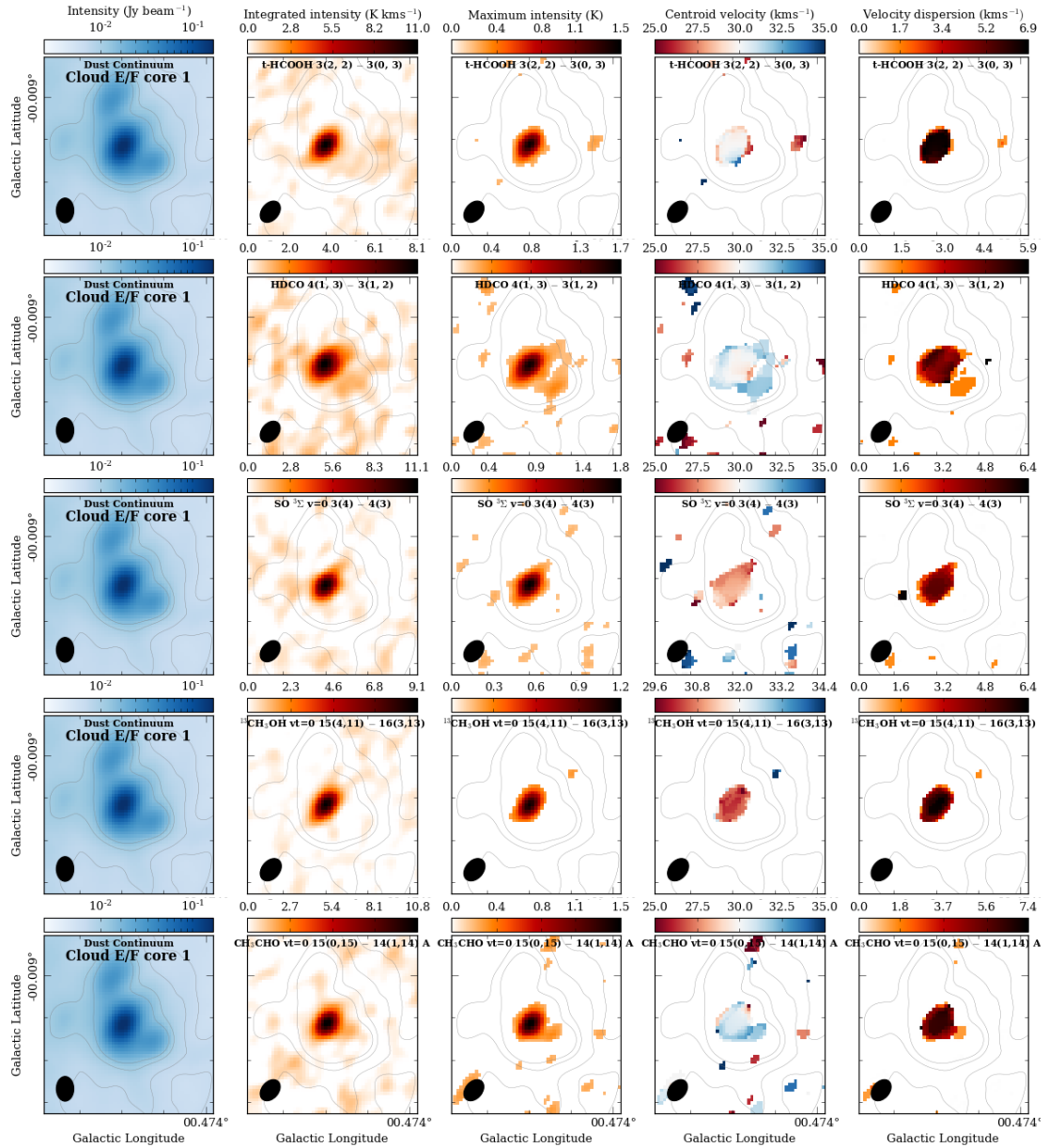


Figure A.8: Moment maps of the core molecules towards Cloud E/F core 1 (see table 5.3). The analysis for the different molecular transitions are presented in each row, with the molecule labeled at the top of each map. Shown from left to right for each molecule are the combined 12m, 7m and single dish continuum map, and moment maps of the integrated intensity, peak intensity, intensity weighted centroid velocity, and intensity weighted velocity dispersion. Contours on each map are of the continuum shown in levels of [8, 15, 30, 50] σ_{rms} , where $\sigma_{\text{rms}} \sim 0.6 \text{ mJy beam}^{-1}$.

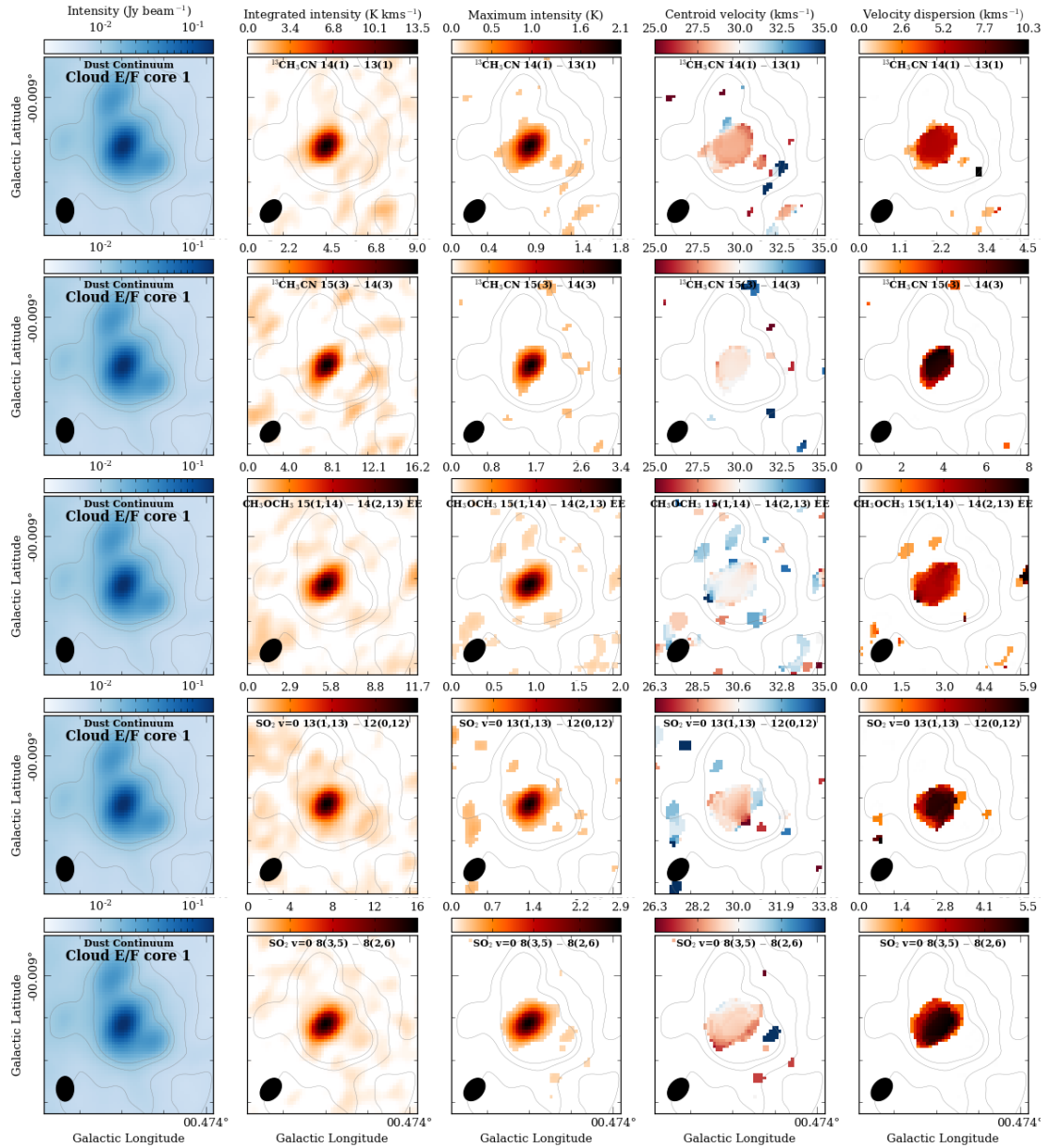


Figure A.9: Moment maps of the core molecules towards Cloud E/F core 1 (see table 5.3). The analysis for the different molecular transitions are presented in each row, with the molecule labeled at the top of each map. Shown from left to right for each molecule are the combined 12m, 7m and single dish continuum map, and moment maps of the integrated intensity, peak intensity, intensity weighted centroid velocity, and intensity weighted velocity dispersion. Contours on each map are of the continuum shown in levels of [8, 15, 30, 50] σ_{rms} , where $\sigma_{\text{rms}} \sim 0.6 \text{ mJy beam}^{-1}$.

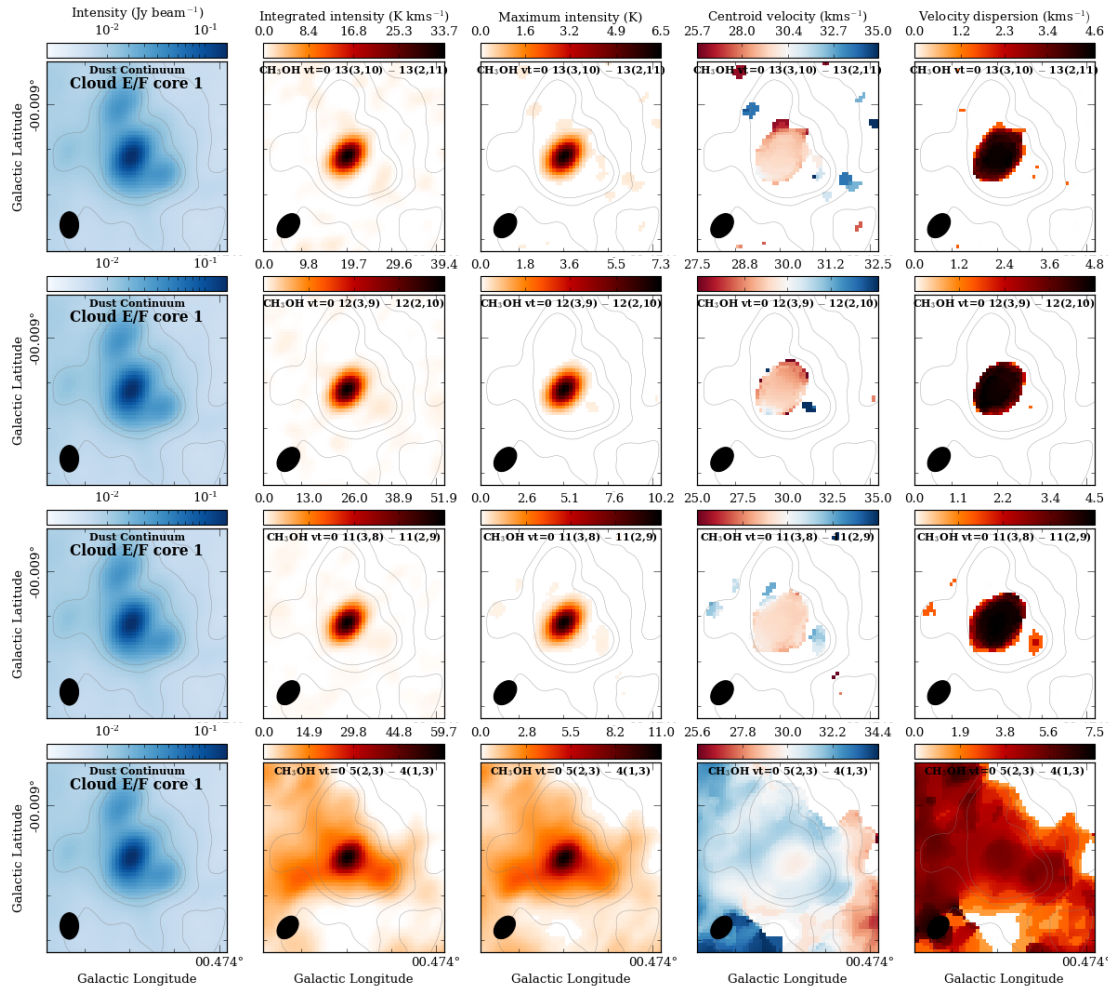


Figure A.10: Moment maps of the core molecules towards Cloud E/F core 1 (see table 5.3). The analysis for the different molecular transitions are presented in each row, with the molecule labeled at the top of each map. Shown from left to right for each molecule are the combined 12m, 7m and single dish continuum map, and moment maps of the integrated intensity, peak intensity, intensity weighted centroid velocity, and intensity weighted velocity dispersion. Contours on each map are of the continuum shown in levels of $[8, 15, 30, 50] \sigma_{\text{rms}}$, where $\sigma_{\text{rms}} \sim 0.6 \text{ mJy beam}^{-1}$.

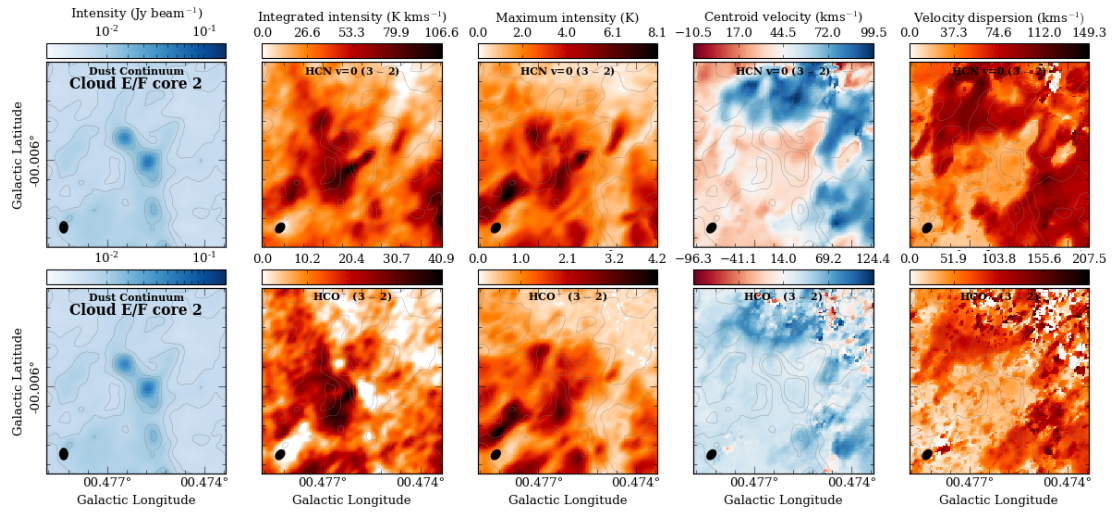


Figure A.11: Moment maps of the extended molecules towards Cloud E/F core 2 (see table 5.3). The analysis for the different molecular transitions are presented in each row, with the molecule labeled at the top of each map. Shown from left to right for each molecule are the combined 12m, 7m and single dish continuum map, and moment maps of the integrated intensity, peak intensity, intensity weighted centroid velocity, and intensity weighted velocity dispersion. Contours on each map are of the continuum shown in levels of [8, 15, 30, 50] σ_{rms} , where $\sigma_{\text{rms}} \sim 0.6 \text{ mJy beam}^{-1}$.

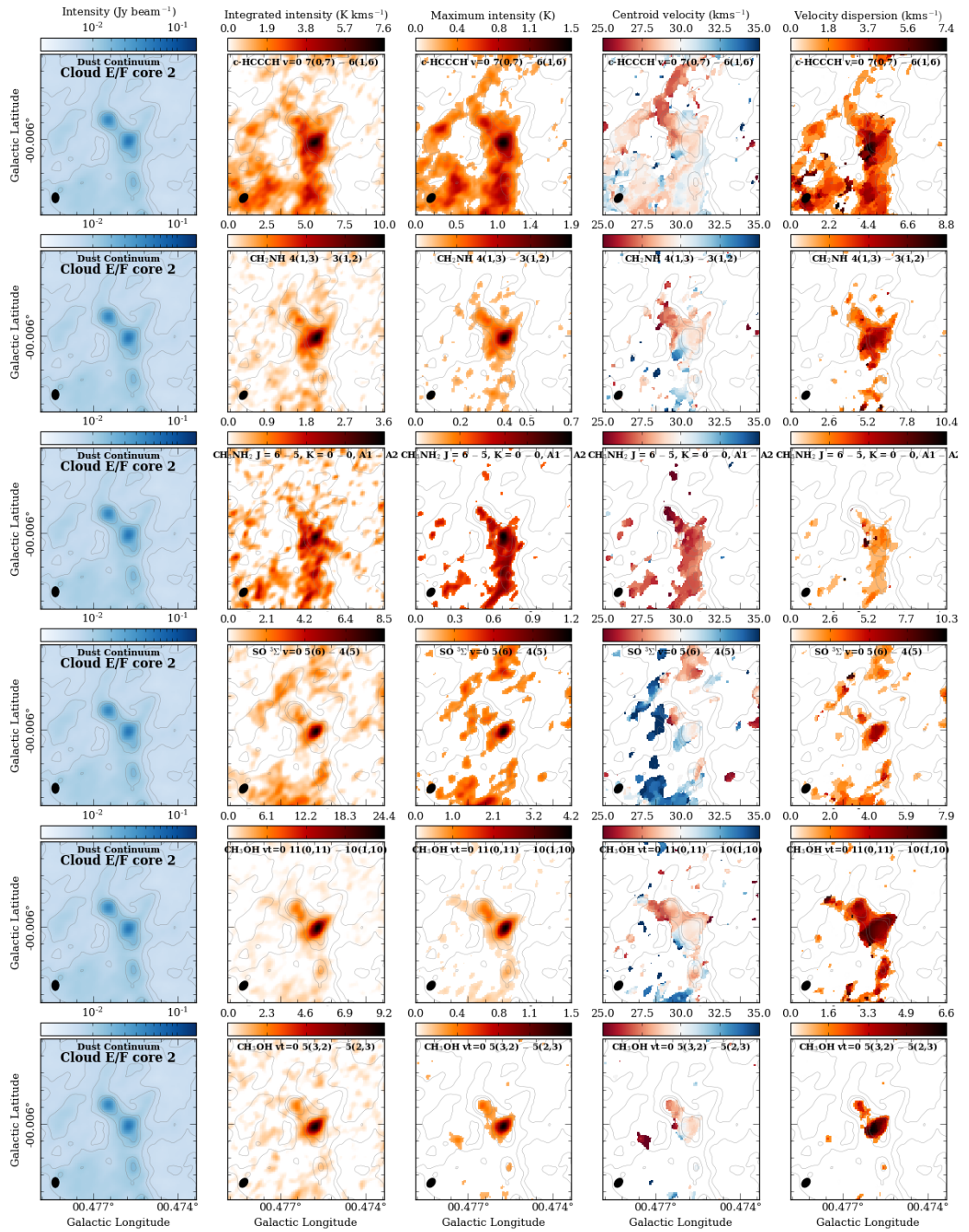


Figure A.12: Moment maps of the moderately extended molecules towards Cloud E/F core 2 (see table 5.3). The analysis for the different molecular transitions is presented in each row, with the molecule labeled at the top of each map. Shown from left to right for each molecule are the combined 12m, 7m and single dish continuum map, and moment maps of the integrated intensity, peak intensity, intensity weighted centroid velocity, and intensity weighted velocity dispersion. Contours on each map are of the continuum shown in levels of $[8, 15, 30, 50] \sigma_{\text{rms}}$, where $\sigma_{\text{rms}} \sim 0.6 \text{ mJy beam}^{-1}$.

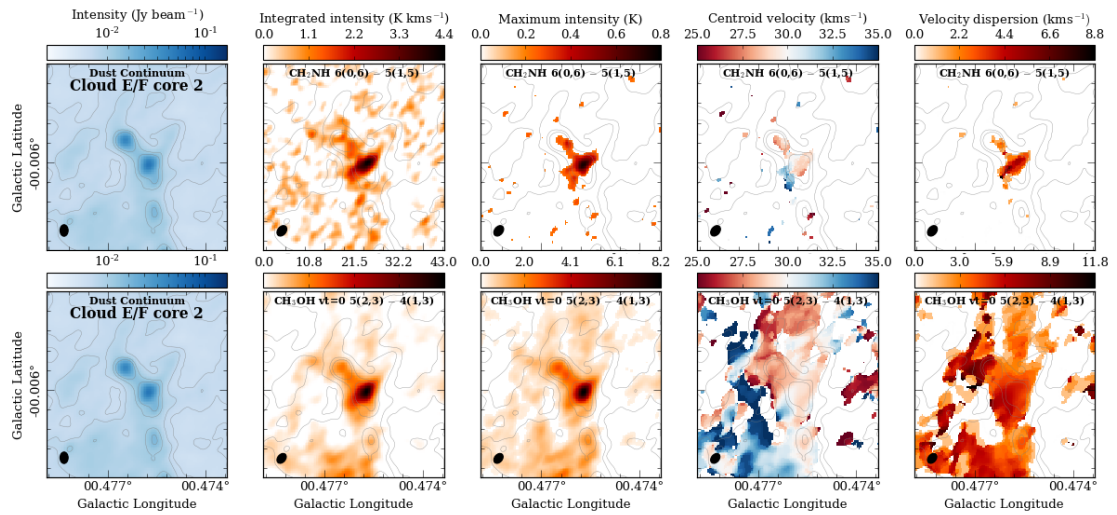


Figure A.13: Moment maps of the core molecules towards Cloud E/F core 2 (see table 5.3). The analysis for the different molecular transitions are presented in each row, with the molecule labeled at the top of each map. Shown from left to right for each molecule are the combined 12m, 7m and single dish continuum map, and moment maps of the integrated intensity, peak intensity, intensity weighted centroid velocity, and intensity weighted velocity dispersion. Contours on each map are of the continuum shown in levels of $[8, 15, 30, 50] \sigma_{\text{rms}}$, where $\sigma_{\text{rms}} \sim 0.6 \text{ mJy beam}^{-1}$.

Bibliography

Allen C. W., 1973, *Astrophysical quantities*

Alonso-Herrero A., Rieke G. H., Rieke M. J., Colina L., Pérez-González P. G., Ryder S. D., 2006, *ApJ*, 650, 835

Alves J., Lombardi M., Lada C. J., 2007, *A&A*, 462, L17

André P., 2017, *Comptes Rendus Geoscience*, 349, 187

André P., Belloche A., Motte F., Peretto N., 2007, *A&A*, 472, 519

André P., Di Francesco J., Ward-Thompson D., Inutsuka S.-I., Pudritz R. E., Pineda J. E., 2014, *Protostars and Planets VI*, 27

André P. et al., 2010, *A&A*, 518, L102

Armijos-Abendaño J., Martín-Pintado J., Requena-Torres M. A., Martín S., Rodríguez-Franco A., 2015, *MNRAS*, 446, 3842

Arzoumanian D. e. a., 2011, *A&A*, 529, L6

Bahcall N. A., Cen R., 1993, *ApJL*, 407, L49

Bailey N. D., Basu S., Caselli P., 2015, *ApJ*, 798, 75

Ballesteros-Paredes J., Hartmann L., Vázquez-Semadeni E., 1999, *ApJ*, 527, 285

Ballesteros-Paredes J., Klessen R. S., Mac Low M.-M., Vazquez-Semadeni E., 2007, *Protostars and Planets V*, 63

Bally J., 2016, *ARA&A*, 54, 491

- Bally J. et al., 2010, *ApJ*, 721, 137
- Bally J., Stark A. A., Wilson R. W., Henkel C., 1988, *ApJ*, 324, 223
- Barnard E. E., 1919, *ApJ*, 49
- Barnes A. T., Henshaw J. D., Caselli P., Jiménez-Serra I., Tan J. C., Fontani F., Pon A., Ragan S., 2018, *MNRAS*
- Barnes A. T., Kong S., Tan J. C., Henshaw J. D., Caselli P., Jiménez-Serra I., Fontani F., 2016, *MNRAS*, 458, 1990
- Barnes A. T., Longmore S. N., Battersby C., Bally J., Kruijssen J. M. D., Henshaw J. D., Walker D. L., 2017, *MNRAS*, 469, 2263
- Bartko H. et al., 2010, *ApJ*, 708, 834
- Bastian N., Covey K. R., Meyer M. R., 2010, *ARA&A*, 48, 339
- Battersby C. et al., 2011, *A&A*, 535, A128
- Belloche A., Müller H. S. P., Menten K. M., Schilke P., Comito C., 2013, *A&A*, 559, A47
- Belloche A., Parise B., van der Tak F. F. S., Schilke P., Leurini S., Güsten R., Nyman L.-Å., 2006, *A&A*, 454, L51
- Bigiel F., Leroy A., Walter F., Brinks E., de Blok W. J. G., Madore B., Thornley M. D., 2008, *AJ*, 136, 2846
- Blitz L., Shu F. H., 1980, *ApJ*, 238, 148
- Blitz L., Stark A. A., 1986, *ApJL*, 300, L89
- Bohlin R. C., Savage B. D., Drake J. F., 1978, *ApJ*, 224, 132
- Bok B. J., Reilly E. F., 1947, *ApJ*, 105, 255
- Bolatto A. D., Leroy A. K., Rosolowsky E., Walter F., Blitz L., 2008, *ApJ*, 686, 948

- Bolatto A. D., Wolfire M., Leroy A. K., 2013, *ARA&A*, 51, 207
- Bonnell I., Bate M., Clarke C., Pringle J., 2001, *Monthly Notices of the Royal Astronomical Society*, 323, 785
- Bonnell I. A., Bate M. R., Clarke C. J., Pringle J. E., 1997, *MNRAS*, 285, 201
- Bonnell I. A., Davies M. B., 1998, *MNRAS*, 295, 691
- Bourke T. L., Myers P. C., Caselli P., Di Francesco J., Belloche A., Plume R., Wilner D. J., 2012, *ApJ*, 745, 117
- Bressert E. et al., 2012, *A&A*, 542, A49
- Bruzual G., Charlot S., 2003, *MNRAS*, 344, 1000
- Butler M. J., Tan J. C., 2009, *ApJ*, 696, 484
- Butler M. J., Tan J. C., 2012, *ApJ*, 754, 5
- Calzetti D. et al., 2007, *ApJ*, 666, 870
- Calzetti D. et al., 2010, *ApJ*, 714, 1256
- Cappellari M. et al., 2012, *Nat*, 484, 485
- Cardillo M. et al., 2014, *A&A*, 565, A74
- Carey S. J., Clark F. O., Egan M. P., Price S. D., Shipman R. F., Kuchar T. A., 1998, *ApJ*, 508, 721
- Carey S. J. et al., 2009, *PASP*, 121, 76
- Carroll J. J., Frank A., Blackman E. G., Cunningham A. J., Quillen A. C., 2009, *ApJ*, 695, 1376
- Caselli P., Benson P. J., Myers P. C., Tafalla M., 2002a, *ApJ*, 572, 238
- Caselli P., Myers P. C., 1995, *ApJ*, 446, 665
- Caselli P., Myers P. C., Thaddeus P., 1995, *ApJL*, 455, L77+

- Caselli P., Walmsley C. M., Tafalla M., Dore L., Myers P. C., 1999, *ApJL*, 523, L165
- Caselli P., Walmsley C. M., Zucconi A., Tafalla M., Dore L., Myers P. C., 2002b, *ApJ*, 565, 344
- Casoli F., Combes F., 1982, *A&A*, 110, 287
- Castelletti G., Dubner G., Brogan C., Kassim N. E., 2007, *A&A*, 471, 537
- Castelletti G., Dubner G., Clarke T., Kassim N. E., 2011, *A&A*, 534, A21
- Caswell J. L., Batchelor R. A., Forster J. R., Wellington K. J., 1983, *Australian Journal of Physics*, 36, 401
- Cazzoli G., Cludi L., Buffa G., Puzzarini C., 2012, *ApJS*, 203, 11
- Cazzoli G., Puzzarini C., Lapinov A. V., 2003, *ApJL*, 592, L95
- Chabrier G., 2003, *PASP*, 115, 763
- Chambers E. T., Jackson J. M., Rathborne J. M., Simon R., 2009, *ApJS*, 181, 360
- Chapman N. L., Mundy L. G., Lai S.-P., Evans, II N. J., 2009, *ApJ*, 690, 496
- Chira R.-A., Kainulainen J., Ibàñez-Mejía J. C., Henning T., Mac Low M.-M., 2017, *ArXiv e-prints*
- Churchwell E. et al., 2009, *PASP*, 121, 213
- Clark P. C., Bonnell I. A., Klessen R. S., 2008, *MNRAS*, 386, 3
- Clemens D. P., 1985, *ApJ*, 295, 422
- Conroy C., van Dokkum P. G., 2012, *ApJ*, 760, 71
- Cosentino G. et al., 2018, *MNRAS*, 474, 3760
- Cotton W. D., 2017, *ArXiv e-prints*
- Crabtree K. N., Indriolo N., Kreckel H., Tom B. A., McCall B. J., 2011, *ApJ*, 729, 15

- Crapsi A., Caselli P., Walmsley C. M., Tafalla M., Lee C. W., Bourke T. L., Myers P. C., 2004, *A&A*, 420, 957
- Crapsi A. et al., 2005, *A&A*, 439, 1023
- Crocker R. M., Jones D. I., Aharonian F., Law C. J., Melia F., Oka T., Ott J., 2011, *MNRAS*, 413, 763
- Cyganowski C. J. et al., 2014, *ApJL*, 796, L2
- Dalgarno A., Black J. H., Weisheit J. C., 1973, *ApL*, 14, 77
- Dalgarno A., Lepp S., 1984, *ApJL*, 287, L47
- Dame T. M., Elmegreen B. G., Cohen R. S., Thaddeus P., 1986, *ApJ*, 305, 892
- Davies B., Hoare M. G., Lumsden S. L., Hosokawa T., Oudmaijer R. D., Urquhart J. S., Mottram J. C., Stead J., 2011, *MNRAS*, 416, 972
- De Pree C. G., Goss W. M., Gaume R. A., 1998, *ApJ*, 500, 847
- Devine K. E., Chandler C. J., Brogan C., Churchwell E., Indebetouw R., Shirley Y., Borg K. J., 2011, *ApJ*, 733, 44
- Dirienzo W. J., Brogan C., Indebetouw R., Chandler C. J., Friesen R. K., Devine K. E., 2015, *AJ*, 150, 159
- Dobbs C. L., Bonnell I. A., Clark P. C., 2005, *MNRAS*, 360, 2
- Dore L., Caselli P., Beninati S., Bourke T., Myers P. C., Cazzoli G., 2004, *A&A*, 413, 1177
- Draine B. T., 2009, in *Astronomical Society of the Pacific Conference Series*, Vol. 414, *Cosmic Dust - Near and Far*, Henning T., Grün E., Steinacker J., eds., p. 453
- Draine B. T., 2011, *Physics of the Interstellar and Intergalactic Medium*
- Draine B. T., Lee H. M., 1984, *ApJ*, 285, 89
- Duarte-Cabral A., Dobbs C. L., 2016, *MNRAS*, 458, 3667

- Dutra C. M., Ortolani S., Bica E., Barbuy B., Zoccali M., Momany Y., 2003, *A&A*, 408, 127
- Egan M. P., Shipman R. F., Price S. D., Carey S. J., Clark F. O., Cohen M., 1998, *ApJL*, 494, L199+
- Elmegreen B. G., 1979, *ApJ*, 231, 372
- Elmegreen B. G., 1999, *ApJ*, 515, 323
- Emsellem E., Renaud F., Bournaud F., Elmegreen B., Combes F., Gabor J. M., 2015, *MNRAS*, 446, 2468
- Enoch M. L., Lee J.-E., Harvey P., Dunham M. M., Schnee S., 2010, *ApJL*, 722, L33
- Epchtein N. et al., 1997, *The Messenger*, 87, 27
- Evans, II N. J., 1999, *ARA&A*, 37, 311
- Federrath C., Klessen R. S., 2012, *ApJ*, 761, 156
- Federrath C., Klessen R. S., Schmidt W., 2008, *ApJL*, 688, L79
- Federrath C. et al., 2016, *ArXiv e-prints*
- Field G. B., Goldsmith D. W., Habing H. J., 1969, *ApJL*, 155, L149
- Figer D. F., Kim S. S., Morris M., Serabyn E., Rich R. M., McLean I. S., 1999, *ApJ*, 525, 750
- Figer D. F., McLean I. S., Morris M., 1999, *ApJ*, 514, 202
- Figer D. F. et al., 2002, *ApJ*, 581, 258
- Fitzpatrick E. L., 1999, *PASP*, 111, 63
- Flower D., 2003, *Molecular Collisions in the Interstellar Medium*. p. 145
- Flower D., des Forets G. P., Field D., May P., 1996, *Monthly Notices of the Royal Astronomical Society*, 280, 447

- Flower D. R., Pineau Des Forêts G., Walmsley C. M., 2006, *A&A*, 456, 215
- Fontani F., Busquet G., Palau A., Caselli P., Sánchez-Monge Á., Tan J. C., Audard M., 2015, *A&A*, 575, A87
- Fontani F., Caselli P., Crapsi A., Cesaroni R., Molinari S., Testi L., Brand J., 2006, *A&A*, 460, 709
- Fontani F. et al., 2011, *A&A*, 529, L7+
- Foster J. B. et al., 2014, *ApJ*, 791, 108
- Foster J. B., Stead J. J., Benjamin R. A., Hoare M. G., Jackson J. M., 2012, *ApJ*, 751, 157
- Fregeau J. M., Joshi K. J., Portegies Zwart S. F., Rasio F. A., 2002, *ApJ*, 570, 171
- Frerking M. A., Langer W. D., Wilson R. W., 1982, *ApJ*, 262, 590
- Friesen R. K., Di Francesco J., Myers P. C., Belloche A., Shirley Y. L., Bourke T. L., André P., 2010, *ApJ*, 718, 666
- Friesen R. K., Kirk H. M., Shirley Y. L., 2013, *ApJ*, 765, 59
- Fumagalli M., da Silva R. L., Krumholz M. R., 2011, *ApJL*, 741, L26
- Gao Y., Solomon P. M., 2004, *ApJ*, 606, 271
- Garay G., Faúndez S., Mardones D., Bronfman L., Chini R., Nyman L.-Å., 2004, *ApJ*, 610, 313
- Gaume R. A., Claussen M. J., de Pree C. G., Goss W. M., Mehringer D. M., 1995, *ApJ*, 449, 663
- Gerner T., Shirley Y., Beuther H., Semenov D., Linz H., Abertsson T., Henning T., 2015, *ArXiv e-prints*
- Gilmore G., 2001, in *Starburst Galaxies: Near and Far*, Tacconi L., Lutz D., eds., p. 34
- Ginsburg A. et al., 2013, *ApJS*, 208, 14

- Ginsburg A. et al., 2016, *A&A*, 586, A50
- Ginsburg A. et al., 2015, *A&A*, 584, L7
- Gómez G. C., Vázquez-Semadeni E., 2014, *ApJ*, 791, 124
- Goodman A. A., Benson P. J., Fuller G. A., Myers P. C., 1993, *ApJ*, 406, 528
- Goodwin S. P., Nutter D., Kroupa P., Ward-Thompson D., Whitworth A. P., 2008, *A&A*, 477, 823
- Gottlieb C. A., Palmer P., Rickard L. J., Zuckerman B., 1973, *ApJ*, 182, 699
- Grenier I. A., Casandjian J.-M., Terrier R., 2005, *Science*, 307, 1292
- Guesten R., Downes D., 1983, *A&A*, 117, 343
- Habing H. J., 1996, *A&AR*, 7, 97
- Hacar A., Alves J., Burkert A., Goldsmith P., 2016a, *A&A*, 591, A104
- Hacar A., Alves J., Forbrich J., Meingast S., Kubiak K., Großschedl J., 2016b, *A&A*, 589, A80
- Hacar A., Alves J., Tafalla M., Goicoechea J. R., 2017, *ArXiv e-prints*
- Hacar A., Kainulainen J., Tafalla M., Beuther H., Alves J., 2016c, *A&A*, 587, A97
- Hacar A., Tafalla M., Alves J., 2017, *ArXiv e-prints*
- Hacar A., Tafalla M., Forbrich J., Alves J., Meingast S., Grossschedl J., Teixeira P. S., 2018, *ArXiv e-prints*
- Hacar A., Tafalla M., Kauffmann J., Kovács A., 2013, *A&A*, 554, A55
- Hartmann L., Ballesteros-Paredes J., Bergin E. A., 2001, *ApJ*, 562, 852
- Hasegawa T., Sato F., Whiteoak J. B., Miyawaki R., 1994, *ApJL*, 429, L77
- Heitsch F., Hartmann L. W., Slyz A. D., Devriendt J. E. G., Burkert A., 2008, *ApJ*, 674, 316

- Heitsch F., Zweibel E. G., Slyz A. D., Devriendt J. E. G., 2004, *ApJ*, 603, 165
- Hennebelle P., Chabrier G., 2011, *ApJL*, 743, L29
- Hennebelle P., Chabrier G., 2013, *ApJ*, 770, 150
- Henshaw J. D., Caselli P., Fontani F., Jiménez-Serra I., Tan J. C., 2014, *MNRAS*, 440, 2860, (Paper VI)
- Henshaw J. D., Caselli P., Fontani F., Jiménez-Serra I., Tan J. C., Hernandez A. K., 2013, *MNRAS*, 428, 3425, (Paper IV)
- Henshaw J. D. et al., 2016a, ArXiv e-prints
- Henshaw J. D. et al., 2017, *MNRAS*, 464, L31
- Henshaw J. D., Longmore S. N., Kruijssen J. M. D., 2016, *MNRAS*, 463, L122
- Henshaw J. D. et al., 2016b, *MNRAS*, 457, 2675
- Hernandez A. K., Tan J. C., 2011, *ApJ*, 730, 44
- Hernandez A. K., Tan J. C., 2015, *ApJ*, 809, 154
- Hernandez A. K., Tan J. C., Caselli P., Butler M. J., Jiménez-Serra I., Fontani F., Barnes P., 2011, *ApJ*, 738, 11, (Paper II)
- Hernandez A. K., Tan J. C., Kainulainen J., Caselli P., Butler M. J., Jiménez-Serra I., Fontani F., 2012, *ApJL*, 756, L13, (Paper III)
- Heyer M., Krawczyk C., Duval J., Jackson J. M., 2009, *ApJ*, 699, 1092
- Högbom J. A., 1974, *A&AS*, 15, 417
- Hosokawa T., Omukai K., 2009, *ApJ*, 691, 823
- Huettmeister S., Wilson T. L., Mauersberger R., Lemme C., Dahmen G., Henkel C., 1995, *A&A*, 294, 667
- Ikeuchi S., Habe A., Tanaka Y. D., 1984, *MNRAS*, 207, 909

- Immer K., Menten K. M., Schuller F., Lis D. C., 2012a, *A&A*, 548, A120
- Immer K., Schuller F., Omont A., Menten K. M., 2012b, *A&A*, 537, A121
- Jackson J. M., Finn S. C., Chambers E. T., Rathborne J. M., Simon R., 2010, *ApJL*, 719, L185
- Jackson J. M. et al., 2006, *ApJS*, 163, 145
- Jeans J. H., 1902, *Philosophical Transactions of the Royal Society of London Series A*, 199, 1
- Jiménez-Serra I., Caselli P., Fontani F., Tan J. C., Henshaw J. D., Kainulainen J., Hernandez A. K., 2014, *MNRAS*, 439, 1996, (Paper V)
- Jiménez-Serra I., Caselli P., Tan J. C., Hernandez A. K., Fontani F., Butler M. J., van Loo S., 2010, *MNRAS*, 406, 187, (Paper I)
- Johnston K. G., Beuther H., Linz H., Schmiedeke A., Ragan S. E., Henning T., 2014, *A&A*, 568, A56
- Jones P. A. et al., 2012, *MNRAS*, 419, 2961
- Kainulainen J., Beuther H., Henning T., Plume R., 2009, *A&A*, 508, L35
- Kainulainen J., Stutz A. M., Stanke T., Abreu-Vicente J., Beuther H., Henning T., Johnston K. G., Megeath S. T., 2017, *A&A*, 600, A141
- Kainulainen J., Tan J. C., 2013, *A&A*, 549, A53
- Kauffmann J., Bertoldi F., Bourke T. L., Evans, II N. J., Lee C. W., 2008, *A&A*, 487, 993
- Kauffmann J., Pillai T., 2010, *ApJL*, 723, L7
- Kauffmann J., Pillai T., Zhang Q., 2013, *ApJL*, 765, L35
- Kauffmann J., Pillai T., Zhang Q., Menten K. M., Goldsmith P. F., Lu X., Guzmán A. E., 2016, *ArXiv e-prints*

- Kennicutt R. C., Evans N. J., 2012, *ARA&A*, 50, 531
- Kennicutt, Jr. R. C., 1998a, *ARA&A*, 36, 189
- Kennicutt, Jr. R. C., 1998b, *ApJ*, 498, 541
- Kereš D., Katz N., Davé R., Fardal M., Weinberg D. H., 2009, *MNRAS*, 396, 2332
- Keto E., Zhang Q., Kurtz S., 2008, *ApJ*, 672, 423
- Kim W.-T., Ostriker E. C., Stone J. M., 2002, *ApJ*, 581, 1080
- Kim W.-T., Ostriker E. C., Stone J. M., 2003, *ApJ*, 599, 1157
- Koepferl C. M., Robitaille T. P., Morales E. F. E., Johnston K. G., 2015, *ApJ*, 799, 53
- Kolmogorov A., 1941, *Akademiia Nauk SSSR Doklady*, 30, 301
- Kong S., Caselli P., Tan J. C., Wakelam V., Sipilä O., 2015, *ApJ*, 804, 98
- Kong S., Tan J. C., Caselli P., Fontani F., Liu M., Butler M. J., 2017, *ApJ*, 834, 193
- Kong S. et al., 2016, *ApJ*, 821, 94
- Könyves V. et al., 2015, *A&A*, 584, A91
- Krieger N. et al., 2017, *ApJ*, 850, 77
- Kroupa P., 2001, *MNRAS*, 322, 231
- Kruijssen J. M. D., Dale J. E., Longmore S. N., 2015, *MNRAS*, 447, 1059
- Kruijssen J. M. D., Longmore S. N., 2013, *MNRAS*, 435, 2598
- Kruijssen J. M. D., Longmore S. N., 2014, *MNRAS*, 439, 3239
- Kruijssen J. M. D., Longmore S. N., Elmegreen B. G., Murray N., Bally J., Testi L., Kennicutt R. C., 2014, *MNRAS*, 440, 3370
- Krumholz M. R., Dekel A., McKee C. F., 2012, *ApJ*, 745, 69
- Krumholz M. R., Kruijssen J. M. D., 2015, *MNRAS*, 453, 739

- Krumholz M. R., Kruijssen J. M. D., Crocker R. M., 2016, ArXiv e-prints
- Krumholz M. R., Matzner C. D., McKee C. F., 2006, *ApJ*, 653, 361
- Krumholz M. R., McKee C. F., 2005, *ApJ*, 630, 250
- Krumholz M. R., McKee C. F., 2008, *Nat*, 451, 1082
- Krumholz M. R., McKee C. F., Klein R. I., 2005, *Nat*, 438, 332
- Kurayama T., Nakagawa A., Sawada-Satoh S., Sato K., Honma M., Sunada K., Hirota T., Imai H., 2011, *PASJ*, 63, 513
- Kutner M. L., Ulich B. L., 1981, *ApJ*, 250, 341
- Kwan J., Valdes F., 1987, *ApJ*, 315, 92
- Lada C. J., Forbrich J., Lombardi M., Alves J. F., 2012, *ApJ*, 745, 190
- Lada C. J., Lada E. A., 2003, *ARA&A*, 41, 57
- Lada C. J., Lada E. A., Clemens D. P., Bally J., 1994, *ApJ*, 429, 694
- Lada C. J., Lombardi M., Alves J. F., 2010, *ApJ*, 724, 687
- Lang C. C., Goss W. M., Cyganowski C., Clubb K. I., 2010, *ApJS*, 191, 275
- Langer W. D., Velusamy T., Pineda J. L., Willacy K., Goldsmith P. F., 2014, *A&A*, 561, A122
- Larson R. B., 1967, *PASP*, 79, 434
- Larson R. B., 1981, *MNRAS*, 194, 809
- Launhardt R. et al., 2010, *ApJS*, 188, 139
- Launhardt R., Zylka R., Mezger P. G., 2002, *A&A*, 384, 112
- Lawton B. et al., 2010, *ApJ*, 716, 453
- Lazareff B., Lucas R., Encrenaz P., 1978, *A&A*, 70, L77

- Le Petit F., Roueff E., Le Bourlot J., 2002, *A&A*, 390, 369
- Lee E. J., Murray N., Rahman M., 2012, *ApJ*, 752, 146
- Leroy A. K. et al., 2016, *ApJ*, 831, 16
- Leroy A. K. et al., 2017, *ApJ*, 846, 71
- Leroy A. K. et al., 2013, *AJ*, 146, 19
- Li Y., Calzetti D., Kennicutt R. C., Hong S., Engelbracht C. W., Dale D. A., Moustakas J., 2010, *ApJ*, 725, 677
- Li Z.-Y., Banerjee R., Pudritz R. E., Jørgensen J. K., Shang H., Krasnopolsky R., Maury A., 2014, *Protostars and Planets VI*, 173
- Linsky J. L. et al., 2006, *ApJ*, 647, 1106
- Lis D. C., Li Y., Dowell C. D., Menten K. M., 1999, in *ESA Special Publication, Vol. 427, The Universe as Seen by ISO*, Cox P., Kessler M., eds., p. 627
- Liu T. et al., 2018, *ArXiv e-prints*
- Longmore S. et al., 2016, *ArXiv e-prints*
- Longmore S. N. et al., 2013a, *MNRAS*, 429, 987
- Longmore S. N. et al., 2013b, *MNRAS*, 433, L15
- Longmore S. N. et al., 2014, *Protostars and Planets VI*, 291
- Longmore S. N. et al., 2012, *ApJ*, 746, 117
- Lopez L. A., Krumholz M. R., Bolatto A. D., Prochaska J. X., Ramirez-Ruiz E., 2011, *ApJ*, 731, 91
- Lopez L. A., Krumholz M. R., Bolatto A. D., Prochaska J. X., Ramirez-Ruiz E., Castro D., 2014, *ApJ*, 795, 121
- Lou Y.-Q., Gao Y., 2011, *MNRAS*, 412, 1755

- Mac Low M.-M., 1999, *ApJ*, 524, 169
- Mac Low M.-M., Klessen R. S., 2004, *Reviews of Modern Physics*, 76, 125
- Mac Low M.-M., Klessen R. S., Burkert A., Smith M. D., 1998, *Physical Review Letters*, 80, 2754
- Marsh K. A. et al., 2016, *MNRAS*, 459, 342
- Mathis J. S., Rumpl W., Nordsieck K. H., 1977, *ApJ*, 217, 425
- Matthews L. D., Greenhill L. J., Goddi C., Chandler C. J., Humphreys E. M. L., Kunz M. W., 2010, *ApJ*, 708, 80
- McKee C. F., Ostriker E. C., 2007, *ARA&A*, 45, 565
- McKee C. F., Ostriker J. P., 1977, *ApJ*, 218, 148
- McKee C. F., Tan J. C., 2002, *Nat*, 416, 59
- McKee C. F., Tan J. C., 2003, *ApJ*, 585, 850
- Mehring D. M., Palmer P., Goss W. M., Yusef-Zadeh F., 1993, *ApJ*, 412, 684
- Mehring D. M., Yusef-Zadeh F., Palmer P., Goss W. M., 1992, *ApJ*, 401, 168
- Meñshchikov A. et al., 2010, *A&A*, 518, L103
- Mestel L., Spitzer, Jr. L., 1956, *MNRAS*, 116, 503
- Miettinen O., 2014, *A&A*, 562, A3
- Miettinen O., Hennemann M., Linz H., 2011, *A&A*, 534, A134
- Millar T. J., Bennett A., Herbst E., 1989, *ApJ*, 340, 906
- Miralles M. P., Rodriguez L. F., Scalise E., 1994, *ApJS*, 92, 173
- Molinari S. et al., 2011, *ApJL*, 735, L33
- Molinari S., Brand J., Cesaroni R., Palla F., 1996, *A&A*, 308, 573

- Molinari S. et al., 2016, *A&A*, 591, A149
- Molinari S. et al., 2010, *PASP*, 122, 314
- Montenegro L. E., Yuan C., Elmegreen B. G., 1999, *ApJ*, 520, 592
- Motte F., Bontemps S., Louvet F., 2017, *ArXiv e-prints*
- Mould J. R., 1982, *ARA&A*, 20, 91
- Mouschovias T. C., Shu F. H., Woodward P. R., 1974, *A&A*, 33, 73
- Mouschovias T. C., Spitzer, Jr. L., 1976, *ApJ*, 210, 326
- Muench A. A., Lada C. J., Luhman K. L., Muzerolle J., Young E., 2007, *AJ*, 134, 411
- Murphy E. J. et al., 2011, *ApJ*, 737, 67
- Murray N., Rahman M., 2010, *ApJ*, 709, 424
- Myers P. C., 1983, *ApJ*, 270, 105
- Myers P. C., Dame T. M., Thaddeus P., Cohen R. S., Silverberg R. F., Dwek E., Hauser M. G., 1986, *ApJ*, 301, 398
- Myers P. C., Evans, II N. J., Ohashi N., 2000, *Protostars and Planets IV*, 217
- Myers P. C., Fuller G. A., 1992, *ApJ*, 396, 631
- Nguyen Luong Q. et al., 2011, *A&A*, 535, A76
- Nordlund Å. K., Padoan P., 1999, in *Interstellar Turbulence*, Franco J., Carraminana A., eds., p. 218
- Offner S. S. R., Clark P. C., Hennebelle P., Bastian N., Bate M. R., Hopkins P. F., Moraux E., Whitworth A. P., 2014, *Protostars and Planets VI*, 53
- Oliveira C. M., Hébrard G., Howk J. C., Kruk J. W., Chayer P., Moos H. W., 2003, *ApJ*, 587, 235
- O'Neil K., 2002, *arXiv preprint astro-ph/0203001*

- Orkisz J. H. et al., 2017, *A&A*, 599, A99
- Ossenkopf V., Henning T., 1994, *A&A*, 291, 943
- Ostriker E. C., Stone J. M., Gammie C. F., 2001, *ApJ*, 546, 980
- Ott J., Weiß A., Staveley-Smith L., Henkel C., Meier D. S., 2014, *ApJ*, 785, 55
- Padoan P., Federrath C., Chabrier G., Evans, II N. J., Johnstone D., Jørgensen J. K.,
McKee C. F., Nordlund Å., 2014, *Protostars and Planets VI*, 77
- Padoan P., Jones B. J. T., Nordlund Å. P., 1997, *ApJ*, 474, 730
- Padoan P., Nordlund Å., 2011, *ApJ*, 730, 40
- Pagani L., Daniel F., Dubernet M., 2009, *A&A*, 494, 719
- Pagani L., Salez M., Wannier P. G., 1992, *A&A*, 258, 479
- Pagani L. et al., 2009, *A&A*, 494, 623
- Palla F., Stahler S. W., 2000, *ApJ*, 540, 255
- Parker E. N., 1966, *ApJ*, 145, 811
- Penzias A. A., Burrus C. A., 1973, *ARA&A*, 11, 51
- Perault M. et al., 1996, *A&A*, 315, L165
- Peretto N., Fuller G. A., 2009, *A&A*, 505, 405
- Peretto N. et al., 2013, *A&A*, 555, A112
- Peretto N. et al., 2010, *A&A*, 518, L98
- Pérez-González P. G. et al., 2006, *ApJ*, 648, 987
- Pezzuto S. et al., 2012, *A&A*, 547, A54
- Pilbratt G. L. et al., 2010, *A&A*, 518, L1

- Pillai T., Kauffmann J., Tan J. C., Goldsmith P. F., Carey S. J., Menten K. M., 2015, *ApJ*, 799, 74
- Pineda J. E. et al., 2011a, *ApJ*, 743, 201
- Pineda J. E., Goodman A. A., Arce H. G., Caselli P., Longmore S., Corder S., 2011b, *ApJL*, 739, L2
- Pineda J. E. et al., 2015, *Nat*, 518, 213
- Plambeck R. L. et al., 2013, *ApJ*, 765, 40
- Polychroni D. et al., 2013, *ApJL*, 777, L33
- Pon A., Caselli P., Johnstone D., Kaufman M., Butler M. J., Fontani F., Jiménez-Serra I., Tan J. C., 2015, *A&A*, 577, A75
- Pon A. et al., 2016a, *A&A*, 587, A96
- Pon A. et al., 2016b, *ApJ*, 827, 107
- Punanova A., Caselli P., Pon A., Belloche A., André P., 2015, *ArXiv e-prints*
- Ragan S. E., Bergin E. A., Wilner D., 2011, *ApJ*, 736, 163
- Ragan S. E., Henning T., Tackenberg J., Beuther H., Johnston K. G., Kainulainen J., Linz H., 2014, *A&A*, 568, A73
- Ramesh B., Bronfman L., Deguchi S., 1997, *PASJ*, 49, 307
- Rathborne J. M., Jackson J. M., Chambers E. T., Simon R., Shipman R., Frieswijk W., 2005, *ApJL*, 630, L181
- Rathborne J. M., Jackson J. M., Simon R., 2006, *ApJ*, 641, 389
- Rathborne J. M., Jackson J. M., Zhang Q., Simon R., 2008, *ApJ*, 689, 1141
- Rathborne J. M. et al., 2015, *ApJ*, 802, 125
- Rathborne J. M. et al., 2014a, *ApJ*, 786, 140

- Rathborne J. M. et al., 2014b, *ApJL*, 795, L25
- Reid M. J., Dame T. M., Menten K. M., Brunthaler A., 2016, *ApJ*, 823, 77
- Reid M. J. et al., 2014, *ApJ*, 783, 130
- Reid M. J. et al., 2009, *ApJ*, 700, 137
- Relaño M., Lisenfeld U., Pérez-González P. G., Vílchez J. M., Battaner E., 2007, *ApJL*, 667, L141
- Rieke G. H., Alonso-Herrero A., Weiner B. J., Pérez-González P. G., Blaylock M., Donley J. L., Marcillac D., 2009, *ApJ*, 692, 556
- Robin A. C., Reylé C., Derrière S., Picaud S., 2003, *A&A*, 409, 523
- Roman-Duval J., Heyer M., Brunt C. M., Clark P., Klessen R., Shetty R., 2016, *ApJ*, 818, 144
- Roman-Duval J., Jackson J. M., Heyer M., Johnson A., Rathborne J., Shah R., Simon R., 2009, *ApJ*, 699, 1153
- Roman-Duval J., Jackson J. M., Heyer M., Rathborne J., Simon R., 2010, *ApJ*, 723, 492
- Rubin R. H., Swenson, Jr. G. W., Benson R. C., Tigelaar H. L., Flygare W. H., 1971, *ApJL*, 169, L39
- Sakai T. et al., 2013, *ApJL*, 775, L31
- Salaris M., Cassisi S., 2005, *Front Matter*. Wiley Online Library
- Salpeter E. E., 1955, *ApJ*, 121, 161
- Sandstrom K. M. et al., 2013, *ApJ*, 777, 5
- Sanhueza P., Garay G., Bronfman L., Mardones D., May J., Saito M., 2010, *ApJ*, 715, 18
- Sato F., Hasegawa T., Whiteoak J. B., Miyawaki R., 2000, *ApJ*, 535, 857

- Scannapieco C. et al., 2012, MNRAS, 423, 1726
- Schlegel D. J., Finkbeiner D. P., Davis M., 1998, ApJ, 500, 525
- Schmidt M., 1959, ApJ, 129, 243
- Schmiedeke A. et al., 2016, ArXiv e-prints
- Schnee S., Di Francesco J., Enoch M., Friesen R., Johnstone D., Sadavoy S., 2012, ApJ, 745, 18
- Schneider S., Elmegreen B. G., 1979, ApJS, 41, 87
- Schödel R., Najarro F., Muzic K., Eckart A., 2010, A&A, 511, A18
- Shepherd D. S., Nürnberger D. E. A., Bronfman L., 2004, ApJ, 602, 850
- Shepherd D. S. et al., 2007, ApJ, 669, 464
- Shetty R., Beaumont C. N., Burton M. G., Kelly B. C., Klessen R. S., 2012, MNRAS, 425, 720
- Shetty R., Ostriker E. C., 2006, ApJ, 647, 997
- Shirley Y. L., 2015, PASP, 127, 299
- Shu F. H., Adams F. C., Lizano S., 1987, ARA&A, 25, 23
- Simon R., Jackson J. M., Rathborne J. M., Chambers E. T., 2006a, ApJ, 639, 227
- Simon R., Rathborne J. M., Shah R. Y., Jackson J. M., Chambers E. T., 2006b, ApJ, 653, 1325
- Sipilä O., Caselli P., Harju J., 2013, A&A, 554, A92
- Smith R. J., Glover S. C. O., Klessen R. S., Fuller G. A., 2016, MNRAS, 455, 3640
- Smith R. J., Shetty R., Beuther H., Klessen R. S., Bonnell I. A., 2013, ApJ, 771, 24
- Sodroski T. J. et al., 1995, ApJ, 452, 262

- Sokolov V. et al., 2017, *A&A*, 606, A133
- Sokolov V. et al., 2018, ArXiv e-prints
- Solomon P. M., Rivolo A. R., Barrett J., Yahil A., 1987, *ApJ*, 319, 730
- Stahler S. W., Palla F., 2005, *The Formation of Stars*. p. 865
- Suutarinen A., Haikala L. K., Harju J., Juvela M., André P., Kirk J. M., Könyves V., White G. J., 2013, *A&A*, 555, A140
- Suzuki T. K., Fukui Y., Torii K., Machida M., Matsumoto R., 2015, *MNRAS*, 454, 3049
- Swinbank A. M. et al., 2011, *ApJ*, 742, 11
- Tackenberg J. et al., 2014, *A&A*, 565, A101
- Tafalla M., Hacar A., 2015, *A&A*, 574, A104
- Tan J. C., Beltrán M. T., Caselli P., Fontani F., Fuente A., Krumholz M. R., McKee C. F., Stolte A., 2014, *Protostars and Planets VI*, 149
- Tan J. C., Kong S., Butler M. J., Caselli P., Fontani F., 2013, *ApJ*, 779, 96
- Tang N., Li D., Heiles C., Wang S., Pan Z., Wang J.-J., 2016, *A&A*, 593, A42
- Tasker E. J., Tan J. C., 2009, *ApJ*, 700, 358
- Taylor G. B., Morris M., Schulman E., 1993, *AJ*, 106, 1978
- Toomre A., 1964, *ApJ*, 139, 1217
- Torrey P., Hopkins P. F., Faucher-Giguère C.-A., Vogelsberger M., Quataert E., Kereš D., Murray N., 2016, ArXiv e-prints
- Vacca W. D., Garmany C. D., Shull J. M., 1996, *ApJ*, 460, 914
- Vazquez-Semadeni E., 1994, *ApJ*, 423, 681
- Vázquez-Semadeni E., Cantó J., Lizano S., 1998, *ApJ*, 492, 596

- Vázquez-Semadeni E., Colín P., Gómez G. C., Ballesteros-Paredes J., Watson A. W., 2010, *ApJ*, 715, 1302
- Vázquez-Semadeni E., Gómez G. C., Jappsen A. K., Ballesteros-Paredes J., González R. F., Klessen R. S., 2007, *ApJ*, 657, 870
- Wakelam V. et al., 2012, *ApJS*, 199, 21
- Walker D. L., Longmore S. N., Bastian N., Kruijssen J. M. D., Rathborne J. M., Galván-Madrid R., Liu H. B., 2016, *MNRAS*
- Walker D. L., Longmore S. N., Bastian N., Kruijssen J. M. D., Rathborne J. M., Jackson J. M., Foster J. B., Contreras Y., 2015, *MNRAS*, 449, 715
- Walker D. L. et al., 2018, *MNRAS*, 474, 2373
- Walmsley C. M., Flower D. R., Pineau des Forêts G., 2004, *A&A*, 418, 1035
- Walsh A. J., Bertoldi F., Burton M. G., Nikola T., 2001, *MNRAS*, 326, 36
- Wang Y., Zhang Q., Rathborne J. M., Jackson J., Wu Y., 2006, *ApJL*, 651, L125
- Watson D., 2011, *A&A*, 533, A16
- Weingartner J. C., Draine B. T., 2001, *ApJ*, 548, 296
- White S. D. M., Rees M. J., 1978, *MNRAS*, 183, 341
- Williams G. M., Peretto N., Avison A., Duarte-Cabral A., Fuller G. A., 2018, *ArXiv e-prints*
- Williams J. P., Blitz L., McKee C. F., 2000, *Protostars and Planets IV*, 97
- Wilson T. L., Matteucci F., 1992, *A&AR*, 4, 1
- Wilson T. L., Rood R., 1994, *ARA&A*, 32, 191
- Wolszczan A., Cordes J. M., Dewey R. J., 1991, *ApJL*, 372, L99
- Wu H., Cao C., Hao C.-N., Liu F.-S., Wang J.-L., Xia X.-Y., Deng Z.-G., Young C. K.-S., 2005, *ApJL*, 632, L79

Xu D., Li D., Yue N., Goldsmith P. F., 2016a, ArXiv e-prints

Xu J.-L., Li D., Zhang C.-P., Liu X.-L., Wang J.-J., Ning C.-C., Ju B.-G., 2016b, ApJ, 819, 117

Yanagida T. et al., 2014, ApJL, 794, L10

Yusef-Zadeh F. et al., 2009, ApJ, 702, 178

Zhang C.-P., Yuan J.-H., Li G.-X., Zhou J.-J., Wang J.-J., 2017, A&A, 598, A76

Zhu Y.-N., Wu H., Cao C., Li H.-N., 2008, ApJ, 686, 155

Zucker C., Battersby C., Goodman A., 2015, ApJ, 815, 23

Zucker C., Battersby C., Goodman A., 2017, ArXiv e-prints